University of Southampton

Faculty of Engineering and Physical Sciences

School of Engineering

Multiscale Mathematical Modelling of Water and Solute Movement in Plant Systems

by

Simon Jack Duncan

Thesis for the degree of Doctor of Philosophy

September 2018

University of Southampton

Abstract

Faculty of Engineering and Physical Sciences
School of Engineering

Doctor of Philosophy

Multiscale Mathematical Modelling of Water and Solute Movement in Plant Systems

by Simon Jack Duncan

This thesis deals with multiscale mathematical modelling of water and solute movement in soil systems, with particular focus on the soil structures that are formed by agricultural practices. The first mathematical model is developed to describe water movement in a generalised ridge and furrow soil system, which is coupled to dynamic surface water infiltration due to ponding. The model is based on a non-linear Darcy-Richards' equation in pressure formulation to describe variably saturated soil. This model is then extended and coupled to an advective-diffusion equation for solute movement. Using the mathematical model, we compare water and solute movement in two soil structures: a ridge and furrow soil and a flat field soil. We highlight scenarios that increase the risk of solute leaching in both flat field and ridged soils. We also discuss the key factors affecting solute leaching in these systems. We then focus on the water dynamics in the regions of soil that contain crops. Using the Darcy-Richards' equation for water movement, we apply multiple scale asymptotic homogenisation to derive an approximate set of equations that captures water movement around crops. We find the approximate equations to be more computationally efficient by a factor of $\mathcal{O}(10^2)$ when compared to the full equations. Extending this idea, we develop a mathematical model that captures crop growth and its effect on solute movement. The growth and development of the crops is dependent on the cumulative uptake of nutrients available to the plant. The soil is modelled as a poroelastic material that is able to deform due to crop growth. Special attention is paid to the reduction in void space, change in local volumetric water content and the impact on solute movement as the crops increase in size. Multiple scale asymptotic homogenisation is used to derive a set of approximate equations that describe macroscale nutrient movement and crop growth in the soil. This approach increases computational efficient by a factor of $\mathcal{O}(10^3)$ while maintaining a percentage error of $\lesssim 2\%$.

Contents

List of Figures

List of Tables

List of Publications

Journal Articles

• Keyes, S., Cooper, L., **Duncan, S.**, Koebernick, N., Fletcher, D. M., Scotson, C., Van Veelen, A., Sinclair, I., and Roose, T. Measurement of micro- scale soil deformation around roots using four-dimensional synchrotron tomography and image correlation. Journal of The Royal Society Interface 14, 136 (2017), 20170560.

• **Duncan, S.**, Daly, K., Sweeney, P., and Roose, T. Mathematical modelling of water and solute movement in ridge plant systems with dynamic ponding. European Journal of Soil Science 69, 2 (2018), 265−278.

• **Duncan, S. J.**, K. R. Daly, P. Sweeney, and T. Roose. Mathematical modelling of water and solute movement in ridge *versus* flat plant systems. European Journal of Soil Science (2018).

Nomenclature

Shown here are the mathematical symbols used throughout the main body of this thesis with their associated units. Symbols used once or in the introductory literature are not listed.

Coefficients

$\lvert z_a \rvert$	m	absolute soil depth
κ_b	s^{-1}	absorption rate
κ_a	m^2	air permeability
C	m	average soil depth
τ	s^{-1}	biodegredation rate
b	$-$	buffer power
p_c	Pa	characteristic suction pressure
ρ	kg m^{-3}	density
κ_d	s^{-1}	desorption rate
D	m^2 s^{-1}	diffusion coefficient
D_f	m^2 s^{-1}	diffusion in free liquid
g	m s^{-2}	gravity
t^*_λ	s	half life
σ	Pa^{-1}	Heaviside transition width
K	m s^{-1}	hydraulic conductivity
$\mathfrak{T}$	$-$	identity tensor
d	$-$	impedance factor
I_c	m s^{-1}	infiltration capacity
p_∞	Pa	initial pressure profile
r^*	m	initial tuber radius
l_x	m	macroscale length
c_{max}	kg m^{-3}	maximum solute concentration
l_y	m	microlength scale
$\tilde{x}_{\text{min}}$	m	minimum pond depth

d_s	kg m^{-3} s^{-1}	net sorption transfer rate
d_l	kg m^{-3} s^{-1}	net transfer rate to solution
ν	$-$	Poisson ratio
p_0	Pa	pressure at the base of the soil
k_r	m^2 s^{-1} Pa^{-1}	radial conductivity
q_s	m s^{-1}	rainfall
α	kg^{-1} m^3	ratio between growth and uptake
ε	$-$	ratio between l_y and l_x
ϕ_r	$-$	residual water content
η	m	ridged domain width
B	m^{-1}	ridge wave number
l_d	m^{-2}	root length density
p_r	Pa	root xylem pressure
ζ_t	Pa	saturated interface pressure
κ_s	m^2	saturated permeability
G	Pa	shear modulus
c_m	kg m^{-2} s^{-1}	solute application rate
ξ	s^{-1}	solute uptake rate
m	$-$	van Genuchten parameter
A	m	variation in soil depth
μ_a	Pa s^{-1}	viscosity of air
μ_w	Pa s^{-1}	viscosity of water
κ_w	m^2	water permeability
λ_c	s^{-1} Pa^{-1}	xylem water conductivity

Variables

$\tilde{\mathbf{v}}_a$	m s^{-1}	air velocity
χ_k	$-$	cell problem variable
$\mathfrak{D}_e$	m^2 s^{-1}	diffusion tensor
H_S	$-$	Heaviside approximation
$\tilde{h}_0\left(\tilde{t}\right)$	m	maximum pond depth
$\boldsymbol{\omega}_{\text{mesh}}$	m s^{-1}	mesh velocity
$\tilde{x}_0\left(\tilde{t}\right)$	m	ponding interface
$\tilde{V}\left(\tilde{t}\right)$	m^3	pond volume
ϕ	$-$	porosity
S	$-$	relative saturation
$\tilde{\mathbf{u}}_s$	m	soil solid displacement

$\tilde{\mathbf{v}}_s$	m s^{-1}	soil solid velocity
$\tilde{\chi}$	m	soil surface function
$\tilde{p}_a$	Pa	soil water air pressure
$\tilde{p}_w$	Pa	soil water pore pressure
$\tilde{c}$	kg m^{-3}	solute in soil solution
$\tilde{c}_s$	kg m^{-3}	sorbed solute concentration
$\mathbf{x}$	m	space $\tilde{\mathbf{x}} = [\tilde{x}_1, \tilde{x}_2, \tilde{x}_3]$
$\tilde{R}_0\left(\tilde{t}\right)$	m^3 s^{-1}	surface runoff
t	s	time
$\tilde{\Xi}$	m	tuber displacement
$\tilde{r}$	m	tuber radius
ϕ_a	$-$	volumetric air content
ϕ_s	$-$	volumetric soil solid
ϕ_w	$-$	volumetric water content
$\tilde{F}_w$	s^{-1}	water root uptake
$\tilde{\mathbf{v}}_w$	m s^{-1}	water velocity

Symbols

$\in$	$-$	contained in
$\sim$	$-$	dimensional variable
$\boldsymbol{\nabla}\cdot$	m^{-1}	divergence operator
$\emptyset$	$-$	empty set
$\|\|\cdot\|\|_2$	$-$	Euclidean norm
$\forall$	$-$	for all
$\boldsymbol{\nabla}$	m^{-1}	gradient operator
$\subset$	$-$	is a subset of
$\boldsymbol{\nabla}_{\mathbf{x}}$	m^{-1}	large scale operator
$\mathbb{N}$	$-$	natural numbers
$\mathbb{R}_{>0}$	$-$	positive real numbers
$\mathbb{R}_{\geq 0}$	$-$	positive real numbers inc. 0
$\mathbb{R}$	$-$	real numbers
$\exists$	$-$	there exists
$[0, \infty)$	$-$	time domain
$\boldsymbol{\nabla}_{\mathbf{y}}$	m^{-1}	small scale operator
$\hat{\mathbf{e}}_k$	$-$	unit vector
$\hat{\mathbf{n}}$	$-$	unit normal
$\|\|\cdot\|\|$	$-$	volume integral
$\cup$	$-$	union of sets

Domains

$\partial\tilde{\Lambda}$	m^2	boundary of a domain
$\tilde{\Lambda}$	m^3	generalised ridged domain
$\tilde{\Psi}$	m^3	macroscale domain
$\tilde{\Pi}$	m^3	microscale domain
$\tilde{\Gamma}$	m^2	microscale internal boundary
$\tilde{\Phi}$	m^3	specific flat domain
$\tilde{\Omega}$	m^3	specific ridged domain

Functions

$T : X \to Y$ The function T maps from the initial set X to the final set Y.

Example $\phi_w : \tilde{\Lambda} \times [0, \infty) \to [0, 1]$ The function ϕ_w takes a point in the domain $\tilde{\Lambda}$ and a point in time $[0, \infty)$ and maps it to a value in the interval $[0, 1]$.

Big $\mathcal{O}$ notation

$\mathcal{O}$ refers to the 'order' of a term or expression.

Example $e^x = 1 + x + x^2/2 + \mathcal{O}(x^3)$ where $\mathcal{O}(x^3)$ is the remaining terms in the expansion which are of order x^3.

Def: $f(x) = \mathcal{O}(g(x))$ as $x \to \infty \iff \exists M \in \mathbb{R}_{>0}$ s.t. $|f(x)| < Mg(x)\ \forall x \geq x_0$.

Author's Declaration

UNIVERSITY OF Southampton

Research Thesis: Declaration of Authorship

Print name:	Simon Duncan

Title of thesis:	Multiscale Mathematical Modelling of Water and Solute Movement in Plant Systems

I declare that this thesis and the work presented in it is my own and has been generated by me as the result of my own original research.

I confirm that:

1. This work was done wholly or mainly while in candidature for a research degree at this University;
2. Where any part of this thesis has previously been submitted for a degree or any other qualification at this University or any other institution, this has been clearly stated;
3. Where I have consulted the published work of others, this is always clearly attributed;
4. Where I have quoted from the work of others, the source is always given. With the exception of such quotations, this thesis is entirely my own work;
5. I have acknowledged all main sources of help;
6. Where the thesis is based on work done by myself jointly with others, I have made clear exactly what was done by others and what I have contributed myself;
7. Either none of this work has been published before submission, or parts of this work have been published as: [please list references below]:

Duncan, S., Daly, K., Sweeney, P. & Roose, T. 2018a. Mathematical modelling of water and solute movement in ridge plant systems with dynamic ponding. *European Journal of Soil Science*, **69,** 265-278.

Duncan, S., Daly, K., Sweeney, P. & Roose, T. 2018b. Mathematical modelling of water and solute movement in ridged versus flat planting systems. *European Journal of Soil Science*.

Signature:		Date:	

Acknowledgements

First and foremost I would like to thank my two supervisors Dr Keith Daly and Professor Tiina Roose for giving me the opportunity to study at PhD level and for their help and guidance throughout my studies. I would like to pay special thanks to Keith who taught me the topic of multiple scale asymptotic homogenisation, which forms the basis of several chapters in this thesis.

I would also like to acknowledge Dr Paul Sweeney who assisted in the design of the mathematical modelling studies.

A special thanks goes to my friends within the department. Particularly Dan McKay Fletcher for answering my many questions regarding functional analysis, and Callum Scotson my experimental counterpart.

I would also like to thank my parents Mark and Karen Duncan for their continued support throughout the whole of my time at university.

Finally I would like to thank my fiancée Rachel for putting up with me throughout my PhD and feigning interest when I would talk about maths.

Baruk Khazâd! Khazâd ai-mênu!

Chapter 1

Introduction

In the year 2016, it was estimated that the total quantity of nitrogen, phosphate and potash fertilisers applied to soils in the United Kingdom was 136 kg ha^{-1}, covering 18,600,000 ha of agricultural land [1, 2]. This totalled 2,530,000,000 kg of agricultural fertilisers with an estimated cost of £506,000,000 [1, 2]. Combined with an estimated 16,000,000 kg of herbicides, fungicides and insecticides applied to arable grassland [3], the total quantity of solutes applied to soils in the United Kingdom is substantial.

Although the use of fertilisers and pesticides can aid in generating considerable improvements to crop yield, excessive use of solutes in arable land is a substantial problem [4]. Overuse of fertilisers and pesticides can have detrimental effects on both human health and farmland ecosystems [5]. Excessive use of pesticides in arable environments can destroy grassland ecosystems by reducing biodiversity [6]. Similarly, overuse of fertilisers can cause accelerated eutrophication due to surface runoff into water systems, in which increased phytoplankton levels disrupt the natural balance of the local ecology [7].

In the United Kingdom, farmers have significantly increased crop yields and production over the 20th century, with crops such as wheat and barley having increased substantially over the past 50 years [8]. However, this has caused a wealth of problems within local environments including: a decline in bird populations, greater gaseous emissions and increased nitrate concentrations in rivers [9]. The estimated annual external cost to agriculture in the United Kingdom is approximately £2,343,000,000 [4], where large portions of this is dedicated to combatting the negative effects of overusing pesticides and fertilisers. The cost to combat pesticide contamination in drinking water is approximately £120,000,000 [4]. Similarly, the expense to combat the effects of nitrate and phosphorous leaching into groundwater is approximately £71,000,000 [4].

In the year 2000, grasslands and arable fields in the United Kingdom had developed a phosphorous surplus of 1000 kg ha^{-1} [10]. Whilst a build up of phosphorous in soil can be beneficial to crop yields due to its low mobility [11], excessive concentrations of phosphorous can be severely detrimental to arable environments. Excessive phosphorous application in the UK has led to considerable increases in lake sediment phosphorous concentrations [12], causing a substantial increase in eutrophication. Given that worldwide phosphorous consumption is steadily increasing [13], and phosphorous resources may run out in as little as 50 years [14], more efficient use of fertilisers is crucial for sustainable life.

Understanding and maximising the beneficial properties of solutes whilst minimising any detrimental effects is a difficult problem [15]. The advantages from solute application in agriculture can benefit consumers, farmers and general society. However, the specific risks associated with individual solutes may never be fully understood [16]. As such, there are various aspects of solute use that must be understood in order to quantitively determine the associated risk.

One aspect of particular importance is the associated risk to solute leaching due to the surface topography of the soil, which results from different agricultural practices. Previous studies have found contrasting results, suggesting that different cultivation techniques can optimise solute leaching [17, 18]. Hence, it is not fully understood which cultivation method is best to reduce leaching with the current methodologies and studies. Therefore, it is necessary to develop a new methodology to determine what influence the surface topography has on solute leaching.

One approach to aid in efficient use of solutes in agriculture is the use of mathematical modelling. Mathematical modelling of soil systems has been studied increasingly in recent years [19]. This technique provides the means to study soil systems and plant-soil interactions, with the benefit of reducing time and resources compared to standard experimental practices. This allows us to understand the relationship between crop management practices and yield rates, whilst predicting the resources required. Combining mathematical modelling with traditional experiments allows us to efficiently improve our understanding of complex soil systems [20, 21]. This can lead to further improvements in agricultural practices and management for greater crop yield while minimising waste of resources.

In this thesis, we aim to develop a range of mathematical models to describe solute movement in soil. The mathematical models will be constructed to accurately capture the transport mechanisms of pesticide and nutrient like solutes in different soil structures that arise due to specific cultivation practices. We aim to determine how the surface topography of the soil influences the transport of solutes and the

associated risk to leaching. Furthermore, we also aim to determine how the presence of crops in soil influences the movement of water and solutes in these systems. Our models will describe several processes in soil, including but not limited to: water dynamics, solute transport, surface ponding, plant root uptake and soil deformation from compaction. We build upon previous mathematical models to incorporate these addtional soil processes to develop a more complete mathematical description of the transport mechanisms within soil. A brief summary of the work conducted in this thesis is given below.

1.1 Layout of the Thesis

A systematic method for modelling simultaneous water and solute movement in soil will be presented. The remainder of Chapter 1 provides a brief introduction to soil and cultivation methods for agricultural practices that form different soil structures. A formal introduction to each of the chapters including a review of the relevant literature is given in the introduction of each chapter. The mathematical analysis of soil processes starts from Chapter 2.

In Chapter 2, we construct a mathematical model that describes water movement in a generalised ridge and furrow soil system using a continuum approach. Special attention is paid to pond formation on the surface of the soil and root water uptake in the ridges of the system. The resulting model comprises a coupled system of partial and ordinary differential equations that describe the mathematical interplay between water movement, surface ponding and dynamic infiltration. Furthermore, we validate the model from previous ridge and furrow ponding modelling data, in which we find a difference of $\approx 4\%$.

In Chapter 3, we extend the water movement and surface ponding model from Chapter 2 to include solute transport. Using this model, we conduct a case study comparison of water and solute dynamics in two soil structures: a ridge and furrow soil, and a flat field soil. We observe that the soil to best reduce solute leaching can be either the ridge and furrow or flat field soil depending on several factors. We find that the key factor in determining solute penetration in soil is the time delay between solute application and rainfall, since the soil surface topology can heavily influence solute transport in soil.

In Chapter 4, we focus on water dynamics in the regions of soil that contain crops. Extending the model from Chapter 2, we develop a model that describes the macroscale movement of water in the plough layer of soil. This is achieved using the mathematical technique of multiple scale asymptotic homogenisation, where we

construct an approximate set of equations that captures macroscale water movement in soil, which is based on the intrinsic microscale soil structure that is formed in the presence of crops and vegetation.

In Chapter 5, we build on the ideas used in developing the model for water movement in the crop zones from Chapter 4. We derive a mathematical model that describes the movement of solutes in soil, in which the soil is treated as a poroelastic material. We allow crops to grow and freely deform the poroelastic soil, where the growth of the crops is dependent on the uptake of the solute. Special attention is paid to the reduction in void space, change in local volumetric water content and the impact on solute diffusion within the poroelastic soil domain as the crops increase in size. Then using multiple scale homogenisation we derive a set of averaged equations that capture macroscale solute movement and crop growth.

Finally, in Chapter 6 we present a summary and the conclusions of the work in this thesis. Furthermore, we provide a brief discussion of possible future work and address the questions that arise within the thesis.

Chapters 2 and 3 in this thesis are based on two pieces of published work. These are 'Duncan, S. *et al*. Mathematical modelling of water and solute movement in ridge plant systems with dynamic ponding. European Journal of Soil Science 69, 2 (2018), 265-278' and 'Duncan, S. *et al*. Mathematical modelling of water and solute movement in ridge versus flat plant systems. European Journal of Soil Science (2018)'. For reference, these papers can be found at the back of this thesis.

1.2 Soil

Soil is a collection of organic and mineral matter that is created by geological processes, organisms and climate [22]. As a naturally occurring and vast substance, there is substantial variation in soil and hence, classification of soil into several key groups is necessary [23].

There are multiple soil classification methods, examples include: the Winter Rainfall Acceptance Potential (WRAP) system and the Hydrology of Soil Types (HOST) classification, which can have up to 29 different classifications of soil types within the United Kingdom alone [24]. However, soil minerals are typically split into one of three core categories based on particle size, these being sand, silt and clay [25]. Classification of the three main mineral categories can be seen in Table 1.1 [26, 27].

Sand and silt particles are very similar by mineral composition and only differ based on their size and quantity in soil [27]. Sand particles are classified as the largest of

Table 1.1: Soil mineral classification [26, 27].

Particle	Particle diameter (mm)	No. particles per gram
Clay	< 0.003	4×10^{11}
Silt	$0.003 - 0.06$	2×10^{7}
Sand	$0.06 - 2$	$112 - 89 \times 10^{5}$

the three types, which provide anchorage for plant roots to establish themselves [28]. Furthermore, they typically increase the available pore space of the soil system, allowing for greater quantities of air to circulate throughout.

Silt particles fall in between sand and clay in terms of particle size. Silt particles are able to retain large quantities of water due to their size, which allows for easy accessibility to the plants. However, they are typically the most erodible of the three soil types, which can be a key factor in determining land-use [29].

Clay particles differ from silt and sand particles (other than by particle size) due to the intense weathering they experience [27]. As such, the chemistry of clay particles is substantially different to the larger soil minerals. Clay particles have a negative charge that binds positively charged cations such as, K^{+}, Ca^{2+} and Cu^{2+} to the mineral surface [30, 31]. This coupled with the large surface area of clay particles due to their small size, allows clay minerals play an important role in supplying sufficient nutrients to plants.

Along with the minerals that exist in soil, organic matter can also be a considerable component of soil. The quantity of organic material in soils can range anywhere from 0.1% in dry desert soils, to over 50% in organic heavy soils [27]. Organic matter holds large quantities of nutrients and water that are readily available to plant roots, providing a vital source of food [32]. In addition to providing sustenance to plants, organic matter also influences soil structure. Organic matter causes soil to bind together creating compact soil aggregates, which readily improves the soil structure and its ability to retain water [33, 34].

The key macroscale properties of soil, *i.e.*, hydraulic conductivity, permeability and porosity are typically governed by the ratio of the three mineral categories within the soil. Shown in Figure 1.1 is the United States of America Department of Agriculture (USDA) soil texture triangle for the classification of 12 different soil types from the ratio of the three soil minerals clay, silt and sand [35, 36].

One of the key soil properties that is vital for agricultural practices is the hydraulic conductivity. The hydraulic conductivity of soil is defined as the ability of a given fluid to move through the pore space of the soil due to gravity [37]. This property of soil heavily influences the transmission of water, and availability of water to plants.

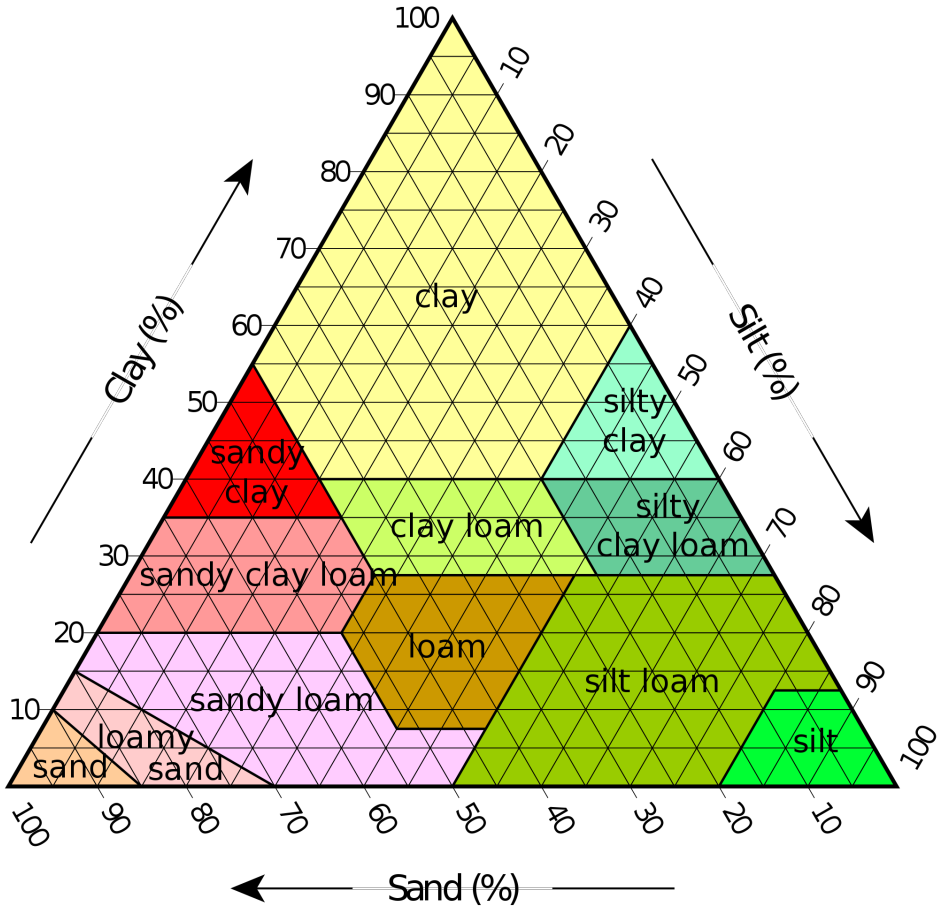

Figure 1.1: The United States of America Department of Agriculture (USDA) soil texture triangle for classification of soil from the three minerals components [35]. Image from Rhodes (2012) [36].

The hydraulic conductivity of soil is related to the soil permeability by linear the relationship,

$$K = \frac{\kappa_s \rho g}{\mu}, \tag{1.1}$$

where K [m s^{-1}] is the hydraulic conductivity, κ_s [m^2] is the saturated permeability, ρ [kg m^{-3}] is the fluid density, μ [Pa s] is the fluid viscosity and g [m s^{-2}] is gravity.

Soil permeability describes the ability of the soil to transmit different fluids under different conditions [37]. The relationship between the soil permeability and the particle size (see Table 1.1) follows the mean square law $\kappa_s = c_g d_g^2$, where d_g [m] is the mean grain size and c_g [$-$] is a constant that is dependent on the pore space configuration [38].

The properties d_g and c_g are closely linked to the porosity of the soil. The porosity of soil is defined as the volume of pore (void) space per volume of soil [39]. This is an indirect measure of the connectivity of the soil, *i.e.*, the relationship between the connection of the pore space throughout the soil, which can be used as a method to

classify soil with respect to the pore space and solid matrix connectivity [40].

The porosity of the soil can play an important role in the transport of solutes such as nutrients or pesticides. The power law relationship between solute diffusion and porosity takes the form [41],

$$D = D_f \phi^d S^d, \tag{1.2}$$

where D [m^2 s^{-1}] is the solute diffusion in soil, D_f [m^2 s^{-1}] is the solute diffusion in free liquid, ϕ [$-$] is the porosity, S [$-$] is the saturation, *i.e.*, the volume of water per volume of void space, and d [$-$] is the impedance factor that accounts for the tortuosity of the soil. In equation (1.2) we observe that the diffusion of solutes is dependent on the porosity of the soil, which will significantly influence solute movement.

From the soil properties above, we find that the soil type plays a vital role in defining the mobility and transport of water and solutes in soil, as many of the soil properties influence one another and contribute to the transport mechanisms within soil. Hence, accurately capturing the influence of the soil type is vital in the development of mathematical models to represent soil systems.

1.3 Soil Geometries

In arable farming row production is a widely used practice. Row production refers to fields that are cultivated to create evenly spaced rows in which seeds are planted, grown and harvested. A large variety of crops are grown using row production; examples include maize (*Zea mays*, L.), pearl millet (*Pennisetum glaucum*, L.), soybean (*Glycine max*, L.), potatoes (*Solanum tubersum*, L.) and sunflowers (*Helianthus annuus*, L.) [42]. There are several cultivation and tillage procedures that utilise row production methods, however, they are often for different soil structures and surface topologies. These cultivation methods include but are not limited to: flat planting [43], ridge planting [44], raised bed planting [45], wide bed planting [46], furrow planting [47] and plastic covered rainfall harvesting systems [48]. Shown in Figure 1.2 are cross section schematics of these cultivation methods.

Several of these cultivation methods utilise a ridge and furrow soil geometry, or a variant of this structure. Ridge and furrow geometries are created when the soil surface is adapted to form a periodic series of peaks and troughs across an arable field. Shown in Figure 1.3 is an example of a ridge and furrow system immediately after crop sowing (Ordnance Survey grid ref. TG337240).

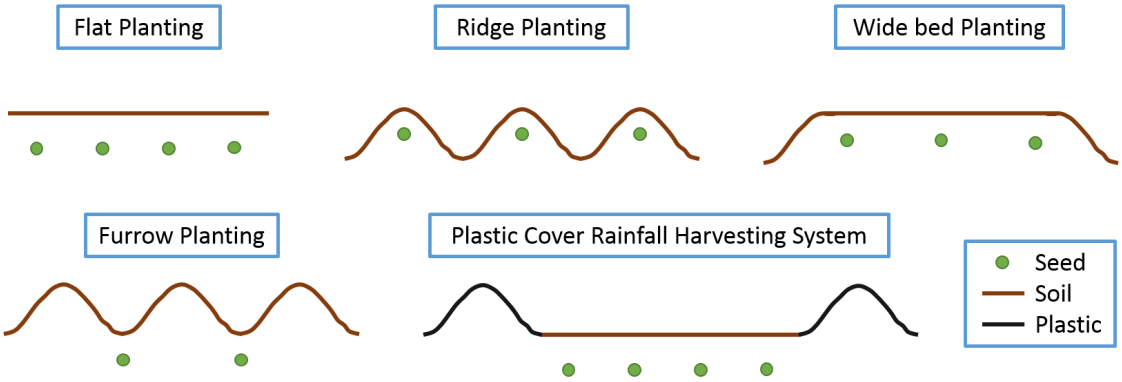

Figure 1.2: Examples of different cultivation methods, including flat planting, ridge planting, wide bed planting, furrow planting and a plastic cover rainfall harvesting system.

The distinguishing feature of ridge and furrow structures is the surface topography that is generated from the cultivation process. This uneven surface can alter the mechanisms and dynamics by which water and solute infiltrate into the soil [44]. Furthermore, this can also affect the distribution of roots within the soil, which can have an influence on the saturation and nutrient profiles throughout the soil.

The ridge and furrow soil structure is often the preferred crop system compared to other alternatives [49]. This is due to multiple reasons including, ease of harvesting [50], assisting with slow seed germination [51], and nutrient replenishment in the soil [52]. A key advantage of ridge and furrow type structures is that they allow water to flow across arable fields providing water to the plants whilst preventing water logging of the root systems [53]. Ridge and furrow structures have also shown to reduce soil erosion compared to other soil profiles [54]. This is attributed to the influence of the ridges, which trap soil particles and reduce the effect of wind damage [55].

Ridge and furrow tillage methods are favourable worldwide across multiple environments and climates. In North-American climates, ridge and furrow planting can protect the crop from seasonal (early and late) frosts, regulate weeds and reduce blight [43]. In European climates, the ridge and furrow structure is frequently used as it allows the crops to remain dryer during heavy rainfall [56]. Additionally, in east Asian climates the ridge and furrow tillage method has shown to significantly increase soil moisture and temperature conditions resulting in greater yields [57]. This makes the ridge and furrow tillage method one of the most important cultivation practices globally.

Although the ridge and furrow cultivation procedure is often the preferred

Figure 1.3: A ridge and furrow cultivated soil system, located in East Anglia, UK (Ordnance Survey grid ref. TG337240).

structure, growing evidence suggests that ridge and furrow soil systems may be vulnerable to solute leaching compared to other tillage methods [18, 58, 59]. This is often due to irrigation, which acts as a dominant transport mechanism for solute movement in ridged soils. The European Food Safety Authority (EFSA) have suggested that ridge and furrow soils can increase leaching six fold when compared to flat soils [60]. This can cause devastating effects to local groundwater contamination. Hence, understanding the effects that the ridge and furrow structure can have on water and solute movement in soil is vital.

Large portions of this thesis are concerned with the mathematical modelling of ridge and furrow structures and how they influence the movement and transport of water and solutes throughout the soil. Due to the unique surface topology they exhibit, they have many advantages but also several drawbacks. We aim to explore the driving mechanisms for solute movement in this planting system to quantitively determine the effect this soil geometry has on soil processes and crop growth.

Chapter 2

Water Movement and Ponding Model

In this chapter, we construct a mathematical model that describes the movement of water in a generalised ridge and furrow soil domain. We focus on two physical processes: root water uptake and pond formation on the soil surface. The resulting model comprises of a coupled system of partial and ordinary differential equations that describe the mathematical interplay between water movement, surface ponding and dynamic infiltration. We validate the model using previous ridge and furrow ponding data. We find a difference of $\approx 4\%$ using data obtained from the literature.

2.1 Introduction

The ridge and furrow farming method is frequently used in the United Kingdom and throughout the rest of Europe. However, large areas of Europe experience substantial rainfall, which can lead to considerable ponding in the furrows of the soil. This can result in significantly decreased yields for crops such as potatoes [61]. This reduction in yield can be due to bacterial diseases such as blackleg or soft rot, which are easily transmitted by water logged soil [62, 63]. As such, ponded water on the surface of the soil is a source of transport for the bacteria, and can also form a host medium to generate new strains of bacteria [64]. Therefore, understanding water movement in ridge and furrow soil systems is of critical importance, with particular focus on the interface between surface and subsurface flow.

One approach that offers significant insight into water movement within soil systems is mathematical modelling (see the comprehensive review for modelling of soil processes by Vereecken *et al*. (2016) [19]). Understanding the mathematical relationship between soil water movement, surface ponding and infiltration can aid in decision making for agricultural practices directly. For example, the depth at

which seeds are sown in ridge and furrow systems is a highly debated topic [65]. Several experimental studies find that deeper seed planting leads to faster emergence, and therefore greater yields [56, 66]. However, contrasting results suggest shallower planting has been more effective for emergence rates [43, 67]. The difference in findings has been shown to be attributed to the moisture conditions in soil. The optimal planting depth is simply the one with the best moisture for growth and emergence [65]. Hence, understanding the time-resolved saturation profile with the use of mathematical modelling for localised regions could aid in determining the optimal planting depth to generate maximum yields.

To model water movement in variably saturated soil, a combination of Richards' equation and Darcy flow are traditionally used [40, 68]. Since we aim to develop a mathematical model to describe water movement in a ridge and furrow system, the mathematical description of the soil surface is a key factor. The soil surface plays an important role describing infiltration of water into the soil, either through rainfall or via ponding in the furrows of the soil. Hence, the boundary condition on the surface of the soil representing the surface-subsurface interaction of water is of critical importance.

The interaction of surface-subsurface flow between a porous material and free liquid has been studied extensively over the past 50 years, both experimentally and theoretically. In the 1960's there was considerable analytic work on the boundary interface between a saturated porous medium (subject to Darcy flow mechanics) and stokes flow outside the porous domain [69, 70]. The porous material and the flow of free liquid were assumed to be connected by pressure gradients and the normal component of the velocity at the interface. Pressure conditions were then matched between the two domains to determine analytic and semi-analytic solutions. However, it was assumed that there was no tangential component of velocity at the surface of the two domains [71].

Beavers and Joseph (1967) [72] expanded on these original ideas, and introduced a 'slip' boundary condition on the porous-free liquid interface, which described the change in water velocity over the interface between the two domains. They proposed that the difference between the slip velocity at the surface interface, and the tangential component of the seepage velocity are proportional to the shear stress that is transmitted to the porous media [73]. The Beavers and Joseph slip boundary takes the form,

$$\partial_z v_f = \alpha_{bj}(v_f - v_d), \tag{2.1}$$

where v_f [m s^{-1}] is the fluid velocity tangential to the surface interface, v_d [m s^{-1}] is the 'seepage velocity' in the porous domain tangential to the surface and α_{bj} [m^{-1}] is

the Beavers and Joseph constant that is determined from the structure of the porous domain. Shown in Figure 2.1 is a schematic of a velocity profile of a fluid between a permeable domain and a free domain that is enclosed by an impermeable surface, in which the Beavers and Joseph condition is used to describe the interface between the two domains.

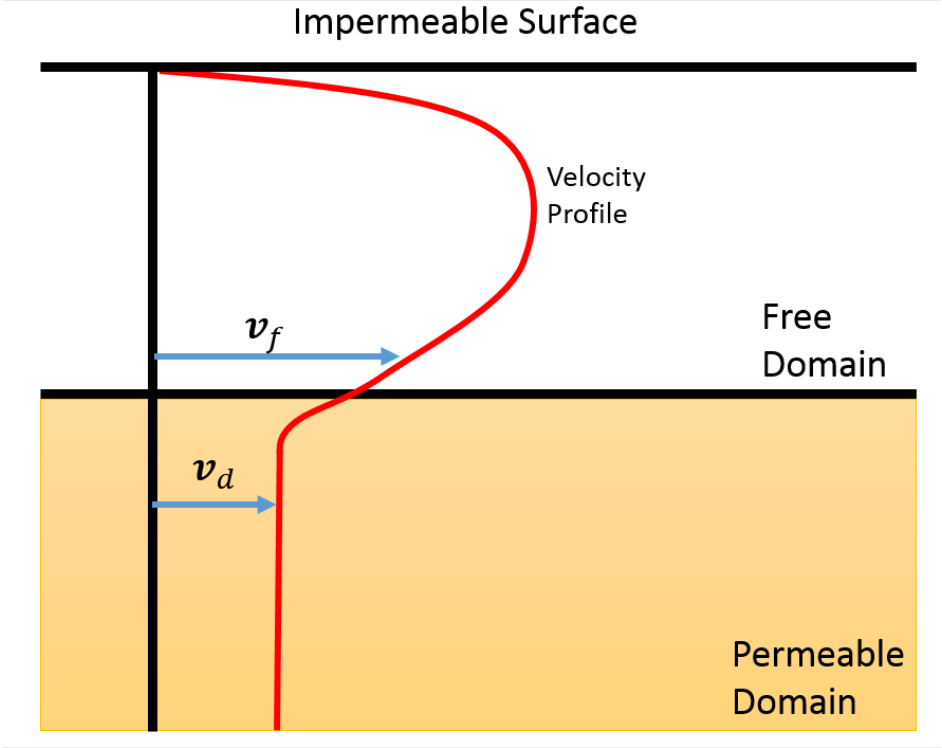

Figure 2.1: A velocity profile of a fluid between a permeable domain and a free domain that is enclosed by an impermeable surface, where v_f is the fluid velocity tangential to the surface interface, v_d is the 'seepage velocity' in the porous domain. Image recreated from Beavers and Joseph (1967) [72].

Several experiments were conducted to test the condition proposed by Beavers and Joseph. It was found that experimental results of laminar flow with the slip condition were in accordance with the theoretic results [74, 75]. In addition, it was found that the boundary condition could also be used to model the flow of gas between a porous medium and an open domain [76].

Saffman (1971) [77] followed on from the Beavers and Joseph slip condition, in which the boundary condition was modified. It was found that the seepage velocity $\mathbf{v}_d$ was small in comparison to the fluid velocity $\mathbf{v}_f$. Saffman proposed that the seepage velocity $\mathbf{v}_d$ could be removed as it was redundant.

The work done by Beavers and Joseph [72] and Saffman [77] has been used frequently to model the continuation between free fluid flow and flow in a porous medium [78]. However, the 'slip' condition is derived under the assumption that the

porous media is fully saturated. When modelling fluid flow of a porous medium such as soil, the domain is frequently partially saturated. Hence, the slip boundary condition is not directly applicable for soil based studies that contain rainfall onto partially saturated soil.

In specific mathematical modelling studies for groundwater and hydrology, there are often areas of the domain that are partially saturated, which are modelled using Richards' equation. Hence, an alternate approach to the Beavers and Joseph condition is required to model soil surfaces. Traditional continuum modelling approaches for describing rainfall infiltration at the soil surface typically fall into one of three types of boundary conditions. The first of these types is to prescribe a Dirichlet boundary condition on the soil surface to provide a constant saturation [79–82]. This condition moderates the filtration rate from the soil surface into the soil. The second type of boundary condition is a Cauchy or Neumann condition. This condition provides a consistent water flux into or out of the soil domain [81, 83]. This flux is typically set to zero in the event of no precipitation, or to a positive non-zero value to simulate constant infiltration. The final type of boundary condition involves a mass balance at the soil surface. This typically revolves around the Penman-Monteith equation [84] or other atmospheric mass balances [85, 86]. These mass balances often explicitly take into account several physical features including evapotranspiration rate, vapour pressures, mean average daily temperature and wind speed.

In addition to these three main groups, there have been attempts to hybridise two of the boundary conditions, by combining a Dirichlet boundary condition with a Cauchy boundary condition in order to better simulate rainfall on the soil surface [87]. In this method the flat ground is split into a set of nodes. A Dirichlet boundary is applied on the nodes that are saturated, and a Cauchy boundary condition of zero flux is applied on the partially saturated nodes. These mathematical representations of fluid flow on the soil surface boundary have been used successfully to model 1D fluid flow in a soil domain. However, these boundary conditions only aim to represent rainfall. To model other scenarios such as ponding and more complex approaches are required.

In recent years, there have been several studies on mathematical modelling of soil surface ponding [88–91]. These studies combined surface and subsurface flow using an exchange flux between the two domains. This exchange flux is based on the surface ponding depth on the soil surface. The standard protocol for combing subsurface flow and surface flow (ponding), is to couple together the mixed form of Richards' equation for variably saturated groundwater flow, and the Saint Venant equations for mass and momentum balance of water movement [89–91].

However, the Saint Venant equation is only valid for shallow water and gentle slopes, specifically when the water depth perpendicular to the slope can be approximated to the absolute depth vertically [89]. Hence, these methods have only been applied to either flat ground or a constant low gradient slope. The Saint Venant equation is not necessarily applicable to substantial ponding in ridge and furrow systems, given the large gradient posed by the ridge and furrow structure [47, 92].

Specific mathematical modelling of water movement in ridge and furrow systems has been developed in recent years [93–97]. However, often the focus of these studies is semi-arid soils, in which the ridge and furrow geometry is used as a means of irrigation. Due to the lack of rainfall in these environments, precipitation and surface runoff from rainfall is often ignored as furrow irrigation is the main priority. From the furrow irrigation, several of these models contain pond infiltration for ridge and furrow structures [82, 86, 94, 97–99]. However, these models typically describe irrigation and drainage along a furrow (often using the zero-inertia model for a moving body of water). Additionally, the ridge and furrow geometry is often approximated as piecewise linear [82, 86, 98, 99].

In this chapter, we develop a mathematical model for water movement in a generalised ridge and furrow system. We focus on root water uptake and dynamic ponding in the furrows of the structure due to transient rainfall events. Since we are concerned with rainfall in a temperate UK environment, we do not consider irrigation or water movement down the furrows. Instead we focus on the phenomena taking place in the cross-section of the furrow.

2.2 Theory

In this section we derive a mathematical model for water movement and dynamic ponding in general ridge and furrow systems. We build the model from first principles and develop a coupled system of partial differential equations (PDEs) and ordinary differential equations (ODEs) to capture the water transport in the ridged system.

2.2.1 Soil Domain

Let $\tilde{\Lambda} \subset \mathbb{R}^3$ [m^3] (shown in Figure 2.2 (a)) be an open bounded subset representing a generalised ridged soil domain. $\tilde{\Lambda}$ has two distinct regions $\tilde{\Lambda}_U$ [m^3] and $\tilde{\Lambda}_A$ [m^3] such that, $\tilde{\Lambda} = \tilde{\Lambda}_U \cup \tilde{\Lambda}_A$ and $\tilde{\Lambda}_U \cap \tilde{\Lambda}_A = \emptyset$. Here $\tilde{\Lambda}_U$ and $\tilde{\Lambda}_A$ are the regions of soil with and without roots respectively.

Although the mathematical model developed in this chapter is applicable for general ridge and furrow soils, to construct domains for numerical simulations we assign a function to describe the surface topology. Due to the symmetry and periodicity of ridged soils, we approximate the surface $\partial\tilde{\Lambda}_S$ by the periodic function $\tilde{\chi} : \tilde{\Lambda} \to \mathbb{R}$ [m] (see Nomenclature section for functional notation),

$$\tilde{\chi} = A\cos(B\tilde{x}_1) + C, \tag{2.2}$$

where $A \in \mathbb{R}_{\geq 0}$ [m] is the variation in soil depth, $B \in \mathbb{R}_{\geq 0}$ [m^{-1}] is the ridge wave number, $C \in \mathbb{R}$ [m] is the average soil depth and $\tilde{x}_1$ is the spatial coordinate in the horizontal direction (see Figure 2.2 (a)). The form of (2.2) allows us to describe the complete soil system with a single half-period of a ridged geometry.

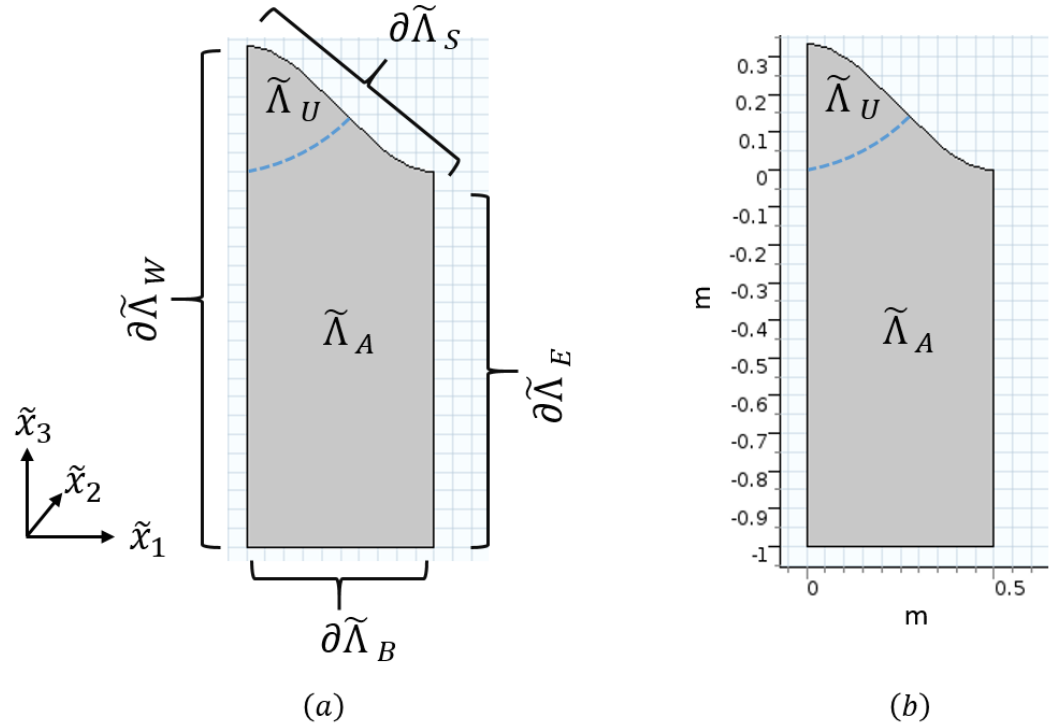

Figure 2.2: (a): A general ridged soil domain, where $\tilde{\Lambda}$ is the total soil domain such that $\tilde{\Lambda} = \tilde{\Lambda}_A \cup \tilde{\Lambda}_U$, where Λ_A is the region of soil absent roots, $\tilde{\Lambda}_U$ is the region of soil with roots, $\partial\tilde{\Lambda}_S$ is the soil surface boundary, $\partial\tilde{\Lambda}_B$ is the base of the domain, $\partial\tilde{\Lambda}_W$ is the boundary adjacent to the ridge, $\partial\tilde{\Lambda}_E$ is the boundary adjacent to the furrow and $\tilde{x}_1,\ \tilde{x}_2,\ \tilde{x}_3$ are the three directional components.
(b): The domain used for the numerical simulation in Section 2.3. The curve $\partial\tilde{\Lambda}_S$ is generated using the values $A = C = 0.1\dot{6}$ and $B = 2\pi$ from (2.2).

2.2.2 Water Movement in Variably Saturated Soil

To describe water movement in ridged soils, we assume there may be regions of soil that are fully saturated, *i.e.*, directly under the pond, and regions that are partially saturated. To account for this, we construct a model that can switch between a partially and a fully saturated soil environment with a moving interface between the two regions.

For water movement in variably saturated soil, Richards' equation is typically used [68]. To derive Richards' equation, we use the mass conservation law [100], *i.e.*,

$$\partial_{\tilde{t}}\phi_w + \tilde{\boldsymbol{\nabla}} \cdot \tilde{\mathbf{v}} = -\tilde{F}_w \quad \text{in} \quad \tilde{\Lambda}^\infty, \tag{2.3}$$

where $\tilde{\Lambda}^\infty = \tilde{\Lambda} \times (0, \infty)$ (where $(0, \infty)$ denotes the time domain). Here $\phi_w : \tilde{\Lambda} \times [0, \infty) \to [0, 1]$ $[-]$ is the soil water fraction, *i.e.*, the volume of water per volume of void space, $\tilde{\mathbf{v}} : \tilde{\Lambda} \times [0, \infty) \to \mathbb{R}^3$ [m s^{-1}] is the volume flux of water and $\tilde{F}_w : \tilde{\Lambda}_U \times [0, \infty) \to \mathbb{R}$ [s^{-1}] is the root water uptake. The saturation of $\tilde{\Lambda}$ is related to ϕ_w by the relationship [101],

$$S = \frac{\phi_w - \phi_r}{\phi - \phi_r}, \tag{2.4}$$

where $S : \tilde{\Lambda} \times [0, \infty) \to [0, 1]$ $[-]$ is the relative saturation, *i.e.*, the volume of water per volume of void space, $\phi_r : \tilde{\Lambda} \times [0, \infty) \to [0, 1]$ $[-]$ is the residual water content, *i.e.*, the water content that cannot be removed due to gravity or the root system, and $\phi : \tilde{\Lambda} \times [0, \infty) \to [0, 1]$ $[-]$ is the porosity, *i.e.*, the volume of void space per volume of soil. Here $\phi = \phi_w + \phi_a$, where $\phi_a : \tilde{\Lambda} \times [0, \infty) \to [0, 1]$ $[-]$ is the soil air fraction, *i.e.*, the volume of air per volume of void space. We note that typically $\phi_r \ll \{\phi, \phi_w\}$ [101], and hence can be neglected. This leads to the relationship $S = \phi_w/\phi$ [41]. For simplicity, we initially assume ϕ to be constant such that,

$$\phi(\tilde{\mathbf{x}}) \equiv \phi \quad \text{in} \quad \tilde{\Lambda}, \tag{2.5}$$

where $\tilde{\mathbf{x}}$ is the spatial component of $\mathbb{R}^3$, $\tilde{\mathbf{x}} := (\tilde{x}_1, \tilde{x}_2, \tilde{x}_3)$. Substituting $S = \phi_w/\phi$ into equation (2.3) yields,

$$\phi\partial_{\tilde{t}} S + \tilde{\boldsymbol{\nabla}} \cdot \tilde{\mathbf{v}} = -\tilde{F}_w \quad \text{in} \quad \tilde{\Lambda}^\infty. \tag{2.6}$$

We define $\tilde{\mathbf{v}}$ using Darcy's law [102]. This takes the form,

$$\tilde{\mathbf{v}} = -\frac{\kappa_s \kappa(S)}{\mu_w} \left(\tilde{\boldsymbol{\nabla}} \tilde{p}_w + \rho g \hat{\mathbf{e}}_3 \right), \tag{2.7}$$

where $\kappa(S) : \tilde{\Lambda} \times [0, \infty) \to [0, 1]$ $[-]$ is the relative soil permeability, $\mu_w \in \mathbb{R}_{>0}$ [Pa s] is the viscosity of water, $\kappa_s \in \mathbb{R}_{>0}$ [m^2] is the saturated hydraulic permeability,

$\tilde{p}_w : \tilde{\Lambda} \times [0, \infty) \to \mathbb{R}$ [Pa] is the soil water pore pressure, $\rho \in \mathbb{R}_{>0}$ [kg m^{-3}] is the density of water, $g \in \mathbb{R}_{>0}$ [m s^{-2}] is the acceleration due to gravity and $\hat{\mathbf{e}}_3 = (0, 0, 1)$ [$-$]. Substituting (2.7) into (2.6) yields the Darcy-Richards' equation in mixed form,

$$\phi \partial_{\tilde{t}} S = \tilde{\boldsymbol{\nabla}} \cdot \left[\frac{\kappa_s \kappa(S)}{\mu_w} \left(\tilde{\boldsymbol{\nabla}} \tilde{p}_w + \rho g \hat{\mathbf{e}}_3 \right) \right] - \tilde{F}_w \quad \text{in} \quad \tilde{\Lambda}^{\infty}. \tag{2.8}$$

The function $\tilde{F}_w$ is only defined in the subdomain $\tilde{\Lambda}_U$, *i.e.*, where roots are present, and is given by the difference in the soil water pore pressure and the pressure in the root xylem [41], *i.e.*,

$$\tilde{F}_w = \begin{cases} \lambda_c (\tilde{p}_w - p_r) & \text{in} \quad \tilde{\Lambda}_U \times [0, \infty) \\ 0 & \text{in} \quad \tilde{\Lambda}_A \times [0, \infty) \end{cases}, \tag{2.9}$$

where $\lambda_c \in \mathbb{R}_{\geq 0}$ [Pa^{-1} s^{-1}] is the product of the root surface area density and the water conductivity of the root cortex and $p_r \in \mathbb{R}_{\leq 0}$ [Pa] is the pressure in the root xylem. We consider the subdomain $\tilde{\Lambda}_U$ to be contained in the ridges of the system, since crops grown in ridge and furrow structures (such as *Solanum tuberosum* L.) typically have roots in the plough layer of soil only, *i.e.*, the top 30 cm of soil [103].

We express S as a function of $\tilde{p}_w$ using the van Genuchten relationship [101],

$$S = \left[\left(\frac{\tilde{p}_a - \tilde{p}_w}{p_c} \right)^{\frac{1}{1-m}} + 1 \right]^{-m}, \tag{2.10}$$

where $\tilde{p}_a : \tilde{\Lambda} \times [0, \infty) \to \mathbb{R}$ [Pa] is the air pressure, $p_c \in \mathbb{R}_{>0}$ [Pa] is the characteristic suction pressure and $m \in [0, 1]$ [$-$] is a van Genuchten parameter. We choose to set $\tilde{p}_a = 0$, such that $\tilde{p}_w$ is defined as the gauge pressure relative to $\tilde{p}_a$ [41]. Here we do not consider the effects from hysteresis, *i.e.*, the changes in the saturation-pressure relation due to wetting and drying, since we assume that this has a negative effect on the field scale transport of water.

We define $\kappa(S)$ using a second van Genuchten formula [101],

$$\kappa(S) = S^{1/2} \left[1 - (1 - S^{1/m})^m \right]^2. \tag{2.11}$$

Combining Richards' Equation (2.8) with the van Genuchten Equations (2.10) $-$

(2.11), we can write the water movement model in terms of $\tilde{p}_w$ only, *i.e.*,

$$\phi\frac{\partial S(\tilde{p}_w)}{\partial \tilde{p}_w}\frac{\partial \tilde{p}_w}{\partial \tilde{t}} = \tilde{\boldsymbol{\nabla}}\cdot\left\{\frac{\kappa_s\kappa[S(\tilde{p}_w)]}{\mu_w}\left(\tilde{\boldsymbol{\nabla}}\tilde{p}_w + \rho g\hat{\mathbf{e}}_3\right)\right\} - \begin{cases}\lambda_c(\tilde{p}_w - p_r), & \text{in} \quad \tilde{\Lambda}_U^\infty \\ 0, & \text{in} \quad \tilde{\Lambda}_A^\infty\end{cases}, \tag{2.12}$$

where,

$$\frac{\partial S(\tilde{p}_w)}{\partial \tilde{p}_w} = \frac{m\left[\left(\frac{-\tilde{p}_w}{p_c}\right)^{\frac{m}{1-m}} + 1\right]^{-m-1}\left(\frac{-\tilde{p}_w}{p_c}\right)^{\frac{m}{1-m}}}{p_c(1-m)}, \tag{2.13}$$

$$\kappa[S(\tilde{p}_w)] = \left[\left(\frac{-\tilde{p}_w}{p_c}\right)^{\frac{m}{1-m}} + 1\right]^{\frac{-m}{2}}\left(1 - \left\{1 - \left[\left(\frac{-\tilde{p}_w}{p_c}\right)^{\frac{m}{1-m}} + 1\right]^{-1}\right\}^m\right)^2, \tag{2.14}$$

$\tilde{\Lambda}_U^\infty = \tilde{\Lambda}_U \times (0,\infty)$ and $\tilde{\Lambda}_A^\infty = \tilde{\Lambda}_A \times (0,\infty)$.

Richards' equation is used to describe water movement in partially saturated soil, *i.e.*, $0 < S(\tilde{p}_w) < 1$. If $S = 1$ singularities are formed, and hence cannot be used to describe a fully saturated domain. However, we can adapt the system of equations (2.12) $-$ (2.14) so that they can represent both a saturated and partially saturated soil by reducing Richards' equation to saturated Darcy flow in the event of full saturation, *i.e.*, for $\tilde{p}_w \geq 0$. We do this by modifying Equations (2.12) $-$ (2.14) in two ways. Firstly, for $\tilde{p}_w \geq 0$ we eliminate the term $\phi\frac{\partial S(\tilde{p}_w)}{\partial \tilde{p}_w}\frac{\partial \tilde{p}_w}{\partial \tilde{t}}$ from Equation (2.12) by setting $\frac{\partial S(\tilde{p}_w)}{\partial \tilde{p}_w} = 0$. Thus, we impose the condition,

$$\frac{\partial \overline{S(\tilde{p}_w)}}{\partial \tilde{p}_w} = \begin{cases}0 & \text{for} \quad S(\tilde{p}_w) = 1 \\ \frac{\partial S(\tilde{p}_w)}{\partial \tilde{p}_w} & \text{for} \quad 0 < S(\tilde{p}_w) < 1\end{cases}. \tag{2.15}$$

To implement (2.15) as a closed-form expression, we use a smoothing approximation to the Heaviside function H so that $\lim_{\tilde{p}_w \to 0^-}\frac{\partial S(\tilde{p}_w)}{\partial \tilde{p}_w} = 0$. This imitates the piecewise condition (2.15) while retaining a level of smoothness over a narrow transition region about $\tilde{p}_w = 0$ to aid in calculating a numerical solution. We add the smoothed Heaviside function $H_S(\tilde{p}_w) : \tilde{\Lambda} \times [0,\infty) \to [0,1]\ [-]$, so that

$$[1 - H_S(\tilde{p}_w)]\phi\frac{\partial S(\tilde{p}_w)}{\partial \tilde{p}_w}\frac{\partial \tilde{p}_w}{\partial \tilde{t}} = \tilde{\boldsymbol{\nabla}}\cdot\left\{\frac{\kappa_s\kappa[S(\tilde{p}_w)]}{\mu_w}\left(\tilde{\boldsymbol{\nabla}}\tilde{p}_w + \rho g\hat{\mathbf{e}}_3\right)\right\} - \tilde{F}_w \quad \text{in} \quad \tilde{\Lambda}^\infty, \tag{2.16}$$

where,

$$H_S(\tilde{p}_w) = \frac{1}{2}[1 + \tanh(\sigma\tilde{p}_w)], \tag{2.17}$$

and $\frac{1}{\sigma}$ [Pa] defines the width of transition between $\frac{\partial S(\tilde{p}_w)}{\partial \tilde{p}_w}$ and 0 about $\tilde{p}_w = 0$.

Secondly, the function $\kappa[S(\tilde{p}_w)]$ is required to be constant when $\tilde{p}_w \geq 0$. Thus, we

introduce a second condition,

$$\overline{\kappa[S(\tilde{p}_w)]} = \begin{cases} 1 & \text{for} \quad p_w \geq -\zeta_t \\ \kappa[S(\tilde{p}_w)] & \text{for} \quad p_w < -\zeta_t \end{cases}, \tag{2.18}$$

where $\zeta_t \in \mathbb{R}_{>0}$ [Pa] is a small transition pressure that acts as the interface between the saturated and partially saturated soil regions. We introduce (2.18) to avoid discontinuities in the numerical solver when evaluating Equation (2.14). These discontinuities occur since the numeric solver is often required to evaluate $\frac{\delta\kappa\left[S(\tilde{p}_w)\right]}{\delta\tilde{p}_w}\Big|_{\tilde{p}_w=0}$. However, $\frac{\delta\kappa\left[S(\tilde{p}_w)\right]}{\delta\tilde{p}_w}$ is singular at the transition between fully and partially saturated soil, so that $\lim_{\tilde{p}_w\to 0^-} \frac{\delta\kappa\left[S(\tilde{p}_w)\right]}{\delta\tilde{p}_w} = \infty$. Hence, we introduce ζ_t so that $\frac{\delta\kappa\left[S(0)\right]}{\delta\tilde{p}_w}$is never evaluated.

2.2.3 Soil Surface Boundary Conditions

To form a complete description of the ridge and furrow system, we derive boundary conditions that are imposed on the edges of $\tilde{\Lambda}$. To represent ponding, which is often present in ridge and furrow systems [82, 98], we split the boundary $\partial\tilde{\Lambda}_S$ [m^2] (see Figure 2.2 (a)) into two distinct regions, separated by the moving interface $\tilde{x}_0 = \tilde{x}_0(\tilde{t})$ [m]. This is shown in Figure 2.3, where $\partial\tilde{\Lambda}_R = \partial\tilde{\Lambda}_S \cap [0, \tilde{x}_0(\tilde{t}))$ [m^2] is the surface of soil that is not ponded, *i.e.*, where rain penetrates the soil directly, and $\partial\tilde{\Lambda}_P = \partial\tilde{\Lambda}_S \cap [\tilde{x}_0(\tilde{t}), \eta]$ [m^2] is the region on which ponding occurs (where η [m] is the width of $\tilde{\Lambda}$ and has the relationship $\eta = \pi/B$).

On the surface $\partial\tilde{\Lambda}_P$ we impose a hydrostatic boundary condition [82, 88, 98], so that directly under the pond we apply the pressure that results from the height of the water column in the pond above it, *i.e.*,

$$\tilde{p}_w = \rho g \tilde{h}(\tilde{x}, \tilde{t}) \quad \text{on} \quad \partial\tilde{\Lambda}_P \times [0, \infty), \tag{2.19}$$

where $\tilde{h}(\tilde{x}, \tilde{t}) : \partial\tilde{\Lambda}_P \times [0, \infty) \to \mathbb{R}_{\geq 0}$ [m] is the depth of the pond.

Precipitation landing on the bare soil $\partial\tilde{\Lambda}_R$ enters $\tilde{\Lambda}$ via a combination of capillary forces and gravitational effects. Therefore, we implement a Cauchy fluid flux condition on $\partial\tilde{\Lambda}_R$ [104], *i.e.*,

$$\hat{\mathbf{n}} \cdot \left\{ \frac{\kappa_s \overline{\kappa[S(\tilde{p}_w)]}}{\mu_w} \left(\tilde{\boldsymbol{\nabla}} \tilde{p}_w + \rho g \hat{\mathbf{e}}_3 \right) \right\} = \tilde{\omega} \quad \text{on} \quad \partial\tilde{\Lambda}_R \times [0, \infty), \tag{2.20}$$

where $\hat{\mathbf{n}} : \mathbb{R}^3 \times [0, \infty) \to \mathbb{R}^3$ [$-$] is the unit normal vector pointing outwards of $\tilde{\Lambda}$,

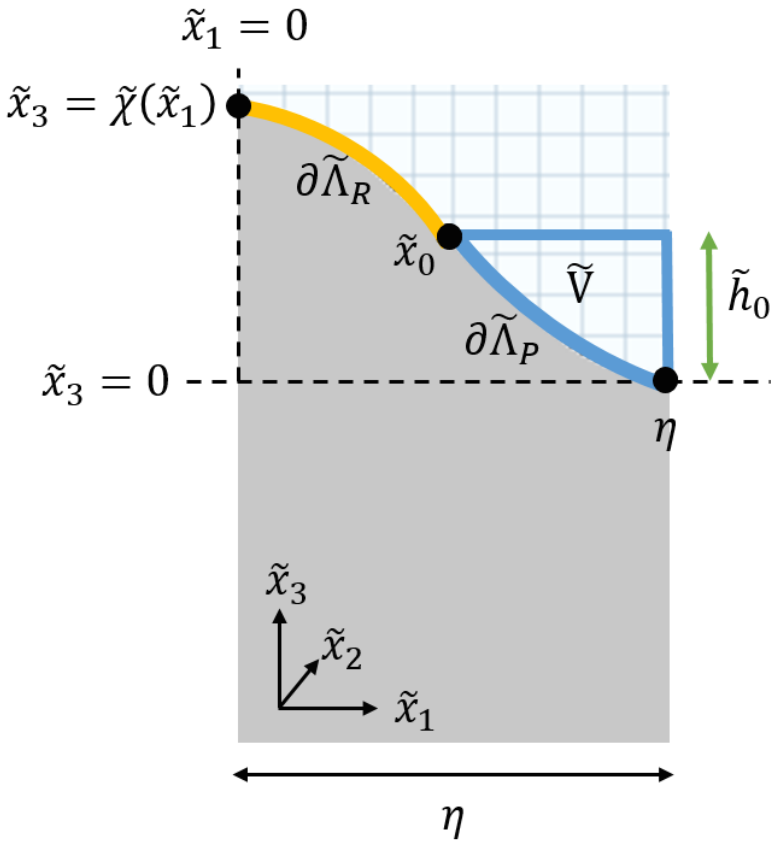

Figure 2.3: Half of a ridge and furrow period, where $\partial\tilde{\Lambda}_P$ is the soil surface on which ponding occurs, $\partial\tilde{\Lambda}_R$ is the soil surface that is not ponded, $\tilde{x}_0 = \tilde{x}_0(\tilde{t})$ is the point on the soil surface $\partial\tilde{\Lambda}_S$ where the pond begins, η is the width of the half period of ridged domain, $\tilde{h}_0$ is the maximum depth of the pond, $\tilde{\chi}(\tilde{x}_1)$ is the curve for the soil surface $\partial\tilde{\Lambda}_S$ and $\tilde{V}$ is the volume of the pond.

$\tilde{\omega} = \tilde{\omega}(\tilde{t}) = \min\{\tilde{q}_s, I_c\}$ [m s^{-1}] is the volume flux of water entering the soil per unit surface area, $\tilde{q}_s = \tilde{q}_s(\tilde{t}) : [0, \infty) \to \mathbb{R}_{\geq 0}$ [m s^{-1}] is the volume flux of water per unit area of soil surface, *i.e.*, rainfall, and $I_c \in \mathbb{R}_{\geq 0}$ [m s^{-1}] is the infiltration capacity of the soil. In the event of sufficiently heavy rainfall, the quantity of water that can enter $\tilde{\Lambda}$ is limited by I_c. Any excess rainfall that exceeds I_c, *i.e.*, $\tilde{q}_s - I_c > 0$ is defined as the surface runoff $\tilde{R}_0 = \tilde{R}_0(\tilde{t}) : [0, \infty) \to \mathbb{R}_{\geq 0}$ [m^3 s^{-1}], and is quantified by,

$$\tilde{R}_0(\tilde{t}) = \begin{cases} \left\{ [\tilde{q}_s(\tilde{t}) - I_c] \int_0^{\tilde{x}_0(\tilde{t})} \sqrt{1 + \left(\frac{d\tilde{\chi}(\tilde{x}_1)}{d\tilde{x}_1}\right)^2} d\tilde{x}_1 \right\} & \text{for} \quad \tilde{q}_s > I_c \\ 0 & \text{for} \quad \tilde{q}_s \leq I_c \end{cases}, \tag{2.21}$$

where $\tilde{\chi}(\tilde{x}_1)$ is the generalised curve of $\partial\tilde{\Lambda}_S$, given by (2.2).

To determine the change in pond depth for the boundary conditions imposed on

$\partial\tilde{\Lambda}_R$ and $\partial\tilde{\Lambda}_P$, we implement an additional ODE that is coupled to the governing water movement model (2.16) $-$ (2.18). This connects the volume of water in the pond $\tilde{V} = \tilde{V}(\tilde{t}) : [0, \infty) \to \mathbb{R}_{\geq 0}$ [m^3], the rate of rainfall $\tilde{q_s}(\tilde{t})$, the surface runoff $\tilde{R}_0(\tilde{t})$ and the infiltration flux entering the soil domain from the pond, *i.e.*, the quantity of water leaving the pond and infiltrating into the soil.

We define the maximum depth of the pond $\tilde{h}_0(\tilde{t}) : [0, \infty) \to \mathbb{R}_{\geq 0}$ [m] (see Figure 2.3) at a given time $\tilde{t}$ to be,

$$\tilde{h}_0(\tilde{t}) = \tilde{\chi}[\tilde{x}_0(\tilde{t})] \tag{2.22}$$

where $\tilde{x}_0(\tilde{t}) : [0, \infty) \to [0, \eta]$ [m] is the $\tilde{x}_1$ co-ordinate at which the pond starts, *i.e.*, the partition between $\partial\tilde{\Lambda}_R$ and $\partial\tilde{\Lambda}_P$. It should be noted that for $\tilde{h}_0(\tilde{t})$ to have this definition, the vertical datum $\tilde{x}_3 = 0$ is measured from the base of the soil curve $\tilde{\chi}(\tilde{x})$ (see Figure 2.3). This allows the hydrostatic boundary condition (2.19) to be re-written such that,

$$\tilde{p}_w = \rho g[\tilde{h}_0(\tilde{t}) - \tilde{\chi}(\tilde{x})] \quad \text{on} \quad \partial\tilde{\Lambda}_P \times [0, \infty), \tag{2.23}$$

where $\tilde{h}_0(\tilde{t}) - \tilde{\chi}(\tilde{x}) = \tilde{h}(\tilde{x}, \tilde{t})$.

In addition, a length η is chosen to represent half a ridge and furrow period (see Figure 2.3). It follows that for a given pond volume $\tilde{V}(\tilde{t})$, $\tilde{x}_0(\tilde{t})$ is calculated by,

$$\tilde{V}(\tilde{t}) = \tilde{h}_0(\tilde{t})[\eta - \tilde{x}_0(\tilde{t})] - \int_{\tilde{x}_0(\tilde{t})}^{\eta} \tilde{\chi}(\tilde{x}) d\tilde{x}. \tag{2.24}$$

The change in pond volume $\tilde{V}(\tilde{t})$ is defined to be,

$$\frac{d\tilde{V}(\tilde{t})}{d\tilde{t}} = \tilde{q_s}(\tilde{t})[\eta - \tilde{x}_0(\tilde{t})] + \tilde{R}_0(\tilde{t}) - \int_{\tilde{x}_0(\tilde{t})}^{\eta} \tilde{\mathbf{v}} \cdot \hat{\mathbf{n}}|_{\partial\tilde{\Lambda}_P} d\tilde{x}, \tag{2.25}$$

where $\tilde{q_s}(\tilde{t}) \cdot [\eta - \tilde{x}_0(\tilde{t})]$ [m^3 s^{-1}] is the rainfall entering the pond, $\tilde{R}_0(\tilde{t})$ is the surface runoff and $\int_{\tilde{x}_0(\tilde{t})}^{\eta} \tilde{\mathbf{v}} \cdot \hat{\mathbf{n}}|_{\partial\tilde{\Lambda}_P} d\tilde{x}$ [m^3 s^{-1}] is the quantity of water leaving the pond and infiltrating into the soil by the boundary condition on $\partial\tilde{\Lambda}_P$ [105]. Substituting (2.24) into (2.25) yields,

$$\frac{\partial}{\partial\tilde{t}}\left\{\tilde{h}_0(\tilde{t})[\eta - \tilde{x}_0(\tilde{t})] - \int_{\tilde{x}_0(\tilde{t})}^{\eta} \tilde{\chi}(\tilde{x}) d\tilde{x}\right\} = \tilde{q_s}(\tilde{t})[\eta - \tilde{x}_0(\tilde{t})] + \tilde{R}_0(\tilde{t}) - \int_{\tilde{x}_0(\tilde{t})}^{\eta} \tilde{\mathbf{v}} \cdot \hat{\mathbf{n}}|_{\partial\tilde{\Lambda}_P} d\tilde{x}, \tag{2.26}$$

where $\tilde{h}_0(\tilde{t})$ is defined by (2.22). Equation (2.26) describes the change in the position of $\tilde{x}_0(\tilde{t})$, given the rainfall entering the pond, surface runoff and water infiltration from the pond into the surrounding soil. To calculate $\tilde{\mathbf{v}} \cdot \hat{\mathbf{n}}|_{\partial\tilde{\Lambda}_P}$, (2.26) is coupled with (2.16) $-$ (2.18) and the boundary condition (2.23).

Through successive application of the Leibniz integral rule and the chain rule, for the generic function $\tilde{\chi}(\tilde{x})$, (2.26) can be expressed explicitly as a function of $\frac{d\tilde{x}_0(\tilde{t})}{d\tilde{t}}$, *i.e.*,

$$\frac{d\tilde{x}_0(\tilde{t})}{d\tilde{t}}\left\{\eta\frac{\partial\tilde{\chi}[\tilde{x}_0(\tilde{t})]}{\partial\tilde{x}_0(\tilde{t})}-\tilde{\chi}[\tilde{x}_0(\tilde{t})]-\tilde{x}_0(\tilde{t})\frac{\partial\tilde{\chi}[\tilde{x}_0(\tilde{t})]}{\partial\tilde{x}_0(\tilde{t})}\right\}-\left[\frac{\partial}{\partial\tilde{t}}\int_{\tilde{x}_0(\tilde{t})}^{\eta}\tilde{\chi}(\tilde{x})d\tilde{x}\right]=$$
$$\tilde{q}_s(\tilde{t})[\eta-\tilde{x}_0(\tilde{t})]+\tilde{R}_0(\tilde{t})+$$
$$\int_{\tilde{x}_0(\tilde{t})}^{\eta}\left(\left\{\frac{\partial\tilde{\chi}(\tilde{x})}{\partial\tilde{x}}\frac{\overline{\kappa[S(\tilde{p}_w)]}}{\mu_w}(\partial_{\tilde{x}}\tilde{p}_w)-\frac{\overline{\kappa[S(\tilde{p}_w)]}}{\mu_w}(\partial_{\tilde{z}}\tilde{p}_w+\rho g)\right\}\Bigg|_{\partial\tilde{\Lambda}_P}\left[1+\left(-\frac{\partial\tilde{\chi}(\tilde{x})}{\partial\tilde{x}}\right)^2\right]^{-0.5}\right)d\tilde{x}. \tag{2.27}$$

Note that for the boundary condition on $\partial\tilde{\Lambda}_P$ (2.23) to be active, we impose a minimum pond depth threshold that must be reached before water leaves the pond and infiltrates into the soil, *i.e.*,

$$\tilde{p}_w=\rho g[\tilde{h}_0(\tilde{t})-\tilde{\chi}(\tilde{x})]\quad\text{on}\quad\partial\tilde{\Lambda}_P\times[0,\infty)\quad\text{for}\quad\tilde{\chi}[\tilde{x}_0(\tilde{t})]>\tilde{x}_{\min}, \tag{2.28}$$

where where $\tilde{x}_{\min}$ [m] is the minimum pond depth. We impose this condition to aid numerical computation, since a pond that is substantially smaller than the mesh size can lead to convergence problems. However, we choose the threshold to be sufficiently small that it has a negligible effect on the numeric results.

2.2.4 Non-surface Boundary Conditions and Initial Conditions

Lateral Boundary Conditions

For the boundaries $\partial\tilde{\Lambda}_E$ and $\partial\tilde{\Lambda}_W$, we set a zero flux boundary condition due to the periodicity of $\tilde{\Lambda}$, *i.e.*,

$$\hat{\mathbf{n}}\cdot\left\{\frac{\kappa_s\overline{\kappa[S(\tilde{p}_w)]}}{\mu_w}\left(\tilde{\boldsymbol{\nabla}}\tilde{p}_w+\rho g\hat{\mathbf{e}}_3\right)\right\}=0\quad\text{on}\quad\partial\tilde{\Lambda}_E\cup\partial\tilde{\Lambda}_W\times[0,\infty). \tag{2.29}$$

Therefore, there is no lateral water movement into or out of $\tilde{\Lambda}$.

Boundary Condition at the Base of the Soil

For the boundary on $\partial\tilde{\Lambda}_B$, we set a Dirichlet boundary condition [93], *i.e.*,

$$\tilde{p}_w=p_0\quad\text{on}\quad\partial\tilde{\Lambda}_B\times[0,\infty). \tag{2.30}$$

This represents a constant saturation level at the base of the domain.

Initial Conditions

For the initial pressure condition $\tilde{p}_w|_{\tilde{t}=0}$, we use the steady state pressure profile, *i.e.*,

$$\tilde{p}_w|_{\tilde{t}=0} = p_\infty(\tilde{\mathbf{x}}) \quad \text{in} \quad \tilde{\Lambda} \times \{\tilde{t} = 0\}, \tag{2.31}$$

where $p_\infty(\tilde{\mathbf{x}})$ [Pa] is the steady pressure profile, *i.e.*, when $\partial\tilde{p}_w/\partial t = 0$. Furthermore, we assume there is no surface ponding present on $\partial\tilde{\Lambda}_S$ at $\tilde{t} = 0$, *i.e.*,

$$\tilde{x}_0(\tilde{t})|_{\tilde{t}=0} = \eta \quad \text{for} \quad \{t = 0\}, \tag{2.32}$$

such that the pond depth is $\tilde{h}_0(\tilde{t})|_{\tilde{t}=0} = \tilde{\chi}[\tilde{x}_0(\tilde{t})|_{\tilde{t}=0}] = 0$.

The system of Equations (2.16) $-$ (2.18), (2.20), (2.27) $-$ (2.32) completes the description of the coupled water balance in the presence of surface ponding.

2.2.5 Non-dimensionalisation

Here we non-dimensionalise the system of equations (2.16) $-$ (2.18), (2.20), (2.27) $-$ (2.32). Whilst the final equations we solve are dimensional, we use non-dimensionalisation to determine the magnitude of influence each parameter has on the system of equations. We non-dimensionalise with the scaling,

$$\tilde{\mathbf{x}} = \eta\mathbf{x}, \ \tilde{t} = \frac{\phi\mu_w\eta^2}{\kappa_s p_c}t, \ \tilde{p}_w = p_c p_w, \ \tilde{\chi} = \eta\chi, \ \tilde{x}_0 = \eta x_0. \tag{2.33}$$

In (2.33) we use the domain width η as the spatial scaling, the 'effective diffusivity' $\frac{\phi\mu_w\eta^2}{\kappa_s p_c}$ for the time scaling and the suction characteristic p_c as the pressure scaling. This leads to the system of equations,

$$[1 - H_S(p_w)]\frac{\partial S(p_w)}{\partial p_w}\frac{\partial p_w}{\partial t} = \boldsymbol{\nabla}\cdot\left\{\overline{\kappa[S(p_w)]}\,(\boldsymbol{\nabla}p_w + \overline{\rho}\hat{\mathbf{e}}_3)\right\} - \begin{cases} (\overline{p}_c p_w - \overline{p}_r) & \text{in} \quad \Lambda_U^\infty \\ 0 & \text{in} \quad \Lambda_A^\infty \end{cases}, \tag{2.34}$$

$$\hat{\mathbf{n}}\cdot\left\{\overline{\kappa[S(p_w)]}\,(\boldsymbol{\nabla}p_w + \overline{\rho}\hat{\mathbf{e}}_3)\right\} = \overline{\omega} \quad \text{on} \quad \partial\Lambda_R \times [0,\infty), \tag{2.35}$$

$$p_w = \overline{\rho}[h_0(t) - \chi(x)] \quad \text{on} \quad \partial\Lambda_P \times [0,\infty), \tag{2.36}$$

$$\hat{\mathbf{n}}\cdot\left\{\overline{\kappa[S(p_w)]}\,(\boldsymbol{\nabla}p_w + \overline{\rho}\hat{\mathbf{e}}_3)\right\} = 0 \quad \text{on} \quad \partial\Lambda_E \cup \partial\Lambda_W \times [0,\infty), \tag{2.37}$$

$$p_w = \overline{p}_0 \quad \text{on} \quad \partial\Lambda_B \times [0,\infty), \tag{2.38}$$

$$\frac{dx_0(t)}{dt}\left\{\eta\frac{\partial\chi[x_0(t)]}{\partial x_0(t)}-\chi[x_0(t)]-x_0(t)\frac{\partial\chi[x_0(t)]}{\partial x_0(t)}\right\}-\left[\frac{\partial}{\partial t}\int_{x_0(t)\eta}^{1}\chi(x)dx\right]=$$
$$\overline{q_s}\cdot[1-x_0(t)]+\overline{R}_0+\phi\int_{x_0(t)}^{\eta}\left(\left\{\frac{\partial\chi(x)}{\partial x}\overline{\kappa[S(p_w)]}(\partial_x p_w)-\overline{\kappa[S(p_w)]}(\partial_z p_w+\overline{\rho})\right\}\Big|_{\partial\Lambda_P}\cdot\right.$$
$$\left.\left[1+\left(-\frac{\partial\chi(x)}{\partial x}\right)^2\right]^{-0.5}\right)dx, \quad (2.39)$$

$$p_w|_{t=0}=\overline{p}_\infty \quad \text{in} \quad \Lambda\times\{t=0\}, \quad (2.40)$$

$$x_0|_{t=0}=1, \quad (2.41)$$

where,

$$\frac{\partial S(p_w)}{\partial p_w}=\frac{m\left[(-p_w)^{\frac{m}{1-m}}+1\right]^{-m-1}(-p_w)^{\frac{m}{1-m}}}{(1-m)}, \quad (2.42)$$

$$\overline{\kappa[S(p_w)]}=\begin{cases}1 & \text{for} \quad p_w\geq-\zeta_t\\ \left[(p_w)^{\frac{m}{1-m}}+1\right]^{\frac{-m}{2}}\left(1-\left\{1-\left[(-p_w)^{\frac{m}{1-m}}+1\right]^{-1}\right\}^m\right)^2 & \text{for} \quad p_w<-\zeta_t\end{cases}, \quad (2.43)$$

and

$$\overline{\rho}=\frac{\rho g\eta}{p_c},\ \overline{p}_c=\frac{\lambda_c p_c\mu_w\eta^2}{\kappa_s p_c},\ \overline{p}_r=\frac{\lambda_c p_r\mu_w\eta^2}{\kappa_s p_c},\ \overline{\omega}=\frac{\eta\mu_w\omega}{\kappa_s p_c},$$
$$\overline{p}_0=\frac{p_0}{p_c},\overline{q_s}=\frac{\eta\mu_w\phi q_s}{\kappa_s p_c},\overline{R}_0=\frac{\mu_w\phi R_0}{\kappa_s p_c},\ \overline{p}_\infty=\frac{p_\infty}{p_c}. \quad (2.44)$$

2.2.6 Parameter Estimation

Here we estimate the parameters contained in equations (2.34) $-$ (2.43) to determine the magnitude of influence that each parameter in (2.44) has on the system of equations. This allows us to identify the key mechanisms that dominate water movement under surface ponding from heavy rainfall. Since this model has been constructed for ridge and furrow soils, we assess the parameter values for silt soils and the plant *Solanum tuberosum* L., since this crop is frequently grown in silt soils in ridged systems [106]. Shown in Table 2.1 is a summary of the parameters used in the non-dimensionalisation estimation.

For silt soils typical saturated permeability values are $1\times10^{-14}\lesssim\kappa_s\lesssim5\times10^{-14}$ m^2 [101], porosity values are $\phi\approx0.4$ [101], and characteristic suction pressures are $p_c\approx2\times10^4$ Pa [101]. Furthermore, average values for pore pressures at field

capacity in silt soils are $p_\infty \approx p_0 \approx \mathcal{O}(10^4)$ Pa [107].

Heavy rainfall in the United Kingdom is classified between the range of $4 \times 10^{-6} \lesssim q_s \lesssim 1 \times 10^{-5}$ m s^{-1} [108], and silt soils have a steady state infiltration capacity of $I_c \approx 2 \times 10^{-6}$ m s^{-1} [109]. Hence, the infiltration and runoff parameters have values $\omega = \mathcal{O}(10^{-6})$ m s^{-1} and $R_0 = \mathcal{O}(10^{-6})$ m^2 s^{-1}.

For the plant *Solanum tuberosum* L., typical root pressures are $p_r \approx 0.05$ MPa [110], and values for the effective uptake parameter are $\lambda_c \approx 3 \times 10^{-11}$ s^{-1} Pa^{-1} [107].

We take the density of water to be $\rho = 1 \times 10^3$ kg m^{-3}, the viscosity of water to be $\mu_w = 1 \times 10^{-3}$ Pa s and gravity to be $g = 9.81$m s^{-2}. Additionally, for ridge and furrow structures, the average width of a half period is $\eta \approx 0.5$ m [47, 92].

Using the values above, we observe that the non-dimensionalised parameters shown in (2.44) have the approximate values,

$$\begin{aligned} \overline{\rho} = \mathcal{O}(1),\ \overline{p}_c = \mathcal{O}(1),\ \overline{p}_r = \mathcal{O}(1),\ \overline{\omega}(t) = \mathcal{O}(1), \\ \overline{p}_0 = \mathcal{O}(1),\ \overline{q_s}(t) = \mathcal{O}(1), \overline{R_0}(t) = \mathcal{O}(1)\ \overline{p}_\infty = \mathcal{O}(1). \end{aligned} \tag{2.45}$$

From (2.45) we observe that all the non-dimensionalised parameters are of the same order of magnitude $\mathcal{O}(1)$, *i.e.*, all components of the governing equations and boundary conditions are important and none can be neglected from the model.

Table 2.1: A table of the parameters used in the non-dimensionalisation and parameter estimation of the water movement and ponding model.

Parameter	Description	Value	Units	Reference
κ_s	saturated permeability	5×10^{-14}	m^2	[101]
ϕ	porosity	0.4	$-$	[101]
p_c	characteristic suction pressure	2×10^4	Pa	[101]
p_0	basal geometry pressure	2×10^4	Pa	[107]
q_s	rainfall	$4 - 10 \times 10^{-6}$	m s^{-1}	[108]
I_c	infiltration capacity	2×10^{-6}	m s^{-1}	[109]
ω	water infiltration	2×10^{-6}	m s^{-1}	[109]
R_0	runoff	$2 - 8 \times 10^{-6}$	m^3 s^{-1}	[109]
p_r	root xylem pressure	5×10^4	Pa	[110]
λ_c	effective uptake	3×10^{-11}	s^{-1} Pa^{-1}	[107]
ρ	density of water	1×10^3	kg m^{-3}	–
μ_w	viscosity of water	1×10^{-3}	Pa s	–
g	gravity	9.81	m s^{-2}	–
η	width of $\tilde{\Lambda}$	0.5	m	[47, 92]

2.2.7 Implementation

Here we describe how we utilise the finite element package COMSOL Multiphysics ver 5.3 (COMSOL Multiphysics, Stockholm, Sweden, www.comsol.com) to solve the mathematical model. To implement the governing equation (2.16), we use the inbuilt 'General Form PDE', which takes the form,

$$e_a \frac{\partial^2 \mathbf{r}}{\partial t^2} + d_a \frac{\partial \mathbf{r}}{\partial t} + \boldsymbol{\nabla} \cdot \boldsymbol{\Theta} = f, \tag{2.46}$$

where $\mathbf{r} = \tilde{p}_w$, and e_a, d_a, $\boldsymbol{\Theta}$ and f are parameters to be defined. To write the model in this form, the parameters are constructed to replicate equation (2.16), *i.e.*,

$$e_a = 0,\ d_a = [1 - H_S(\tilde{p}_w)]\phi \frac{\partial S(\tilde{p}_w)}{\partial \tilde{p}_w},\ \boldsymbol{\Theta} = -\frac{\kappa_s \overline{\kappa[S(\tilde{p}_w)]}}{\mu_w}\left(\tilde{\boldsymbol{\nabla}}\tilde{p}_w + \rho g \hat{\mathbf{e}}_3\right),$$
$$f = -\begin{cases} \lambda_c(\tilde{p}_w - p_r), & \text{in} \quad \tilde{\Lambda}_U^\infty \\ 0, & \text{in} \quad \tilde{\Lambda}_A^\infty \end{cases}, \tag{2.47}$$

where the functions $H_S(\tilde{p}_w)$, $S(\tilde{p}_w)$ and $\kappa[S(\tilde{p}_w)]$ are explicitly defined.

For the ODE to describe the moving point $\tilde{x}_0$ on the surface $\partial\tilde{\Lambda}_S$, *i.e.*, equation (2.27), we use the inbuilt ODE equation 'Global ODE' to implicitly calculate $\tilde{x}_0(\tilde{t})$. The 'Global ODE' takes the form,

$$f(q, q_t, q_t t, t) = 0. \tag{2.48}$$

To write equation (2.27) in this form for the curve $\tilde{\chi}(\tilde{x})$, the 'Global ODE' is set up so that,

$$\{AB[\tilde{x}_0(\tilde{t}) - \eta]\sin[B\tilde{x}_0(\tilde{t})]\}\frac{d\tilde{x}_0(\tilde{t})}{d\tilde{t}} - [\Upsilon_r(\tilde{t}) + \Upsilon_p(\tilde{x}, \tilde{t})] = 0, \tag{2.49}$$

where,

$$\Upsilon_r(\tilde{t}) = \tilde{q_s}(\tilde{t}) \cdot [\eta - \tilde{x}_0(\tilde{t})] + \tilde{R}_0(\tilde{t}), \tag{2.50}$$

and,

$$\Upsilon_p(\tilde{x}, \tilde{t}) = \int_{\tilde{x}_0}^{\eta} \frac{\left[\frac{\kappa(\tilde{p}_w)}{\mu}\partial_{\tilde{z}}\tilde{p}_w + \rho g\right] + \left[AB\sin(B\tilde{x})\frac{\kappa(\tilde{p}_w)}{\mu}\partial_{\tilde{x}}\tilde{p}_w\right]}{\sqrt{1 + \left[AB\sin(B\tilde{x})\right]^2}}. \tag{2.51}$$

For the flux boundaries, *i.e.*, equations (2.20) and (2.29), we use the inbuilt flux boundary condition that takes the form,

$$\hat{\mathbf{n}} \cdot \boldsymbol{\Theta} = g_1 - g_2 \mathbf{r}, \tag{2.52}$$

where g_1 and g_2 depend on the specific flux boundary. For equation (2.20) we set $g_1 = \tilde{\omega}(\tilde{t})$ and $g_2 = 0$, and for equation (2.29) we assign $g_1 = g_2 = 0$. Similarly, for the boundary condition (2.30), we use the inbuilt Dirichlet boundary condition. This takes the form,

$$\mathbf{r} = r_0, \tag{2.53}$$

where $r_0 = p_0$.

For the hydrostatic boundary condition, equation (2.28), we are not able to impose the generic inbuilt Dirichlet boundary condition since the software treats the boundary condition as a step function so that,

$$\tilde{p}_w = \begin{cases} \rho g[\tilde{h}_0(\tilde{t}) - \tilde{\chi}(\tilde{x})] & \text{on} \quad \partial\tilde{\Lambda}_P \times [0,\infty) \\ 0 & \text{on} \quad \partial\tilde{\Lambda}_R \times [0,\infty) \end{cases}. \tag{2.54}$$

This in turn leads to a permanent fully saturated boundary along the bare soil surface $\partial\tilde{\Lambda}_R$. To avoid this problem, we re-write equation (2.28) as a flux condition along $\partial\tilde{\Lambda}_P$ that mimics a Dirichlet condition. This is achieved by,

$$\hat{\mathbf{n}} \cdot \boldsymbol{\Theta} = \begin{cases} k_\infty\{\rho g[\tilde{h}_0(\tilde{t}) - \tilde{\chi}(\tilde{x})] - \tilde{p}_w\} & \text{on} \quad \partial\tilde{\Lambda}_P \times [0,\infty) \\ 0 & \text{on} \quad \partial\tilde{\Lambda}_R \times [0,\infty) \end{cases}, \tag{2.55}$$

where $k_\infty \gg 1\ [-]$. As k_∞ increases, equation (2.55) reduces to $p_w \approx \rho g[\tilde{h}_0(\tilde{t}) - \tilde{\chi}(\tilde{x})]$ on $\partial\tilde{\Lambda}_P$. Therefore, equation (2.28) can be approximated and imposed as a flux condition along the partition $\partial\tilde{\Lambda}_P$ only, providing $k_\infty \gg 1$ is sufficiently large. In order to ensure that k_∞ is large enough so that $k_\infty^{-1}\hat{\mathbf{n}} \cdot \boldsymbol{\Theta} \approx 0$, we run a series of simulations to determine when the flux effect is negligible. We find that $k_\infty = \text{ord}(10^6)$ is sufficiently large to negate any influence from the term $\hat{\mathbf{n}} \cdot \boldsymbol{\Theta}$.

The model is solved using the MUMPS (Multifrontal Massive Parallel Sparse Direct Solver) subroutine, which is a direct method that utilises Gaussian elimination from multiple LU decompositions. The subroutine utilises the sparsity of the system of equations by constructing matrices for subsets of elements [111].

2.2.8 Model Validation

To validate the model, we use data from the ponding study by Siyal *et al.* (2012) [112]. In that study a trapezoidal ridge and furrow geometry was created using a loam soil in which a constant flow of water flowed longitudinally down the furrow until a pond height of 0.1 m was reached. Once the desired pond height was reached, the flow of water was stopped and the time required for the pond to

infiltrate fully into the soil was measured.

The model derived in this chapter uses the sinusoidal function $\tilde{\chi}(\tilde{x}) = A\cos(B\tilde{x}) + C$ to model the periodic surface topology of ridge and furrow structures, *i.e.*, $\partial\tilde{\Lambda}_S$. It is impossible to resolve a piecewise trapezoidal surface with the sinusoidal surface shown in equation (2.2). However, we construct a domain using equation (2.2) that minimises the difference to the trapezoidal structure in Siyal *et al.* (2012) [112]. This was achieved with the geometry parameters $A = C = 0.12$ m, $B = 2\pi$ m^{-1} and $\eta = 0.5$ m in equation (2.2).

In the paper by Siyal *et al.* (2012) [112], the time taken to generate the 0.1 m deep pond was 5.6 hours, and the time required for the water to fully infiltrate into the soil was 16 hours. To replicate these conditions, we simulate a rainfall event that lasted 5.6 hours with an intensity of 14.8 mm hour^{-1} to equate the total pond volume in the simulated sinusoidal geometry with that of ponded water in the trapezoidal geometry of Siyal *et al.* (2012) [112].

We measure the time required for the pond to fully infiltrate into the soil by conducting a simulation, in which we use same parameter values as those used in Siyal *et al.* (2012) [112]. These parameters were estimated experimentally for the soil and were calculated to be $\phi = 0.43$, $\kappa_s = 2.63 \times 10^{-13}$ m^2 (assuming the fresh water properties $\rho = 1000$ kg m^{-3}, $\mu_w = 1 \times 10^{-3}$ kg m^{-1}s^{-1} and $g = 9.81$ m s^{-2}), $m = 0.36$ and $p_c \approx 2500$ Pa.

In the numerical simulation, we observed that the pond caused by the rainfall event fully dissipated into the soil after approximately $15.\dot{3}$ hours, which is $\approx 4\%$ different to the results found in Siyal *et al.* (2012) [112]. This result gives us confidence that the model derived in this chapter can accurately describe time-variable ponding in ridge and furrow soil systems.

2.3 Numerical Solutions

To demonstrate the mathematical model, we explore how the water profile in ridge and furrow soils is affected by heavy rainfall that generates substantial ponding. We simulate one heavy rainfall event that generates substantial ponding in the furrow of the soil, and analyse the infiltration of water into the soil and the influence on the soil pressure profile. Additionally, we include vegetation in the ridges of the soil. The crop we choose to simulate is the potato *Solanum tuberosum* L. as this crop is traditionally grown in ridge and furrow structures.

Table 2.2: A table of the parameters used in the numerical simulations for a single heavy rainfall event using a ridge and furrow geometry.

Parameter	Description	Value	Units	Reference
κ_s	saturated permeability	5.2×10^{-14}	m^2	[101]
m	van Genuchten parameter	0.5	$-$	[101]
ϕ	porosity	0.396	$-$	[101]
p_c	characteristic suction pressure	23200	Pa	[101]
p_0	basal geometry pressure	-1×10^4	Pa	$-$
q_s	rainfall	3.75×10^{-6}	m s^{-1}	$-$
I_c	infiltration capacity	1.6×10^{-6}	m s^{-1}	[109]
p_r	root xylem pressure	-5×10^4	Pa	[110]
λ_c	effective uptake	3.14×10^{-11}	$\text{s}^{-1}\ \text{Pa}^{-1}$	[107]
ρ	density of water	1×10^3	kg m^{-3}	$-$
μ_w	viscosity of water	1×10^{-3}	Pa s	$-$
g	gravity	9.81	m s^{-2}	$-$
ζ_t	saturated-partially saturated interface	1×10^{-1}	Pa	$-$
σ	Heaviside transition	1×10^4	Pa^{-1}	$-$
$\tilde{x}_{\text{min}}$	minimum ponding depth	3×10^{-4}	m	$-$
A	variation in soil depth	0.16	m	[47, 92]
B	ridge wave number	2π	m^{-1}	[47, 92]
C	average soil depth	0.16	m	[47, 92]
η	width of $\tilde{\Lambda}$	0.5	m	[47, 92]

2.3.1 Parameter Values

Summarised in Table 2.2 are a list of the parameters used in the numerical simulation. Detailed below are the parameter values and their origins.

To replicate the dimensions of typical ridge and furrow geometries, we use the values $\eta = 0.5$ m, $A = C = 1/6$ m and $B = 2\pi$ m^{-1} for the function $\tilde{\chi}(\tilde{x})$ that describes $\partial\tilde{\Lambda}_S$ [47, 92]. Furthermore, the crop *Solanum tuberosum*, L. is shallow rooted with the majority of its roots in the plough layer, *i.e.*, the top 0.3 m of soil [103]. Therefore, we choose the size of the soil root region $\tilde{\Lambda}_U$ to be the top 0.3 m of soil extending radially from the top of the ridge. The domain used can be seen in Figure 2.2 (b).

The crop *Solanum tuberosum*, L. is frequently grown in silt loam soils [113]. Hence, for the soil parameters, we choose values for typical silt loam soils, $\phi = 0.396$, $m = 0.51$, $\kappa_s = 5.2 \times 10^{-14}$ m^2 and $p_c = 23200$ Pa [101]. For the viscosity of water we use $\mu_w = 1 \times 10^{-3}$ Pa s, for acceleration due to gravity $g = 9.81$ m s^{-2} and for the density of water $\rho = 1000$ kg m^{-3}.

The parameter λ_c is the product of the root surface area density and water

conductivity of the root cortex, which can be expressed by,

$$\lambda_c = k_r l_d, \tag{2.56}$$

where l_d is the root length density and k_r is the radial conductivity of root cortex per unit root length. l_d values for *Solanum tuberosum*, L. are typically $l_d \approx 4 \times 10^4$ m^{-2} [114]. Additionally, in maize (*Zea mays* L.), the radial conductivity is $k_r \approx 7.85 \times 10^{-10}$ m^2 s^{-1} MPa^{-1} [41]. Since maize and potato roots have similar root radii and structure [115, 116], we assume this value is representative of potato roots in soil. This leads to the parameter value $\lambda_c = 3.14 \times 10^{-5}$ s^{-1} MPa^{-1}.

The root pressure p_r can vary considerably in *Solanum tuberosum*, L. plants depending on several factors including soil saturation and atmospheric conditions [117]. Liu et al. (2006) [110] found that the root water potential changes substantially based on the method of irrigation applied to the crop. A value of $p_r \approx -0.01$ MPa was present in the roots for a fully irrigated system and of -0.2 MPa $\lesssim p_r \lesssim -0.02$ MPa for areas of soil with partial root drying. Given this we choose the value $p_r = -0.2$ MPa.

For the parameters ζ_t and $\tilde{x}_{\text{min}}$, we selected small values that have a negligible effect on the numerical solution. For ζ_t we select the value $\zeta_t = 1 \times 10^{-1}$ Pa. Given that pressure in soil is often measured in $\mathcal{O}(10^4)$ Pa, ζ_t is sufficiently small to have a negligible effect. Furthermore, for $\tilde{x}_{\text{min}}$ (the minimum pond depth) we choose $\tilde{x}_{\text{min}} = 3 \times 10^{-4}$ m. Therefore, the hydrostatic boundary condition Equation (2.28) is activated once the pond depth surpasses 0.3 mm.

For the parameter σ in the smoothed Heaviside function $H_S(\tilde{p}_w)$, we assign the value $\sigma = 1000$ Pa^{-1}. This limits the width of the transition between partially and fully saturated soil regions such that the transition is completed across 0.001 Pa. Given that pressure in soil is often measured in $\mathcal{O}(10^4)$ Pa, this value is sufficiently small to have a negligible effect.

To describe the base of the geometry, we assign a constant soil water pore pressure of $p_0 = -10$ kPa. This equates to a saturation level of approximately $S \approx 0.9$ for a silt loam soil, thereby replicating a shallow water table. For the initial soil water pore pressure profile $p_\infty(\tilde{\mathbf{x}})$, we choose the steady state profile that forms in $\tilde{\Lambda}$ prior to any rainfall. Hence, in the simulation, we allow steady state to form so that $\partial_t \tilde{p}_w = 0$ before initiating the rainfall event.

We simulate a single heavy rainfall event that lasts 4 hours with an intensity of 13.5 mm hr^{-1} after the soil pressure has reached steady state. The severity of the ponding is primarily determined by the infiltration capacity I_c of soil. I_c is known to

depend on several factors including volumetric water content, soil type, recent rain events and tillage methods [118]. Therefore, it is difficult to assign a single value to the infiltration capacity of a soil. Morin & Benyamini (1977) [109] found that steady state infiltration of bare loam soil was reached after approximately 20 minutes into a rainfall event. We simulate a rainfall event that is an order of magnitude longer than this, thus, we assign a constant value for the infiltration capacity. Morin & Benyamini (1977) [109] found the steady state infiltration rate of bare loam soil is between $1.3 - 2.2 \times 10^{-6}$ m s^{-1}. Hence, we assign the value $I_c = 1.6 \times 10^{-6}$ m s^{-1}.

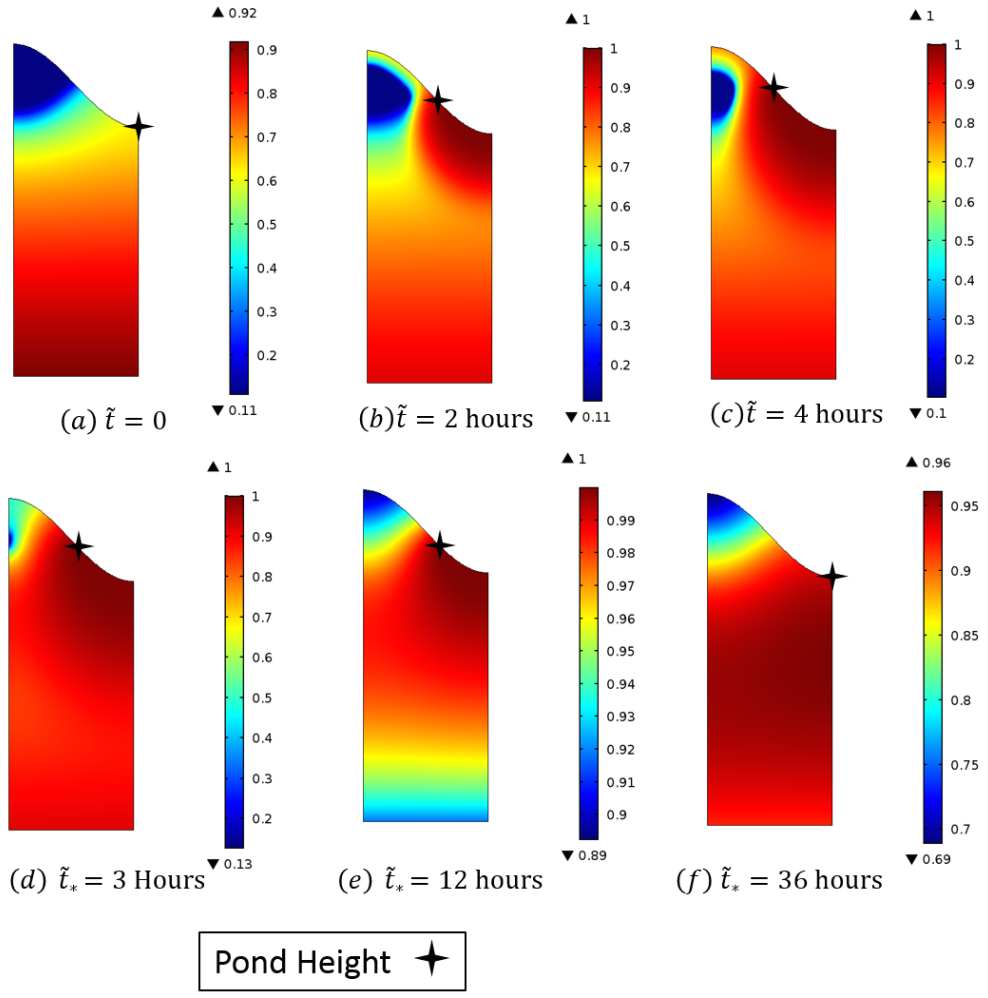

Figure 2.4: Time series of saturation $S(\tilde{p}_w)$ plots across the domain $\tilde{\Lambda}$ at times before, during and after the rainfall event. The first three plots $(a) - (c)$ show the $S(\tilde{p}_w)$ profile before, during and at the end of the rainfall event, respectively, where $\tilde{t} = 0$ represents the start of the 4 hour rain event. The second three plots $(d) - (i)$ show the $S(\tilde{p}_w)$ profile after the rain event, where $\tilde{t}_* = 0$ denotes the end of the rainfall event. The pond location $\tilde{x}_0$ is indicated by a black star along $\partial\tilde{\Lambda}_S$.

2.3.2 Results

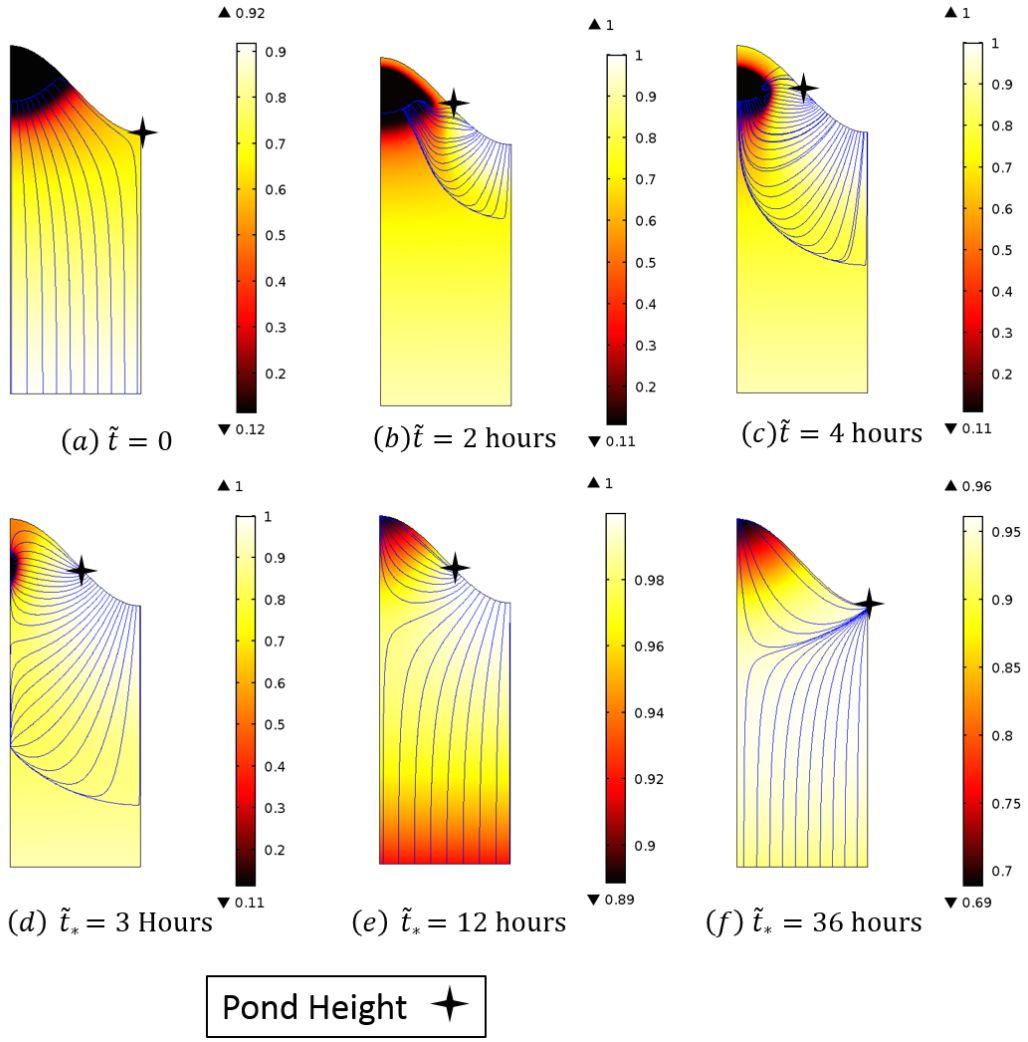

Figure 2.5: Time series of water flux streamline (flow vectors) plots across the domain $\tilde{\Lambda}$ at times before, during and after the rainfall event. The first three plots $(a) - (c)$ show the water flux streamlines before, during and at the end of the rainfall event respectively, where $\tilde{t} = 0$ represents the start of the 4 hour rain event. The second three plots $(d) - (i)$ show the water flux streamlines after the rain event, where $\tilde{t}_* = 0$ denotes the end of the rainfall event. The pond location $\tilde{x}_0$ is indicated by a black star along $\partial\tilde{\Lambda}_S$.

Shown in Figures 2.4 – 2.6 are the numeric results of the simulation. Figures 2.4 – 2.6 show the saturation profile, water flux streamlines and region of full saturation in $\tilde{\Lambda}$ respectively. The times chosen in each of the figures were selected to emphasise the formation, growth and dissipation of the pond in the furrow. In each of the figures, the first three subplots $(a) - (c)$ show the domain $\tilde{\Lambda}$ before, during and at the end of the 4 hour rainfall event respectively, where $\tilde{t} = 0$ represents the start of the rainfall. The second three plots $(d) - (f)$ show the domain $\tilde{\Lambda}$ after the rainfall event

has finished, where $\tilde{t}_* = 0$ denotes the time at the end of the rainfall event. It should be noted that each subplot $(a) - (f)$ has a different colour scale bar. Since large soil water pore pressure differences form throughout the simulation, the saturation gradients that result from ponding would otherwise be reduced in appearance if the scale considered both low and high saturation when ponding is present.

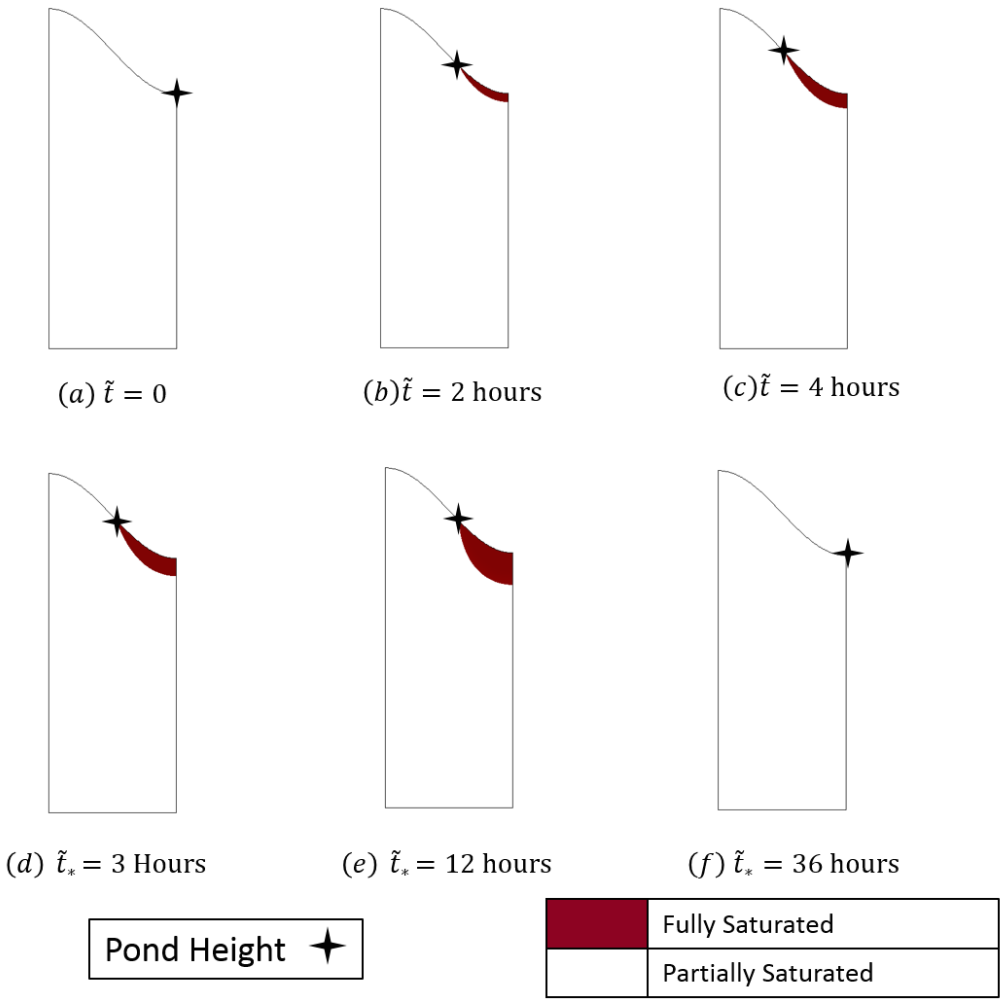

Figure 2.6: Time series of plots across the domain $\tilde{\Lambda}$ at times before, during and after the rainfall event highlighting the region of full saturation. The first three plots $(a) - (c)$ show the fully saturated region of soil before, during and at the end of the rainfall event respectively, where $\tilde{t} = 0$ represents the start of the 4 hour rain event. The second three plots $(d) - (i)$ show the fully saturated region of soil after the rain event, where $\tilde{t}_* = 0$ denotes the end of the rainfall event. The pond location $\tilde{x}_0$ is indicated by a black star along $\partial\tilde{\Lambda}_S$. The red regions represent fully saturated soil and the white regions represent partially saturated soil.

At $\tilde{t} = 0$, we observe the steady state conditions that form from the boundary conditions imposed on $\tilde{\Lambda}$, which are achieved after approximately one week. From Figure 2.4 (a) we find that the saturation $S(\tilde{p}_w)$ in $\tilde{\Lambda}_U$ is substantially reduced

compared to $\tilde{\Lambda}_A$. This is to be expected as there is a dominant pressure gradient formed by the difference in soil water pore pressure and the pressure in the root xylem. This can be clearly seen in Figure 2.5 (a) where the flux streamlines show the movement of water from the base of the domain (originating from the Dirichlet condition on $\partial\tilde{\Lambda}_B$) to the subdomain $\tilde{\Lambda}_U$.

Once the rainfall event starts, we can see the effect of the pond depth in the top of $\tilde{\Lambda}$. At $\tilde{t} = 2$ hours, there is a maximum pond depth of approximately $\tilde{h}_0 = 9$ cm. The effect of the pond on the soil surface can be seen in 2.4 (b) in which the soil adjacent to the furrow has the highest degree of saturation. We observe that the pond on the soil surface creates a region of fully saturated soil, *i.e.*, $\tilde{p}_w \geq 0$, just below the pond, which can be seen in Figure 2.6 (b). Furthermore, due to the dominant pressure in the root xylem, in Figure 2.5 (b) we observe that the immediate water that infiltrates into the soil is transported to the ridges and the vegetation in $\tilde{\Lambda}_U$.

At the end of the rainfall event, the pond on $\partial\tilde{\Lambda}_S$ reaches a maximum depth of $\tilde{h}_0 = 14$ cm. From Figure 2.4 (c) we observe that in the ridges of $\tilde{\Lambda}$ the region of dry soil from the roots is reduced as the infiltration of rainfall along the partition $\partial\tilde{\Lambda}_R$ dominates the rate at which the plant can draw up water from the soil. Additionally, the water that infiltrates into the soil from the ponded furrow is transported to the ridges, thereby increasing the degree of saturation. In Figure 2.6 (c), we observe that the region of fully saturated soil has increased due to the increase in ponding depth.

Once the rainfall event has ended, the effect from surface ponding becomes evident. In Figure 2.6 (d), we find that the region of fully saturated soil has increased. Additionally, we observe in Figure 2.5 (d) that as the pond decreases and infiltrates into the soil, the dominant water transport mechanism is no longer due to root water uptake, but is instead controlled by the infiltration of water from $\partial\tilde{\Lambda}_P$. From Figure 2.4 (d) we find that the region of soil adjacent to the ridge surface of $\tilde{\Lambda}$ becomes the driest region of soil due to the termination of rainfall along $\partial\tilde{\Lambda}_R$.

At the time point $\tilde{t}_* = 12$ hours, we observe that the infiltration of water from the pond fully suppresses the uptake of water by the roots in $\tilde{\Lambda}_U$. In Figure 2.4 (e) we observe that the value of $S(\tilde{p}_w)$ in $\tilde{\Lambda}_U$ has increased dramatically compared to the prior time points. As the water infiltrates from the pond and decreases in height, this causes the region of soil that is fully saturated to extend deeper into the soil, this can be seen in Figure 2.6 (e). Furthermore, from Figure 2.5 (e) we observe that the majority of the water from the pond is transported to the base of $\tilde{\Lambda}$ and is removed from the system due to the Dirichlet condition on $\partial\tilde{\Lambda}_S$. Hence, the infiltration of water from the pond becomes the overwhelming mechanism for water movement.

Once the pond has fully infiltrated into the soil, *i.e.*, $\tilde{t}_* = 36$ hours, we observe that $\tilde{\Lambda}$ returns to being partially saturated, this is seen in Figure 2.6 (f). Although the degree of saturation in $\tilde{\Lambda}_U$ is substantially higher than in the steady state solution, from Figure 2.4 (f) we find that the saturation profile in $\tilde{\Lambda}$ reflects the same characteristics as Figure 2.4 (a), *i.e.*, the top of $\tilde{\Lambda}$ has the lowest saturation and increases with depth in soil. Furthermore, from Figure 2.5 (f) we observe that all the water adjacent to the soil surface $\partial\tilde{\Lambda}_S$ is transported to $\tilde{\Lambda}_U$. However, we see that as the large body of ponded water moves down through the soil domain, this remains largely unaffected by the influence of the pressure gradient due to the root xylem. Hence, even after the pond has fully dissipated, the infiltration of water is still the dominant transport mechanism.

2.4 Conclusions

In this chapter, we developed a system of equations that describe the movement of water in soil. These equations were coupled to an equation for dynamic ponding on the soil surface as a function of rainfall, surface runoff and infiltration of water from the pond into the soil. We validated the model using data from a ridge and furrow study that modelled the infiltration time of a pond into a loam soil, and found a difference of $\approx 4\%$ between the numeric results of the study and our model simulation.

As a case study to demonstrate the model, we conducted a simulation to represent a heavy rainfall event that generates substantial ponding on the soil surface for a silt loam soil. We simulated plant roots and vegetation in the ridges of the soil for the crop *Solanum tuberosum* L., which is typically grown in silt loam soils in ridge and furrow structures.

We observe that when ponding is absent, the dominant transport mechanism for water movement is determined by the pressure gradient that forms between the soil water pore pressure and the pressure in the root xylem. This causes the majority of water to be transported to the ridges of the soil structure. However, during the ponding event, we find that the water infiltration from the soil surface is the dominant mechanism, which draws water down to the base of the domain.

Chapter 3

Coupled Solute Transport and Water Dynamics Model

In this chapter, we extend the water movement and surface ponding model from Chapter 2 to incorporate the transport of solutes, thereby creating a coupled solute and water movement model with the addition of surface ponding. Using this model we conduct a comparison of water and solute movement in two key soil structures: a ridge and furrow soil, and a flat field. We observe that the surface topology to best reduce solute leaching can be either the ridge and furrow or flat geometry depending on several factors. We find that the key factor in determining solute penetration in these systems is the time delay between solute application and rainfall, since the surface topology can heavily influence solute transport.

3.1 Introduction

In arable farming there are multiple row production planting methods that are used to cultivate crops [45], which are briefly discussed in Chapter 1. Two of the key planting methods are ridge and furrow planting [47], and flat planting [43]. These cultivation methods are particularly important for crops like the potato, *i.e.*, *Solanum tuberosum* L. [119], which is an essential crop in temperate European environments [120].

There have been multiple experimental studies comparing crop yield between ridge and furrow and flat tillage methods in order to determine the difference in *Solanum tuberosum* L. growth and yield. Lewis *et al.* (1973) [43] found there to be no measurable differences in the total crop yield between the two tillage methods, however, there was found to be a significant difference in marketable yield. There

was a reduction in marketable *Solanum tuberosum* L. tubers in the flat tillage field as the surface topology caused the tubers to be susceptible to sunburn causing damaged and inedible crops. Furthermore, Alva *et al*. (2002) [121] conducted a four year field rotation study between ridge and furrow and flat planting systems. There were no significant differences between the two planting methods over the first two years of the study. However, there was a substantial difference in crop production in the third year, in which there was a significant yield reduction using the flat tillage method. This was due to nutrient replenishment problems in the flat system [121].

While both the ridge and furrow planting and flat planting methods can result in similar yields, tuber size and productivity [43, 121]; the ridge and furrow planting method has been found to be the preferred tillage method [49]. This is due to several reasons including: ease of harvesting [50], assisting with slow seed germination [51], and nutrient replenishment in the soil [52].

Although the ridge and furrow cultivation procedure is often the preferred planting system, growing evidence suggests that ridge and furrow soil systems may be vulnerable to solute leaching compared to other tillage methods [18, 58, 59], due to ponding on the soil surface [122]. Experimentally, solutes (including pesticides and dyes) have been applied to ridges and furrows of potato fields in order to determine the depth of solute penetration in different areas of the soil [50, 123, 124]. In these studies, it was found that the substance in the furrows moved to a deeper absolute depth in the soil, supporting the suggested vulnerability of the ridge and furrow geometry to solute leaching. Furthermore, a recent European Food Safety Authority (EFSA) report indicated that ridge and furrow soils may increase leaching six-fold when compared to flat soils [60], which can cause devastating effects for local groundwater contamination.

In ridge and furrow soil systems, a key result of the soil surface topology is the influence of solute transport from localised rainfall. Rainfall that lands on the top of the ridges is transported to the furrow and then into the soil, which has been shown to increase the movement of several mobile solutes such as nitrogen, bromide and herbicides (alachlor) deep into the soil profile [125].

However, there is also evidence to suggest that ridge and furrow planting can significantly reduce leaching if solute management techniques are used [17]. This can substantially reduce the negative environmental impact [126], even compared to flat planting cultivation [127]. Furthermore, ridge and furrow structures have been shown to reduce surface water contamination from pesticides since soil erosion in ridged systems is reduced [128].

It has been observed that ridge and furrow systems, and flat field systems show similar levels of plant root uptake for mobile solutes, such as nitrogen [129]. However, in ridge and furrow systems, rainfall landing on the canopy of the plant can transport water into the furrow generating increased ponding. This can lead to greater infiltration of water and solutes into the soil through the furrow compared to an analogous flat ground profile. As such, one hypothesis to reduce leaching and optimising yields for mobile solutes such as nitrogen, is to place the solute solely on the ridges of the soil as this may reduce deep penetration [129, 130]. However, once the crops are removed from the ridge and furrow soil after harvesting, any remaining solute that is left in the soil may be vulnerable to leaching from furrow irrigation [131], as there is reduced solute penetration into the soil when plant root uptake of water is present [132].

For climates in which the ridge and furrow structure is used for formal water irrigation, it has been suggested that sprinkler irrigation (that avoids surface ponding) would reduce nitrogen leaching compared to traditional furrow irrigation [131]. This is due to the fact that prolonged surface ponding at low water depths causes substantially higher dispersion of solutes in soil compared to short ponding events with high water depths [133]. Additionally, to help combat the effects of deep solute penetration from surface ponding, it has been hypothesised that compressing the soil in the furrows may reduce potential leaching from mobile solutes [112].

Conducting experimental solute movement studies in ridge and furrow, and flat tillage systems is often very time consuming and expensive due to the large volume of soil and equipment required, such as dialysis probes and lysimeters. Hence, using mathematical modelling to determine solute movement in soil can significantly reduce the time required to understand the influence of specific environmental factors.

Mathematical models for solute movement in soil are typically based on the advection-diffusion-reaction equation [134], *i.e.*,

$$\partial_t c = D\partial_{xx} c - V\partial_x c - F, \tag{3.1}$$

where c [kg m^{-3}] is the solute concentration, D [m^2 s^{-1}] is the diffusion coefficient, V [m s^{-1}] is the volumetric water flux and F [kg^2 m^{-3} s^{-1}] is zero/first order source/sink term. Originally these models were solved analytically for one spatial dimension and one time dimension with either full or pseudo-analytical solutions for a range of simple boundary conditions [135, 136]. These often resulted in solving a series of eigenvalue problems to develop a series solution, which was

troublesome due to the large number of values required for the series to converge.

Since then, the advection-diffusion-reaction equation for solute movement in soil has been extended to include stochastic processes [137], non-linearity [138], dual porosity [139], and heterogeneities with the soil domain [140].

There have been several studies utilising mathematical modelling to determine solute movement in ridge and furrow structures [94, 112, 130, 131, 138, 141–143]. In all these studies the solute that is analysed is nitrogen or a nitrate based fertiliser. All these models use the advection-diffusion-reaction equation to describe solute movement within the soil system [142]. Several of the mathematical models couple the advection-diffusion-reaction equation with Richards' equation to create a system of equations that describe simultaneous water and solute movement [130, 131], *i.e.*,

$$\partial_t S + \boldsymbol{\nabla} \cdot \mathbf{v} = 0, \tag{3.2}$$

$$\partial_t c + \boldsymbol{\nabla} \cdot (D(S)\boldsymbol{\nabla} c - V(S)c) = -F_c, \tag{3.3}$$

where S $[-]$ is saturation, $\mathbf{v}$ [m s^{-1}] is the volume flux of water, c [kg m^{-3}] is the solute concentration, $D(S)$ [m^2 s^{-1}] is the saturation dependent diffusion, $V(S)$ [m s^{-1}] is the saturation dependent advective flux and F_c [kg m^{-3} s^{-1}] is a sink term. Here $V(S)$ is usually described by $\mathbf{v}$ so that the advective flux is described by the movement of water within the soil domain.

Equations (3.2) and (3.3) have been used to describe nitrogen movement in one-dimensional soil domains [143], as well as two-dimensional domains. However, in many of the two-dimensional studies, the ridge and furrow structure is often described by a trapezoidal piece-wise geometry which may not be representative of the true structure of ridge and furrow soils [94, 112, 131, 138, 141].

In this chapter, we aim to determine the water and solute movement mechanisms and key environmental factors that influence leaching in ridge and furrow, and flat planting systems. This will allow us to understand how the soil surface topology affects solute transport within the soil. Understanding the key factors that impact solute leaching will allow us to qualitatively determine the increased risk to solute leaching between the two planting methods. This knowledge can assist us in developing solute application protocols unique to each planting method in order to reduce solute leaching and maintain higher nutrient availability to the crops.

Specifically, we model the transport of solutes with varying mobility and degradation in both soil geometries over 24 week periods. During this time vegetation is present in soil for the first 16 weeks, *i.e.*, a full growing season. We apply solutes at different times throughout the growing season to observe the effects

of early and late applications.

3.2 Theory

In this section, we extend the water movement and surface ponding model from Chapter 2 to include solute transport in soil. We construct a non-linear advection-diffusion-reaction equation that is coupled to equations (2.16) – (2.18) using a similar approach used by Roose & Fowler (2004) [41].

3.2.1 Solute Movement in Variably Saturated Soil

Solutes such as nutrients, fertilisers and pesticides typically exist in one of two states in soil, either sorbed to the soil surface or dissolved in the soil pore water [144]. We state that the solute concentration in the sorbed state follows a reversible linear binding reaction so that,

$$\partial_{\tilde{t}}\tilde{c}_s = d_s \quad \text{in} \quad [0,\infty), \tag{3.4}$$

where $\tilde{c}_s : [0,\infty) \to \mathbb{R}_{\geq 0}$ [kg m^{-3}] is the sorbed solute concentration and $d_s \in \mathbb{R}$ [kg m^{-3} s^{-1}] is the transfer rate to the sorbed phase from the pore water phase. From conservation of mass, the rate of change of the solute concentration in the soil pore water phase is,

$$\partial_{\tilde{t}}(\phi_w \tilde{c}) + \tilde{\boldsymbol{\nabla}} \cdot (\tilde{c}\tilde{\mathbf{v}}_c) = \tilde{\boldsymbol{\nabla}} \cdot \left(D\phi_w \tilde{\boldsymbol{\nabla}}\tilde{c} \right) + d_l - \begin{cases} (\tau+\xi)\tilde{c} & \text{in} \quad \tilde{\Lambda}_U^\infty \\ \tau\tilde{c} & \text{in} \quad \tilde{\Lambda}_A^\infty \end{cases}, \tag{3.5}$$

where $\tilde{c} : \tilde{\Lambda} \times [0,\infty) \to \mathbb{R}_{\geq 0}$ [kg m^{-3}] is the solute concentration in the soil pore water, $\tilde{\mathbf{v}}_c : \tilde{\Lambda} \times [0,\infty) \to \mathbb{R}^3$ [m s^{-1}] is the volume flux, $d_l \in \mathbb{R}$ [kg m^{-3} s^{-1}] is the transfer rate to the pore water phase from the sorbed phase, $D \in \mathbb{R}_{>0}$ [m^2 s^{-1}] is the diffusion coefficient, $\tau \in \mathbb{R}_{\geq 0}$ [s^{-1}] is the biodegradation rate, $\xi \in \mathbb{R}_{\geq 0}$ [s^{-1}] is the uptake rate from plant roots and we recall $\phi_w : \tilde{\Lambda} \times [0,\infty) \to [0,1]$ [–] is the soil water fraction. Adding (3.4) and (3.5) yields,

$$\partial_{\tilde{t}}(\tilde{c}_s + \phi_w \tilde{c}) + \tilde{\boldsymbol{\nabla}} \cdot (\tilde{c}\tilde{\mathbf{v}}_c) = \tilde{\boldsymbol{\nabla}} \cdot \left(D\phi_w \tilde{\boldsymbol{\nabla}}\tilde{c} \right) + d_s + d_l - \begin{cases} (\tau+\xi)\tilde{c} & \text{in} \quad \tilde{\Lambda}_U^\infty \\ \tau\tilde{c} & \text{in} \quad \tilde{\Lambda}_A^\infty \end{cases}. \tag{3.6}$$

We assume there is a direct jump between the solute in the two states with no

intermediate phase, such that $d_s + d_l = 0$. Furthermore, we define d_s to be,

$$d_s = k_a\tilde{c} - k_d\tilde{c}_s, \tag{3.7}$$

where $k_a \in \mathbb{R}_{>0}$ [s^{-1}] is the adsorption rate of the solute in solution and $k_d \in \mathbb{R}_{>0}$ [s^{-1}] is the desorption rate. We assume k_d is sufficiently large such that $d_s/k_d \ll 1$ and $k_a \sim k_d$ so that,

$$\tilde{c}_s = b\tilde{c}, \tag{3.8}$$

where $b = k_a/k_d$ [$-$] is the buffer power of the solute [27, 145]. This leads to the governing equation for solute movement,

$$\partial_{\tilde{t}}(b\tilde{c} + \phi_w\tilde{c}) + \tilde{\boldsymbol{\nabla}} \cdot (\tilde{c}\tilde{\mathbf{v}}_c) = \tilde{\boldsymbol{\nabla}} \cdot \left(D\phi_w\tilde{\boldsymbol{\nabla}}\tilde{c}\right) - \begin{cases} (\tau + \xi)\tilde{c} & \text{in} \quad \tilde{\Lambda}_U^\infty \\ \tau\tilde{c} & \text{in} \quad \tilde{\Lambda}_A^\infty \end{cases}. \tag{3.9}$$

To couple equation (3.9) to the water movement model (2.16) $-$ (2.18), we alter (3.9) in three ways. Firstly, we state that $\tilde{\mathbf{v}}_c$ is defined by the Darcy mechanics from equation (2.7), *i.e.*,

$$\tilde{\mathbf{v}}_c = \tilde{\mathbf{v}} = -\frac{\kappa_s\kappa(S)}{\mu_w}\left(\tilde{\boldsymbol{\nabla}}\tilde{p}_w + \rho g\hat{\mathbf{e}}_3\right). \tag{3.10}$$

Secondly, we relate D to $S(p_w)$ using the power law [41],

$$D = D_f\phi^d S(p_w)^d, \tag{3.11}$$

where $D_f \in \mathbb{R}_{>0}$ [m^2 s^{-1}] is the diffusion coefficient in free liquid and $d \in [0.5, 2]$ [$-$] is the impedance factor of the solute that accounts for the tortuosity of the solute moving through the soil pore space [145]. Lastly, we relate ϕ_w to $S(p_w)$ using the relationship $S(p_w) = \phi_w/\phi$ from equation (2.4).

Combining (3.9) with the three alterations and the governing water movement equations with (2.16) $-$ (2.18), the model for solute movement is given by,

$$\begin{aligned}\frac{\partial\tilde{c}}{\partial\tilde{t}}\Big[b + \phi S(\tilde{p}_w)\Big] + \frac{\partial\tilde{p}_w}{\partial\tilde{t}}\left\{[1 - H_S(\tilde{p}_w)]\phi\frac{\partial S(\tilde{p}_w)}{\partial\tilde{p}_w}\tilde{c}\right\} = \tilde{\boldsymbol{\nabla}} \cdot \Big[D_f\phi^{d+1}S(\tilde{p}_w)^{d+1}\tilde{\boldsymbol{\nabla}}\tilde{c}\Big] + \\ \tilde{\boldsymbol{\nabla}} \cdot \left\{\tilde{c}\frac{\kappa_s\overline{\kappa[S(\tilde{p}_w)]}}{\mu_w}\left(\tilde{\boldsymbol{\nabla}}\tilde{p}_w + \rho g\hat{\mathbf{e}}_3\right)\right\} - \begin{cases} (\tau + \xi)\tilde{c} & \text{in} \quad \tilde{\Lambda}_U^\infty \\ \tau\tilde{c} & \text{in} \quad \tilde{\Lambda}_A^\infty \end{cases}.\end{aligned} \tag{3.12}$$

To ensure the solute model is valid for a variably saturated soil domain, *i.e.*, $\tilde{p}_w \geq 0 \cap \tilde{p}_w < 0$, a similar condition to (2.18) is imposed. This condition sets the coefficient $[b + \phi S(\tilde{p}_w)]$, and the diffusion coefficient $[D_f\phi_w^{d+1}S(\tilde{p}_w)^{d+1}]$ to be

constant when $S(\tilde{p}_w) = 1$, *i.e.*,

$$\overline{b + \phi S(\tilde{p}_w)} = \begin{cases} b + \phi & \text{for} \quad p \geq -\zeta_t \\ b + \phi S(\tilde{p}_w) & \text{for} \quad p < -\zeta_t \end{cases}, \tag{3.13}$$

$$\overline{D_f \phi^{d+1} S(\tilde{p}_w)^{d+1}} = \begin{cases} D_f \phi^{d+1} & \text{for} \quad p \geq -\zeta_t \\ D_f \phi^{d+1} S(\tilde{p}_w)^{d+1} & \text{for} \quad p < -\zeta_t \end{cases}, \tag{3.14}$$

where we recall $\zeta_t \in \mathbb{R}_{>0}$ [Pa] is a small transition pressure that acts as the interface between the saturated and partially saturated soil regions.

The solute transport model (3.12) $-$ (3.14) is then coupled to the water movement model (2.16) $-$ (2.18) to achieve a system of partial differential equations that describes simultaneous water and solute movement in soil.

3.2.2 Boundary and Initial Conditions

To form a complete description of solute transport in ridge and furrow systems, we derive boundary conditions that are imposed on the edges of $\tilde{\Lambda}$, see Figure 2.2 (a).

Surface Boundary Conditions

For the boundary $\partial\tilde{\Lambda}_S$, we assume that solute applications are during dry conditions or when rainfall is sufficiently low that it does not break the minimum pond depth $\tilde{x}_{\min}$. Therefore, on the boundary $\partial\tilde{\Lambda}_S$ we impose a Cauchy flux condition, *i.e.*,

$$\hat{\mathbf{n}} \cdot \left\{ \overline{D_f \phi^{d+1} S(\tilde{p}_w)^{d+1}} \tilde{\boldsymbol{\nabla}} \tilde{c} + \tilde{c} \frac{\kappa_s \overline{\kappa[S(\tilde{p}_w)]}}{\mu_w} \left(\tilde{\boldsymbol{\nabla}} \tilde{p}_w + \rho g \hat{\mathbf{e}}_3 \right) \right\} = c_m \quad \text{on} \quad \partial\tilde{\Lambda}_S \times [0, \infty), \tag{3.15}$$

where $c_m = c_m(t) : [0, \infty) \to \mathbb{R}_{\geq 0}$ [kg m^{-2} s^{-1}] is the volume flux of solute per unit soil surface area per unit time entering the soil domain.

Lateral Boundary Conditions

For the boundaries $\partial\tilde{\Lambda}_E$ and $\partial\tilde{\Lambda}_W$, we set a zero flux boundary condition due to the periodicity of $\tilde{\Lambda}$, *i.e.*,

$$\hat{\mathbf{n}} \cdot \left\{ \overline{D_f \phi^{d+1} S(\tilde{p}_w)^{d+1}} \tilde{\boldsymbol{\nabla}} \tilde{c} + \tilde{c} \frac{\kappa_s \overline{\kappa[S(\tilde{p}_w)]}}{\mu_w} \left(\tilde{\boldsymbol{\nabla}} \tilde{p}_w + \rho g \hat{\mathbf{e}}_3 \right) \right\} = 0 \quad \text{on} \quad \partial\tilde{\Lambda}_E \cup \partial\tilde{\Lambda}_W \times [0, \infty). \quad (3.16)$$

Therefore, there is no lateral solute movement into or out of $\tilde{\Lambda}$.

Boundary condition at the base of the soil

For the boundary on $\partial\tilde{\Lambda}_B$, we set a Dirichlet boundary condition set to the initial condition, *i.e.*,

$$\tilde{c} = \tilde{c}|_{\tilde{t}=0} \quad \text{on} \quad \partial\tilde{\Lambda}_B \times [0, \infty). \quad (3.17)$$

Initial conditions

Since we wish to understand how the soil surface topology influences solute movement in soil, we choose the initial solute concentration in $\tilde{\Lambda}$ to be,

$$\tilde{c}|_{t=0} = 0 \quad \text{in} \quad \tilde{\Lambda} \times \{\tilde{t} = 0\}, \quad (3.18)$$

as our equations are linear in $\tilde{c}$, we may consider this system to describe the movement of added solute.

The system of Equations (2.16) $-$ (2.18), (2.20), (2.27) $-$ (2.32), (3.12) $-$ (3.18) completes the description of simultaneous water and solute movement in the presence of surface ponding.

3.2.3 Non-dimensionalisation

Here we non-dimensionalise the system of equations (3.12) $-$ (3.18) shown above to determine the magnitude of influence each parameter has on the system of equations. We choose the same scaling as that in the non-dimensionalisation of the water movement and ponding model (shown in Section 2.2.5) with the addition of

the scaling for $\tilde{c}$, *i.e.*,

$$\tilde{\mathbf{x}} = \eta\mathbf{x},\ \tilde{t} = \frac{\phi\mu_w\eta^2}{\kappa_s p_c}t,\ \tilde{p}_w = p_c p_w,\ \tilde{\chi} = \eta\chi,\ \tilde{c} = c_m c,\ \tilde{x}_0 = \eta x_0. \tag{3.19}$$

In (3.19) we use the domain width η as the spatial scaling, the 'effective diffusivity' $\frac{\phi\mu_w\eta^2}{\kappa_s p_c}$ for the time scaling, the suction characteristic p_c as the pressure scaling and the solute application rate c_m as the concentration scaling. This leads to the system of equations,

$$\frac{\partial c}{\partial t}\left[\overline{b^* + S(p_w)}\right] + \frac{\partial p_w}{\partial t}\left\{[1 - H_S(p_w)]\frac{\partial S(p_w)}{\partial p_w}c\right\} = \boldsymbol{\nabla}\cdot\left[\overline{D_f^*\phi^{d+1}S(p_w)^{d+1}}\boldsymbol{\nabla}c\right] + \boldsymbol{\nabla}\cdot\left\{c\overline{\kappa[S(p_w)]}\left(\boldsymbol{\nabla}p_w + \overline{\rho}\hat{\mathbf{e}}_3\right)\right\} - \begin{cases}(\overline{\xi}+\overline{\tau})c & \text{in} \quad \Lambda_U^\infty \\ \overline{\tau}c & \text{in} \quad \Lambda_A^\infty\end{cases}, \tag{3.20}$$

$$\hat{\mathbf{n}}\cdot\left\{\overline{D_f^*\phi^{d+1}S(p_w)^{d+1}}\boldsymbol{\nabla}c + c\overline{\kappa[S(p_w)]}\left(\boldsymbol{\nabla}p_w + \overline{\rho}\hat{\mathbf{e}}_3\right)\right\} = \overline{c_m} \quad \text{on} \quad \partial\Lambda_S\times[0,\infty), \tag{3.21}$$

$$\hat{\mathbf{n}}\cdot\left\{\overline{D_f^*\phi^{d+1}S(p_w)^{d+1}}\boldsymbol{\nabla}c + c\overline{\kappa[S(p_w)]}\left(\boldsymbol{\nabla}p_w + \overline{\rho}\hat{\mathbf{e}}_3\right)\right\} = 0 \quad \text{on} \quad \partial\tilde{\Lambda}_E\cup\partial\tilde{\Lambda}_W\times[0,\infty), \tag{3.22}$$

$$c = 0 \quad \text{on} \quad \partial\Lambda_B\times[0,\infty), \tag{3.23}$$

$$c|_{t=0} = 0 \quad \text{in} \quad \Lambda\times\{t=0\}, \tag{3.24}$$

and

$$\overline{\rho} = \frac{\rho g\eta}{p_c},\ b^* = \frac{b}{\phi},\ D_f^* = \frac{D_f\phi^{d+1}\mu_w}{p_c\kappa_s},\ \overline{\tau} = \frac{\tau\eta^2\mu_w}{p_c\kappa_s},\ \overline{\xi} = \frac{\xi\eta^2\mu_w}{p_c\kappa_s}\ \overline{c_m} = \frac{\eta\mu_w}{p_c\kappa_s}. \tag{3.25}$$

3.2.4 Parameter Estimation

Here we estimate the parameters contained in equations (3.20) $-$ (3.24) to determine the magnitude of influence each parameter has on the system of equations. This allows us to identify the key mechanisms that dominate solute movement in soil. We continue to assess the parameter values for silt soils and the plant *Solanum tuberosum* L. Table 3.1 shows a summary of all parameters used in the non-dimensionalisation. Several of the parameters used are discussed in Chapter 2 and will be assumed here.

The value for the buffer power b depends heavily on the solute that is applied to the soil. For extremely mobile solutes such as the pesticide Primisulfuron, the buffer power takes the value $b \approx 0.1$ [146]. However, for solutes such as phosphorous or

Table 3.1: A table of the parameters used in the non-dimensionalisation and parameter estimation of the solute movement and ponding model.

Parameter	Description	Value	Units	Reference
κ_s	saturated permeability	5×10^{-14}	m^2	[101]
ϕ	porosity	0.4	$-$	[101]
p_c	characteristic suction pressure	2×10^4	Pa	[101]
b	buffer power	$[0.1, 1000]$	$-$	[41, 146]
D_f	diffusion in free liquid	2×10^9	$\text{m}^2\ \text{s}^{-1}$	[31]
τ	biodegradation rate	$[0, 8 \times 10^{-7}]$	s^{-1}	[147]
d	impedance factor	2	$-$	[145]
ξ	solute uptake	1×10^{-9}	s^{-1}	[148, 149]
ρ	density of water	1×10^3	kg m^{-3}	$-$
μ_w	viscosity of water	1×10^{-3}	Pa s	$-$
g	gravity	9.81	m s^{-2}	$-$
η	width of $\tilde{\Lambda}$	0.5	m	[47, 92]

zinc that rapidly bind to the soil particles, the buffer power can be $b \approx 1000$ [27]. Hence, there is a very large range that b can take, covering several orders of magnitude.

Similarly, the degradation rate τ varies considerably based on the solute that is chosen. The solute decay constant τ relates to the half-life $t_{1/2}$ [s] by the relationship,

$$\tau = \frac{\ln(2)}{t_{1/2}}. \tag{3.26}$$

Solutes such as the pesticide Fenamiphos have particularly fast biodegradation rates equating to a half-life of approximately 10 days [147]. In contrast, stable nutrients in soil can take tens of years to decay in the soil environment. As such, τ also covers a large range of values.

To estimate the solute uptake parameter ξ, we find that the crop *Solanum tuberosum* L. has an uptake rate for the nutrient nitrogen of $\xi \approx 1 \times 10^{-9}\ \text{s}^{-1}$ [148, 149]. Additionally, we observe that the diffusion coefficient in free liquid for simple electrolytes is typically $D_f \approx 2 \times 10^{-9}\ \text{m}^2\ \text{s}^{-1}$ [31]. Finally, the impedance coefficient d has the approximate value $d \approx 2$ for moist environments, *i.e.*, those that are subject to surface ponding [145].

Using the values above, we observe that the non-dimensionalised parameters shown in (3.25) have the approximate values,

$$\overline{\rho} = \mathcal{O}(1),\ b^* \in [0.2, 2500],\ D_f^* = \mathcal{O}(10^{-4}),\ \overline{\tau} \in [0.2, 0],\ \overline{\xi} = \mathcal{O}(10^{-4}),\ \overline{c_m} = \mathcal{O}(10^5). \tag{3.27}$$

From (3.27) we find that the non-dimensionalised parameters cover several orders

of magnitude. We initially observe that the parameter $D_f^* \ll 1$, implying that for solute transport, diffusion is substantially weaker than the advective forces that occur due to water movement in soil, *i.e.*, solute movement is largely governed by water movement rather than by diffusion, which is consistent with the literature [145].

There are two mechanisms that reduce the quantity of solutes within the soil: solute uptake by plants and biodegradation. For solutes that have a short half-life (typically pesticides), we find that $\overline{\tau} \gg \overline{\xi}$, *i.e.*, biodegradation dominates solute uptake. However, as the half-life is increased then $\tau \to 0$, and solute uptake becomes the key mechanism governing reduction in solute in soil. Therefore, the primary reduction mechanism is heavily dependent on the specific solute properties.

Finally, we observe that the adjusted buffer power b^* can take a wide range of values. For mobile solute such as nitrogen, we observe that $b^* = \mathcal{O}(1)$. However, for solutes such as zinc, which has a substantially higher buffer power, we find that $b^* = \mathcal{O}(10^4)$. For higher buffer powers, the term $\overline{b^* + S(p_w)}$ becomes the most dominant in equation (3.20) and we find that the effects of diffusion $\boldsymbol{\nabla} \cdot \left[\overline{D_f^* \phi_{d+1} S(p_w)^{d+1}} \boldsymbol{\nabla} c \right]$ and advection $\boldsymbol{\nabla} \cdot \left\{ c \overline{\kappa[S(p_w)]} \left(\boldsymbol{\nabla} p_w + \overline{\rho} \hat{\mathbf{e}}_3 \right) \right\}$ are negligible. Hence, the buffer power b of the solute will vital in determining the key transport mechanics.

3.2.5 Implementation

Here we describe how we utilise the finite element package COMSOL Multiphysics (COMSOL Multiphysics, Stockholm, Sweden, www.comsol.com) to solve the coupled solute-water model. To implement the governing equation (3.12) coupled with the governing equation for water movement (2.16), we use the inbuilt 'General Form PDE', which takes the form,

$$e_a \frac{\partial^2 \mathbf{r}}{\partial t^2} + d_a \frac{\partial \mathbf{r}}{\partial t} + \boldsymbol{\nabla} \cdot \boldsymbol{\Theta} = \mathbf{f}, \tag{3.28}$$

where $\mathbf{r} = [\tilde{p}_w, \tilde{c}]^T$, and e_a, d_a, $\mathbf{\Theta}$ and $\mathbf{f}$ are parameters to be defined. To write the model in this form, the parameters were constructed so that,

$$e_a = \begin{bmatrix} 0 & 0 \\ 0 & 0 \end{bmatrix}, \; d_a = \begin{bmatrix} [1 - H_S(\tilde{p}_w)]\phi \frac{\partial S(\tilde{p}_w)}{\partial \tilde{p}_w} & 0 \\ [1 - H_S(\tilde{p}_w)]\phi \frac{\partial S(\tilde{p}_w)}{\partial \tilde{p}_w} c & \overline{b + S(\tilde{p}_w)} \end{bmatrix},$$

$$\mathbf{\Theta} = \begin{bmatrix} -\frac{\kappa_s \overline{\kappa[S(\tilde{p}_w)]}}{\mu_w} \left(\tilde{\boldsymbol{\nabla}} \tilde{p}_w + \rho g \hat{\mathbf{e}}_3 \right) \\ \overline{D_f \phi^{d+1} S(\tilde{p}_w)^{d+1}} \boldsymbol{\nabla} \tilde{c} + \tilde{c} \overline{\kappa[S(\tilde{p}_w)]} \left(\boldsymbol{\nabla} \tilde{p}_w + \overline{\rho} \hat{\mathbf{e}}_3 \right) \end{bmatrix}^T, \; \mathbf{f} = \begin{bmatrix} -\lambda_c (\tilde{p}_w - p_r) \\ -(\tau + \xi)\tilde{c} \end{bmatrix}. \quad (3.29)$$

where the functions $H_S(\tilde{p}_w)$, $S(\tilde{p}_w)$ and $\kappa[S(\tilde{p}_w)]$ are explicitly defined.

For the flux boundaries, *i.e.*, equations (3.15) and (3.16), we use the inbuilt flux boundary condition that takes the form,

$$\hat{\mathbf{n}} \cdot \mathbf{\Theta} = g_1 - g_2 \mathbf{r}, \quad (3.30)$$

where g_1 and g_2 depend on the specific flux boundary. Similarly, for the boundary condition (3.17), we use the inbuilt Dirichlet boundary condition. This takes the form,

$$\mathbf{r} = \mathbf{r_0}. \quad (3.31)$$

As in Chapter 2, the model is solved using the MUMPS (Multifrontal Massive Parallel Sparse Direct Solver) subroutine.

3.3 Soil Domains and Parameter Values

In this section, we discuss the parameters used to conduct a numerical comparison of solute transport between ridge and furrow soil structures, and flat field structures. Based on the non-dimensionalisation above, we choose to compare multiple solutes covering a wide range of parameter values for b and τ to determine how various solutes are affected by the soil geometries, since we find that certain mechanisms can either dominate or be neglected. Furthermore, we assume no solute uptake by plant roots, since we are primarily concerned with the solute transport problem, *i.e.*, modelling the worst case scenario, which applies to passive solutes.

3.3.1 Soil Domains

To model the differences in solute and water movement between a ridge and furrow geometry and a flat geometry, we construct two domains. Let $\tilde{\Omega} \subset \mathbb{R}^3$ [m^3] and

$\tilde{\Phi} \subset \mathbb{R}^3$ [m^3] be open bounded subsets representing a ridged soil and flat soil respectively. These can be seen in Figure 3.1.

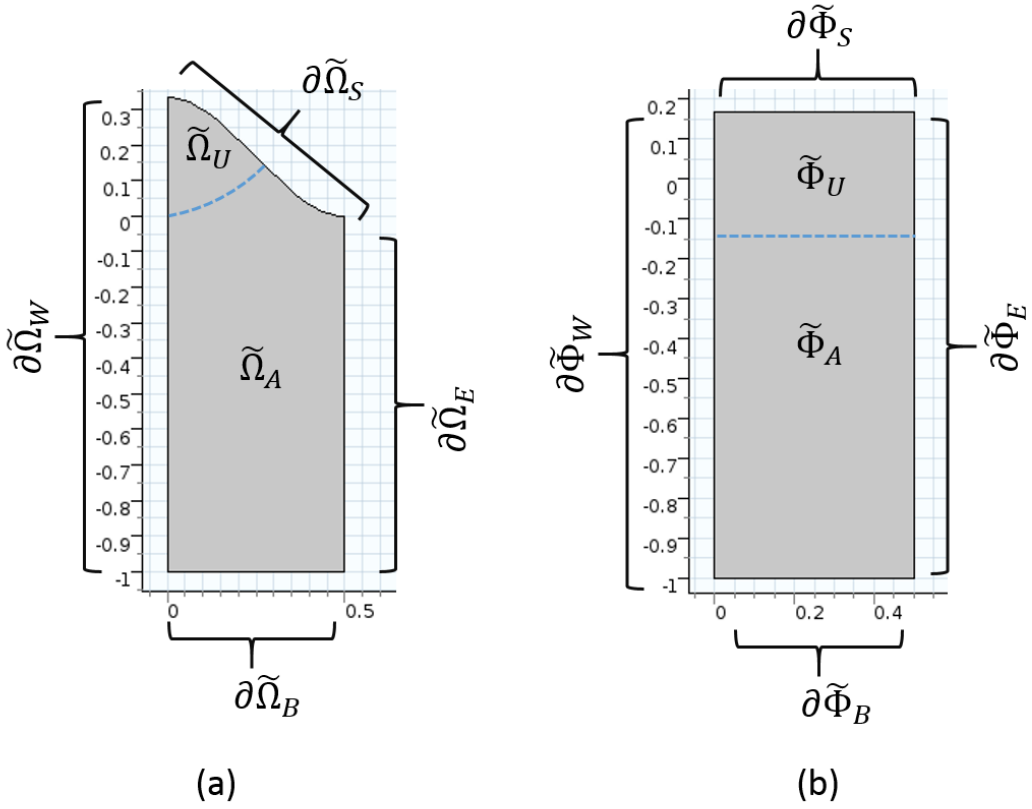

Figure 3.1: Simulated soil domains for a ridge and furrow geometry and a flat soil geometry, where $\tilde{\Omega}$ and $\tilde{\Phi}$ are the ridged and flat domains respectively, $\partial\tilde{\Omega}_S$ and $\partial\tilde{\Phi}_S$ are the soil surface boundaries, $\partial\tilde{\Omega}_B$ and $\partial\tilde{\Phi}_B$ are the base boundaries, $\partial\tilde{\Omega}_W$, $\partial\tilde{\Phi}_W$, $\partial\tilde{\Omega}_E$ and $\partial\tilde{\Phi}_E$ are the lateral boundaries, $\partial\tilde{\Omega}_A$ and $\partial\tilde{\Phi}_A$ are the regions absent of root activity and $\partial\tilde{\Omega}_U$ and $\partial\tilde{\Phi}_U$ are the regions of soil containing roots.

To capture typical ridge and furrow dimensions, for $\tilde{\Omega}$ we use the values $\eta = 0.5$ m, $A = C = 1/6$ m and $B = 2\pi$ m^{-1} in equation (2.2) [47, 92]. Furthermore, for $\tilde{\Phi}$ we set $\eta = 0.5$ m, $A = 0$ m, $C = 1/6$ m and $B = 2\pi$ m^{-1} to ensure $\int_{\tilde{\Omega}} d\tilde{\Omega} = \int_{\tilde{\Phi}} d\tilde{\Phi}$.

In the ridge and furrow geometry we choose $\tilde{\Omega}_U$, *i.e.*, the region of soil where roots are present, to be the top 30 cm (*i.e.*, the plough layer [103]) of soil extending radially from the top of the ridge. Similarly, we choose the subdomain $\tilde{\Phi}_U$ to be the top 30 cm of soil (see Figure 3.1). We note that $\int_{\tilde{\Omega}_U} d\tilde{\Omega}_U \neq \int_{\tilde{\Phi}_U} d\tilde{\Phi}_U$, however, this is taken into account when establishing the parameter for root length density l_d.

3.3.2 Parameter Values

Summarised in Tables 3.2 and 3.3 are a list of the parameters used in the numerical simulations. Detailed below are the parameter values and their origins.

Geometric, Soil, Environmental, Plant and Solute Parameter values

We use the same soil parameters as those discussed in Chapter 2 for a silt loam soil *i.e.*, $\phi = 0.396$, $m = 0.51$, $\kappa_s = 5.2 \times 10^{-14}$ m^2 and $p_c = 23200$ Pa [101]. It should be noted that in some cases different tillage methods applied to soil can alter ϕ within the system [150]. However, to ensure a 'like for like' comparison, we keep ϕ the same in both soil domains to ensure that any differences we observe are an effect of the soil geometry and not dependent on small local porosity variations within the soil. For the viscosity of water we use $\mu_w = 1 \times 10^{-3}$ Pa s, for acceleration due to gravity $g = 9.81$ m s^{-2} and for the density of water $\rho = 1000$ kg m^{-3}.

Table 3.2: A table of all the parameters used in the numerical simulations for ridge and furrow, and flat field tillage.

Parameter	Description	Value	Units	Reference
κ_s	saturated permeability	5.2×10^{-14}	m^2	[101]
m	van Genuchten parameter	0.5	$-$	[101]
ϕ	porosity	0.396	$-$	[101]
p_c	characteristic suction pressure	23200	Pa	[101]
p_0	basal geometry pressure	-1×10^4	Pa	$-$
I_c	infiltration capacity	1.6×10^{-6}	m s^{-1}	[109]
p_r	root xylem pressure	-5×10^4	Pa	[110]
λ_c	effective uptake	2.355×10^{-11}	s^{-1} Pa^{-1}	[103, 115] [41, 116]
D_f	diffusion in free liquid	2×10^{-9}	m^2 s^{-1}	[31]
d	impedance factor	2	$-$	[145]
ρ	density of water	1×10^3	kg m^{-3}	$-$
μ_w	viscosity of water	1×10^{-3}	Pa s	$-$
g	gravity	9.81	m s^{-2}	$-$
ζ_t	saturated-partially saturated interface	1×10^{-1}	Pa	$-$
σ	Heaviside pressure	1×10^4	Pa^{-1}	$-$
$\tilde{x}_{\text{min}}$	minimum ponding depth	3×10^{-4}	m	$-$
A	variation in soil depth	$0.16/0$	m	[47, 92]
B	ridge wave number	$2\pi/0$	m^{-1}	[47, 92]
C	average soil depth	0.16	m	[47, 92]
η	width of $\tilde{\Lambda}$	0.5	m	[47, 92]

The impedance coefficient is bounded by $d \in [0.5, 2]$ [145]. Furthermore, $\phi_w \propto d$ so that increased volumetric moisture content leads to an increase in the impedance factor for a solute [151]. Given that we model a temperate UK climate with

frequent heavy rainfall events, we take $d = 2$. Additionally, the diffusion coefficient in free liquid for simple electrolytes is typically $1 \times 10^{-9} \leq D_F \leq 3 \times 10^{-9}$ m^2 s^{-1} [31]. Hence, we select $D_f = 2 \times 10^{-9}$ m^2 s^{-1}.

We simulate 24 weeks of solute and water movement in soil, in which vegetation is present for the first 16 weeks as this is typical for *Solanum tuberosum* L. crops [152]. However, *Solanum tuberosum* L. root length density changes significantly over a 16 week growing season [103]. Lesczynski and Tanner (1976) [103] found that over the first 30 days the root length density develops to $l_d \approx 3 \times 10^4$ m^{-2} in the plough layer. This remains fairly constant until ≈ 90 days, in which l_d density declines. In order to capture this growth and development, we assign $l_d(t)$ the piecewise function (in m^{-2}),

$$l_d(t) = \begin{cases} 1 \times 10^3 t & 0 \leq t < 30 \\ 3 \times 10^4 & 30 \leq t < 90 \\ 3 \times 10^4 - (1 \times 10^3)(t - 90) & 90 \leq t < 120 \\ 0 & 120 \leq t \end{cases}. \tag{3.32}$$

We note that these results were obtained with ridge and furrow tillage, hence we account for this when determining $l_d(t)$ for the flat domain $\tilde{\Phi}$. In order to ensure $\int_{\tilde{\Omega}_U} l_d(t) d\tilde{\Omega}_U = \int_{\tilde{\Phi}_U} l_d(t) d\tilde{\Phi}_U$, we scale $l_d(t)$ in the flat geometry by the ratio of the two root active areas $\int_{\tilde{\Omega}_U} d\tilde{\Omega}_U : \int_{\tilde{\Phi}_U} d\tilde{\Phi}_U$.

As in Chapter 2, we choose the parameter λ_c to take the value $\lambda_c = 3.14 \times 10^{-5}$ s^{-1} MPa^{-1}, and we assign the value for the infiltration capacity to be $I_c = 1.6 \times 10^{-6}$ m s^{-1}. Furthermore, for the root pressure p_r, given that we model heavy rainfall that promotes considerable ponding, we chose the values $p_r = -0.05$ MPa.

We show results of numerical simulations for multiple hypothetical solutes with varying degradation rates and buffering capacity to determine the differences in solute movement mechanisms between the ridge and furrow and flat soil geometries. Table 3.3 shows a matrix of the solute parameters that are used in the simulations.

We choose to model extremely mobile solutes $(\alpha_1, \alpha_2, \alpha_3)$ with a buffer power of $b = 0.1$, highly mobile solutes $(\beta_1, \beta_2, \beta_3)$ with a buffer power of $b = 1$, and moderately mobile solutes $\gamma_1,\ \gamma_2$ and γ_3 with a buffer power of $b = 10$.

It is generally accepted that degradation rates of pesticide-like solutes in soil decrease with depth [153]. Hence one value for the decay constant τ is not valid for the entirety of the soil domains in Figure 3.1. For the pesticides Isoproturon and

Table 3.3: Matrix of simulated solutes used in the numerical simulations.

	Extremely Mobile $b = 0.1$	Highly Mobile $b = 1$	Moderately Mobile $b = 10$
High Degradation $t^*_\lambda = 10$ days	α_1	β_1	γ_1
Medium Degradation $t^*_\lambda = 50$ days	α_2	β_2	γ_2
Low Degradation $t^*_\lambda = 500$ days	α_3	β_3	γ_3

Metolachlor, the half-life is approximately doubled between the initial $0-30$cm of soil and 1m below the soil surface [154, 155]. Therefore, for spatially varying degradation, we impose the function,

$$t_\lambda(\tilde{\mathbf{x}}) = t^*_\lambda + |z_a| t^*_\lambda \tag{3.33}$$

where, t^*_λ is the half-life of the solute in the plough layer and $|z_a|$ is the absolute depth below soil surface.

For the high degrading solutes $(\alpha_1, \beta_1, \gamma_1)$ we choose the value for the half life $t^*_\lambda = 10$ days, for moderately degrading solutes $(\alpha_2, \beta_2, \gamma_2)$ we select the value $t^*_\lambda = 50$ days, and for slow degrading solutes $(\alpha_3, \beta_3, \gamma_3)$ we select the value $t^*_\lambda = 500$ days. Recall that the half-life t^*_λ relates to the solute decay constant τ by $\tau = \frac{\ln(2)}{t^*_\lambda}$.

Boundary and Initial Condition Parameters Values

For p_0 which describes a constant saturation at the base of the geometry, we assign a value of $p_0 = -10$ kPa. This equates to a saturation level of approximately $S \approx 0.9$ for a silt loam soil, thereby replicating a shallow water table. For the initial condition for soil water pore pressure $p_\infty(\tilde{\mathbf{x}})$, we choose the steady state profile that forms in $\tilde{\Omega}$ and $\tilde{\Phi}$ prior to any rainfall. Hence, in each of the simulations, we allow steady state to form so that $\partial_t p_w = 0$ before initiating rainfall.

Rainfall and Solute Application Parameter Values

We simulate solute and water movement over a 24 week period, in which vegetation is present for the first 16 weeks. *Solanum tuberosum* L. crops are typically sown from April to June and are harvested in September to November [152, 156]. As such, we simulate this 'growth and harvesting' timeframe with an additional 8 weeks to determine how solutes move once the crops are harvested.

For the volume flux of water per unit soil surface area $\tilde{\Gamma}(t)$, *i.e.*, rainfall, we use 6 months of rainfall field data from a site in Newbury, UK between 1st June 2006 and 31st December 2006. This data can be seen in Figure 3.2. The data was recorded from instruments that were installed into a slope next to the A34 Newbury bypass (Ordnance Survey grid ref. SU455652). Acquisition of the data is described in Smethurst *et al.* (2006) [157]. The return period for the rainfall, *i.e.*, the likelihood that the amount of rainfall is exceeded in subsequent years for the total annual rainfall is 17 in 39 [158]. Hence, there is a 43.6 % chance this level of annual rainfall will be exceeded in the future.

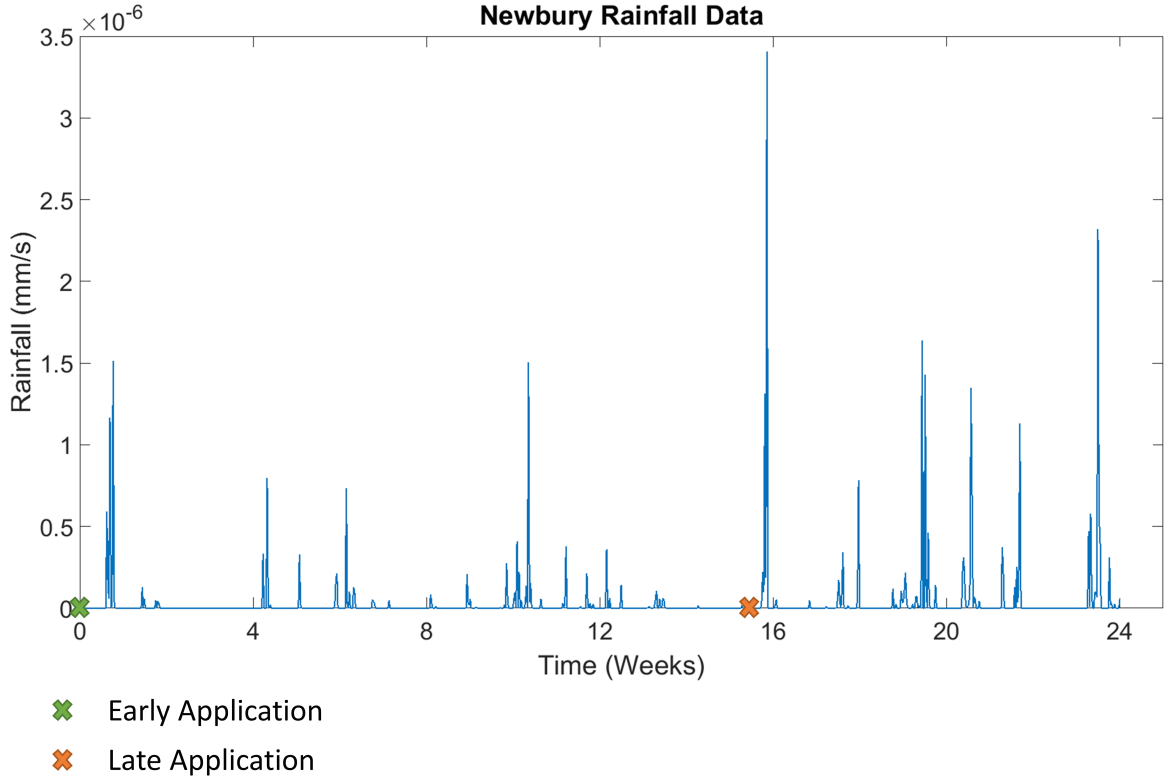

Figure 3.2: Newbury site experimental rainfall data over a 6 month period between 1st June 2006 and 31st December 2006. The green cross indicates the time for an early solute application, and the orange cross indicates the time for a late solute application.

We apply the solutes at one of two times during the numerical simulations, denoted as the early and late applications. For the early application, the solute is applied to the soil surface at the start of the simulation over the initial 24 hours, with a total application of 1 kg ha^{-1}, *i.e.*, an application rate of $c_m(t) = 1.157 \times 10^{-9}$ kg m^{-2} s^{-1}. We choose to have a total application of 1 kg ha^{-1} as this is typical for fungicides like Mancozeb, which have been applied to potato fields at multiple times throughout the growing season [159].

Similarly, for the late application, a solute is applied for 24 hours with the same application rate at the beginning of the 15$^{\text{th}}$ week. These can be seen in Figure 3.2. The early and late application times where chosen in order to determine how solute movement is affected during a growing and degrading root system respectively. Thus, for the early application, the solute is applied as soon as the root system begins to grow, since it is common practice to apply herbicides pre-emergence of the crops [159]. The late application is applied shortly after the root length density begins to decrease, since pestiicides are frequently applied towards the end of growing seasons for defoliation, *i.e.*, to reduce the foliage of the crops [159].

3.4 Numerical Solutions

We conduct a total of 36 simulations; 9 simulations for the ridged geometry $\tilde{\Omega}$ with an early application (for all 9 hypothetical solutes in Table 3.3), 9 simulations for $\tilde{\Omega}$ with a late application, 9 simulations for the flat geometry $\tilde{\Phi}$ with an early application and 9 simulations for $\tilde{\Phi}$ with a late application.

3.4.1 Early Application Results

Shown in Figure 3.3 are the results for the early application solutes for both the domains $\tilde{\Omega}$ and $\tilde{\Phi}$ for the moderately mobile solutes, *i.e.*, $\gamma_1,\ \gamma_2$ and γ_3 (see Table 3.3). The results in Figure 3.3 show the solute profiles in the two soil domains at the time points of 16 and 24 weeks after the solute application. At 16 weeks after the solute application, water uptake from vegetation stops as this simulates harvesting and the removal of crops, and 24 weeks after the solute application is the end of the simulation timeframe. Furthermore, an additional contour plot of concentration $10\ \mu\text{g l}^{-1}$ (shown in white) is added to each profile; since this concentration is frequently used as a pesticide safety threshold for root and tuber vegetables [160]. In Figure 3.4 and Figure 3.5 we show the results for the highly mobile $(\beta_1, \beta_2, \beta_3)$ and extremely mobile $(\alpha_1, \alpha_2, \alpha_3)$ solutes respectively.

For the moderately mobile solutes $(\gamma_1, \gamma_2, \gamma_3)$, we find that there is not significant penetration of the solutes into either of the soil geometries due to the buffer power of the solutes (see Figure 3.3). However, there are several features of solute movement that can be identified. Firstly, we find the solute adjacent to the furrow has penetrated deeper into the soil compared to the solute contained in the ridge. Experimentally, deep furrow penetration has been attributed to the effects of ponding in the furrow of the geometry from soil surface runoff [50], which is

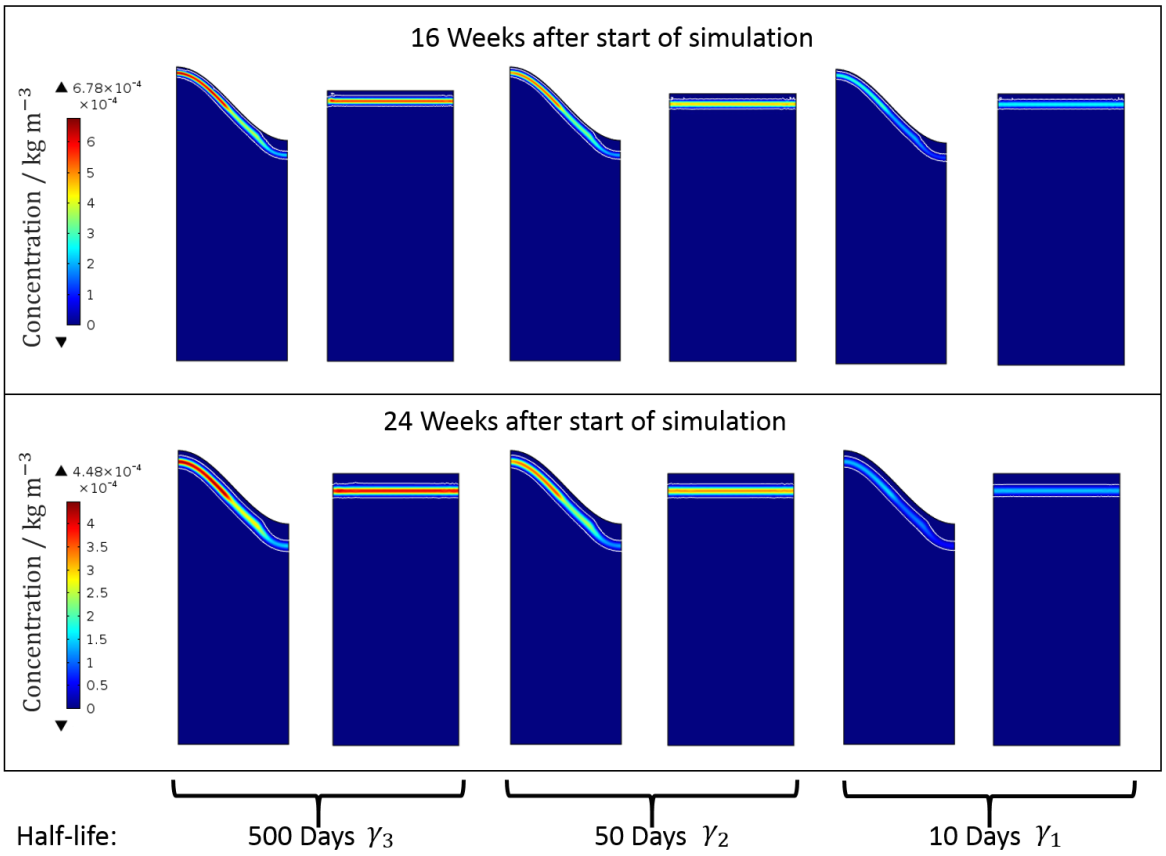

Figure 3.3: Early application solute profiles in the ridged and flat domains for the moderately mobile solutes $(\gamma_1, \gamma_2, \gamma_3)$ after 16 and 24 weeks post solute application. A white contour line indicating a safety threshold of 10 μg l^{-1} is also plotted. The ridge and furrow, and flat domains are the same as those shown in Figure 3.1.

evident in the simulation results.

Furthermore, we note that due to roots taking up water, solute is drawn up towards the ridges through the difference between the soil water pore pressure and pressure in the root system. Chen *et al.* (2011) [161] found that in ridge and furrow structures, water that infiltrated into the furrows of the system was transported to the ridges, which in turn reduced water movement directly below the ridge. In the simulations, this results in greater concentrations of solute in the ridges of the system due to water transporting the solute. This coincides with the results of Smelt *et al.* (1981) [123], who found the most solute residues in the ridges of the ridge and furrow structures at the end of growing seasons. Similarly, Jaynes & Swan (1999) [17] found substantially higher concentrations in the ridges of the structure compared to the furrows.

In the flat soil domain, we find that the solute moves down uniformly and is temporarily impeded by the roots that are present in the plough layer. When we compare the solute penetration between the flat and ridged soils, we find the solute

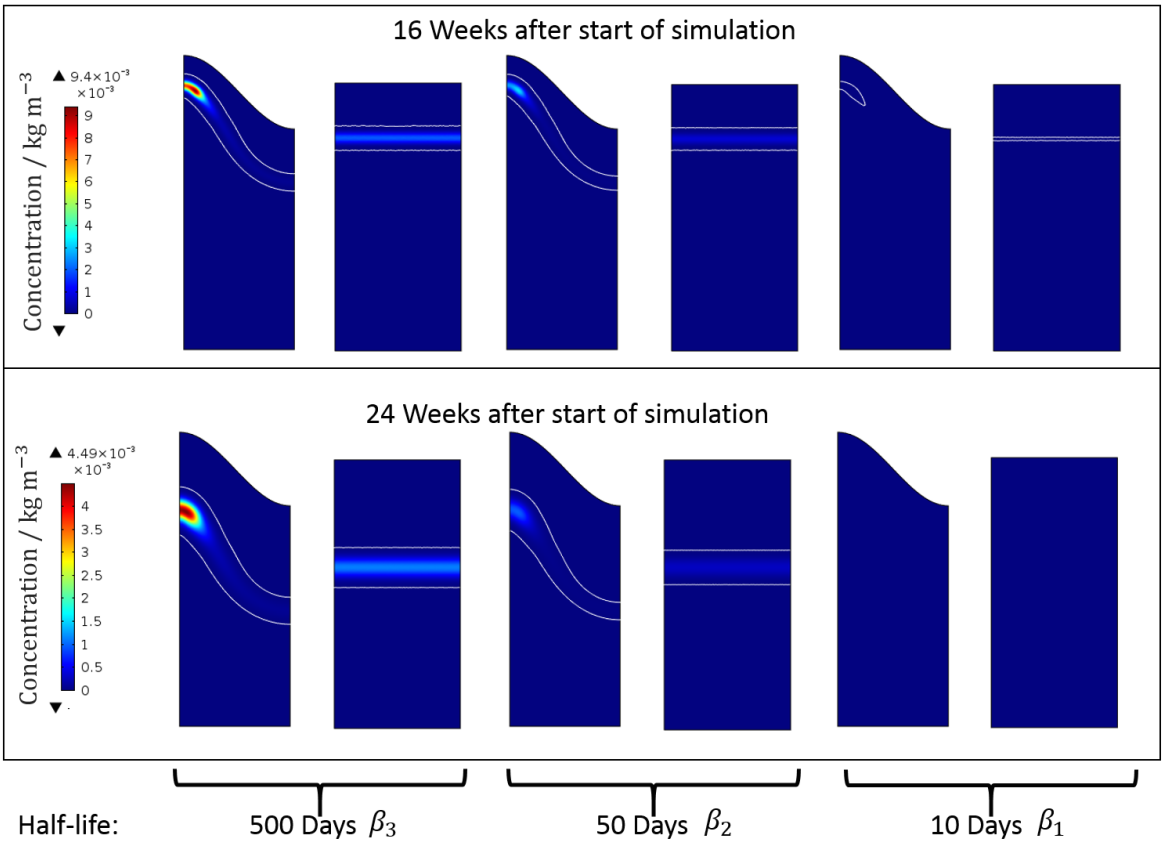

Figure 3.4: Early application solute profiles in the ridged and flat domains for the highly mobile solutes $(\beta_1, \beta_2, \beta_3)$ after 16 and 24 weeks post solute application. A white contour line of the safety threshold of 10 μg l^{-1} is also plotted. The ridge and furrow, and flat geometries are the same as those shown in Figure 3.1.

in the flat domain moves to a greater absolute depth below the soil surface than the solute contained in the ridges. This result coincides with Hamlett *et al.* (1990) [162], who identified that placing solutes on the ridges of the structure substantially reduced the amount leached compared to the flat field application. Jaynes & Swan (1999) [17] supported this hypothesis, and in addition found that applications to the ridges could provide increased quantities of solute to the plant, *i.e.*, nutrients and fertilisers.

However, we observe that the solute in the flat soil penetrates less than the solute contained in the furrows of the ridged soil. This can be explained by the distribution of ponding on the two soil domains. When ponding occurs on the flat soil, the ponding depth is significantly shallower than the ridged soil, since the pond is uniformly spread over the entire soil surface. Conversely, in the ridged soil the pond is solely situated in the furrow. This in turn causes a greater body of water to infiltrate into the furrow, causing deep solute penetration in this region of the soil, but reducing the penetration of solutes in the ridges of the domain.

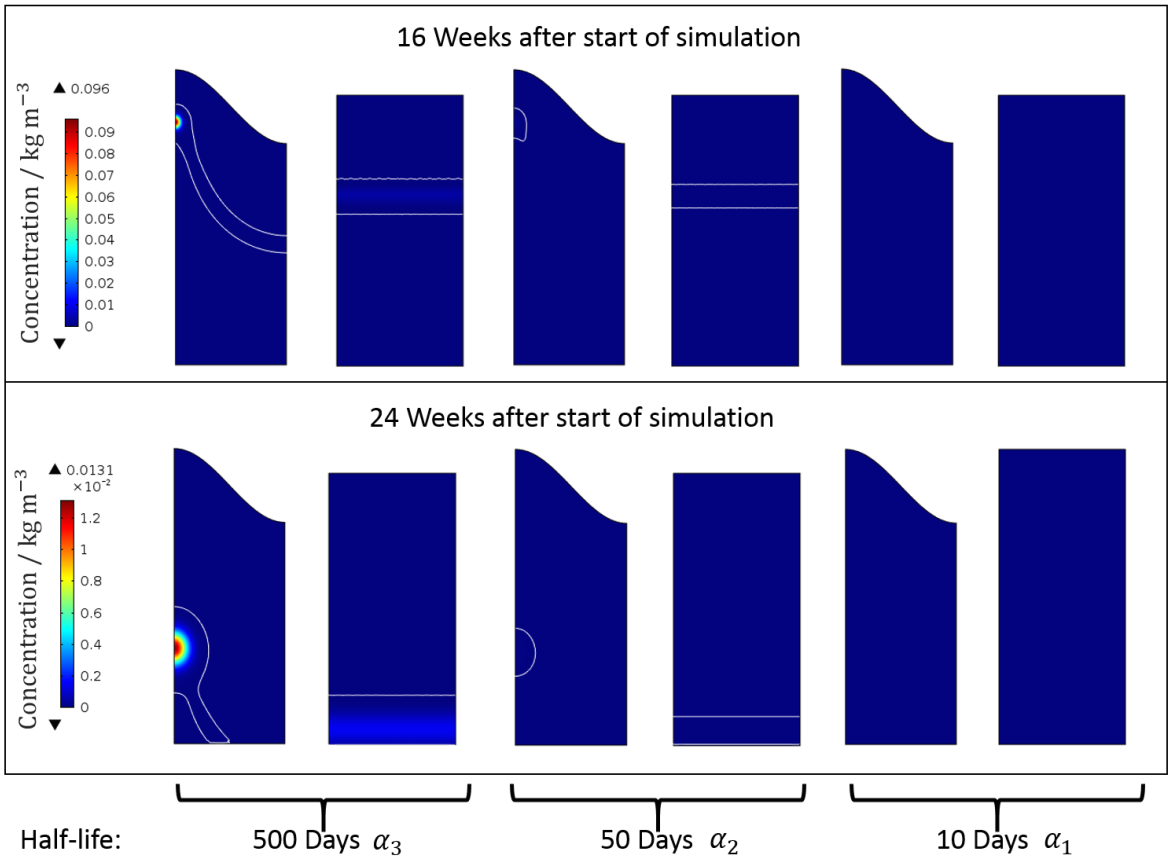

Figure 3.5: Early application solute profiles in the ridged and flat domains for the extremely mobile solutes $(\alpha_1, \alpha_2, \alpha_3)$ after 16 and 24 weeks post solute application. A white contour line indicating a safety threshold of 10 μg l^{-1} is also plotted. The ridge and furrow, and flat domains are the same as those shown in Figure 3.1.

Similar properties can be observed in Figure 3.4 (for the solutes $\beta_1, \beta_2, \beta_3$) and Figure 3.5 (for the solutes $\alpha_1, \alpha_2, \alpha_3$) for the simulations containing highly and extremely mobile solutes respectively. For the highly mobile solutes β_1, β_2 and β_3 in the ridged system (see Figure 3.4), the effect of solute accumulation in the ridges is more pronounced. In the ridge simulation containing solute β_3, we find that at 16 weeks post-solute application, a large quantity of the solute is contained in the region of soil adjacent to the plant roots due to water transport to the ridges created by the ridge and furrow structure [161, 163].

At 24 weeks (the end of the simulation), we find that the solute has penetrated down into the soil as a concentrated spot that slowly diffuses out. We understand that there is reduced solute movement when root uptake is present in soil [132]. Since roots are only present for the first 16 weeks, in the remaining 8 weeks the solute is influenced to a greater extent by rainfall into the ridges. Hence, we observe deeper solute penetration in the later portion of the simulation. Furthermore, we note that for the highly degrading solute β_1, the concentration drops below the

$10\ \mu$g l^{-1} threshold for both soil domains $\tilde{\Omega}$ and $\tilde{\Phi}$. This is due to the combination of fast dispersion and short half-life. Therefore, in either geometry it is the slowly degrading solutes $(\alpha_3, \beta_3, \gamma_3)$ that are of critical importance.

Shown in Figure 3.5 are the results for the extremely mobile solutes α_1, α_2 and α_3. For the solute α_3, we find that a quantity of the solute leaves the base of both soil domains. In the ridge simulation, as an effect of the solute accumulating in the ridges, the solute moves down the soil profile as a highly concentrated spot. Given that the solute is drawn up into the ridges early in the simulation, the majority of the solute is not influenced by later ponding in the furrows. Therefore, the solute moves down solely under the influence of the rainfall that enters the ridge of the soil, and thus takes longer to reach the base of the domain. Conversely, in the flat simulation, we find that all of the solute is affected by ponding (albeit significantly less than the furrow in the ridged soil). This leads to large quantities of the solute reaching the base of the domain. We find that the total amount of solute that crosses the base of the domain to be 0.26 mg in the ridged system, and 3.5 mg in the flat system. These findings support the results observed by Hamlett et al. (1990)[162] and Jaynes & Swan (1999)[17], who found that placing solutes on the ridges of the structure may substantially reduce leaching compared to the flat field application. Since applying the solute solely to the ridges negates the effects of ponding, this reduces the penetration depth in the soil [130]. Furthermore, root uptake reduces the solute movement in the ridges [132]. This causes the solute to remain near the surface, allowing for easy solute extraction from the soil after harvesting.

In the ridge and furrow simulations, we observe that as an effect of water uptake from plant roots, the movement of the solute from the furrow to the ridges protects the solute from deep penetration, which would otherwise be caused by furrow ponding. In comparison, the flat ground has a uniform surface that offers no protection, hence all the solute is affected by ponding and rainfall. Therefore, the average depth of the solute is reduced in the ridged soil compared to the flat soil when this spot formation mechanic is present.

3.4.2 Late Application Results

Figure 3.6 shows the solute profiles for the early and late applications of the solutes $\alpha_3,\ \beta_3$ and γ_3, *i.e.*, those with slow degradation, in $\tilde{\Omega}$ and $\tilde{\Phi}$ at the end of the simulations. It should be noted that in the early application simulations the solutes are in the soil for a full 24 weeks, and for the late application simulations the solutes have a total of 9 weeks in the soil. We choose to only show the slow degrading solutes as these results show the most extreme behaviours and best highlight the

effects of surface ponding. However, all other solutes exhibit similar qualitative behaviour.

From the results presented in Figure 3.6 we can highlight several key features. In the simulations containing the late application of the solutes α_3, β_3 and γ_3 in $\tilde{\Omega}$, we find that a substantial quantity of solute penetrates into the furrow. This is significantly different compared to the solute profile in the early application ridge and furrow simulations, in which the solutes move towards the ridge and form a concentrated spot.

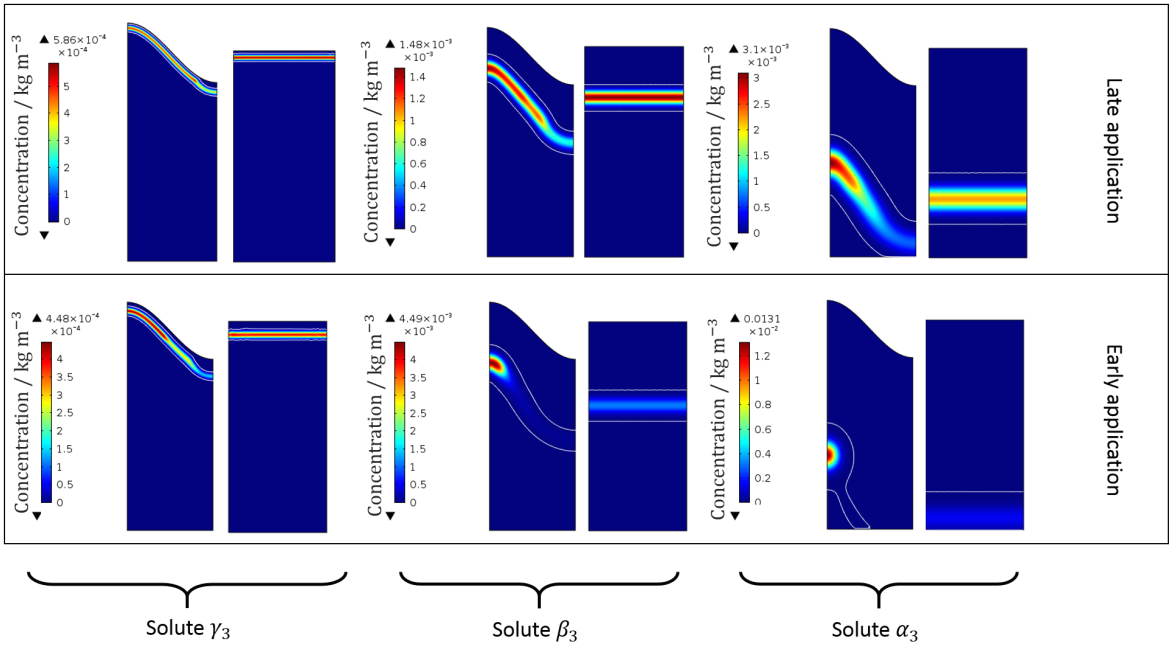

Figure 3.6: Early and late application solute profiles in the ridged and flat domains for the slow degrading solutes α_3, β_3 and γ_3 at the end of the 24 week simulations. A white contour line indicating a safety threshold of 10 μg l^{-1} is also plotted. The ridge and furrow, and flat domains are the same as those shown in Figure 3.1.

Differences in the solute profiles between the early and late applications in the ridge and furrow soil are attributed to three reasons. Firstly, we note that in the late application simulation, the period of time that the solute is in the soil is less than in the early application. Therefore, in the late application simulations, there has not been sufficient time for the solute to be transported towards the ridge of the structure via water that infiltrates into the furrows and moves to the ridges [161, 163]. Secondly, in the late application, the root length density is beginning to decline such that the root uptake is not as strong as earlier in the simulated growing season (refer to equation (3.32)). Hence, the difference in the soil water pore pressure between the ridge and the furrow is decreased, which causes less movement of water and solute towards the ridge, which causes greater solute

penetration [132]. The third reason for the reduction in spot formation comes from the rainfall that occurs immediately after the late application. From Figure 3.3, we note that there is an intense rainfall event shortly after the late application, which causes significant ponding in the furrow of the soil structure. Given that the solute has recently been applied to the soil, there has not been sufficient time for the solute to collect in the ridges of the structure. Therefore, the solute contained in the region of soil adjacent to the furrow is moved deep into the soil from water infiltration via the pond, since surface runoff leading to pond infiltration acts as a key transport mechanism for solutes [50].

From the rainfall data shown in Figure 3.3, we can see that the second three months (representing the winter months) have more frequent 'high-intensity' rainfall events compared to the first three months. In the late application simulations, this causes the solute in the furrow of $\tilde{\Omega}$ to move deep into the soil, and does not allow for the formation of a spot in the ridges. This makes the solute in the furrow vulnerable to leaching since heavy water treatments can generate substantial dispersion of solutes in ridged soils [164]. The effect of the 'time of ponding' can be clearly seen in the difference between the early and late application simulation results for the solute α_3 in $\tilde{\Omega}$. In the early application, the solute collects in the ridges of the system due to little ponding and a growing root system, and then proceeds to move down as a highly concentrated spot as the root length density decreases. However, in the late application, through immediate surface ponding and a lack of roots, the solute moves down with a wider distribution under the influence of infiltration of water from the pond.

For the simulations of the extremely mobile solute α_3, we note that in several cases, at the end of the simulations some solute leaves the system via the base of the geometry. Furthermore, we find that the total quantity that crosses the base of the domain depends on the soil surface topology and time of application. In the early application simulations, we find that the ridge domain leaches 0.26 mg, whereas the flat system leaches 3.5 mg. However, in the late application, we find that the in ridge domain the amount leached is 0.15 mg and in the flat system the amount leached is 0 mg.

The model results suggest that the optimal geometry to reduce solute leaching is dependent on two key aspects: the immediate rainfall regime after a solute application, and the quantity of roots in the soil. We find that in the early solute application simulations, there is not a substantial quantity of rainfall that generates significant furrow ponding. This allows the solute to move towards the ridges of the system under the influence of water movement, which is often observed in ridge and furrow soils [161, 163]. This then protects the solute from future furrow

ponding since root uptake can reduce the solute movement in the ridges [132]. Contrastingly, in the late application simulations, we note that there is an immediate heavy rainfall event after the solute application that causes substantial ponding. This generates greater ponding in $\tilde{\Omega}$ compared to $\tilde{\Phi}$, which results in the solute in the furrow to be transported deeper into the soil. This makes $\tilde{\Omega}$ substantially more vulnerable to solute leaching compared to $\tilde{\Phi}$. Therefore, considerable rainfall that causes ponding after a solute application may make the ridge tillaged soils more susceptible to solute leaching.

3.4.3 Time of Rainfall *versus* Solute Leaching

From the results above, we conduct a series of simulations in order to test the hypothesis that the time between solute application and a heavy rainfall event influences the quantity of leaching in ridged soils. We set up five ridged and five flat soil simulations, in which a solute (with the same properties as the solute α_3) is applied uniformly to each soil. One heavy rainfall event that generates substantial ponding is then simulated at different times after the solute application in each simulation. The rainfall event is chosen to last for 4 hours and have a rainfall intensity of 12 mm hr^{-1}, and the times between the solute application and the rainfall event are chosen to be 1 day, 2 days, 4 days, 1 week and 2 weeks. One day after the rainfall event, the total amount of solute that crosses the plough layer is then calculated. The plough layer is chosen to be the soil above the horizontal line of -0.15 m in both soil domains shown in Figure 3.1.

Figure 3.7 shows the total amount of solute (as a percentage of solute applied) that crossed the horizontal line of -0.15 m in $\tilde{\Omega}$ and $\tilde{\Phi}$. For the simulations where the heavy rainfall event is 1 day after the solute application, there are trace amounts of leaching in $\tilde{\Phi}$. However, in $\tilde{\Omega}$ 11% of the solute that was applied leaches past the plough layer. This is due to the infiltration of water into the furrow from ponding, which transports the solute in the adjacent regions deep into the soil, since under heavy rainfall, ridge and furrow systems can generate substantial dispersion of solutes [164].

In the simulations that allow for longer periods of time between the solute application and the rainfall event, the relationship between the amounts of solute that are leached in the two domains changes. In the $\tilde{\Omega}$ simulations, as the time between solute application and rainfall event is delayed, more of the solute can move towards the ridges of the soil via water transport to the ridges from the furrows [161]. This causes less solute to be affected by the ponding and water infiltration from the heavy rainfall event, causing less solute to move past the

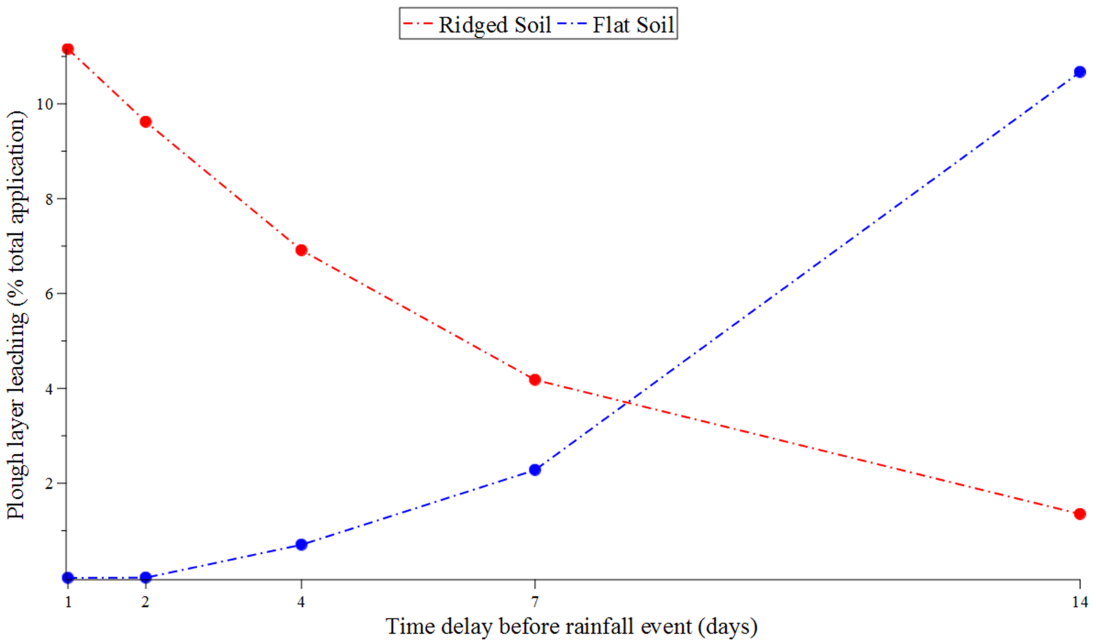

Figure 3.7: Total amount of solute leached past the plough layer in the ridge and furrow soil $\tilde{\Omega}$ and flat soil $\tilde{\Phi}$ for simulations that delay the period of time between a solute application and a heavy rainfall event.

plough layer. For example, when the time period between the solute application and the rainfall is 14 days, we find that $\approx 1.5\%$ of the solute applied is leached past the plough layer.

However, $\tilde{\Phi}$ exhibits the opposite behaviour. As the time between solute application and rainfall event is delayed, a greater amount of solute is leached past the plough layer. This is due to the solute diffusion in the system before the rainfall event. Since we simulate an extremely mobile solute, the longer the solute is in the system the more it diffuses. This causes the rainfall and pond infiltration to have a greater effect on the transport of the solute. In the simulation with a 14 day period between the solute application and the rainfall event, the total amount of leached solute is $\approx 11\%$.

Figure 3.7 illustrates a crossover between the total quantities of solute leached in the plough layer for $\tilde{\Omega}$ and $\tilde{\Phi}$ after approximately 8 days. In the case study of an extremely mobile solute and a single heavy rainfall event in a silt loam soil, we find that any time below an 8 day delay between the solute application and the rainfall event, the flat domain $\tilde{\Phi}$ better reduces leaching. However, any time after an 8 day delay, the ridge and furrow domain $\tilde{\Omega}$ better reduces leaching, since the solute can move towards the ridges and create a 'zone of protection' from ponding. However, this crossover period will change significantly depending on the mobility of solute, rainfall regime, and type of plant roots, *i.e.*, in scenarios where the applied solute is

less mobile and there are lower root densities present in the soil. This will require greater time to observe the ridge accumulation, thereby delaying the crossover period. Regardless, these results suggest that in specific situations, it could be either the ridge and furrow soil or the flat soil that better reduces leaching.

In previous research, it has been found that ridge and furrow planting often leads to greater leaching of solutes compared to the flat system [18, 58, 59]. However, it has been observed that certain application procedures may reduce leaching in ridged fields compared to flat fields [17, 126, 127]. This supports our findings as we observe that water movement from the furrows into the ridges [163], can transport solutes into the root adjacent zones of the structure and while held there by plant roots [132], reduce the effect from dominant surface runoff and subsequent infiltration [50]. As such, we find that ridge and furrow systems can also reduce solute leaching.

3.4.4 Assumption Limitations

In order to ensure that any differences that were observed were geometry dependent (between $\tilde{\Omega}$ and $\tilde{\Phi}$), we made several key assumptions. Hence, it may be of interest to incorporate ridge and furrow specific factors in order to determine the magnitude and severity of the mechanisms that were observed.

One of the key factors to consider is the soil water content in each of the ridge and furrow and flat domains. Since water movement is the key transport mechanism for solutes in soil [145], it is vital to accurately characterise the soil water profile in both $\tilde{\Omega}$ and $\tilde{\Phi}$. In the mathematical model, a boundary condition on the base of the domains was imposed such that a shallow water table approximately 1 m below the soil surface is replicated. This allowed us to model solute movement within an idealised soil domain. However, incorporating high spatial resolution field data to capture the soil water profile in the domains $\tilde{\Omega}$ and $\tilde{\Phi}$ could indicate how different water profiles influence the solute dynamics and mechanisms that were observed, *i.e.*, penetration from furrow ponding and transport to the ridges from the furrow.

Understanding the water profile in soil would also aid in accurately capturing the infiltration mechanics of rainfall into the soil. We used hourly time resolved rainfall data for a 24 week period, which limits the accuracy in capturing any change in infiltration capacity. This could play a key role in determining the severity of ponding and therefore the movement of solutes from the furrow to the ridges. Thus, understanding the infiltration capacity and soil water content on a higher time and spatial resolution may aid us in understanding the magnitude of the effects

observed.

To further understand the solute collection and 'hot spot' formation mechanism that was observed, knowledge of the root architecture would play a key role. This would allow us to understand the distribution of root pressures in the root zones, *i.e.*, $\tilde{\Omega}_U$ and $\tilde{\Phi}_U$, and hence predict the spatial distribution of solutes that collect in the ridges of the soil geometry. This would provide a more quantitate analysis of specific case studies relating to different solutes and root systems. Furthermore, knowledge of the harvestable crop product distribution, *i.e.*, tubers in the soil could be included. We neglect any influence from tubers in the soil, which may impede the transport of water and solutes due to their size and clustered growth. This could be a key aspect that may affect solute movement to the ridges of ridged soils.

Earlier we stated that in order to obtain a 'like for like' comparison, we kept the porosity ϕ between the ridge and furrow and flat systems the same. However, we understand that some tillage methods can affect ϕ. Hence, it would be useful to determine how any effect from tillage would affect the solute movement from the furrows to the ridges and therefore the impact on the spot formation in the ridges. This could have a substantial effect on the time required for the solute in the furrows to move to the ridges of the system.

In all of the simulations we neglected any solute uptake by roots, and only modelled passive solutes that are not actively taken up by plants. This was in order to model the 'worst case scenario', such that we could observe the most devastating effects from leaching. However, we have set up the model so that including solute uptake by plants could be easily incorporated, which would allow us to examine case studies in which the solute is actively removed from the system due to plant roots.

3.5 Conclusions

In this chapter, we extended the model from Chapter 2 to construct a system of equations that describe coupled solute transport, water movement and ponding within a ridge and furrow soil system. Using the model we presented a comparison of water and solute movement between a ridge and furrow, and a flat planting system. We simulated the movement of solutes with varying mobility and degradation in the two systems to observe how the structure of the soil surface influences solute movement.

Previous literature found contrasting results, suggesting that ridge and furrow systems may be vulnerable to solute leaching [18, 58, 59], or can significantly

reduce solute leaching [17, 126, 127]. The numerical modelling results explained this discrepancy and showed that the ridge and furrow structure could either impede or increase the penetration of solutes in soil, depending on the immediate rainfall activity after a solute application and the quantity of roots in the soil. In scenarios in which there was considerable rainfall that generated substantial ponding immediately after a solute application, we found that due to the water infiltration from the surface, advection acted as a strong transport mechanism for solutes in the furrow. This caused solutes in the furrow to move to a significantly greater depth when compared to the flat ground profile, in which due to the surface topology the influence of ponding is not so substantial.

However, we found that these trends are reversed for scenarios in which there is not significant ponding after a solute application. Instead, we observed that with the presence of roots in the ridges, this caused a dominant pressure gradient to form between the soil water pore pressure and the pressure in the root xylem. This in turn, caused the solute in the ridged system to move toward the root abundant soil, where the solute accumulates into a concentrated spot adjacent to the root zone in the ridges of the structure. This effect impedes the movement of the solute compared to the flat field, as the large majority is contained in the ridge of the structure, and is only influenced directly by infiltrated rainfall on the ridges, *i.e.*, no influence from furrow ponding. This mechanism can substantially reduce the quantity of solute that moves deep into the soil.

We observed that the vulnerability of the ridged system stems from the immediate ponding on the soil surface after the application of a solute, and is not a function of the structure itself. This solute movement mechanism should be noted when farming in semi-arid soils in which, formal irrigation down the furrow is required, *i.e.*, creating constant furrow ponding to allow sufficient water to the crop, since this mechanism may be contributing to the deep penetration of solutes into soils.

Chapter 4

Multiple Scale Homogenisation of Water Movement

In this chapter, we use the water movement model from Chapter 2 and apply the method of multiple scale homogenisation to develop a set of approximate equations. These equations describe water movement in the plough layer of soil, where crops are planted, grown and harvested. Particular focus is paid to the impedance of water movement due to crops in the soil, *i.e.*, potato tubers. We validate the homogenisation procedure by comparing the full set of equations to the approximate equations and find there to be a difference of $\lesssim 2\%$ between the two sets of solutions. Furthermore, we find that the computation time for the approximate equations is reduced by a factor of $\mathcal{O}(10^2)$ compared to the full set of equations for a typical 3D problem.

4.1 Introduction

Often when studying plant-soil systems, the experimental or mathematical techniques used are governed by the scale that is being analysed. Naturally, there are several different scales of interest when analysing plant-soil systems. These range from the large field scale to the very small pore scale [165]. Understanding the scale of interest is vital when considering possible experimental techniques. For example, X-ray computed tomography methods are used to examine small scale root hair distributions [166], and field scale dissections are used to observe large macroscale changes [167].

Similarly, when constructing mathematical models to represent plant-soil systems, the scale considered is crucial when developing models to capture the important

physical processes. For small scale pore studies, mathematical models can utilise equations such as the Cahn-Hilliard equation for phase separation between air and water, in order to understand the interaction at the air-water interface and on the soil mineral surfaces [168]. However, employing Cahn-Hilliard type mathematical models would be unnecessary and computationally prohibitive when considering a large 'plant scale' study. The computational requirement to resolve a plant scale geometry at the resolution to employ air-water interface models would be monumental. For example, if we consider a cylindrical soil column with a radius of 5 cm and a depth of 20 cm, this would have a volume of 500π cm^3. The typical air-water interface is approximately 0.1 μm, hence an element size of 0.02 μm would be required. This would generate $\approx 10^{12}$ elements, which would require several terabytes to simply store the solution. Instead, for larger scales, continuum mathematical models are implemented. For example, to model partially-saturated soil on the plant/field scale (as in Chapters 2 and 3), Richards' equation is used [169]. Hence, there is an effective discontinuity between the two scales in which physics on the small pore scale can be lost when deriving continuum models.

There has been substantial mathematical research conducted on bridging the gap between small and large scale models to create concrete continuum models that are derived from small scale models, in which more specific physics is considered [170]. One technique that has been particularly important in analysing the influence of small scale physics on the large scale is the method of multiple scale homogenisation [171]. This technique has been vital in combining small and large scale physics in porous media covering a wide range of applications [172].

Multiple scale homogenisation is a mathematical technique that is used to derive a system of averaged macroscopic equations that are parameterised by associated cell problems, derived from the inherent microscopic structure of the domain/geometry that is considered [171]. The underlying assumption of homogenisation is that there are two independent length scales, these being the micro- (l_y) and macro- (l_x) length scales. The ratio between the two length scales is often very small and is denoted $l_y/l_x = \varepsilon \ll 1$. It is this small parameter that forms the basis for homogenisation.

Homogenisation was first developed for periodic heterogeneous structures, however this technique has been used successfully in a wide range of porous media and soil applications including: modelling saturated fluid flow [173], two-phase fluid flow [174], wave propagation in poroelastic materials [175] and single-phase fluid flow in double porosity systems [176].

Frequently when studying the transport of water and solutes in soil, complex geometries are often required to capture the intrinsic details contained in the

microscopic structure of the scale that is considered. This typically requires vast amounts of computation time and resources [177]. Hence, it is often favourable to construct an averaged macroscopic domain such that the macroscale transport properties can be obtained directly from the microscale information [178].

One of the key results using homogenisation in porous media is the derivation of Darcy's law from Stokes flow [172]. Darcy's law was first proposed in 1856 to describe the the velocity of liquids in porous materials under specific pressure gradients [102]. Darcy's law takes the form,

$$\mathbf{v} = -\frac{\kappa}{\mu}(\boldsymbol{\nabla} p + \rho g \hat{\mathbf{e}}_3), \tag{4.1}$$

where $\mathbf{v}$ [m s^{-1}] is the fluid velocity, κ [m^2] is the permeability of the porous domain, p [Pa] is the fluid pressure, μ [Pa s] is the fluid viscosity, ρ [kg m^{-3}] is the fluid density and g [m s^{-2}] is gravity. Darcy's law was initially derived empirically from a series of sand flow experiments [102]. However, by applying multiple scale homogenisation to the equations for Stokes flow in a periodic porous domain, *i.e.*,

$$\mu \nabla^2 \mathbf{v} - \boldsymbol{\nabla} p = 0, \tag{4.2}$$

$$\boldsymbol{\nabla} \cdot \mathbf{v} = 0, \tag{4.3}$$

the resulting governing equation becomes,

$$\mathbf{v} = -\frac{\mathfrak{K}}{\mu}(\boldsymbol{\nabla} p + \rho g \hat{\mathbf{e}}_3), \tag{4.4}$$

where $\mathfrak{K}$ [m^2] is the 'effective permeability', a second rank tensor that is calculated from an associated cell problem, based on the intrinsic microscopic structure of the porous material [179]. Here equation (4.4) has the same functional form as Darcy flow in equation (4.1).

This example is shown in Figure 4.1, where the geometry dependent equations for Stokes flow, *i.e.*, equations (4.2) and (4.3) are imposed on the heterogeneous soil domain in Figure 4.1 (a). Shown in Figure 4.1 (b) is the homogeneous domain that results from the homogenisation procedure, in which the geometry independent equations for Darcy flow are imposed, *i.e.*, equation (4.4). In order to parameterise the effective permeability parameter $\mathfrak{K}$ in equation (4.4), a cell problem is solved to determine the 'effective impedance' from the heterogeneous domain shown in Figure 4.1 (a).

Another key result is the rigorous derivation of Richards' equation for water movement and transport in partially saturated soil. Richards' equation forms the

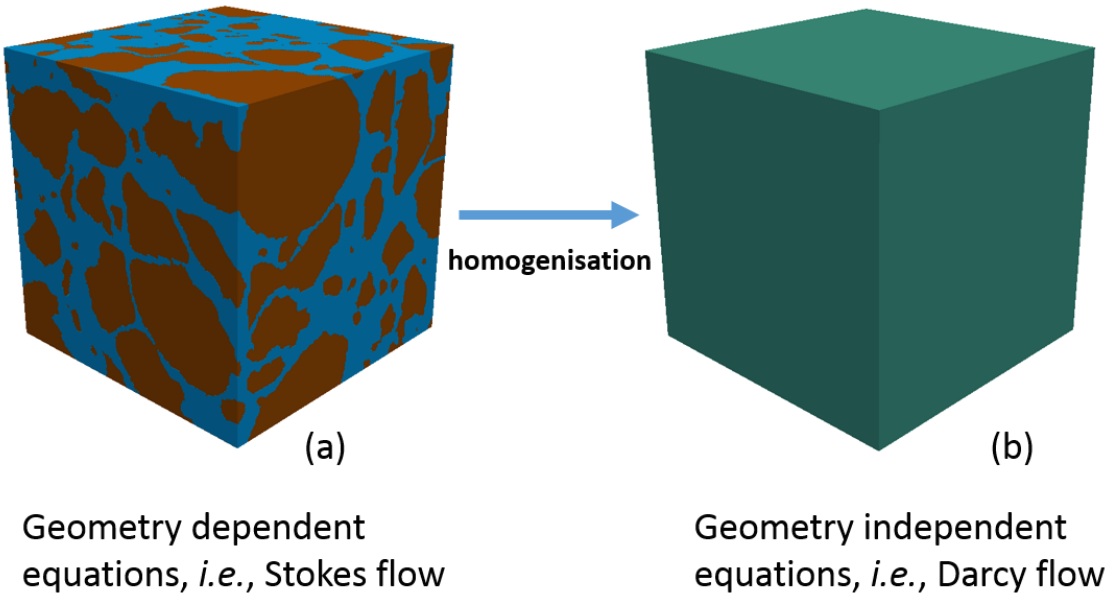

Figure 4.1: An example of multiple scale homogenisation. (a): Shown is a heterogeneous soil domain in which the geometry dependent equations of Stokes flow are imposed.
(b): Shown is the homogenous domain that results from the homogenisation procedure, in which the geometry independent equations of Darcy flow are imposed. Here the equations for Darcy flow are parameterised from a cell problem that captures the effective impedance from (a).

basis of the models developed in the first two chapters of this thesis, since it describes water movement as a continuum, which is important for describing saturation gradients across large areas of soil. Richards' equation was first published in 1931 [100], and is typically parameterised from experimental water-release curves [68, 180]. However, recently Richards' equation has been formally derived from the Cahn-Hilliard model using homogenisation [174]. This takes the first principle approach for minimising a free energy interface between air and water, *i.e.*, modelling a partially saturated soil, and using the upscaling technique, a macroscale set of equations are determined, which are parameterised by the microscale soil structure. The water-release curves to parameterise Richards' equation can then be determined from a series of cell problems, avoiding the requirement to conduct expensive and time consuming experiments.

In this chapter, we construct a set of macroscale equations using homogenisation to describe the movement and transport of water in the plough layer of soil in which crops are grown and harvested, *i.e.*, the subdomain $\tilde{\Lambda}_U$ as shown in Figure 2.2 (a). Using the water movement model from Chapter 2 and a soil domain that contains

potato tubers, we apply the method of multiple scale homogenisation to derive a set of averaged equations that accurately capture the movement of water in this region of soil. This model can then be incorporated into the water movement and ponding model from Chapter 2.

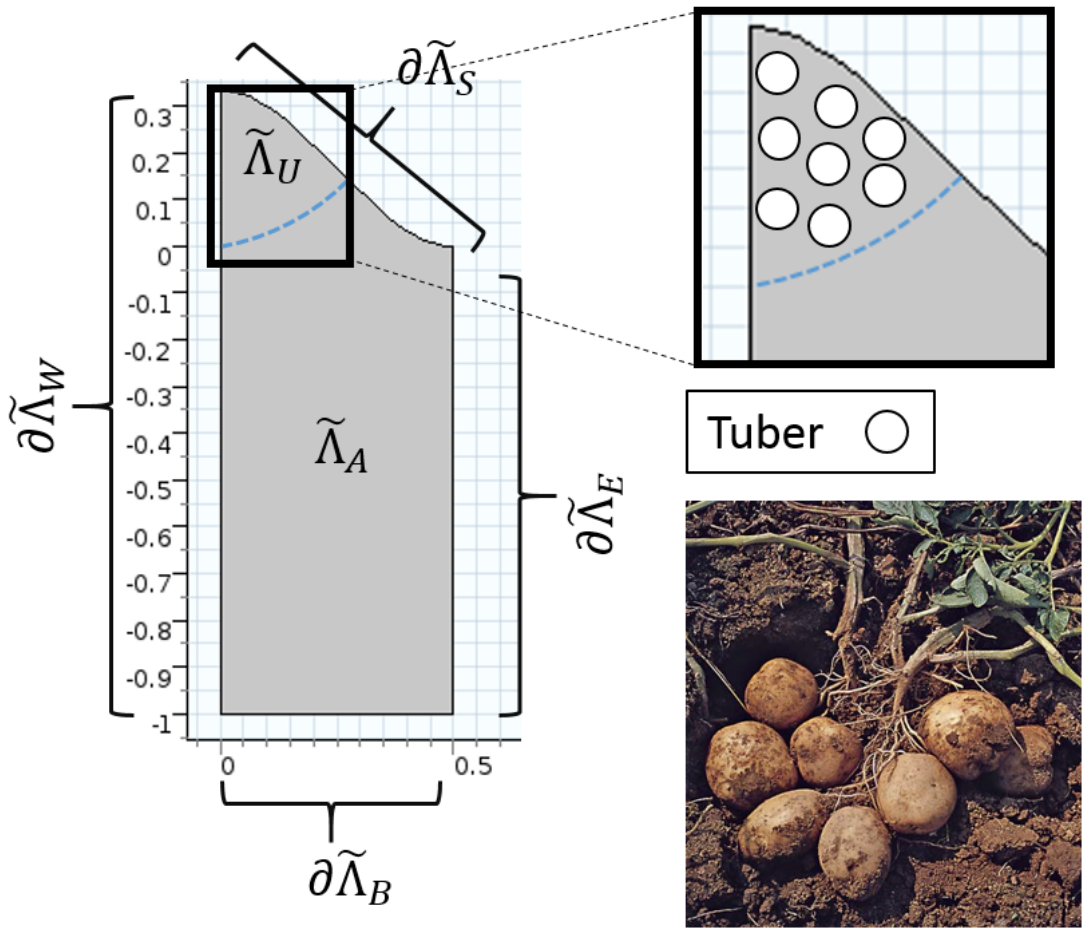

Figure 4.2: A schematic diagram of potato tubers in the plough layer of soil. Here $\tilde{\Lambda}_A$ is the region of soil absent roots, $\tilde{\Lambda}_U$ is the region of soil with roots, $\partial\tilde{\Lambda}_S$ is the soil surface boundary, $\partial\tilde{\Lambda}_B$ is the base of the domain, $\partial\tilde{\Lambda}_W$ is the boundary adjacent to the ridge, $\partial\tilde{\Lambda}_E$ is the boundary adjacent to the furrow and a visualisation of tubers in $\tilde{\Lambda}_U$ is shown. Furthermore, a photo of a recently harvested potato plant is shown. Photo from https://mumbaifarmer.files.wordpress.com/2014/09/potato-harvest.jpg

4.2 Crop Growth in Ridged Soils

The water movement and ponding model from Chapter 2 was developed for a generalised ridge and furrow domain $\tilde{\Lambda}$, as shown in Figure 2.2 (a). We considered the entire soil domain $\tilde{\Lambda}$ to be uniform and homogenous with the only difference

within the soil being the region of water uptake by plant roots. We denoted the subdomain $\tilde{\Lambda}_U \subset \tilde{\Lambda}$ to be the region of soil that contains plant roots, since crops are typically sown in the ridges of ridge and furrow soils. As such, when the plants develop and grow, the subdomain $\tilde{\Lambda}_U$ will begin to contain harvestable crop products, *i.e.*, potato tubers. A schematic of this is shown in Figure 4.2.

In the region of soil $\tilde{\Lambda}_U$, large clusters of potatoes can occupy much of the space in the ridges of the soil, particularly near harvest (see photo in Figure 4.2). In these regions, as the potato tubers increase in size and volume, they impede the movement of water that infiltrates due to rainfall. This reduces the rate at which water is transported through the plough layer of soil. Hence, fully grown potato tubers may have a significant effect on the movement of water in the plough layer and adjacent areas of soil. Additionally, since water movement is a key mechanism for solute transport, this may heavily influence the transport of nutrients and fertilisers in the root abundant areas of soil.

In the following section, we use the water movement model from Chapter 2 and apply multiple scale homogenisation to develop a set of averaged equations specific to the region of soil $\tilde{\Lambda}_U$. This will allow us to describe macroscopic water movement in the plough layer while capturing the effect of impedance from the potato tubers without having to explicitly account for every tuber, since modelling each individual potato tuber in the plough layer of soil, would be a heavily user-intensive process. For simplicity, we assume the tubers to be spherical, however, it is trivial to extend for any shape to represent carrots, turnips etc.

4.3 Theory

4.3.1 Plough Layer Domain

In order to develop a system of equations for water movement in the plough layer of soil, *i.e.*, $\tilde{\Lambda}_U$, we consider an idealised geometry in which the potato tubers are repeating and periodic. This can be seen in Figure 4.3 (a), where $\tilde{\Psi}$ [m^3] is the plough layer domain, $\tilde{\Psi}_S$ [m^3] is the soil subdomain and $\tilde{\Psi}_{p_j}$ [m^3] are the $j = 1, \ldots, N$ potato tubers each with a boundary $\tilde{\Gamma}_j$ [m^2] between the tubers $\tilde{\Psi}_{p_j}$ and the soil $\tilde{\Psi}_S$.

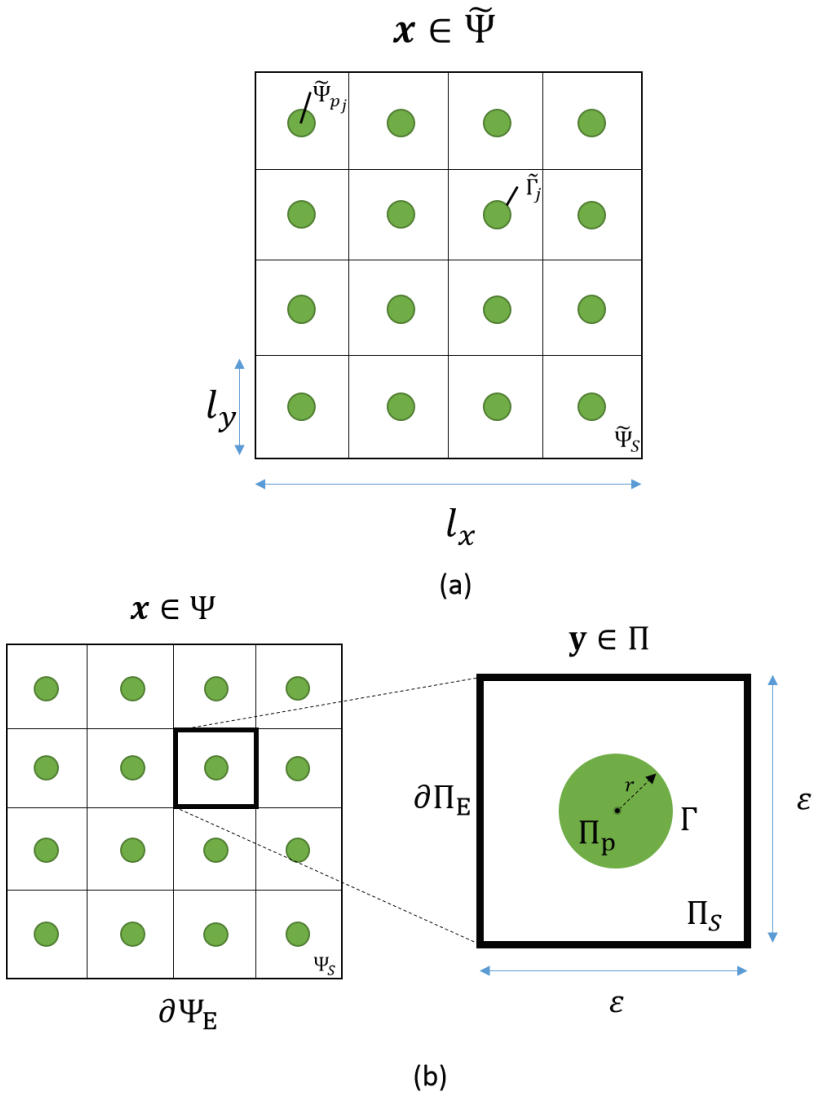

Figure 4.3: (a): Dimensional schematic of a plough layer domain containing potato tubers, where $\tilde{\Psi}$ is the total plough layer domain, $\tilde{\Psi}_S$ is the soil subdomain, $\tilde{\Psi}_{p_j}$ are the $j = 1, \ldots, N$ potato tubers and $\tilde{\Gamma}_j$ are the boundaries between the tubers and the soil. In addition, l_x is the macroscale, l_y is the microscale and $\varepsilon = l_y/l_x$.
(b): Schematic of the dimensionless macroscale domain Ψ and microscale domain Π, where Ψ_S is the soil domain, $\partial\Psi_E$ is the external boundary of Ψ, Π_S is the soil domain, Π_p is a potato tuber, Γ is the boundary between Π_S and Π_p, $\partial\Pi_E$ is the external boundary of the periodic cell and r is the radius of Π_p.

4.3.2 Governing Equations

On the soil domain $\tilde{\Psi}_S \subset \tilde{\Psi}$ we impose the governing equations from the model in Chapter 2, *i.e.*,

$$[1-H_S(\tilde{p}_w)]\phi\frac{\partial S(\tilde{p}_w)}{\partial \tilde{p}_w}\frac{\partial \tilde{p}_w}{\partial \tilde{t}} = \tilde{\boldsymbol{\nabla}}\cdot\left\{\frac{\kappa_s\overline{\kappa[S(\tilde{p}_w)]}}{\mu_w}\left(\tilde{\boldsymbol{\nabla}}\tilde{p}_w+\rho g\hat{\mathbf{e}}_3\right)\right\}-\lambda_c(\tilde{p}_w-p_r) \quad \text{in} \quad \tilde{\Psi}_S^{\infty}, \tag{4.5}$$

where, $\tilde{\Psi}_S^{\infty}=\tilde{\Psi}_S\times(0,\infty)$ (where $(0,\infty)$ denotes the time domain), and,

$$\frac{\partial S(\tilde{p}_w)}{\partial \tilde{p}_w} = \frac{m\left[\left(\frac{-\tilde{p}_w}{p_c}\right)^{\frac{m}{1-m}}+1\right]^{-m-1}\left(\frac{-\tilde{p}_w}{p_c}\right)^{\frac{m}{1-m}}}{p_c(1-m)}, \tag{4.6}$$

$$\overline{\kappa[S(\tilde{p}_w)]} = \begin{cases} 1 & \text{for} \quad p_w \geq -\zeta_t \\ \left[\left(\frac{-\tilde{p}_w}{p_c}\right)^{\frac{m}{1-m}}+1\right]^{\frac{-m}{2}}\left(1-\left\{1-\left[\left(\frac{-\tilde{p}_w}{p_c}\right)^{\frac{m}{1-m}}+1\right]^{-1}\right\}^m\right)^2 & \text{for} \quad p_w < -\zeta_t \end{cases}. \tag{4.7}$$

Since we now consider the individual potato tubers $\tilde{\Psi}_{p_j}$ in $\tilde{\Psi}$, we require an additional boundary condition on the surface of the tubers $\tilde{\Gamma}_j$. We assume that water does not infiltrate the tubers, hence, we impose a zero flux boundary condition on $\tilde{\Gamma}_j$, *i.e.*,

$$\hat{\mathbf{n}}\cdot\left\{\frac{\kappa_s\overline{\kappa[S(\tilde{p}_w)]}}{\mu_w}\left(\tilde{\boldsymbol{\nabla}}\tilde{p}_w+\rho g\hat{\mathbf{e}}_3\right)\right\}=0 \quad \text{on} \quad \tilde{\Gamma}_j. \tag{4.8}$$

It should be noted that in this model, we limit the boundary condition on the surface of the tubers to a zero flux condition, *i.e.*, ignoring any effects from preferential flow, which may be caused by the interface between the soil and tuber. We strictly consider the impedance caused due to the tuber occupying space within the soil domain.

4.3.3 Non-dimensionalisation

Here we non-dimensionalise the system of equations (4.5) $-$ (4.8). We are interested in the macroscopic properties of the system of equations whilst retaining the influence of the microscopic structure. From Figure 4.3 we identify there are two different length scales, the microscopic length scale l_y [m] and the macroscopic length scale l_x [m], where $l_y/l_x=\varepsilon\ll 1\ [-]$. We choose to non-dimensionalise (4.5) $-$ (4.8) using the scaling,

$$\tilde{\mathbf{x}}=l_x\mathbf{x},\ \tilde{t}=\frac{\phi\mu_w l_x^2}{\kappa_s p_c}t,\ \tilde{p}_w=p_c p_w. \tag{4.9}$$

Shown in Figure 4.3 (b) is the non-dimensionalised macroscopic domain Ψ and microscopic domain Π. In (4.9) we use the macroscopic length scale l_x as the spatial scaling to capture the large scale effects, the 'effective diffusivity' $\frac{\phi\mu_w l_x^2}{\kappa_s p_c}$ for the time scaling and the suction characteristic p_c as the pressure scaling. It follows that the system of equations becomes,

$$[1 - H_S(p_w)]\frac{\partial S(p_w)}{\partial p_w}\frac{\partial p_w}{\partial t} = \boldsymbol{\nabla}\cdot\left\{\overline{\kappa[S(p_w)]}\left(\boldsymbol{\nabla}p_w + \overline{\rho}\hat{\mathbf{e}}_3\right)\right\} - \left(\overline{p}_c p_w - \overline{p}_r\right) \quad \text{in} \quad \Psi_S^{\infty}, \tag{4.10}$$

$$\hat{\mathbf{n}}\cdot\left\{\frac{\kappa[S(\tilde{p}_w)]}{\mu_w}\left(\tilde{\boldsymbol{\nabla}}\tilde{p}_w + \overline{\rho}\hat{\mathbf{e}}_3\right)\right\} = 0 \quad \text{on} \quad \Gamma_j, \tag{4.11}$$

where,

$$\frac{\partial S(p_w)}{\partial p_w} = \frac{m\left[(-p_w)^{\frac{m}{1-m}} + 1\right]^{-m-1}(-p_w)^{\frac{m}{1-m}}}{(1-m)}, \tag{4.12}$$

$$\overline{\kappa[S(p_w)]} = \begin{cases} 1 & \text{for} \quad p_w \geq -\zeta_t \\ \left[(p_w)^{\frac{m}{1-m}} + 1\right]^{\frac{-m}{2}}\left(1 - \left\{1 - \left[(-p_w)^{\frac{m}{1-m}} + 1\right]^{-1}\right\}^m\right)^2 & \text{for} \quad p_w < -\zeta_t \end{cases}, \tag{4.13}$$

and

$$\overline{\rho} = \frac{\rho g l_x}{p_c},\ \overline{p}_c = \frac{\lambda_c p_c \mu_w l_x^2}{\kappa_s p_c},\ \overline{p}_r = \frac{\lambda_c p_r \mu_w l_x^2}{\kappa_s p_c}. \tag{4.14}$$

In Chapter 2, we estimated the parameters contained in the water-ponding model, which are contained in Table 2.1. Here we have one new parameter to consider, the macro length scale l_x. Since we are considering the plough layer of soil, we choose the parameter to be the average plough layer depth, *i.e.*, $l_x = 0.3$ m [103].

Using the estimated parameters from Table 2.1 and $l_x = 0.3$ m, we observe that all the non-dimensionalised parameters in (4.14) are of the same order of magnitude, *i.e.*, $\overline{\rho} = \overline{p}_c = \overline{p}_r = \mathcal{O}(1)$. Hence, there are no terms in the system of equations (4.10) $-$ (4.13) that are $\mathcal{O}(\varepsilon)$ other than the ratio between l_y and l_x.

4.3.4 Homogenisation

In this section, we use multiple scale homogenisation to develop a set of averaged macroscale equations that describe the movement of water in the plough layer of soil. We observe there are two different length scales present in the geometry $\tilde{\Psi}$, the macro length scale l_x and the micro length scale l_y. Any change of $\mathcal{O}(1)$ on the macroscopic length scale will result in a $\mathcal{O}(\varepsilon)$ change on the microscopic length scale. We can formalise this by assuming that the dependent variable p_w is a

function of the small scale $\mathbf{y}$ and large scale $\mathbf{x}$. We denote the unit cell Π representing the microscale domain $\mathbf{y} \in \Pi \equiv [-1/2, 1/2]^3$. Using the two length scales and chain rule, the gradient operator is written,

$$\boldsymbol{\nabla} = \boldsymbol{\nabla}_{\mathbf{x}} + \varepsilon^{-1}\boldsymbol{\nabla}_{\mathbf{y}}. \tag{4.15}$$

Furthermore, we expand p_w such that,

$$p_w = p_{w0} + \varepsilon p_{w1} + \varepsilon^2 p_{w2} + \mathcal{O}(\varepsilon^3). \tag{4.16}$$

The system of equations we homogenise is given by,

$$[1 - H_S(p_w)]\frac{\partial S(p_w)}{\partial p_w}\frac{\partial p_w}{\partial t} = \boldsymbol{\nabla} \cdot \left\{ \overline{\kappa[S(p_w)]} \left(\boldsymbol{\nabla} p_w + \overline{\rho}\hat{\mathbf{e}}_3 \right) \right\} - (\overline{p}_c p_w - \overline{p}_r) \quad \text{in} \quad \Pi_S^{\infty}, \tag{4.17}$$

$$\hat{\mathbf{n}} \cdot \left\{ \overline{\kappa[S(p_w)]} \left(\boldsymbol{\nabla} p_w + \overline{\rho}\hat{\mathbf{e}}_3 \right) \right\} = 0 \quad \text{on} \quad \Gamma \times [0, \infty), \tag{4.18}$$

$$\text{periodic} \quad \text{on} \quad \partial\Pi_E, \tag{4.19}$$

where Π_S is the microscale domain shown in Figure 4.3.

The first step of the homogenisation procedure is to determine the most dominant terms in the system of equations (4.17) $-$ (4.19). To do this, we substitute equations (4.15) and (4.16) into (4.17) $-$ (4.19) and collect the largest terms of order $\mathcal{O}(\varepsilon^{-2})$. This yields,

$$\boldsymbol{\nabla}_{\mathbf{y}} \cdot \left\{ \overline{\kappa[S(p_{w0})]} \boldsymbol{\nabla}_{\mathbf{y}} p_{w0} \right\} = 0 \quad \text{in} \quad \Pi_S, \tag{4.20}$$

$$\hat{\mathbf{n}} \cdot \left\{ \overline{\kappa[S(p_{w0})]} \boldsymbol{\nabla}_{\mathbf{y}} p_{w0} \right\} = 0 \quad \text{on} \quad \Gamma, \tag{4.21}$$

$$\text{periodic} \quad \text{on} \quad \partial\Pi_E. \tag{4.22}$$

Theorem 4.3.1. *Equations (4.20) $-$ (4.22) have the solution $p_{w0} = p_{w0}(\mathbf{x}, t)$, i.e., p_{w0} has large scale dependence only.*

Proof. We observe from (4.20) that,

$$\int_{\Pi_S} p_{w0} \boldsymbol{\nabla}_{\mathbf{y}} \cdot \left\{ \overline{\kappa[S(p_{w0})]} \boldsymbol{\nabla}_{\mathbf{y}} p_{w0} \right\} d\Pi_S = 0. \tag{4.23}$$

Applying Green's first identity to (4.23) yields,

$$\int_{\Gamma} p_{w0} \hat{\mathbf{n}} \cdot \left\{ \overline{\kappa[S(p_{w0})]} \boldsymbol{\nabla}_{\mathbf{y}} p_{w0} \right\} d\Gamma - \int_{\Pi_S} \boldsymbol{\nabla}_{\mathbf{y}} p_{w0} \cdot \left\{ \overline{\kappa[S(p_{w0})]} \boldsymbol{\nabla}_{\mathbf{y}} p_{w0} \right\} d\Pi_S = 0. \tag{4.24}$$

Using (4.21) to eliminate the first term, we find,

$$\int_{\Pi_S} \boldsymbol{\nabla}_{\mathbf{y}} p_{w0} \cdot \left\{ \overline{\kappa[S(p_{w0})]} \boldsymbol{\nabla}_{\mathbf{y}} p_{w0} \right\} d\Pi_S = 0. \tag{4.25}$$

Equation (4.25) can be expressed as,

$$\int_{\Pi_S} ||\boldsymbol{\nabla}_{\mathbf{y}} p_{w0}||^2_{L^2} \overline{\kappa[S(p_{w0})]}\, d\Pi_S = 0, \tag{4.26}$$

where $||\cdot||_{L^2}$ is the L^2 norm, *i.e.*, $||\mathbf{x}||_{L^2} = \sqrt{\langle \mathbf{x}, \mathbf{x} \rangle} = \sqrt{x_1^2 + ... + x_n^2}$. We observe that $\overline{\kappa[S(p_{w0})]} > 0$, since $\overline{\kappa[S(p_w)]} \to 0$ as $p_w \to -\infty$, therefore in order satisfy (4.26), $||\boldsymbol{\nabla}_{\mathbf{y}} p_{w0}||^2_{L^2} = 0$. By definition, $||\mathbf{x}||_{L^2} = 0 \iff \mathbf{x} = 0$, hence,

$$||\boldsymbol{\nabla}_{\mathbf{y}} p_{w0}||^2_{L^2} = 0 \quad \Rightarrow \quad \boldsymbol{\nabla}_{\mathbf{y}} p_{w0} = 0 \quad \Rightarrow \quad p_{w0} = C, \tag{4.27}$$

where C is independent of the small scale $\mathbf{y}$. Therefore, $p_{w0} = p_{w_0}(\mathbf{x}, t)$. □

From Theorem 4.3.1 we observe that p_{w0} has large scale dependence only and is independent of the small scale $\mathbf{y}$, however, we receive no other information regarding the solution of p_{w0}.

To proceed, we collect the second most important terms in the system of equations (4.17) − (4.19). This is achieved by collecting terms of order $\mathcal{O}(\varepsilon^{-1})$, *i.e.*,

$$\boldsymbol{\nabla}_{\mathbf{y}} \cdot \left\{ \overline{\kappa[S(p_{w0})]} \boldsymbol{\nabla}_{\mathbf{y}} p_{w1} + \overline{\kappa[S(p_{w0})]} \boldsymbol{\nabla}_{\mathbf{x}} p_{w0} + p_{w1} \frac{\delta \overline{\kappa}}{\delta p_w}\bigg|_{p_w = p_{w0}} \boldsymbol{\nabla}_{\mathbf{y}} p_{w0} + \overline{\rho} \overline{\kappa[S(p_{w0})]} \hat{\mathbf{e}}_3 \right\} + \boldsymbol{\nabla}_{\mathbf{x}} \cdot \left\{ \overline{\kappa[S(p_{w0})]} \boldsymbol{\nabla}_{\mathbf{y}} p_{w0} \right\} = 0 \quad \text{in} \quad \Pi_S, \tag{4.28}$$

$$\hat{\mathbf{n}} \cdot \left\{ \overline{\kappa[S(p_{w0})]} \boldsymbol{\nabla}_{\mathbf{y}} p_{w1} + \overline{\kappa[S(p_{w0})]} \boldsymbol{\nabla}_{\mathbf{x}} p_{w0} + p_{w1} \frac{\delta \overline{\kappa}}{\delta p_w}\bigg|_{p_w = p_{w0}} \boldsymbol{\nabla}_{\mathbf{y}} p_{w0} + \overline{\rho} \overline{\kappa[S(p_{w0})]} \hat{\mathbf{e}}_3 \right\} = 0 \quad \text{on} \quad \Gamma, \tag{4.29}$$

$$\text{periodic} \quad \text{on} \quad \partial\Pi_E. \tag{4.30}$$

Using the result from Theorem 4.3.1, *i.e.*, $\boldsymbol{\nabla}_{\mathbf{y}} p_{w0} = 0$, the system of equations (4.28) − (4.30) reduces to,

$$\boldsymbol{\nabla}_{\mathbf{y}} \cdot \left\{ \overline{\kappa[S(p_{w0})]} \boldsymbol{\nabla}_{\mathbf{y}} p_{w1} \right\} = 0 \quad \text{in} \quad \Pi_S, \tag{4.31}$$

$$\hat{\mathbf{n}} \cdot \left\{ \overline{\kappa[S(p_{w0})]} \boldsymbol{\nabla}_{\mathbf{y}} p_{w1} + \overline{\kappa[S(p_{w0})]} \boldsymbol{\nabla}_{\mathbf{x}} p_{w0} + \overline{\rho} \overline{\kappa[S(p_{w0})]} \hat{\mathbf{e}}_3 \right\} = 0 \quad \text{on} \quad \Gamma, \tag{4.32}$$

$$\text{periodic} \quad \text{on} \quad \partial\Pi_E. \tag{4.33}$$

To ensure that equations (4.31) $-$ (4.33) form a well-posed problem, *i.e.*, the equations have a solution that agrees with the boundary conditions, we assess the solvability of the equations. To check the solvability of the system (4.31) $-$ (4.33), we apply the divergence theorem to equation (4.31) and use the boundary condition (4.32) such that,

$$\begin{aligned}\int_{\Pi_S} \boldsymbol{\nabla}_{\mathbf{y}} \cdot \left\{ \overline{\kappa[S(p_{w0})]} \boldsymbol{\nabla}_{\mathbf{y}} p_{w1} \right\} d\Pi_S = \int_{\Gamma} \hat{\mathbf{n}} \cdot \left\{ \overline{\kappa[S(p_{w0})]} \boldsymbol{\nabla}_{\mathbf{y}} p_{w1} \right\} d\Gamma = \\ - \int_{\Gamma} \hat{\mathbf{n}} \cdot \left\{ \overline{\kappa[S(p_{w0})]} \boldsymbol{\nabla}_{\mathbf{x}} p_{w0} + \overline{\rho} \overline{\kappa[S(p_{w0})]} \hat{\mathbf{e}}_3 \right\} d\Gamma = \\ - \int_{\Pi_S} \boldsymbol{\nabla}_{\mathbf{y}} \cdot \left\{ \overline{\kappa[S(p_{w0})]} \boldsymbol{\nabla}_{\mathbf{x}} p_{w0} + \overline{\rho} \overline{\kappa[S(p_{w0})]} \hat{\mathbf{e}}_3 \right\} d\Pi_S = 0.\end{aligned} \tag{4.34}$$

Equation (4.34) confirms the problem is well-posed as the governing equations and boundary conditions agree.

To proceed with the homogenisation procedure, we rescale p_{w1} such that,

$$p_{w1}(\mathbf{x}, \mathbf{y}) = \sum_{k=1}^{3} \chi_k(\mathbf{y}) \partial_{x_k} p_{w0} + \gamma_k(\mathbf{y}) \overline{\rho} + \breve{p}_{w1}(\mathbf{x}), \tag{4.35}$$

where $\breve{p}_{w1}(\mathbf{x})$ is the component of $p_{w1}(\mathbf{x}, \mathbf{y})$ that is large scale only. Substituting (4.35) into (4.31) $-$ (4.33) yields,

$$\boldsymbol{\nabla}_{\mathbf{y}} \cdot \left\{ \overline{\kappa[S(p_{w0})]} \boldsymbol{\nabla}_{\mathbf{y}} \chi_k \right\} \partial_{x_k} p_{w0} + \boldsymbol{\nabla}_{\mathbf{y}} \cdot \left\{ \overline{\rho} \overline{\kappa[S(p_{w0})]} \boldsymbol{\nabla}_{\mathbf{y}} \gamma_k \right\} = 0 \quad \text{in} \quad \Pi_S, \tag{4.36}$$

$$\hat{\mathbf{n}} \cdot \left\{ \overline{\kappa[S(p_{w0})]} \boldsymbol{\nabla}_{\mathbf{y}} \chi_k + \hat{e}_k \right\} \partial_{x_k} p_{w0} + \hat{\mathbf{n}} \cdot \left\{ \overline{\rho} \overline{\kappa[S(p_{w0})]} \boldsymbol{\nabla}_{\mathbf{y}} \gamma_k + \overline{\rho} \overline{\kappa[S(p_{w0})]} \hat{\mathbf{e}}_3 \right\} = 0 \quad \text{on} \quad \Gamma, \tag{4.37}$$

$$\text{periodic} \quad \text{on} \quad \partial\Pi_E. \tag{4.38}$$

Equations (4.36) $-$ (4.38) can then be reduced to the two problems denoted (A) and (B),

$$\text{A} = \begin{cases} \boldsymbol{\nabla}_{\mathbf{y}} \cdot (\boldsymbol{\nabla}_{\mathbf{y}} \chi_k) = 0 \quad \text{in} \quad \Pi_S \\ \hat{\mathbf{n}} \cdot (\boldsymbol{\nabla}_{\mathbf{y}} \chi_k + \hat{\mathbf{e}}_k) = 0 \quad \text{on} \quad \Gamma \\ \text{periodic} \quad \text{on} \quad \partial\Pi_E \end{cases}, \tag{4.39}$$

$$\text{B} = \begin{cases} \boldsymbol{\nabla}_{\mathbf{y}} \cdot (\boldsymbol{\nabla}_{\mathbf{y}} \gamma_k) = 0 \quad \text{in} \quad \Pi_S \\ \hat{\mathbf{n}} \cdot (\boldsymbol{\nabla}_{\mathbf{y}} \gamma_k + \hat{\mathbf{e}}_3) = 0 \quad \text{on} \quad \Gamma \\ \text{periodic} \quad \text{on} \quad \partial\Pi_E \end{cases}, \tag{4.40}$$

for $k = 1, \ldots, 3$. Note that that (B) $=$ (A) when $k = 3$. The problems (A) and (B) are

denoted cell problems, which take into account the intrinsic repeated microscale geometry within the macroscale domain. The cell problems in this application capture the water impedance around the tubers and are used as a representative of the periodic domain. The cell problem solutions χ_k [m] and γ_k [m] in (A) and (B) are used in the final stage of the homogenisation procedure. Examples of the cell problem (A) can be seen in Figure 4.4 for tubers of varying sizes.

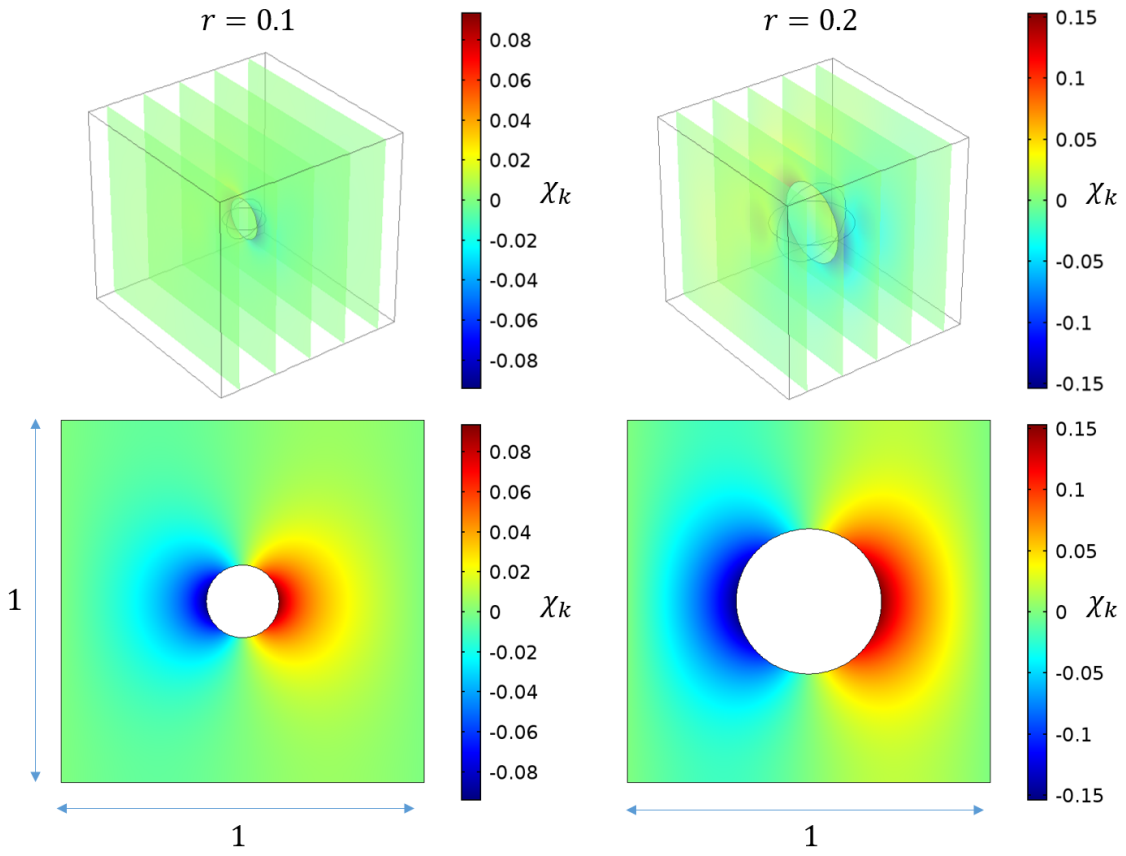

Figure 4.4: Examples of solutions to the cell problem (A) in (4.39) for the non-dimensionalised tuber radii $r = 0.1$ and $r = 0.2$. The top two images show the full solutions in three dimensions. The bottom two images show the central solution slice in two dimensions.

The final stage of the homogenisation procedure is to collect terms $\mathcal{O}(\varepsilon^0)$. This leads

to the system of equations,

$$[1-H_S(p_{w0})]\frac{\partial S(p_{w0})}{\partial p_{w0}}\frac{\partial p_{w0}}{\partial t} = \boldsymbol{\nabla}_{\mathbf{y}}\cdot\left\{\overline{\kappa[S(p_{w0})]}\left(\boldsymbol{\nabla}_{\mathbf{y}}p_{w2}+\boldsymbol{\nabla}_{\mathbf{x}}p_{w1}\right)+p_{w1}\frac{\delta\overline{\kappa}}{\delta p_w}\bigg|_{p_w=p_{w0}}\right.$$
$$\left.\left(\boldsymbol{\nabla}_{\mathbf{y}}p_{w1}+\boldsymbol{\nabla}_{\mathbf{x}}p_{w0}\right)+\left(p_{w2}\frac{\delta\overline{\kappa}}{\delta p_w}\bigg|_{p_w=p_{w0}}+\frac{1}{2}p_{w1}^2\frac{\delta^2\overline{\kappa}}{\delta p_w^2}\bigg|_{p_w=p_{w0}}\right)\boldsymbol{\nabla}_{\mathbf{y}}p_{w0}+\overline{\rho}p_{w1}\frac{\delta\overline{\kappa}}{\delta p_w}\bigg|_{p_w=p_{w0}}\hat{\mathbf{e}}_3\right\}+$$
$$\boldsymbol{\nabla}_{\mathbf{x}}\cdot\left\{\overline{\kappa[S(p_{w0})]}\left(\boldsymbol{\nabla}_{\mathbf{y}}p_{w1}+\boldsymbol{\nabla}_{\mathbf{x}}p_{w0}\right)+p_{w1}\frac{\delta\overline{\kappa}}{\delta p_w}\bigg|_{p_w=p_{w0}}\boldsymbol{\nabla}_{\mathbf{y}}p_{w0}+\overline{\rho}\overline{\kappa[S(p_{w0})]}\hat{\mathbf{e}}_3\right\}-$$
$$(\overline{p}_c p_{w0}-\overline{p}_r)\quad\text{in}\quad\Pi_S^{\infty},\quad(4.41)$$

$$\hat{\mathbf{n}}\cdot\left\{\overline{\kappa[S(p_{w0})]}\left(\boldsymbol{\nabla}_{\mathbf{y}}p_{w2}+\boldsymbol{\nabla}_{\mathbf{x}}p_{w1}\right)+p_{w1}\frac{\delta\overline{\kappa}}{\delta p_w}\bigg|_{p_w=p_{w0}}\left(\boldsymbol{\nabla}_{\mathbf{y}}p_{w1}+\boldsymbol{\nabla}_{\mathbf{x}}p_{w0}\right)+\right.$$
$$\left.\left(p_{w2}\frac{\delta\overline{\kappa}}{\delta p_w}\bigg|_{p_w=p_{w0}}+\frac{1}{2}p_{w1}^2\frac{\delta^2\overline{\kappa}}{\delta p_w^2}\bigg|_{p_w=p_{w0}}\right)\boldsymbol{\nabla}_{\mathbf{y}}p_{w0}+\overline{\rho}p_{w1}\frac{\delta\overline{\kappa}}{\delta p_w}\bigg|_{p_w=p_{w0}}\hat{\mathbf{e}}_3\right\}=0\quad\text{on}\quad\Gamma\times[0,\infty),\tag{4.42}$$

$$\text{periodic}\quad\text{on}\quad\partial\Pi_E\times[0,\infty).\tag{4.43}$$

To check equations (4.41) $-$ (4.43) provide a well-posed problem, we check the solvability of the system of equations. To check for solvability we integrate equation (4.41) over the domain Π_S,

$$\int_{\Pi_S}[1-H_S(p_{w0})]\frac{\partial S(p_{w0})}{\partial p_{w0}}\frac{\partial p_{w0}}{\partial t}\,d\Pi_S=\int_{\Pi_S}\boldsymbol{\nabla}_{\mathbf{y}}\cdot\left\{\overline{\kappa[S(p_{w0})]}\left(\boldsymbol{\nabla}_{\mathbf{y}}p_{w2}+\boldsymbol{\nabla}_{\mathbf{x}}p_{w1}\right)+\right.$$
$$p_{w1}\frac{\delta\overline{\kappa}}{\delta p_w}\bigg|_{p_w=p_{w0}}\left(\boldsymbol{\nabla}_{\mathbf{y}}p_{w1}+\boldsymbol{\nabla}_{\mathbf{x}}p_{w0}\right)+\left(p_{w2}\frac{\delta\overline{\kappa}}{\delta p_w}\bigg|_{p_w=p_{w0}}+\frac{1}{2}p_{w1}^2\frac{\delta^2\overline{\kappa}}{\delta p_w^2}\bigg|_{p_w=p_{w0}}\right)\boldsymbol{\nabla}_{\mathbf{y}}p_{w0}+$$
$$\left.\overline{\rho}p_{w1}\frac{\delta\overline{\kappa}}{\delta p_w}\bigg|_{p_w=p_{w0}}\hat{\mathbf{e}}_3\right\}d\Pi_S+\int_{\Pi_S}\boldsymbol{\nabla}_{\mathbf{x}}\cdot\left\{\overline{\kappa[S(p_{w0})]}\left(\boldsymbol{\nabla}_{\mathbf{y}}p_{w1}+\boldsymbol{\nabla}_{\mathbf{x}}p_{w0}\right)+p_{w1}\frac{\delta\overline{\kappa}}{\delta p_w}\bigg|_{p_w=p_{w0}}\right.$$
$$\left.\boldsymbol{\nabla}_{\mathbf{y}}p_{w0}+\overline{\rho}\overline{\kappa[S(p_{w0})]}\hat{\mathbf{e}}_3\right\}d\Pi_S\;-\int_{\Pi_S}(\overline{p}_c p_{w0}-\overline{p}_r)\,d\Pi_S.\quad(4.44)$$

By applying the divergence theorem to equation (4.44) and using boundary condition (4.42) we observe that,

$$\int_{\Pi_S}[1-H_S(p_{w0})]\frac{\partial S(p_{w0})}{\partial p_{w0}}\frac{\partial p_{w0}}{\partial t}\,d\Pi_S=\int_{\Pi_S}\boldsymbol{\nabla}_{\mathbf{x}}\cdot\left\{\overline{\kappa[S(p_{w0})]}\left(\boldsymbol{\nabla}_{\mathbf{y}}p_{w1}+\boldsymbol{\nabla}_{\mathbf{x}}p_{w0}\right)+\right.$$
$$\left.p_{w1}\frac{\delta\overline{\kappa}}{\delta p_w}\bigg|_{p_w=p_{w0}}\boldsymbol{\nabla}_{\mathbf{y}}p_{w0}+\overline{\rho}\overline{\kappa[S(p_{w0})]}\hat{\mathbf{e}}_3\right\}d\Pi_S\;-\int_{\Pi_S}(\overline{p}_c p_{w0}-\overline{p}_r)\,d\Pi_S.\quad(4.45)$$

We define,

$$||\cdot|| = \int_{\cdot} d\cdot, \tag{4.46}$$

and use equation (4.35) to yield,

$$||\Pi_S||[1 - H_S(p_{w0})]\frac{\partial S(p_{w0})}{\partial p_{w0}}\frac{\partial p_{w0}}{\partial t} = \int_{\Pi_S} \frac{\partial}{\partial x_i}\left\{\overline{\kappa[S(p_{w0})]}\left(\frac{\partial \chi_j}{\partial y_i}\frac{\partial p_{w0}}{\partial x_j} + \frac{\partial p_{w0}}{\partial x_i}\right) + \overline{\rho}\overline{\kappa[S(p_{w0})]}\left(\frac{\partial \gamma_k}{\partial y_i} + \hat{\mathbf{e}}_3\right)\right\} d\Pi_S \; - ||\Pi_S||(\overline{p}_c p_{w0} - \overline{p}_r) \quad \text{in} \quad \Pi_S^{\infty}, \tag{4.47}$$

where $||\Pi_S||$ is the volume integral of the cell problem.

Through algebra manipulation, equation (4.47) results in the equation for p_{w0},

$$||\Pi_S||[1 - H_S(p_{w0})]\frac{\partial S(p_{w0})}{\partial p_{w0}}\frac{\partial p_{w0}}{\partial t} = \boldsymbol{\nabla}_{\mathbf{x}} \cdot \left\{\overline{\kappa[S(p_{w0})]}\mathfrak{D}_e \boldsymbol{\nabla}_{\mathbf{x}} p_{w0} + \overline{\rho}\overline{\kappa[S(p_{w0})]}\mathfrak{K}_e\right\} - ||\Pi_S||(\overline{p}_c p_{w0} - \overline{p}_r) \quad \text{in} \quad \Pi_S^{\infty}, \tag{4.48}$$

where,

$$\mathfrak{D}_e = \int_{\Pi_S} \boldsymbol{\nabla}_{\mathbf{y}} \chi_k \otimes \hat{\mathbf{e}}_k + \mathfrak{T}\, d\Pi_S, \tag{4.49}$$

$$\mathfrak{K}_e = \int_{\Pi_S} \boldsymbol{\nabla}_{\mathbf{y}} \gamma_k + \hat{\mathbf{e}}_3\, d\Pi_S, \tag{4.50}$$

where $\mathfrak{T}\,[-]$ is the second rank identity tensor. This results identifies that equations (4.41) $-$ (4.43) provide a well-posed problem if and only if equation (4.48) has a solution.

Since $\mathfrak{K}_e = \mathfrak{D}_e \hat{\mathbf{e}}_3$, we can re-write (4.48) as,

$$||\Pi_S||[1 - H_S(p_{w0})]\frac{\partial S(p_{w0})}{\partial p_{w0}}\frac{\partial p_{w0}}{\partial t} = \boldsymbol{\nabla}_{\mathbf{x}} \cdot \left\{\overline{\kappa[S(p_{w0})]}\mathfrak{D}_e\left(\boldsymbol{\nabla}_{\mathbf{x}} p_{w0} + \overline{\rho}\hat{\mathbf{e}}_3\right)\right\} - ||\Pi_S||(\overline{p}_c p_{w0} - \overline{p}_r) \quad \text{in} \quad \Pi_S. \tag{4.51}$$

Here equation (4.51) is known as the homogenised equation for the system of equations (4.17) $-$ (4.19). Recall the relationship $p_w = p_{w0} + \varepsilon p_{w1} + \varepsilon^2 p_{w2} + \mathcal{O}(\varepsilon^3)$. The full equations (4.17) $-$ (4.19) solve for p_w, whereas the homogenised equation (4.51) solves for the leading component only, *i.e.*, p_{w0}. In order to solve the homogenised equation (4.51) however, the cell problem solutions for (A) and (B) are used to determine $\mathfrak{D}_e$ [m^2 s^{-1}] and $||\Pi_S||$ $[-]$, which capture the impedance effect from the tubers.

We observe that the homogenisation procedure has resulted in the approximate equation (4.51), which takes a similar functional form to Richards' equation, *i.e.*,

(4.17). Hence, a homogenised Richards' equation is simply another Richards' equation. This result is common to homogenisation, in which homogenised second order parabolic PDEs often result in an 'effective' second order parabolic PDE.

Theorem 4.3.2. *The parameter $\mathfrak{D}_e$ has unique values generated from the cell problem (4.39).*

Proof. Let χ_k^a and χ_k^B be solutions to (4.39) and define $\varphi_k = \chi_k^a - \chi_k^b$. We observe that φ_k satisfies the problem,

$$\begin{cases} \boldsymbol{\nabla}_{\mathbf{y}} \cdot (\boldsymbol{\nabla}_{\mathbf{y}} \varphi_k) = 0 \quad \text{in} \quad \Pi_S \\ \hat{\mathbf{n}} \cdot (\boldsymbol{\nabla}_{\mathbf{y}} \varphi_k) = 0 \quad \text{on} \quad \Gamma \\ \text{periodic} \quad \text{on} \quad \partial\Pi_E \end{cases} . \tag{4.52}$$

It follows that,

$$\int_{\Pi_S} \varphi_k \boldsymbol{\nabla}_{\mathbf{y}} \cdot (\boldsymbol{\nabla}_{\mathbf{y}} \varphi_k) \; d\Pi_S = 0. \tag{4.53}$$

Applying Green's first identity to (4.53) yields,

$$\int_{\Gamma} \varphi_k \hat{\mathbf{n}} \cdot (\boldsymbol{\nabla}_{\mathbf{y}} \varphi_k) \; d\Gamma - \int_{\Pi_S} \boldsymbol{\nabla}_{\mathbf{y}} \varphi_k \cdot (\boldsymbol{\nabla}_{\mathbf{y}} \varphi_k) \; d\Pi_S = 0, \tag{4.54}$$

using $\hat{\mathbf{n}} \cdot (\boldsymbol{\nabla}_{\mathbf{y}} \varphi_k) = 0$, (4.54) reduces to,

$$\int_{\Pi_S} ||\boldsymbol{\nabla}_{\mathbf{y}} \varphi_k||_{L^2}^2 \; d\Pi_S = 0. \tag{4.55}$$

By definition $||\cdot||_{L^2} \geq 0$, hence,

$$||\boldsymbol{\nabla}_{\mathbf{y}} \varphi_k||_{L^2}^2 \geq 0 \quad \Rightarrow \quad ||\boldsymbol{\nabla}_{\mathbf{y}} \varphi_k||_{L^2} = 0. \tag{4.56}$$

Furthermore, $||\mathbf{x}||_{L^2} = 0 \iff \mathbf{x} = 0$, hence,

$$\boldsymbol{\nabla}_{\mathbf{y}} \varphi_k = 0 \quad \Rightarrow \quad \boldsymbol{\nabla}_{\mathbf{y}} \chi_k^a = \boldsymbol{\nabla}_{\mathbf{y}} \chi_k^b. \tag{4.57}$$

Therefore (4.39) has a unique gradient of the solution $\boldsymbol{\nabla}_{\mathbf{y}} \chi_k$, *i.e.*, a unique solution χ_k with an additive constant. Since $\mathfrak{D}_e = \mathfrak{D}_e(\boldsymbol{\nabla}_{\mathbf{y}} \chi_k)$, $\mathfrak{D}_e$ is unique. □

4.4 Validation of the Homogenisation Procedure

To validate the mathematical steps used in the homogenisation procedure, we compare the homogenised equations (4.49) and (4.51) to the full set of equations

(4.17) − (4.19) for two different saturation regimes. Firstly, we consider a partially saturated soil domain, since potatoes typically grow in partially saturated soil. However, to test the homogenisation procedure, we also consider a variably saturated soil that has regions of partially and fully saturated soil to highlight that the approximate equations successfully capture a moving saturated-partially saturated interface. In each of the saturation regimes we conduct multiple comparisons by varying the parameters in the two sets of equations for four different soil types. To cover a wide range of parameters, we consider a sandy soil, a clay soil, a silt soil and a loam soil. Shown in Table 4.1 are the parameters for the different soil types.

Table 4.1: A list of the soil parameters used in the homogenisation validation for four different soil types (sand, silt, loam and clay).

Soil	ϕ	κ_s (m^2)	p_c (Pa)	m	Reference
sand	0.25	1×10^{-12}	12000	0.7	[181]
silt	0.4	5×10^{-14}	23200	0.5	[101]
loam	0.52	3×10^{-13}	8500	0.5	[101]
clay	0.4	8×10^{-16}	60000	0.2	[181]

4.4.1 Implementation

Here we describe how we utilise the finite element package COMSOL Multiphysics (COMSOL Multiphysics, Stockholm, Sweden, www.comsol.com) to solve the full and homogenised sets of equations. To solve both sets of equations we generate two geometries, one for the full set of equations (4.17) − (4.19) containing potato tubers, and a second uniform geometry for the homogenised set of equations (4.49) and (4.51). We choose the domain length of each of the geometries to be composed of eight periodic cells. The geometries can be seen in Figure 4.5, in which Ψ^{Full} denotes the geometry for the full set of equations and Ψ^{Hom} denotes the geometry for the homogenised set of equations.

Full Equations

To implement the full set of equations (4.17) − (4.19), we use the inbuilt 'General Form PDE', *i.e.*,

$$e_a \frac{\partial^2 \mathbf{r}}{\partial t^2} + d_a \frac{\partial \mathbf{r}}{\partial t} + \boldsymbol{\nabla} \cdot \boldsymbol{\Theta} = f, \tag{4.58}$$

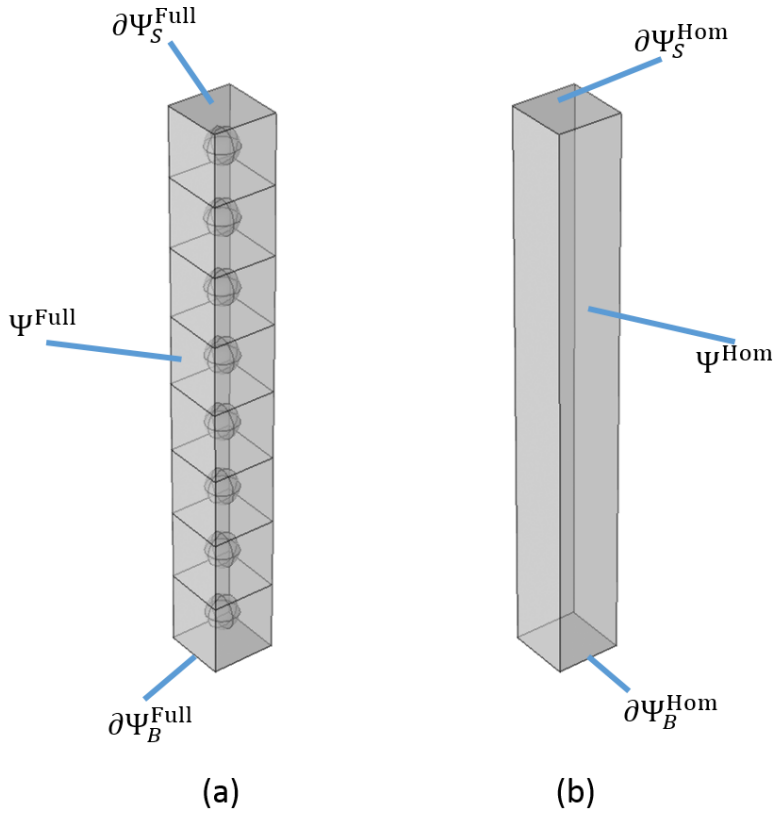

Figure 4.5: The geometries used to validate the homogenisation procedure (a): The full set of equations (4.17) − (4.19) are solved on the domain Ψ^{Full}, where $\partial\Psi_B^{\text{Full}}$ is the boundary at the base of the domain and $\partial\Psi_S^{\text{Full}}$ is the boundary on the top of the domain.
(b): The homogenised set of equations (4.49) and (4.51) are solved on the domain Ψ^{Hom}, where $\partial\Psi_B^{\text{Hom}}$ is the boundary at the base of the domain and $\partial\Psi_S^{\text{Hom}}$ is the boundary on the top of the domain.

where,

$$\mathbf{r} = p_w,\ e_a = 0,\ d_a = [1 - H_S(p_w)]\phi\frac{\partial S(p_w)}{\partial p_w},$$
$$\boldsymbol{\Theta} = \overline{\kappa[S(p_w)]}\left(\boldsymbol{\nabla} p_w + \overline{\rho}\hat{\mathbf{e}}_3\right),\ f = -(\overline{p}_c p_w - \overline{p}_r). \quad (4.59)$$

Appropriate boundary conditions are then applied to $\partial\Psi^{\text{Full}}$ depending on the saturation regime considered (see Sections 4.4.2 and 4.4.3 for details).

Homogenised Equations

To implement the homogenised set of equations (4.49) and (4.51), we also use the inbuilt 'General Form PDE' where,

$$\mathbf{r} = p_{w0},\ e_a = 0,\ d_a = ||\Pi_S||[1 - H_S(p_{w0})]\frac{\partial S(p_{w0})}{\partial p_{w0}},$$
$$\boldsymbol{\Theta} = \overline{\kappa[S(p_{w0})]}\mathfrak{D}_e\left(\boldsymbol{\nabla}_{\mathbf{x}} p_{w0} + \overline{\rho}\hat{\mathbf{e}}_3\right),\ f = -||\Pi_S||(\overline{p}_c p_{w0} - \overline{p}_r). \quad (4.60)$$

Appropriate boundary conditions are then applied to $\partial\Psi^{\text{Hom}}$ depending on the saturation regime considered.

To parameterise the homogenised equations we are also required to solve the cell problem (4.39) for a given radius r to calculate $||\Pi_S||$ and $\mathfrak{D}_e$. This involves solving three different cell problems for $k = 1, \ldots, 3$, *i.e.*, for each of the three spatial components x_1, x_2 and x_3.

To solve the cell problem, we use the inbuilt 'General Form PDE' for the governing equation where,

$$\mathbf{r} = \chi_k,\ e_a = 0,\ d_a = 0, \boldsymbol{\Theta} = \boldsymbol{\nabla}_{\mathbf{y}}\chi_k,\ f = 0, \quad (4.61)$$

for $k = 1, \ldots, 3$.

For the boundary condition on Γ, *i.e.*, the tuber, we use the inbuilt flux boundary condition that takes the form,

$$\hat{\mathbf{n}} \cdot \boldsymbol{\Theta} = g_1 - g_2\mathbf{r}, \quad (4.62)$$

where $g_1 = -\hat{\mathbf{n}} \cdot \hat{\mathbf{e}}_k$ and $g_2 = 0$.

On the external boundaries of the cell $\partial\Pi_E$ we impose three sets of 'Periodic Boundary Conditions', so that each pair of opposite external boundaries are an effective continuum. Furthermore, since (4.39) has a non-unique solution (see Theorem 4.3.2), we are required to impose a 'Pointwise Constraint' such that we allow COMSOL to pick an arbitrary solution. Since $||\Pi_S||$ does not depend the solution and $\mathfrak{D}_e$ uses the gradient of the solution (which is unique), allowing the software to choose a solution does not affect the final result.

4.4.2 Partially Saturated Regime

To test the homogenisation procedure for a partially saturated soil regime, we simulate the wetting of dry soil from a shallow water table at the base of the domains Ψ^{Hom} and Ψ^{Full}. To do this, we impose the following boundary and initial

conditions: on the boundaries Ψ_B^{Hom} and Ψ_B^{Full}, we impose the boundary condition,

$$p_w = -0.5 \quad \text{on} \quad \partial\Psi_B^{\text{Full}} \times [0, \infty), \tag{4.63}$$

$$p_{w0} = -0.5 \quad \text{on} \quad \partial\Psi_B^{\text{Hom}} \times [0, \infty), \tag{4.64}$$

which equates to the dimensional pressure of $\tilde{p}_w \approx -10,000$ Pa (equating to a saturation of $S \approx 0.9$), *i.e.*, simulating a shallow water table at the base of the two domains. On all other boundaries we impose a zero flux boundary condition, *i.e.*,

$$\hat{\mathbf{n}} \cdot \left\{ \overline{\kappa[S(p_w)]} \left(\boldsymbol{\nabla} p_w + \overline{\rho} \hat{\mathbf{e}}_3 \right) \right\} = 0 \quad \text{on} \quad \partial\Psi^{\text{Full}} \setminus \partial\Psi_B^{\text{Full}} \times [0, \infty), \tag{4.65}$$

$$\hat{\mathbf{n}} \cdot \left\{ \overline{\kappa[S(p_{w0})]} \mathfrak{D}_e \left(\boldsymbol{\nabla}_{\mathbf{x}} p_{w0} + \overline{\rho} \hat{\mathbf{e}}_3 \right) \right\} = 0 \quad \text{on} \quad \partial\Psi^{\text{Hom}} \setminus \partial\Psi_B^{\text{Hom}} \times [0, \infty). \tag{4.66}$$

Finally, in Ψ^{Hom} and Ψ^{Full} we impose the initial condition,

$$p_w|_{t=0} = -2 \quad \text{in} \quad \Psi^{\text{Full}} \times \{t = 0\}, \tag{4.67}$$

$$p_{w0}|_{t=0} = -2 \quad \text{in} \quad \Psi^{\text{Hom}} \times \{t = 0\}, \tag{4.68}$$

which equates to the dimensional pressure of $\tilde{p}_w \approx -40,000$ Pa (equating to a saturation of $S \approx 0.3$). Furthermore, we choose a non-dimesionalised tuber radius of $r = 0.025$. This equates dimensionally to a radius of 1.3 cm, *i.e.*, a diameter of 2.6 cm. Additionally, the side length of the cell surrounding each tuber is 5.2 cm, leading to a dimensional cell volume of 140.608 cm^3. This tuber size is typical for early season tubers, since potato tubers can grow substantially larger. We choose this radius to highlight that even for small tuber radii, there is a notable effect on water movement in soil from the influence of tuber impedance.

Shown in Figure 4.6 are the non-dimensional pressure solutions for the homogenised and full sets of equations at the time point $t = 2.78$, which equates dimensionally to one day after the start of the simulation. For all four soil types, we observe that the two sets of solutions for p_w (full) and p_{w0} (homogenised) are qualitatively identical. We find there to be a maximum error of $\lesssim 2\%$ between the two sets of solutions. However, the loam and clay profiles show small differences between the full and homogenised solutions. This is due to the soil parameters of the loam and clay soils. We note from homogenisation theory that $p_{w0} \to p_w$ as $\varepsilon \to 0$, *i.e.*, the two solutions converge as the micro to macro ratio decreases. As a result of the slow water mobility in the clay and loam soils, the infiltration of water from the base of the domain covers a maximum of three cells, hence ε is relatively large, and therefore the error is larger when compared to the sand and silt soil

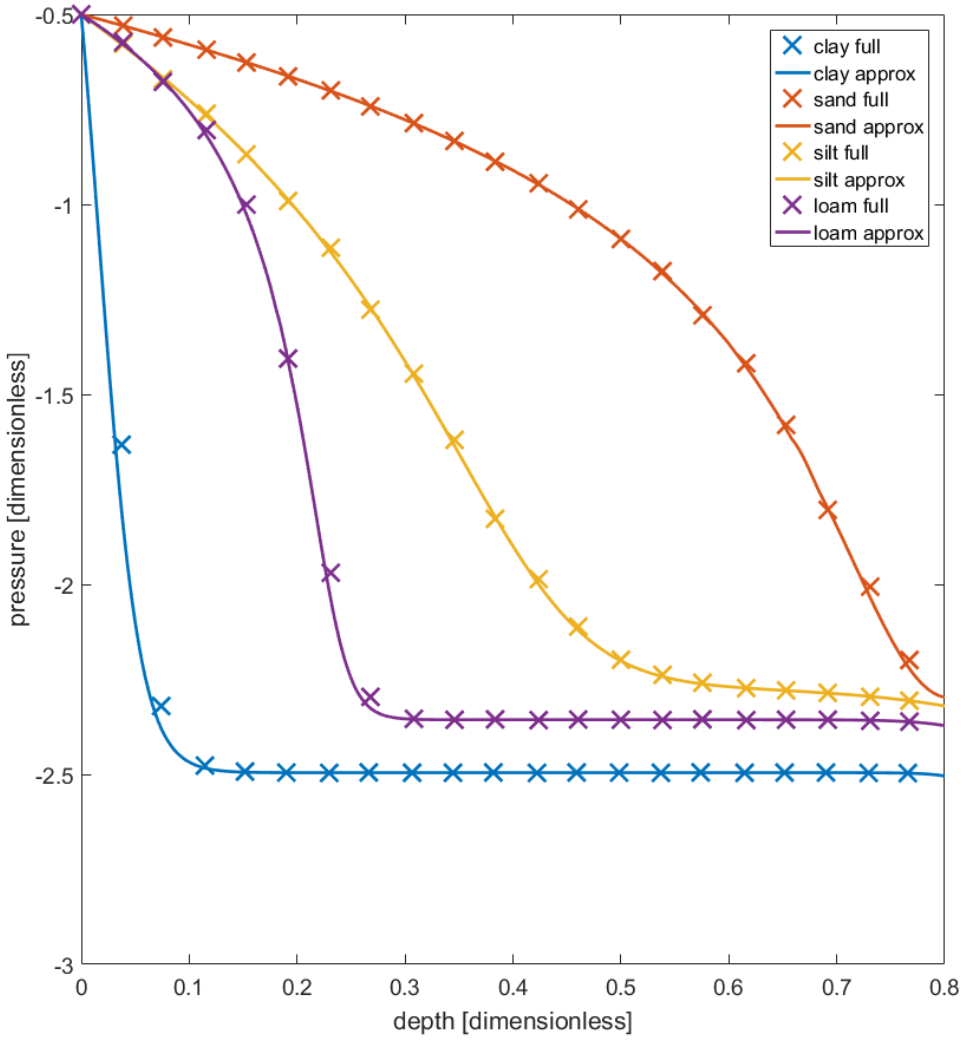

Figure 4.6: Validation of homogenised equations (4.49) and (4.51) against the original set of equations (4.17) $-$ (4.19) in a partially saturated soil regime. The plot shows the solutions to the two sets of equations for the simulations described by equations (4.63) $-$ (4.68) at the time point $t = 2.78$, which equates dimensionally to one day. There are multiple comparisons for four different soil types, these being clay, sand, silt and loam type soils.

profiles, where the water penetrates substantially further. However, if we asses the pressure profiles in the clay and loam soils at a later time period in which the water infiltrates further into the soil, we observe that the error between the two solutions becomes smaller and similar to the sand and silt soils.

We find that the full set of equations (4.17) $-$ (4.19) in three dimensions requires ≈ 100 seconds to solve one simulation for eight periodic cells. Conversely, solving the homogenised equations (4.49) and (4.51) requires ≈ 3 seconds to solve an

analogous 3D problem. Furthermore, the homogenised set of equations can be reduced to a 1D problem, which will achieve the same results as the 3D problem due to the homogenisation procedure. We find that the computation time to solve the 1D problem is $\ll 1$ second, which is substantially faster than the full set of equations.

Although, a cell problem is required to parameterise equation (4.51) via the terms $||\Pi_S||$, $\mathfrak{D}_e$ and $\mathfrak{K}_e$. The cell problem requires ≈ 3 seconds to solve and is only required to be solved once for each radius tuber r. Hence, the homogenised set of equations can considerably reduce the computation time whilst retaining a high level of accuracy for partially saturated soil domains.

4.4.3 Variably Saturated Regime

To test the homogenisation procedure for a variably saturated soil regime, we simulate water movement in the domains Ψ^{Hom} and Ψ^{Full} due to wetting from a shallow water table at the base of the domains, and infiltration from constant ponding on the soil surface. The pond on the soil surface will create a zone of fully saturated soil which will have a moving interface with the partially saturated soil region.

To replicate these conditions, we impose the following boundary and initial conditions: on the boundaries Ψ_B^{Hom} and Ψ_B^{Full}, we impose the boundary condition,

$$p_w = -0.5 \quad \text{on} \quad \partial\Psi_B^{\text{Full}} \times [0, \infty), \tag{4.69}$$

$$p_{w0} = -0.5 \quad \text{on} \quad \partial\Psi_B^{\text{Hom}} \times [0, \infty), \tag{4.70}$$

which equates to the dimensional pressure of $\tilde{p}_w \approx -10,000$ Pa (equating to a saturation of $S \approx 0.9$), *i.e.*, simulating a shallow water table at the base of the two domains.

On the boundaries Ψ_S^{Hom} and Ψ_S^{Full}, we impose the boundary condition,

$$p_w = -0.05 \quad \text{on} \quad \partial\Psi_S^{\text{Full}} \times [0, \infty), \tag{4.71}$$

$$p_{w0} = -0.05 \quad \text{on} \quad \partial\Psi_S^{\text{Hom}} \times [0, \infty), \tag{4.72}$$

which equates to the dimensional pressure of $\tilde{p}_w \approx 1,000$ Pa, *i.e.*, simulating a pond of ≈ 10 cm on the surface of each of the domains. On all other boundaries we impose a zero flux boundary condition, *i.e.*,

$$\hat{\mathbf{n}} \cdot \left\{ \overline{\kappa[S(p_w)]} \left(\boldsymbol{\nabla} p_w + \overline{\rho} \hat{\mathbf{e}}_3 \right) \right\} = 0 \quad \text{on} \quad \partial\Psi^{\text{Full}} \setminus \left(\partial\Psi_B^{\text{Full}} \cap \partial\Psi_S^{\text{Full}} \right) \times [0, \infty), \tag{4.73}$$

$$\hat{\mathbf{n}} \cdot \left\{ \overline{\kappa[S(p_{w0})]} \mathfrak{D}_e \left(\boldsymbol{\nabla}_{\mathbf{x}} p_{w0} + \overline{\rho} \hat{\mathbf{e}}_3 \right) \right\} = 0 \quad \text{on} \quad \partial\Psi^{\text{Hom}} \setminus \left(\partial\Psi_B^{\text{Hom}} \cap \partial\Psi_S^{\text{Hom}} \right) \times [0, \infty). \tag{4.74}$$

Finally, in Ψ^{Hom} and Ψ^{Full} we impose the initial condition,

$$p_w|_{t=0} = -1 \quad \text{in} \quad \Psi^{\text{Full}} \times \{t = 0\}, \tag{4.75}$$

$$p_{w0}|_{t=0} = -1 \quad \text{in} \quad \Psi^{\text{Hom}} \times \{t = 0\}, \tag{4.76}$$

which equates to the dimensional pressure of $\tilde{p}_w \approx -40,000$ Pa (equating to a saturation of $S \approx 0.3$).

Shown in Figure 4.7 are the non-dimensional pressure solutions for the homogenised and full sets of equations at the time point $t = 2.78$ (equating dimensionally to 1 day) for the variably saturated soil regime described by equations (4.69) $-$ (4.76). For all four soil types, we find there to be a maximum error of $\lesssim 1\%$ between the two sets of solutions. We observe that the homogenisation procedure successfully captures the moving saturated-partially saturated interface, whilst retaining a high level of accuracy for a large range of soil parameters. Again, we find that the full set of equations (4.17) $-$ (4.19) in three dimensions requires ≈ 120 seconds to solve one simulation for eight periodic cells. Conversely, solving the homogenised equations (4.49) $-$ (4.51) requires ≈ 3 seconds to solve an analogous 3D problem.

To highlight the accuracy of the homogenisation procedure and the influence of tubers on water movement, shown in Figure 4.8 is a comparison of the dimensionless pressure profiles for the sandy soil under partially saturated conditions. In Figure 4.8 (a) we impose the full set of equations (4.17) $-$ (4.19) in the full geometry and the homogenised geometry. We observe that the pressure profiles in each of the geometries is different due to the presence of the tubers. Hence, we cannot simply apply the original equations in the subdomain that contains tubers. In Figure 4.8 (b) we impose the full set on the full geometry and the homogenised set on the homogenised geometry. This allows us to clearly identify that the homogenised system of equations captures this phenomena.

From the results shown in Figures 4.6 and 4.7, we observe that there is a maximum error between the full set of equations and approximate equations of $\lesssim 2\%$. However, we observe there to be a difference of $\mathcal{O}(10^2)$ in computation time between the two sets of equations. Therefore, we find that the homogenised set of equations can reduce the computation time significantly whilst retaining a high level of accuracy.

In the soil region $\tilde{\Lambda}_U$ in Figure 2.2, we are able impose the homogenised set of

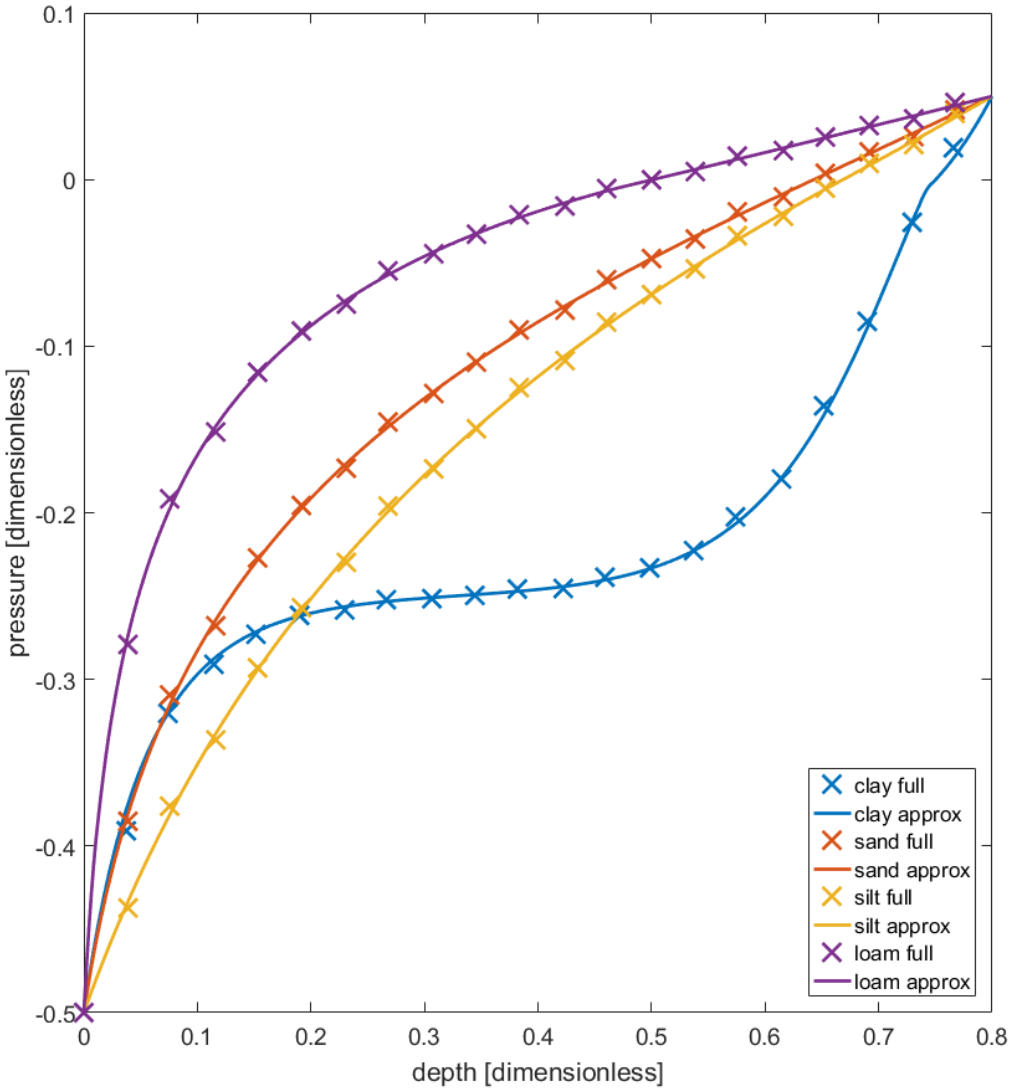

Figure 4.7: Validation of homogenised equations (4.49) and (4.51) against the original set of equations (4.17) – (4.19) in a variably saturated soil regime. The plot shows the solutions to the two sets of equations for the simulation described in equations (4.69) – (4.76) at the time point $t = 2.78$, which equates dimensionally to 1 day. There are multiple comparisons for four different soil types, these being clay, sand, silt and loam type soils.

equations (4.49) and (4.51) to capture the water impedance from potato tubers in the plough layer of soil. This can then be coupled to equations (2.16) – (2.18) for the soil region $\tilde{\Lambda}_A$. Providing knowledge of the potato radius and inter-tuber distance is known, this will allow us to accurately model the average infiltration of water in the ridges of the system without requiring substantial computational power to model each individual tuber in the soil.

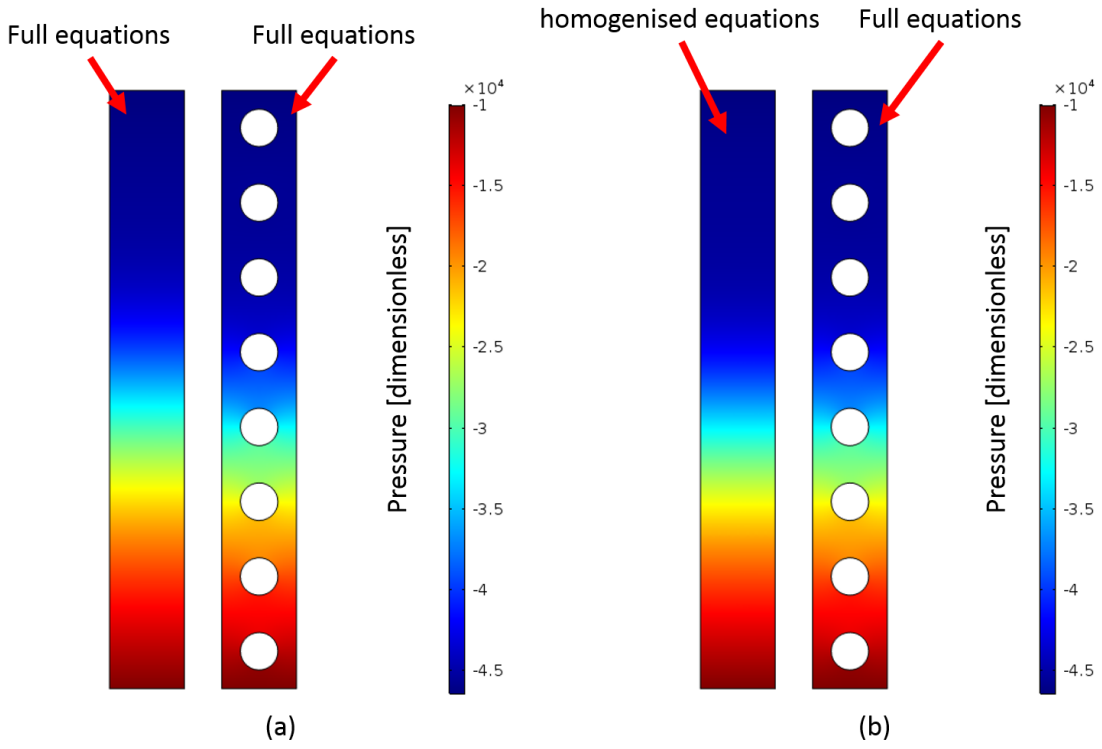

Figure 4.8: Two-dimensional pressure profiles for a sandy soil under partially saturated conditions. (a): The full set of equations (4.17) – (4.19) are solved on both domains Ψ^{Full} and Ψ^{Hom}.
(b): The homogenised set of equations (4.49) and (4.51) are solved on the domain Ψ^{Hom}, and the full set of equations (4.17) – (4.19) are solved on the full domain Ψ^{Full}.

4.5 Conclusions

In this chapter, we derived a model for water movement in variably saturated soil in the plough layer in which crops are planted, grown and harvested. Using the method of multiple scale homogenisation, we developed a set of approximate equations to capture the impedance of water movement in the plough layer due to the influence of crops. This allows us to directly obtain the macroscale properties of the system without requiring all the intrinsic detail of the soil structure.

To validate the homogenisation procedure, we compared the full set of equations for water movement around tubers in soil to the approximate set of equations. We ran simulations for four different soil types for two different saturation regimes. We found there to be a maximum difference between the solutions of $\lesssim 2\%$. However, we observed that the approximate equations were faster by a factor of $\mathcal{O}(10^2)$ for a 3D problem. The difference between the two computation times could be increased,

since the homogenised set of equations can be solved on a 1D domain to achieve the same solution.

The homogenised set of equations can then be imposed in the plough layer subdomain $\tilde{\Lambda}_U$ and coupled to the remaining soil $\tilde{\Lambda}_A$ for the model presented in Chapter 2. This will allow us to develop a system of equations that describes water movement through the soil, whilst capturing the impedance of water movement due to the crops forming in the ridges of the ridge and furrow soil.

Chapter 5

Multiple Scale Homogenisation of Crop Growth

In this chapter, we build on the ideas in Chapter 4 and use multiple scale homogenisation to derive a set of averaged macroscale equations, which describe the movement of nutrients in partially saturated soil that contains growing potato tubers. The soil is modelled as a poroelastic material, which is deformed by the growth of the tubers. The growth of each tuber is assumed to be dependent on the uptake of nutrients via a sink term within the soil representing nutrient uptake by roots. To validate the homogenisation procedure, we compare the system of homogenised equations to the original set of equations and find that the solutions between the two models differ by $\lesssim 2\%$. As in Chapter 4, we find that the computation time between the two sets of equations differs by several orders of magnitude. This is because the equations imposed on the dynamic three-dimensional geometry, which captures tuber growth and soil deformation, are simplified by homogenisation to a coupled set of one dimensional ODEs and PDEs.

5.1 Introduction

In each of the previous chapters we considered the soil to be a static porous structure that remained unchanged. As such, the entire soil domain was governed by a set of constant parameters, *i.e.*, hydraulic conductivity, porosity and saturated permeability. However, it is well known that soil is a heterogeneous medium due to the distribution of soil particles and water/air filled pores [23]. The distributions of these soil components can be due to natural heterogeneities in the soil or due to an external influence, *i.e.*, soil compression [182].

A key factor that affects the local properties of soil in the plough layer is the influence from the growth and development of crops. In Chapter 4 we incorporated potato tubers into the soil domain $\tilde{\Lambda}_U$. We assumed they were a constant size, since potato tuber size remains approximately constant on the timescale of water transport. However, throughout an entire growing season, the growth of crops will compress the soil within and immediately adjacent to the crop zone, leading to a change in the local porosity and other soil properties. These changes will affect dynamic soil processes, *i.e.* transport of nutrients. In this chapter, we explore the effects of crop growth and how this influences soil properties.

To capture the influence of crop growth, we no longer consider the soil domain to be static. Rather, we model the soil a poroelastic medium [183]. The behaviour of poroelastic materials are governed by the phenomena that couples the solid and fluid components of the material, in which either a change in the solid matrix results in a change in fluid pressure (or mass), or a change in fluid pressure results in a change in the volume of the solid matrix [184].

The topic of poroelasticity has been studied in a wide range of scientific fields, since poroelastic theory has been used to successfully model a wide range of applications including: the internal mechanics of bone, specifically for deformation of bone tissue due to bone fluid [185, 186], the properties of fluid movement in rocks and anisotropic geological media [187, 188], and cells and their constituent parts such as cytoplasm [189, 190].

Standard theory for linear poroelasticity is based on Biot's original paper for consolidation of soils entitled 'General Theory of Three-Dimensional Consolidation' [191]. This work was published in 1941 and developed mathematical theory for the settlement of soils due to consolidation, which is synonymous with the squeezing of liquid out of a porous medium that has elastic properties [191]. The governing equations for linear poroelasticity are derived from coupling Darcy flow with linear constitutive equations, to form a time-dependent relationship between the deformation of the solid matrix and fluid pore pressure [184].

The governing poroelastic equations for a two-phase material (solid matrix and fully saturated fluid) are given by [192],

$$\boldsymbol{\nabla} \cdot (\partial_t \mathbf{u}_s) = \frac{\mathfrak{K}}{\mu} \boldsymbol{\nabla} \cdot (\boldsymbol{\nabla} p_w) - q, \tag{5.1}$$

$$\boldsymbol{\nabla} \cdot \mathfrak{G} = 0, \tag{5.2}$$

where $\mathbf{u}_s$ [m] is the displacement of the solid matrix, μ [Pa s^{-1}] is the fluid viscosity, p_w [Pa] is the fluid pore pressure, q [s^{-1}] is a fluid sink term, $\mathfrak{K}$ [m^2] is the

permeability tensor of the porous medium and $\mathfrak{G}$ [Pa] is the stress tensor. Equations (5.1) and (5.2) are coupled together to form a relationship between fluid pressure and the stress on the medium. Biot's equations for poroelastic materials have been used successfully to model a wide range of materials including but not limited to: modelling tumour growth and development [193], compaction of soils [177] and fluid transport in biological tissues [192].

In this chapter, we model the growth of potato tubers in soil. We assume that the growth is dependent on the quantity of nutrients the plant is able to draw up from the soil. Subsequently, any growth from a single crop will influence the water content adjacent to the plant and therefore the movement of nutrients in the vicinity, since from Chapter 3 we found that solute movement is heavily influenced by water content.

Equations (5.1) and (5.2) describe the interaction between a two-phase poroelastic material that contains a solid matrix and a fluid component. However, partially saturated soil is a three-phase poroelastic material that contains a solid matrix representing the solid minerals, a fluid representing water and a fluid representing air. Hence, equations (5.1) and (5.2) cannot be directly applied to the system we aim to model. Therefore, we construct a model from first principles coupling the constituent equations for the three-phases with Darcy's law to derive a model for a three-phase poroelastic material.

Using a similar approach to the methodology in Chapter 4, we aim to apply the technique of multiple scale homogenisation. This will allow us to develop a macroscale model that captures the global movement of nutrients in soil and uptake from plants, and subsequent growth of the potato tubers. Applying this method to the system described will require homogenising a moving boundary problem, since the microscale domain containing the tubers will change depending on the nutrient uptake and growth of each tuber.

Rigorous homogenisation theory for two-scale convergence of moving interfaces has been increasingly studied in recent years, with particular focus on first and second order partial differential equations [194, 195]. One application using homogenisation of moving interfaces is the periodic solidification (transfer from a liquid/gas to a solid) of periodic heterogeneous materials [196, 197]. This incorporates a microscale moving interface that separates a solid domain and fluid domain with a flux discontinuity on the interface. We aim to implement similar protocols to describe the moving interface of the potato tubers as they grow and compress the poroelastic soil.

For simplicity we choose to model the tubers as spherical objects in soil, however,

this can be extended to any 3D geometry, including, but not limited to, ovoids, capsules and cylinders. There have been recent models derived using homogenisation that model the diffusion of a species with spatially varying spheres in porous media [178]. However, in these cases the local porosity is approximated using Rayleigh's multipole method to determine a spatially dependent effective diffusion coefficient based on the size of the sphere within the microscopic periodic geometry [198]. This relies on underlying assumptions that ignore the poroelastic properties of the material. Instead it is assumed that the solid matrix is incompressible. Hence, it is inferred that the local porosity is a ratio of available space to a constant solid fraction. Here we extend this idea to model both spatially and temporally varying objects in poroelastic media, which are coupled to the diffusion of the species within the material itself.

To validate the homogenisation procedure, we compare the solution of the homogenised equations against the full system for a series of case studies. This shows that the homogenised equations successfully capture the 'effective' growth of the tubers and the change in nutrient diffusion from the reduction of volume within the domain.

5.2 Theory

5.2.1 Three-Phase Poroelastic Soils

Let $\tilde{\Psi} \subset \mathbb{R}^3$ [m^3] be an open bounded subset representing a soil system (see Figure 5.1 (a)) that contains $N \in \mathbb{N}$ potato tubers. We define $\tilde{\Psi} = \left(\sum_{j=1}^{N} \tilde{\Psi}_{S_j}\right) \cup \left(\sum_{j=1}^{N} \tilde{\Psi}_{p_j}\right)$, where $\sum_{j=1}^{N} \tilde{\Psi}_{S_j} = \tilde{\Psi}_S$ [m^3] is the deformable poroelastic soil domain that is composed of water, air and solid components, and $\tilde{\Psi}_{p_j}$ [m^3] are the $j = 1, \ldots, N$ tubers each with a boundary $\tilde{\Gamma}_j$ [m^2].

To describe the deformable poroelastic soil domain $\tilde{\Psi}_S$, we impose a system of equations that describe a three-phase poroelastic material. To derive the system of equations, we use conservation laws for mass and momentum. The conservation of mass equations for the three phases of air, water and soil solid are,

$$\partial_{\tilde{t}} \phi_a = -\tilde{\boldsymbol{\nabla}} \cdot (\phi_a \tilde{\mathbf{v}}_a) \quad \text{in} \quad \tilde{\Psi}_S^{\infty}, \tag{5.3}$$

$$\partial_{\tilde{t}} \phi_w = -\tilde{\boldsymbol{\nabla}} \cdot (\phi_w \tilde{\mathbf{v}}_w) - \lambda_c(\tilde{p}_w - p_r) \quad \text{in} \quad \tilde{\Psi}_S^{\infty}, \tag{5.4}$$

$$\partial_{\tilde{t}} \phi_s = -\tilde{\boldsymbol{\nabla}} \cdot (\phi_s \tilde{\mathbf{v}}_s) \quad \text{in} \quad \tilde{\Psi}_S^{\infty}, \tag{5.5}$$

$$\phi_a + \phi_w + \phi_s = 1, \tag{5.6}$$

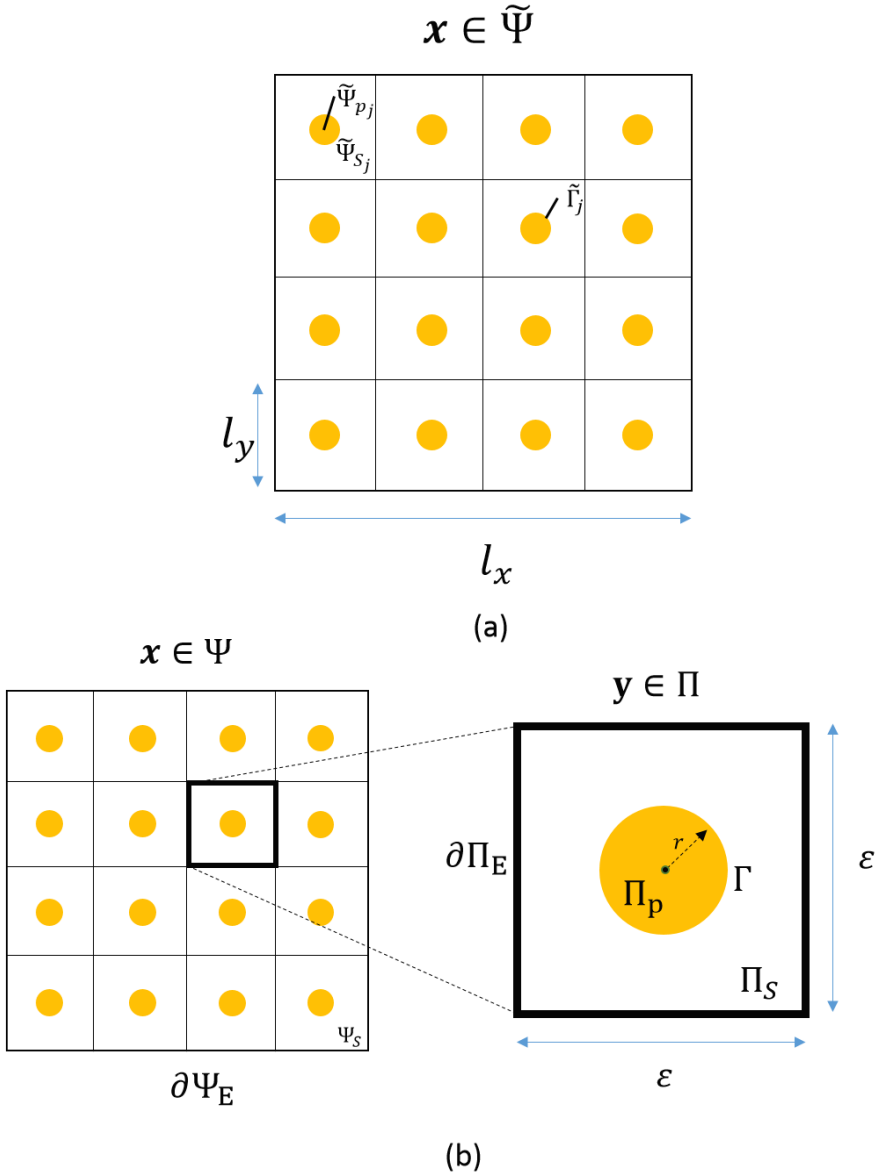

Figure 5.1: (a): Schematic of a dimensional poroelastic domain, where $\tilde{\Psi}$ is the total domain, $\tilde{\Psi}_S$ is the deformable poroelastic soil domain, $\tilde{\Psi}_{p_j}$ are the potato tubers, $\tilde{\Psi}_{S_j}$ is the poroelastic soil subdomains adjacent to each tuber and $\tilde{\Gamma}_j$ are the boundaries between $\tilde{\Psi}_{p_j}$ and $\tilde{\Psi}_S$. In addition, l_x is the macroscale and l_y is the microscale.
(b): Schematic of the dimensionless macroscale domain Ψ and microscale domain Π, where Ψ_S is the poroelastic soil domain, $\partial\Psi_E$ is the external boundary of Ψ, Π_S is the microscale poroelastic soil domain, Π_p is a tuber, Γ is the boundary between Π_S and Π_p, $\partial\Pi_E$ is the external boundary of the periodic cell and r is the radius of Π_p.

where $\phi_a : \tilde{\Psi}_S \times [0,\infty) \to [0,1]\ [-]$ is the volumetric air content, *i.e.*, the volume of air per volume of soil, $\phi_w : \tilde{\Psi}_S \times [0,\infty) \to [0,1]\ [-]$ is the volumetric water content, *i.e.*, the volume of water per volume of soil, $\phi_s : \tilde{\Psi}_S \times [0,\infty) \to [0,1]\ [-]$ is the volumetric soil solid content, *i.e.*, the volume of soil solid per volume of soil,
$\tilde{p}_w : \tilde{\Psi}_S \times [0,\infty) \to \mathbb{R}$ [Pa] is the soil water pore pressure,
$\tilde{\mathbf{v}}_a : \tilde{\Psi}_S \times [0,\infty) \to \mathbb{R}^3$ [m s^{-1}] is the air velocity, $\tilde{\mathbf{v}}_w : \tilde{\Psi}_S \times [0,\infty) \to \mathbb{R}^3$ [m s^{-1}] is the

water velocity, $\tilde{\mathbf{v}}_s : \tilde{\Psi}_S \times [0,\infty) \to \mathbb{R}^3$ [m s^{-1}] is the velocity of the soil solid component, $\lambda_c \in \mathbb{R}_{\geq 0}$ [Pa^{-1} s^{-1}] is the product of the root surface area density and the water conductivity of the root cortex, and $p_r \in \mathbb{R}_{\leq 0}$ [Pa] is the pressure in the root xylem. The conservation of momentum equation is [184],

$$\tilde{\boldsymbol{\nabla}} \cdot \left\{ G \left[\left(\tilde{\boldsymbol{\nabla}} \tilde{\mathbf{u}}_s \right) + \left(\tilde{\boldsymbol{\nabla}} \tilde{\mathbf{u}}_s \right)^T + \frac{\nu}{1-2\nu} \tilde{\boldsymbol{\nabla}} \cdot \tilde{\mathbf{u}}_s \mathfrak{T} \right] - \zeta \tilde{p}_w \mathfrak{T} - \tilde{p}_a \mathfrak{T} \right\} = 0 \quad \text{in} \quad \tilde{\Psi}_S^{\infty}, \tag{5.7}$$

where $\tilde{\mathbf{u}}_s : \tilde{\Psi}_S \times [0,\infty) \to \mathbb{R}^3$ [m] is the displacement of the solid component, $\tilde{p}_a : \tilde{\Psi}_S \times [0,\infty) \to \mathbb{R}$ [Pa] is the soil air pore pressure, $G \in \mathbb{R}_{>0}$ [Pa] is the shear modulus of the soil, $\nu \in [0, 0.5]$ [$-$] is the Poisson ratio and $\zeta \in \mathbb{R}_{>0}$ [$-$] is the effective ratio between the air and water phases. The displacement $\tilde{\mathbf{u}}_s$ is related to $\tilde{\mathbf{v}}_s$ by the relationship,

$$\tilde{\mathbf{v}}_s = \partial_{\tilde{t}} \tilde{\mathbf{u}}_s. \tag{5.8}$$

Furthermore, Darcy's law for the relative phase velocity of air and water is written as,

$$\phi_a \left(\tilde{\mathbf{v}}_a - \tilde{\mathbf{v}}_s \right) = -\frac{\kappa_a}{\mu_a} \tilde{\boldsymbol{\nabla}} \tilde{p}_a \quad \text{in} \quad \tilde{\Psi}_S^{\infty}, \tag{5.9}$$

$$\phi_w \left(\tilde{\mathbf{v}}_w - \tilde{\mathbf{v}}_s \right) = -\frac{\kappa_w}{\mu_w} \tilde{\boldsymbol{\nabla}} \tilde{p}_w \quad \text{in} \quad \tilde{\Psi}_S^{\infty}, \tag{5.10}$$

where $\kappa_a \in \mathbb{R}_{>0}$ [s^{-1}] and $\kappa_w \in \mathbb{R}_{>0}$ [s^{-1}] are the air and water permeabilities respectively, and $\mu_a \in \mathbb{R}_{>0}$ [Pa s^{-1}] and $\mu_w \in \mathbb{R}_{>0}$ [Pa s^{-1}] are the viscosities of air and water respectively. In equations (5.9) and (5.10) we assume that air and water are independent on the pore scale, *i.e.*, air and water move freely.

The air and water pressures $\tilde{p}_a$ and $\tilde{p}_w$, and the air and water fractions ϕ_a and ϕ_w are related via the van Genuchten saturation expression [101],

$$\frac{\phi_w}{\phi_w + \phi_a} = \left[\left(\frac{\tilde{p}_a - \tilde{p}_w}{p_c} \right)^{\frac{1}{1-m}} + 1 \right]^{-m}, \tag{5.11}$$

where $p_c \in \mathbb{R}_{>0}$ [Pa] is the characteristic suction pressure and $m \in [0,1]$ [$-$] is the van Genuchten parameter. The system of equations (5.3) $-$ (5.11) completes a full description of a three-phase poroelastic soil.

5.2.2 Diffusion of Nutrients in Soil

To describe nutrient movement in the poroelastic domain $\tilde{\Psi}_S$, we recall the model for solute movement from Chapter 3, *i.e.*, equation (3.9),

$$(\phi_w + b)\partial_{\tilde{t}}\tilde{c} + \tilde{c}\partial_{\tilde{t}}\phi_w = \tilde{\boldsymbol{\nabla}} \cdot \left(D\phi_w \tilde{\boldsymbol{\nabla}}\tilde{c}\right) - \xi\tilde{c} \quad \text{in} \quad \tilde{\Psi}_S^{\infty}. \tag{5.12}$$

where $\tilde{c} : \tilde{\Psi}_S \times [0,\infty) \to \mathbb{R}_{\geq 0}$ [kg m^{-3}] is the nutrient concentration in pore water, $b \in \mathbb{R}_{\geq 0}$ [$-$] is the nutrient buffer power, $D \in \mathbb{R}_{>0}$ [m^2 s^{-1}] is the diffusion coefficient and $\xi \in \mathbb{R}_{\geq 0}$ [s^{-1}] is the nutrient uptake rate from plant roots. Equation (5.12) is coupled to (5.3) $-$ (5.11) to construct a complete system describing nutrient movement in a poroelastic medium.

5.2.3 Boundary Conditions

Here we define a series of boundary conditions on the interfaces $\tilde{\Gamma}_j$, *i.e.*, between the deformable poroelastic soil domain $\tilde{\Psi}_S$ and the potato tubers $\tilde{\Psi}_{p_j}$. To describe the nutrient interaction on $\tilde{\Gamma}_j$ we impose a zero flux condition, since potato tubers do not take up nutrients, *i.e.*,

$$\hat{\mathbf{n}} \cdot \left(D\phi_w \tilde{\boldsymbol{\nabla}}\tilde{c}\right) = 0 \quad \text{on} \quad \tilde{\Gamma}_j \times [0,\infty), \tag{5.13}$$

where $\hat{\mathbf{n}} : \mathbb{R}^3 \times [0,\infty) \to \mathbb{R}^3$ [$-$] is the unit normal vector pointing out of the geometry. Furthermore, on $\tilde{\Gamma}_j$ we assume the soil solid is displaced normally to the direction of the growing tuber and has no tangential velocity, hence,

$$(2\hat{\mathbf{n}} \otimes \hat{\mathbf{n}} - \mathfrak{T}) \cdot \tilde{\mathbf{u}}_s = \hat{\mathbf{n}}\tilde{\Xi}_j \quad \text{on} \quad \tilde{\Gamma}_j \times [0,\infty), \tag{5.14}$$

where $\tilde{\Xi}_j \geq 0$ [m] is the displacement of tuber j given by,

$$\tilde{\Xi}_j = \tilde{r}_j - r^*, \tag{5.15}$$

where $r^* \in \mathbb{R}_{>0}$ [m] is the initial radius of the tuber and $\tilde{r}_j : [0,\infty) \to \mathbb{R}_{\geq r^*}$ [m] is the radius of the j^{th} tuber, which is related to the total amount of nutrients taken up by the roots. The growth of each tuber is expressed as,

$$\partial_{\tilde{t}}\tilde{V}_j = \alpha \int_{\tilde{\Psi}_{S_j}} \xi\tilde{c}\, d\tilde{\Psi}_{S_j}, \tag{5.16}$$

where $\tilde{V}_j$ [m^3] is the tuber volume, $\xi \in \mathbb{R}_{\geq 0}$ [s^{-1}] is the nutrient uptake rate from plant roots, $\alpha \in \mathbb{R}_{>0}$ [m^3 kg^{-1}] is the ratio between the rate of growth and uptake of

nutrient, and $\tilde{\Psi}_{S_j}$ is the volume of soil adjacent to each potato tuber j (see Figure 5.1 (a)). Here we model the early-stage development of potato tubers, and assume the tubers to be spherical. Therefore, equation (5.16) can be written in terms of the radius $\tilde{r}_j$ only, *i.e.*,

$$\partial_{\tilde{t}}\tilde{r}_j = \frac{\alpha}{4\pi\tilde{r}_j^2}\int_{\tilde{\Psi}_{S_j}} \xi\tilde{c}\, d\tilde{\Psi}_{S_j}. \tag{5.17}$$

We state that the water and air components of $\tilde{\Psi}_S$ do not penetrate the tubers $\tilde{\Psi}_{p_j}$, thus, we require the Darcy velocities normal to the interface to be zero, *i.e.*,

$$\hat{\mathbf{n}}\cdot\left(\frac{\kappa_w}{\mu_w}\tilde{\boldsymbol{\nabla}}\tilde{p}_w\right) = 0 \quad \text{on} \quad \tilde{\Gamma}_j\times[0,\infty), \tag{5.18}$$

$$\hat{\mathbf{n}}\cdot\left(\frac{\kappa_a}{\mu_a}\tilde{\boldsymbol{\nabla}}\tilde{p}_a\right) = 0 \quad \text{on} \quad \tilde{\Gamma}_j\times[0,\infty). \tag{5.19}$$

Finally, on $\tilde{\Gamma}_j$ we assume the the air and water velocities are equal to the growth of the tubers, *i.e.*,

$$(2\hat{\mathbf{n}}\otimes\hat{\mathbf{n}} - \mathfrak{T})\cdot\tilde{\mathbf{v}}_w = \hat{\mathbf{n}}\partial_{\tilde{t}}\tilde{r}_j \quad \text{on} \quad \tilde{\Gamma}_j\times[0,\infty), \tag{5.20}$$

$$(2\hat{\mathbf{n}}\otimes\hat{\mathbf{n}} - \mathfrak{T})\cdot\tilde{\mathbf{v}}_a = \hat{\mathbf{n}}\partial_{\tilde{t}}\tilde{r}_j \quad \text{on} \quad \tilde{\Gamma}_j\times[0,\infty). \tag{5.21}$$

5.2.4 Non-Dimensionalisation

To simplify the model and understand the magnitude of influence of each parameter, we non-dimensionalise the system of equations described above. We are interested in the macroscopic properties of the system of equations whilst retaining the influence of the microscopic structure. Hence, we identify there are two different length scales, the microscopic length scale l_y [m] and the macroscopic length scale l_x [m], where $l_y/l_x = \varepsilon \ll 1$ [$-$]. We choose to non-dimensionalise using the scaling,

$$\tilde{\mathbf{x}} = l_x\mathbf{x},\ \tilde{t} = \frac{l_x^2}{D}t,\ \tilde{\mathbf{u}}_s = l_y\mathbf{u}_s,\ \tilde{c} = c_{\text{max}}c,\ \tilde{p}_i = Gp_i,\ \tilde{\mathbf{v}}_i = \frac{l_yD}{l_x^2}\mathbf{v}_i,\ \tilde{r} = l_yr, \tag{5.22}$$

where $c_{\text{max}} \geq 0$ [kg m^{-3}] is the maximum concentration of the nutrient applied to $\tilde{\Psi}_S$ and $i = \{w, a\}$. In (5.22) we use the macroscopic length scale l_x as the spatial scaling to observe the macroscale propeties, the diffusion timescale $\frac{l_x^2}{D}$ for the time scaling as diffusion is the dominant transport mechanism, and the shear modulus G for the pressure scaling. Shown in Figure 5.1 (b) is the non-dimensionalised macroscopic domain Ψ and microscopic domain Π. It follows that the system of equations becomes,

$$\partial_t \phi_a = -\varepsilon \boldsymbol{\nabla} \cdot (\phi_a \mathbf{v}_a) \quad \text{in} \quad \Psi_S^\infty, \tag{5.23}$$

$$\partial_t \phi_w = -\varepsilon \boldsymbol{\nabla} \cdot (\phi_w \mathbf{v}_w) - \overline{\lambda_c}(p_w - \overline{p_r}) \quad \text{in} \quad \Psi_S^\infty, \tag{5.24}$$

$$\partial_t (1 - \phi_a - \phi_w) = -\varepsilon \boldsymbol{\nabla} \cdot [(1 - \phi_a - \phi_w)\partial_t \mathbf{u}_s] \quad \text{in} \quad \Psi_S^\infty, \tag{5.25}$$

$$\boldsymbol{\nabla} \cdot \left[(\boldsymbol{\nabla} \mathbf{u}_s) + (\boldsymbol{\nabla} \mathbf{u}_s)^T + \overline{\nu} \boldsymbol{\nabla} \cdot \mathbf{u}_s \mathfrak{T} - \varepsilon^{-1}(\zeta p_w \mathfrak{T} - p_a \mathfrak{T}) \right] = 0 \quad \text{in} \quad \Psi_S^\infty, \tag{5.26}$$

$$\phi_a \left(\mathbf{v}_a - \partial_t \mathbf{u}_s \right) = -\overline{\kappa}_a \boldsymbol{\nabla} p_a \quad \text{in} \quad \Psi_S^\infty, \tag{5.27}$$

$$\phi_w \left(\mathbf{v}_w - \partial_t \mathbf{u}_s \right) = -\overline{\kappa}_w \boldsymbol{\nabla} p_w \quad \text{in} \quad \Psi_S^\infty, \tag{5.28}$$

$$\frac{\phi_w}{\phi_w + \phi_a} = \left\{ \left[\overline{G}(p_a - p_w) \right]^{\frac{1}{1-m}} + 1 \right\}^{-m}, \tag{5.29}$$

$$(\phi_w + b)\partial_t c + c \partial_t \phi_w = \boldsymbol{\nabla} \cdot (\phi_w \boldsymbol{\nabla} c) - \overline{\xi} c \quad \text{in} \quad \Psi_S^\infty, \tag{5.30}$$

$$\hat{\mathbf{n}} \cdot (\phi_w \boldsymbol{\nabla} c) = 0 \quad \text{on} \quad \Gamma_j \times [0, \infty), \tag{5.31}$$

$$(2\hat{\mathbf{n}} \otimes \hat{\mathbf{n}} - \mathfrak{T}) \cdot \mathbf{u}_s = \hat{\mathbf{n}}(r_j - \overline{r^*}) \quad \text{on} \quad \Gamma_j \times [0, \infty), \tag{5.32}$$

$$\hat{\mathbf{n}} \cdot (\boldsymbol{\nabla} p_w) = 0 \quad \text{on} \quad \Gamma_j \times [0, \infty), \tag{5.33}$$

$$\hat{\mathbf{n}} \cdot (\boldsymbol{\nabla} p_a) = 0 \quad \text{on} \quad \Gamma_j \times [0, \infty), \tag{5.34}$$

$$(2\hat{\mathbf{n}} \otimes \hat{\mathbf{n}} - \mathfrak{T}) \cdot \mathbf{v}_w = \hat{\mathbf{n}} \partial_t r_j \quad \text{on} \quad \Gamma_j \times [0, \infty), \tag{5.35}$$

$$(2\hat{\mathbf{n}} \otimes \hat{\mathbf{n}} - \mathfrak{T}) \cdot \mathbf{v}_a = \hat{\mathbf{n}} \partial_t r_j \quad \text{on} \quad \Gamma_j \times [0, \infty). \tag{5.36}$$

$$\partial_t r_j = \frac{\overline{\alpha}}{4\pi r_j^2} \int_{\Psi_{S_j}} c \, d\Psi_{S_j}, \tag{5.37}$$

where,

$$\overline{\lambda_c} = \frac{\lambda_c G l_x^2}{D}, \ \overline{p_r} = \frac{p_r}{G}, \ \overline{\nu} = \frac{\nu}{1 - 2\nu}, \ \overline{\kappa}_a = \frac{\kappa_a G \varepsilon^{-1}}{D \mu_a}, \ \overline{\kappa}_w = \frac{\kappa_w G \varepsilon^{-1}}{D \mu_w},$$
$$\overline{G} = \frac{G}{p_c}, \ \overline{\xi} = \frac{\xi l_x^2}{D}, \ \overline{r^*} = \frac{r^*}{l_y}, \ \overline{\alpha} = \frac{c_{\max} \alpha \xi l_x^2}{D}. \tag{5.38}$$

5.2.5 Parameter Estimation

Here we estimate the parameters contained in equations (5.23) − (5.37) to determine the magnitude of influence each parameter has on the system of equations. Since this model is motivated by the growth of potato tubers in soil, we assess the parameter values for silt soils as potatoes are frequently grown in this soil type [106].

Potato plants are typically grown in ridge and furrow geometries and are contained

in the plough layer of soil, which is the top 30 cm [103]. Therefore, we choose the macroscopic length scale to be $l_x \approx 0.3$ m. Similarly, we assume that the tubers have an inter-tuber distance that is substantially less than the total length of the plough layer. We choose an inter-tuber distance of approximately $l_y \approx 0.05$ m, resulting in the ratio of the two length scales to be $\varepsilon \approx 0.1$. We also assume an initial tuber radius of $r^* = \mathcal{O}(0.05)$ m $\lesssim l_y$.

Values for the Poisson ratio of silt soils are approximately $0.3 \lesssim \nu \lesssim 0.35$ [199], and the shear modulus is $G \approx 1 \times 10^7$ Pa [200]. Furthermore, typical characteristic suction pressures for silt soils are approximately $p_c \approx 3 \times 10^4$ Pa [101], with soil permeabilities of $\kappa_w \approx \kappa_a \approx 5 \times 10^{-14}$ m^2 [101]. The viscosity of water is $\mu_w = 1 \times 10^{-3}$ Pa s and the viscosity of air is $\mu_a = 1 \times 10^{-5}$ Pa s.

One of the key nutrients responsible for plant growth and development is nitrogen [145]. We choose to model this nutrient since plant growth is closely linked to an abundance of nitrogen in soil. Nitrogen has a diffusion coefficient in soil water of $D \approx 2.5 \times 10^{-10}$ m^2 s^{-1} [27] and for the potato plant *Solanum tuberosum* L., the uptake rate of the nutrient nitrogen is $\xi \approx 1 \times 10^{-9}$ s^{-1} [148, 149], for nitrogen concentrations in soil $c_{\text{max}} \approx 10^{-1}$ kg m^{-3} [149].

In the early-stages of growth for *Solanum tuberosum* L., the tuber radius growth rate is approximately 1×10^{-9} m s^{-1} [201]. If we assume that the quantity of nitrogen taken up by the plant is proportional to the growth of the tuber, then we can estimate the ratio between the rate of growth and the uptake, *i.e.*, $\alpha \approx 1 \times 10^1$ kg^{-1} m^3 [148, 149].

Using the values above, we find that the parameters $\overline{\kappa}_a$ and $\overline{\kappa}_w$ contained in (5.27) and (5.28) are $\overline{\kappa}_a = \mathcal{O}(10^9)$ and $\overline{\kappa}_w = \mathcal{O}(10^7)$. This is significantly larger than the other terms in the equations. Hence, we re-write equations (5.27) and (5.28) so that,

$$\overline{\kappa}_a \boldsymbol{\nabla} p_a \approx 0 \quad \text{in} \quad \Psi_S, \tag{5.39}$$

$$\overline{\kappa}_w \boldsymbol{\nabla} p_w \approx 0 \quad \text{in} \quad \Psi_S, \tag{5.40}$$

which have the solutions $p_a =$ constant and $p_w =$ constant, *i.e.*, the consolidation of the soil is substantially faster than the diffusion of solutes. Since $p_w =$ constant, we find that the sink term in equation (5.4) representing root uptake is constant, *i.e.*, $\lambda_c(\tilde{p}_w - p_r) = F$, where F is the water uptake rate by plant roots. The uptake rate of water by *Solanum tuberosum* L. roots over a growing season is $F \approx 1 \times 10^{-8}$ s^{-1} [202].

The result of $p_a =$ constant and $p_w =$ constant allows us to reduce the system of

equations (5.23) $-$ (5.37) to,

$$\partial_t \phi_w = -\varepsilon \boldsymbol{\nabla} \cdot (\phi_w \mathbf{v}_w) - \overline{F} \quad \text{in} \quad \Psi_S^\infty, \tag{5.41}$$

$$\boldsymbol{\nabla} \cdot \Big[(\boldsymbol{\nabla} \mathbf{u}_s) + (\boldsymbol{\nabla} \mathbf{u}_s)^T + \overline{\nu} \boldsymbol{\nabla} \cdot \mathbf{u}_s \mathfrak{T} \Big] = 0 \quad \text{in} \quad \Psi_S, \tag{5.42}$$

$$\mathbf{v}_w - \partial_t \mathbf{u}_s = 0, \tag{5.43}$$

$$(\phi_w + b)\partial_t c + c\partial_t \phi_w = \boldsymbol{\nabla} \cdot (\phi_w \boldsymbol{\nabla} c) - \overline{\xi} c \quad \text{in} \quad \Psi_S^\infty, \tag{5.44}$$

$$(2\hat{\mathbf{n}} \otimes \hat{\mathbf{n}} - \mathfrak{T}) \cdot \mathbf{u}_s = \hat{\mathbf{n}}(r_j - \overline{r^*}) \quad \text{on} \quad \Gamma_j, \tag{5.45}$$

$$\hat{\mathbf{n}} \cdot (\phi \boldsymbol{\nabla} c) = 0 \quad \text{on} \quad \Gamma_j \times [0, \infty), \tag{5.46}$$

$$\partial_t r_j = \frac{\overline{\alpha}}{4\pi r_j^2} \int_{\Psi_{S_j}} c \, d\Psi_{S_j}, \tag{5.47}$$

where $\overline{F} = F l_x^2 / D$.

This reduction of equations results from several physical processes having a negligible effect on the system described. Since the air and water pressures are constant on the timescale of solute diffusion, this causes the equation for conservation of momentum for a poroelastic material (5.26) to reduce to the equation for conservation of momentum for an elastic material, *i.e.*, equation (5.42). This then allows us to neglect the influence of air movement within the soil, *i.e.*, equation (5.23). This then leads to the system of equations (5.41) $-$ (5.47).

Using the values discussed above, we find that the parameters contained in equations (5.41) $-$ (5.47) have the approximate values,

$$\overline{F} = \mathcal{O}(1), \ \overline{\nu} = \mathcal{O}(1), \ \overline{\xi} = \mathcal{O}(1), \ \overline{r^*} = \mathcal{O}(1), \ \overline{\alpha} = \mathcal{O}(1). \tag{5.48}$$

For the remainder of this Chapter, equations (5.41) $-$ (5.47) will be referred to as the 'full set' of equations to describe solute movement and tuber growth.

5.2.6 Homogenisation

In this section, we use multiple scale homogenisation to develop a set of averaged macroscale equations that describe the movement of nutrients and tuber growth in soil. From equation (5.41) we observe that the volumetric water content ϕ_w is affected by two mechanisms: firstly by soil compression due to the growth of the tuber, *i.e.*, $\varepsilon \boldsymbol{\nabla} \cdot (\phi_w \mathbf{v}_w)$, and secondly by root water uptake, *i.e.*, $\overline{F}$. From the non-dimensionalisation, we observe that the maximum displacement is bounded such that $\mathbf{u}_s \ll \overline{F}$. This leads to the result $\mathbf{v}_s \ll \overline{F}$, and hence, $\varepsilon \boldsymbol{\nabla} \cdot (\phi_w \mathbf{v}_w) \ll \overline{F}$.

Therefore, we find that the root water uptake term dominates the change in water content. Hence, for the homogenisation procedure, we neglect the term regarding soil compression, and the system of equations we homogenise reduces to,

$$\partial_t \phi_w = -\overline{F} \quad \text{in} \quad \Pi_S^\infty, \tag{5.49}$$

$$(\phi_w + b)\partial_t c + c\partial_t \phi_w = \boldsymbol{\nabla} \cdot (\phi_w \boldsymbol{\nabla} c) - \overline{\xi} c \quad \text{in} \quad \Pi_S^\infty, \tag{5.50}$$

$$\hat{\mathbf{n}} \cdot (\phi_w \boldsymbol{\nabla} c) = 0 \quad \text{on} \quad \Gamma \times [0, \infty), \tag{5.51}$$

$$\partial_t r = \frac{\overline{\alpha}}{4\pi r^2} \int_{\Pi_S} c \, d\Pi_S. \tag{5.52}$$

$$\text{periodic} \quad \text{on} \quad \partial\Pi_E. \tag{5.53}$$

To validate this assumption, we compare the full set of equations (5.41) $-$ (5.47) to the homogenised system of equations derived from (5.49) $-$ (5.53) in the following section.

As in Chapter 4, we observe there are two different length scales present in the geometry $\tilde{\Psi}$, the macroscale l_x and the mircoscale l_y. Any change of $\mathcal{O}(1)$ on the length scale l_x will result in a $\mathcal{O}(\varepsilon)$ change on the length scale l_y. We can formalise this by assuming that the dependent variables ϕ_w, c and r are functions of a small scale $\mathbf{y}$ and a large scale $\mathbf{x}$. We denote the unit cell Π representing the microscale domain $\mathbf{y} \in \Pi \equiv [-1/2, 1/2]^3$. Using the two length scales and chain rule, the gradient operator is written as,

$$\boldsymbol{\nabla} = \boldsymbol{\nabla}_{\mathbf{x}} + \varepsilon^{-1} \boldsymbol{\nabla}_{\mathbf{y}}. \tag{5.54}$$

Furthermore, we expand ϕ_w, c and r such that,

$$\phi_w = \phi_{w_0} + \mathcal{O}(\varepsilon), \tag{5.55}$$

$$c = c_0 + \varepsilon c_1 + \varepsilon^2 c_2 + \mathcal{O}(\varepsilon^3), \tag{5.56}$$

$$r = r_0 + \mathcal{O}(\varepsilon). \tag{5.57}$$

The first step of the homogenisation procedure is to determine the most dominant terms in the system of equations (5.49) $-$ (5.53). To do this we substitute equations (5.54) $-$ (5.57) into (5.49) $-$ (5.53) and collect the largest terms of $\mathcal{O}(\varepsilon^{-2})$. This results in the system of equations,

$$\boldsymbol{\nabla}_{\mathbf{y}} \cdot (\phi_{w_0} \boldsymbol{\nabla}_{\mathbf{y}} c_0) = 0 \quad \text{in} \quad \Pi_S, \tag{5.58}$$

$$\hat{\mathbf{n}} \cdot (\phi_{w_0} \boldsymbol{\nabla}_{\mathbf{y}} c_0) = 0 \quad \text{on} \quad \Gamma, \tag{5.59}$$

$$\text{periodic} \quad \text{on} \quad \partial\Pi_E. \tag{5.60}$$

From Chapter 4, we observed in Theorem 4.3.1 that the leading order term p_{w0} had large scale dependence only and was independent of the small scale $\mathbf{y}$. By applying the same theorem methodology to equations (5.58) $-$ (5.60) we find that $c_0 = c_0(\mathbf{x}, t)$, *i.e.*, c_0 has large scale dependence only and is independent of the small scale $\mathbf{y}$.

To proceed with the homogenisation methodology, we collect the next most dominant terms in the system of equations. This is achieved by collecting terms $\mathcal{O}(\varepsilon^{-1})$ and using the result $\boldsymbol{\nabla}_{\mathbf{y}} c_0 = 0$, *i.e.*,

$$\boldsymbol{\nabla}_{\mathbf{y}} \cdot (\phi_{w_0} \boldsymbol{\nabla}_{\mathbf{y}} c_1 + \phi_{w_0} \boldsymbol{\nabla}_{\mathbf{x}} c_0) = 0 \quad \text{in} \quad \Pi_S, \tag{5.61}$$

$$\hat{\mathbf{n}} \cdot (\phi_{w_0} \boldsymbol{\nabla}_{\mathbf{y}} c_1 + \phi_{w_0} \boldsymbol{\nabla}_{\mathbf{x}} c_0) = 0 \quad \text{on} \quad \Gamma, \tag{5.62}$$

$$\text{periodic} \quad \text{on} \quad \partial\Pi_E. \tag{5.63}$$

To continue with the analysis, we must ensure that equations (5.61) $-$ (5.63) form a well-posed problem, *i.e.*, the equations have a solution that agrees with the boundary conditions. We can show the system is well-posed by applying the divergence theorem to equation (5.61) and use boundary condition (5.62) such that,

$$\int_{\Pi_S} \boldsymbol{\nabla}_{\mathbf{y}} \cdot (\phi_{w_0} \boldsymbol{\nabla}_{\mathbf{y}} c_1 + \phi_{w_0} \boldsymbol{\nabla}_{\mathbf{x}} c_0)\, d\Pi_S = \int_{\partial\Pi_S} \hat{\mathbf{n}} \cdot (\phi_{w_0} \boldsymbol{\nabla}_{\mathbf{y}} c_1 + \phi_{w_0} \boldsymbol{\nabla}_{\mathbf{x}} c_0)\, d\partial\Pi_S = 0. \tag{5.64}$$

Next, we choose to rescale c_1 so that,

$$c_1(\mathbf{x}, \mathbf{y}) = \sum_{k=1}^{3} \chi_k(\mathbf{y}) \partial_{x_k} c_0 + \bar{c_1}(\mathbf{x}), \tag{5.65}$$

where $\bar{c_1}(\mathbf{x})$ is the large scale component of $c_1(\mathbf{x}, \mathbf{y})$. Substituting (5.65) into equations (5.61) $-$ (5.63) yields the cell problem for χ_k,

$$\boldsymbol{\nabla}_{\mathbf{y}} \cdot (\boldsymbol{\nabla}_{\mathbf{y}} \chi_k + \hat{\mathbf{e}}_k) = 0 \quad \text{in} \quad \Pi_S, \tag{5.66}$$

$$\hat{\mathbf{n}} \cdot (\boldsymbol{\nabla}_{\mathbf{y}} \chi_k + \hat{\mathbf{e}}_k) = 0 \quad \text{on} \quad \Gamma, \tag{5.67}$$

$$\text{periodic} \quad \text{on} \quad \partial\Pi_E. \tag{5.68}$$

Recall that the tubers grow in the soil domain, hence, the cell problem solution χ_k [m] is dependent on the radius of the tuber. Since the cell problem is a representation of the impedance of nutrient movement due to the tuber obstruction, and as the tuber grows the impact on nutrient transport will change, therefore we have the relationship $\chi_k = \chi_k(r)$, *i.e.*, the cell problem solution is dependent on the radius of the tuber.

The last step of the homogenisation procedure is to collect terms $\mathcal{O}(\varepsilon^0)$. This results in the system of equations,

$$\partial_t \phi_{w_0} = -\overline{F} \quad \text{in} \quad \Pi_S^\infty, \tag{5.69}$$

$$(\phi_{w_0} + b)\partial_t c_0 + c_0 \partial_t \phi_{w_0} = \boldsymbol{\nabla}_{\mathbf{y}} \cdot (\phi_{w_0} \boldsymbol{\nabla}_{\mathbf{y}} c_2 + \phi_{w_0} \boldsymbol{\nabla}_{\mathbf{x}} c_1) + \boldsymbol{\nabla}_{\mathbf{x}} \cdot (\phi_{w_0} \boldsymbol{\nabla}_{\mathbf{y}} c_1 + \phi_{w_0} \boldsymbol{\nabla}_{\mathbf{x}} c_0) - \overline{\xi} c \quad \text{in} \quad \Pi_S^\infty, \tag{5.70}$$

$$\hat{\mathbf{n}} \cdot (\phi_{w_0} \boldsymbol{\nabla}_{\mathbf{y}} c_2 + \phi_{w_0} \boldsymbol{\nabla}_{\mathbf{x}} c_1) = 0 \quad \text{on} \quad \Gamma \times [0, \infty), \tag{5.71}$$

$$\text{periodic} \quad \text{on} \quad \partial \Pi_E, \tag{5.72}$$

$$\partial_t r_0 = \frac{\overline{\alpha}}{4\pi r_0^2} \int_{\Pi_S} c_0 \, d\Pi_S. \tag{5.73}$$

To check (5.70) $-$ (5.73) provide a well-posed problem, we check the solvability of the system of equations. To check for solvability we integrate equation (5.70) over the domain Π_S and apply the divergence theorem, *i.e.*,

$$\int_{\Pi_S} (\phi_{w_0} + b)\partial_t c_0 + c_0 \partial_t \phi_{w_0} \, d\Pi_S = \int_{\Pi_S} \boldsymbol{\nabla}_{\mathbf{y}} \cdot (\phi_{w_0} \boldsymbol{\nabla}_{\mathbf{y}} c_2 + \phi_{w_0} \boldsymbol{\nabla}_{\mathbf{x}} c_1) \, d\Pi_S + \int_{\Pi_S} \boldsymbol{\nabla}_{\mathbf{x}} \cdot (\phi_{w_0} \boldsymbol{\nabla}_{\mathbf{y}} c_1 + \phi_{w_0} \boldsymbol{\nabla}_{\mathbf{x}} c_0) \, d\Pi_S - \int_{\Pi_S} \overline{\xi} c \, d\Pi_S, \tag{5.74}$$

and using the boundary condition (5.71) yields,

$$\int_{\Pi_S} (\phi_{w_0} + b)\partial_t c_0 + c_0 \partial_t \phi_{w_0} \, d\Pi_S = \int_{\Pi_S} \boldsymbol{\nabla}_{\mathbf{x}} \cdot (\phi_{w_0} \boldsymbol{\nabla}_{\mathbf{y}} c_1 + \phi_{w_0} \boldsymbol{\nabla}_{\mathbf{x}} c_0) \, d\Pi_S - \int_{\Pi_S} \overline{\xi} c \, d\Pi_S. \tag{5.75}$$

We define,

$$||\Pi_S(r)|| = \int_{\Pi_S(r)} d\Pi_S, \tag{5.76}$$

to be the volume integral of the cell problem, which is dependent of the radius of the

tuber. It follows that by using equation (5.65), equation (5.75) can be written as,

$$||\Pi_S(r)||[(\phi_{w_0}+b)\partial_t c_0 + c_0\partial_t\phi_{w_0}] = \frac{\partial}{\partial x_i}\int_{\Pi_S(r)}\left[\phi_{w_0}\left(\frac{\partial c_0}{\partial x_i}+\frac{\partial\chi_j(r)}{\partial y_i}\frac{\partial c_0}{\partial x_j}\right)\right]d\Pi_S - ||\Pi_S(r)||\overline{\xi}c_0 \quad \text{in} \quad \Pi_S^\infty. \tag{5.77}$$

This results in the system of equations for ϕ_{w_0}, c_0 and r_0,

$$\partial_t\phi_{w_0} = -\overline{F} \quad \text{in} \quad \Pi_S^\infty, \tag{5.78}$$

$$||\Pi_S(r_0)||[(\phi_{w_0}+b)\partial_t c_0 + c_0\partial_t\phi_{w_0}] = \phi_{w_0}\boldsymbol{\nabla}_{\mathbf{x}}\mathfrak{D}_{\mathfrak{e}}(r_0)\boldsymbol{\nabla}_{\mathbf{x}}c_0 - ||\Pi_S(r_0)||\overline{\xi}c_0 \quad \text{in} \quad \Pi_S^\infty, \tag{5.79}$$

$$\partial_t r_0 = \frac{\overline{\alpha}}{4\pi r_0^2}||\Pi_S(r_0)||c_0, \tag{5.80}$$

where,

$$\mathfrak{D}_{\mathfrak{e}}(r_0) = \int_{\Pi_S(r_0)}\mathfrak{T} + \boldsymbol{\nabla}_{\mathbf{y}}\chi_k(r_0)\otimes\hat{\mathbf{e}}_k\, d\Pi_S, \tag{5.81}$$

for $k = (1, ..., 3)$. Here the averaged terms $||\Pi_S(r_0)||\ [-]$ and $\mathfrak{D}_{\mathfrak{e}}(r_0)$ [m^2 s^{-1}] are parameterised from the cell problem (5.66) $-$ (5.68). This results identifies that equations (5.70) $-$ (5.73) provide a well-posed problem if and only if the system of equations (5.78) $-$ (5.81) have a solution.

In the system (5.78) $-$ (5.81), the parameterised coefficients $||\Pi_S(r_0)||$ and $\mathfrak{D}_{\mathfrak{e}}(r_0)$ describe the soil volume that is not occupied by the tuber, and the effective diffusion due to impedance from the tuber respectively. Therefore, both these coefficients are dependent on the radius of the tuber.

In Chapter 4, we developed a system of homogenised equations, in which the homogenised coefficients were calculated from a static cell problem. However, in this system we have a cell problem that is dependent on the radius of the tuber. Hence, we have a coupled system which implicitly calculates the transport of the nutrients, the uptake of nutrients by the plant, and the growth of the tubers.

For the remainder of this chapter, equations (5.78) $-$ (5.81) will be referred to as the 'homogenised set' of equations to describe solute movement and tuber growth.

5.3 Validation of the Homogenisation Procedure

We validate the mathematical steps used in the homogenisation procedure by comparing the homogenised set of equations (5.78) − (5.81) to the full set of equations (5.41) − (5.47). We consider multiple comparisons by varying parameters for the buffer power b, root uptake rate $\overline{F}$ and initial porosity $\phi_w|_{t=0}$ to examine the accuracy of the averaging procedure.

5.3.1 Implementation

Here we describe how we utilise the finite element package COMSOL Multiphysics (COMSOL Multiphysics, Stockholm, Sweden, www.comsol.com) to solve the full and homogenised sets of equations. To solve both sets of equations we generate two geometries, one for the full set of equations (5.41) − (5.47) containing potato tubers, and a second uniform geometry for the homogenised equations (5.78) − (5.81). We choose the domain length of each geometry to be composed of eight periodic cells. Due to the homogenisation procedure, the approximate equations (5.78) − (5.81) do not require any tubers as the influence of the microscale geometry is contained in the paramterised terms $||\Pi_S(r_0)||$ and $\mathfrak{D}_\mathfrak{e}(r_0)$. Shown in Figure 5.2 are the geometries used to validate the homogenisation procedure.

Full Equations

Implementation of the full set of equations (5.41) − (5.47) requires the implementation of a complex moving boundary problem. This accounts for the uptake of nutrients by each tuber Ψ_{p_j}, the subsequent growth of Ψ_{p_j}, and the reduction in volumetric water content ϕ_w. The geometry we impose the full set of equations on can be seen in Figure 5.2 (a). However, we require two versions of this geometry: an undeformed geometry that is constant in time, and a deforming geometry that is dependent on tuber growth, since different components of the system (5.41) − (5.47) are solved on either an undeformed or deforming frame of reference. There are three main components that are required to be implemented in order to solve (5.41) − (5.47), these are: the poroelastic equations, the compaction and deformation of soil, and the nutrient movement equations.

The implementation of the poroelastic equations (5.41) − (5.43) and (5.45) for the local displacement $\mathbf{u}^s$ and reduction in ϕ_w is straightforward, since these equations are solved on the undeformed geometry regardless of tuber size. This is achieved

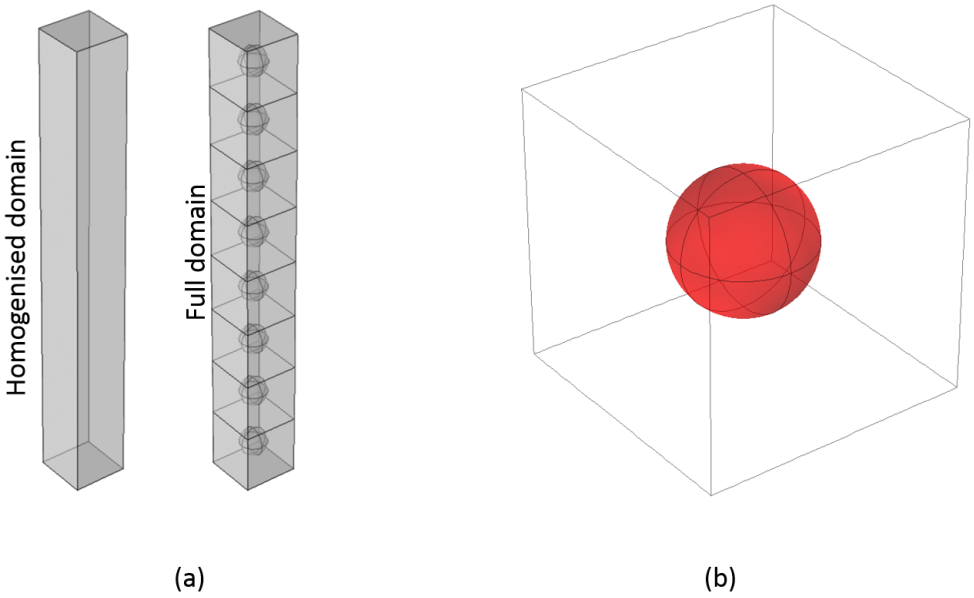

Figure 5.2: The geometries used to validate the homogenisation procedure (a): The approximate equations (5.78) – (5.81) are solved on the left geometry, whereas the original set of equations (5.41) – (5.47) are solved on the right geometry that contains potato tubers. (b): The cell problem is solved on a single unit cell that contains a potato tuber (coloured in red).

using the inbuilt 'General Form PDE', *i.e.*,

$$e_a \frac{\partial^2 \mathbf{r}}{\partial t^2} + d_a \frac{\partial \mathbf{r}}{\partial t} + \boldsymbol{\nabla} \cdot \boldsymbol{\Theta} = f, \tag{5.82}$$

where $\mathbf{r} = [\phi_w, \mathbf{u}_s]^T$ and,

$$e_a = \begin{bmatrix} 0 & 0 \\ 0 & 0 \end{bmatrix}, \; d_a = \begin{bmatrix} 1 & 0 \\ 0 & 0 \end{bmatrix}, \boldsymbol{\Theta} = \begin{bmatrix} \varepsilon \phi_w \partial_t \mathbf{u}_s \\ (\boldsymbol{\nabla} \mathbf{u}_s) + (\boldsymbol{\nabla} \mathbf{u}_s)^T + \overline{\nu} \boldsymbol{\nabla} \cdot \mathbf{u}_s \mathfrak{T} \end{bmatrix}, f = \begin{bmatrix} -\overline{F} \\ 0 \end{bmatrix}. \tag{5.83}$$

Using this solution at each time step, we can prescribe a deformation (for the deforming geometry) within the soil domain to correspond with the increase in tuber size. This is achieved by implementing a 'Domain Deformation' in which we prescribe the mesh displacement in the the three spatial directions x_1,x_2 and x_3 using the solution for $\mathbf{u}_s$.

The nutrient equations (5.44) and (5.46) – (5.47) are solved on the deforming

geometry to correspond with the growth of the tubers. However, these equations use the poroelastic solution from the undeformed geometry. Hence, we implement a reference frame change such that poroelastic solution can be mapped from the undeformed geometry to the deformed geometry. This allows us to solve the nutrient equations on the deformed geometry corresponding with the prescribed tuber deformation.

Since the nutrient equations are solved on a deforming geometry, extra care is required to ensure that c is conserved. This is achieved by making two alterations to (5.44) and (5.46). Firstly, we note Reynolds Transport Theorem,

$$\frac{d}{dt}\int_{\theta(t)} \mathbf{F}\, dV = \int_{\theta(t)} \frac{\partial \mathbf{F}}{\partial t}\, dV + \int_{\partial\theta(t)} (\boldsymbol{\omega}\cdot\hat{\mathbf{n}})\mathbf{F}\, dA, \tag{5.84}$$

where, dV [m^3] and dA [m^2] are volume and surface elements respectively, $\boldsymbol{\omega}$ [m s^{-1}] is the velocity of the surface element, $\hat{\mathbf{n}}$ is the normal vector pointing out of the geometry, $\mathbf{F}$ is any function of $\mathbf{x}$ and t, and $\theta(t)$ [m^3] is the domain. Reynolds Transport Theorem states that the change in nutrient concentration in a domain is equal to the change in concentration within the domain plus the rate at which nutrient is entering the domain. Applying equation (5.84) to the full set of equations (5.41) $-$ (5.47) leads to,

$$\frac{d}{dt}\int_{\Psi_{\text{Soil}(t)}} c\, d\Psi_{\text{Soil}(t)} = \int_{\Psi_{\text{Soil}(t)}} \frac{\partial c}{\partial t}\, d\Psi_{\text{Soil}(t)} + \int_{\partial\Psi_{\text{Soil}(t)}} (\boldsymbol{\omega}_{\text{mesh}}\cdot\hat{\mathbf{n}})c\, d\partial\Psi_{\text{Soil}(t)}, \tag{5.85}$$

where, $\boldsymbol{\omega}_{\text{mesh}}$ [m s^{-1}] is the velocity of the boundaries Ψ_{p_j}. This requires us to adapt equation (5.46) so that,

$$\hat{\mathbf{n}}\cdot(\phi_w\boldsymbol{\nabla}c) = -(\boldsymbol{\omega}_{\text{mesh}}\cdot\hat{\mathbf{n}})c \quad \text{on} \quad \Gamma_j\times[0,\infty). \tag{5.86}$$

Equation (5.86) then satisfies the conservation law for moving boundaries.

Secondly, as Ψ_{p_j} grows and Ψ_S is deformed, this causes an advective movement effect on c within Ψ_S. This can be interpreted as the boundaries of the tubers Γ_j physically pushing the nutrients. Hence, we are required to add a conservative advection term to equation (5.44) accounting for the individual elements within the mesh moving, *i.e.*,

$$(\phi_w+b)\partial_t c + c\partial_t\phi_w = \boldsymbol{\nabla}\cdot(\phi_w\boldsymbol{\nabla}c - \boldsymbol{\omega}_{\text{mesh}}c) - \overline{\xi}c \quad \text{in} \quad \Psi_S^{\infty}. \tag{5.87}$$

This modified system of equations can then be successfully used to model coupled nutrient movement and poroelastic deformation from growing tubers. To implement

equations (5.87) and (5.86), we use the inbuilt 'General Form PDE' where,

$$\mathbf{r} = c,\ e_a = 0,\ d_a = (\phi_w + b),\ \boldsymbol{\Theta} = \phi_w \boldsymbol{\nabla} c - \boldsymbol{\omega}_{\text{mesh}} c,\ f = -\overline{\xi} c, \tag{5.88}$$

and use the inbuilt flux boundary condition that takes the form,

$$\hat{\mathbf{n}} \cdot \boldsymbol{\Theta} = g_1 - g_2 \mathbf{r}, \tag{5.89}$$

where $g_1 = 0$ and $g_2 = -(\boldsymbol{\omega}_{\text{mesh}} \cdot \hat{\mathbf{n}})$. Finally, to implicitly solve for the tuber radii r_j in equation (5.47), we use the inbuilt ODE equation 'Global ODE' which takes the form,

$$f(q, q_t, q_t t, t) = 0. \tag{5.90}$$

This is used in tandem with an 'Integral Component Coupling' to establish the integral in (5.47), *i.e.*, $\int_{\Psi_{S_j}} \overline{\xi} c \, d\Psi_{S_j}$.

Homogenised Equations

The geometry on which we impose the homogenised set of equations (5.78) $-$ (5.81) can be seen in Figure 5.2 (a). To implement the equations (5.78) and (5.80) is substantially simpler. We use the inbuilt ODE equation 'Global ODE' which takes the form shown in equation (5.90).

To implement (5.79) we use the inbuilt 'Coefficient Form PDE' that takes the form,

$$e_a \frac{\partial^2 \mathbf{r}}{\partial t^2} + d_a \frac{\partial \mathbf{r}}{\partial t} + \boldsymbol{\nabla} \cdot (-c \boldsymbol{\nabla} \mathbf{r} - \alpha \mathbf{r} + \gamma) + \beta \cdot \boldsymbol{\nabla} \mathbf{r} + a \mathbf{r} = f, \tag{5.91}$$

where $\mathbf{r} = c_0$, $e_a = 0$, $d_a = ||\Pi_S(r_0)||(\phi_{w_0} + b)$, $c = \phi_{w_0} \mathfrak{D}_{\mathfrak{e}}(r_0)$, $\alpha = 0$, $\gamma = 0$, $\beta = 0$, $a = ||\Pi_S(r_0)|| \partial_t \phi_{w_0}$ and $f = -||\Pi_S(r_0)|| \overline{\xi} c_0$.

However, to solve equation (5.79), we are required to solve a series of cell problems, *i.e.*, equations (5.66) $-$ (5.68), to calculate the terms $||\Pi_S(r_0)||$ and $\mathfrak{D}_{\mathfrak{e}}(r_0)$ that paramterise equation (5.79) and (5.80). Since the geometric properties of the domain Π are contained in $||\Pi_S(r_0)||$ and $\mathfrak{D}_{\mathfrak{e}}(r_0)$, we solve the cell problem for a series of different tuber radii to correspond with different levels of growth/displacement from the original tuber size. Using the results from the cell problems, we can construct interpolated functions to describe $||\Pi_S(r_0)||$ and $\mathfrak{D}_{\mathfrak{e}}(r_0)$ as functions of the homogenised radius r_0.

The cell problem is solved on the geometry shown in Figure 5.2 (b), and we use the

inbuilt 'General Form PDE' for the governing equation where,

$$\mathbf{r} = \chi_k,\ e_a = 0,\ d_a = 0,\ \mathbf{\Theta} = \boldsymbol{\nabla}_{\mathbf{y}}\chi_k + \hat{\mathbf{e}}_k,\ f = 0, \tag{5.92}$$

for $k = 1, \ldots, 3$.

For the boundary condition on Γ, *i.e.*, the tuber, we use the inbuilt flux boundary condition that takes the form,

$$\hat{\mathbf{n}} \cdot \mathbf{\Theta} = g_1 - g_2\mathbf{r}, \tag{5.93}$$

where $g_1 = 0$ and $g_2 = 0$.

On the external boundaries of the cell $\partial\Pi_E$ we impose three sets of 'Periodic Boundary Conditions', so that each pair of opposite external boundaries are an effective continuum. Furthermore, since (5.66) has a non-unique solution, we are required to impose a 'Pointwise Constraint' such that COMSOL can find a specific solution. As $||\Pi_S(r_0)||$ does not depend on the solution to the cell problem, and $\mathfrak{D}_e(r_0)$ depends only on the gradient of the solution (which is unique), this arbitrary choice of a specific solution does not affect the final result.

5.3.2 Results

To validate the homogenisation procedure we compare the homogenised equations (5.78) − (5.81) against the original set of equations (5.41) − (5.47). We choose to run a series of case studies by varying the parameters $b,\ \overline{F}$ and $\phi_w|_{t=0}$. For the buffer power b we choose the values $b \in \{0.5, 5\}$ since this covers a range of buffer powers for the nutrients nitrogen, boron, magnesium, zinc and molybdenum [27]. From the non-dimensionalisation and parameter estimation we observe the value for root water uptake is $\overline{F} = \mathcal{O}(1)$. However to test the homogenisation procedure, we select the values $\overline{F} \in \{0.1, 10\}$ for low and high levels of water uptake respectively. Finally, for the initial porosity $\phi_w|_{t=0}$ we assign the values $\phi_w|_{t=0} \in \{0.4, 0.6\}$ as these are approximate upper and lower bounds for silty soils [203].

In each of the simulations we impose a Dirichlet condition of $c = c_0 = 1$ on the top of each of the geometries shown in Figure 5.2 (a). Additionally, we choose the initial non-dimensionalised tuber radius to be $\overline{r^*} = 0.025$ and choose the remaining parameters to be $\overline{\xi} = \overline{\alpha} = 1$. We also impose a stop condition on each of the simulations so that when the non-dimensionalised volume of a tuber has doubled, the simulation is terminated. Finally, in order to construct interpolated functions to describe $||\Pi_S(r_0)||$ and $\mathfrak{D}_{\mathfrak{e}}(r_0)$ in equations (5.79) and (5.80), we solve 6 cell

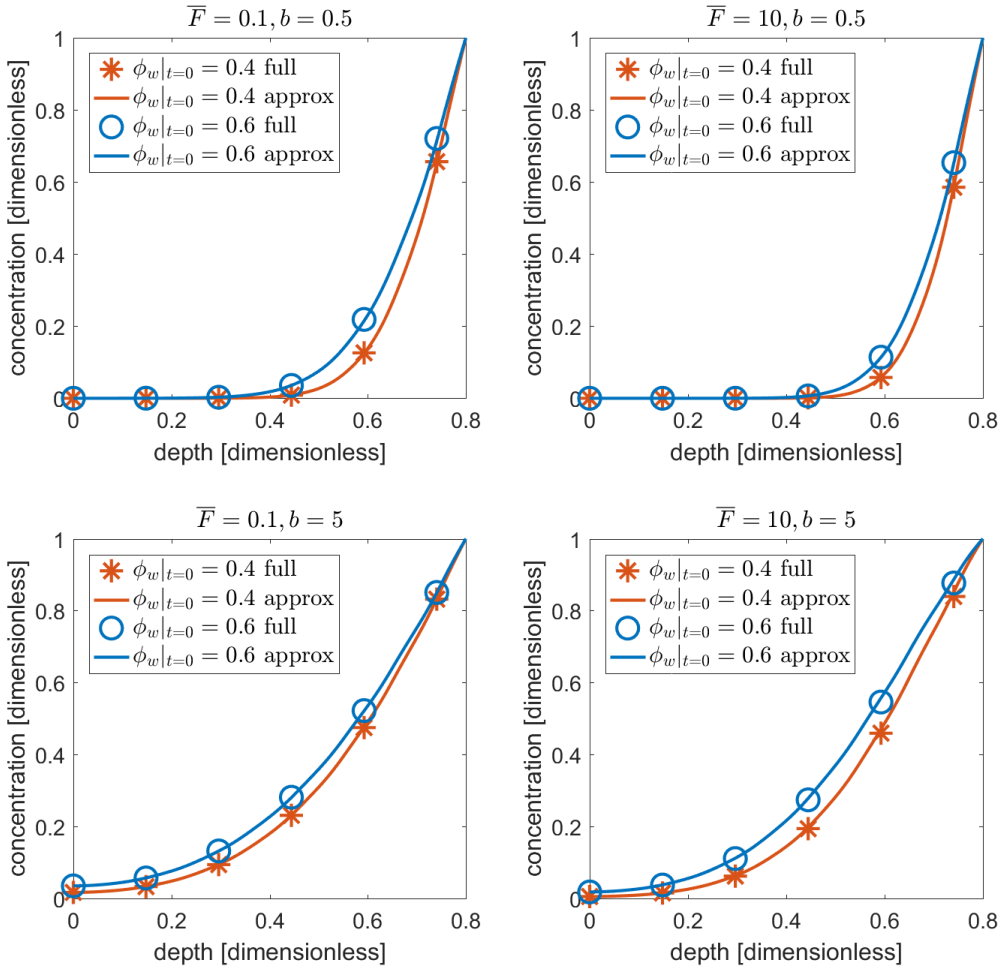

Figure 5.3: Validation of homogenised equations (5.78) − (5.81) against the original set of equations (5.41) − (5.47). The plots show the nutrient profile c and c_0 down the length of the domains shown in Figure 5.2 (a) for a series of case studies using the parameter values $b \in \{0.5, 5\}$, $\overline{F} \in \{0.1, 10\}$, $\phi_w|_{t=0} \in \{0.4, 0.6\}$.

problems in radius increments of 0.02 from a sphere radius of $r = 0.25$ to a sphere radius $r = 0.35$.

Shown in Figure 5.3 are the nutrient profiles for c and c_0 down the length of the geometries shown in Figure 5.2 (a). We observe for all buffer powers, root uptake values and initial porosities, the homogenised nutrient profile for c_0 is qualitatively identical to the full nutrient concentration c. We find there to be a maximum error of $\lesssim 2\%$ between the solutions across all scenarios.

Additionally, shown in Figure 5.4 are the individual tuber radii r_j for the full set of equations and the approximate radius r_0 from the homogenised equations. We find that the effective radius r_0 successfully captures the growth of each tuber within the

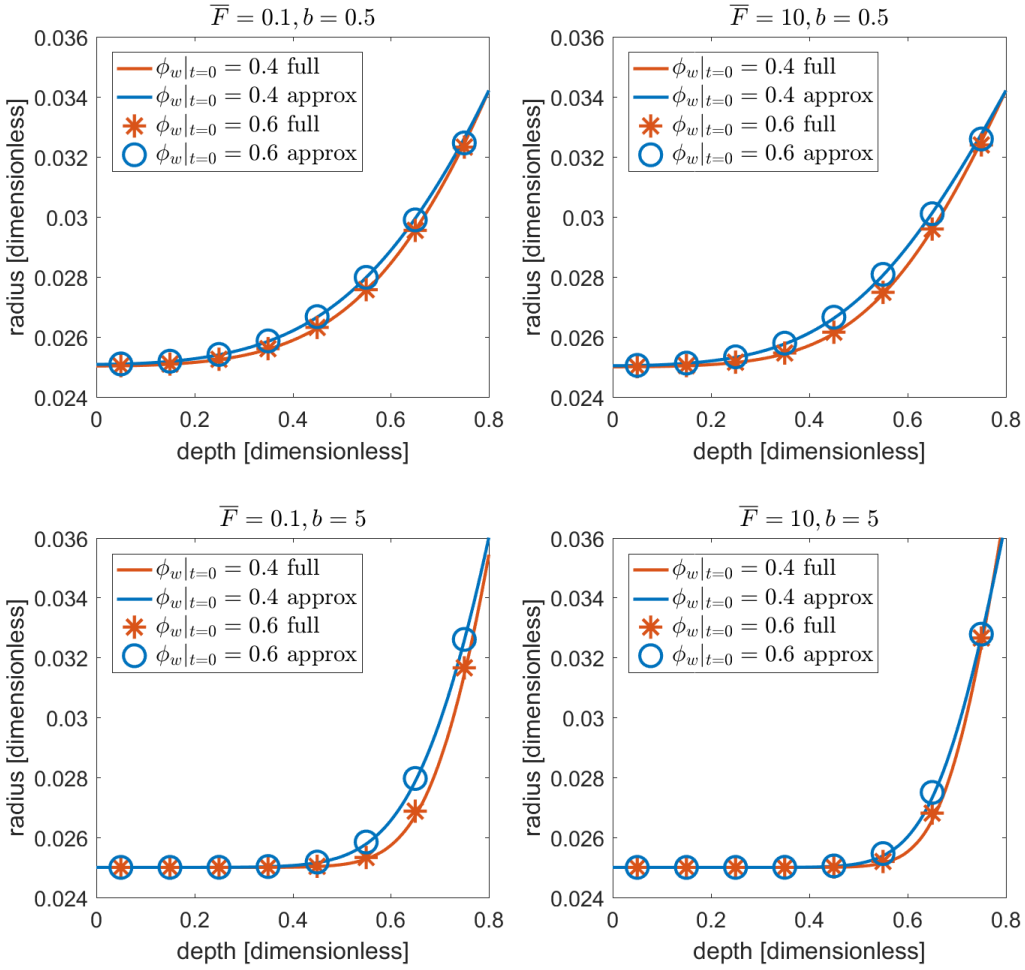

Figure 5.4: Validation of homogenised equations (5.78) − (5.81) against the original set of equations (5.41) − (5.47). The plots show the effective radius r_0 against the actual radius r_j of the tubers down the length of the domains shown in Figure 5.2 (a) for a series of case studies using the parameter values $b \in \{0.5, 5\}$, $\overline{F} \in \{0.1, 10\}$, $\phi_w|_{t=0} \in \{0.4, 0.6\}$.

full domain shown in Figure 5.2 (a). We find there to be a maximum error of $\lesssim 2\%$ between the actual and effective tuber radius.

To highlight the accuracy of the homogenised set of equations, shown in Figure 5.5 are detailed results for the simulation using the parameters $\overline{F} = 0.1, b = 0.5$ and $\phi_w|_{t=0} = 0.4$. From Figure 5.5 (a) we observe that the effective radius r_0 is able to mimic the growth of the tubers in the full geometry. The growing tubers can be seen in Figure 5.5 (b), in which the tubers at the top of the full equation domain at the time point $t =$ end have grown substantially larger than those at the base of the domain. Furthermore, we find that the solute concentration profiles exhibit identical traits between the full and homogenised domains.

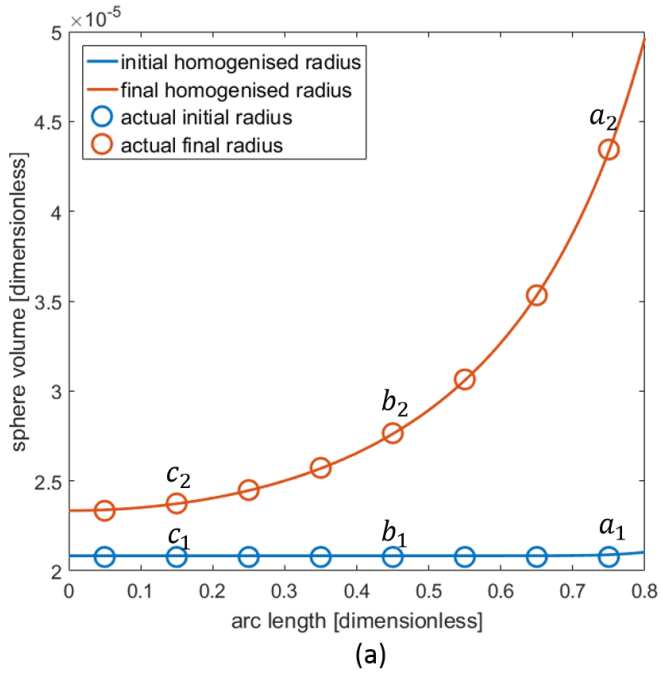

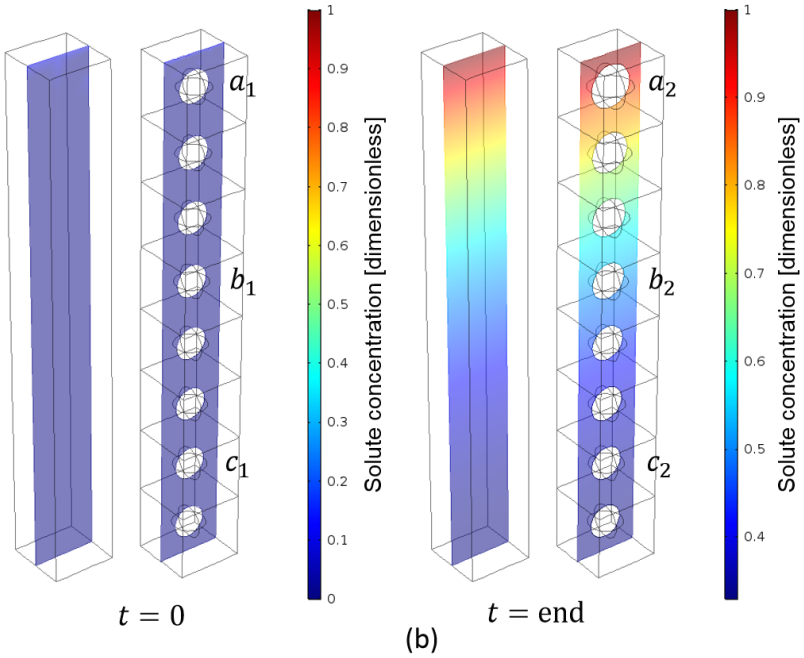

Figure 5.5: (a): Shown are the results for the actual and effective tuber volumes for the simulation using the parameters $\overline{F} = 0.1, b = 0.5$ and $\phi_w|_{t=0} = 0.4$ at the beginning and end of the simulation.
(b): Shown are the results for the actual and effective solute concentration for the same simulation as (a). Additionally the geometries capturing the tuber growth are shown.

From Figures 5.3 and 5.4, we observe that the homogenised equations successfully capture the nutrient movement and tuber growth in soil. However, the computation time for the two systems of equations differs by several orders of magnitude. We

find that the full set of equations in three dimensions requires ≈ 5 minutes (300 seconds) to solve one simulation for eight periodic cells. Conversely, solving the homogenised equations requires ≈ 10 seconds to solve an analogous 3D simulation. Furthermore, the homogenised set of equations can be reduced to a 1D problem which will achieve the same results as the 3D problem due to the homogenisation procedure. We find that the computation time to solve the 1D problem is $\ll 1$ second, which is substantially faster than the full set of equations. However, a set of 3D cell problems is required to parameterise the homogenised set of equations for the terms $||\Pi_S(r_0)||$ and $\mathfrak{D}_\epsilon(r_0)$. In this case study, we chose to conduct six cell problems for varying sphere radii. Each of the cell problems requires ≈ 10 seconds to solve. However, these cell problems are only required to be solved once for each set of parameters. Hence, we find that the homogenised set of equations can reduce the computation time substantially whilst retaining a high level of accuracy.

5.4 Conclusions

In this chapter, we derived a set of averaged equations that describe the macroscopic transport of nutrients in a partially saturated soil with growing potato tubers. We used the method of multiple scale homogenisation that uses a set of representative cell problems to parametrise the averaged equations, which are based on the microscopic properties of the domain. We described the movement of nutrients that are taken up by roots in soil, which induced growth of potato tubers and in turn compress the surrounding soil, thereby changing the rate of nutrient diffusion and the total volume of soil.

The full system equations required the implementation of a complex moving boundary problem. This required the use of multiple domains to solve different components of the equations, and subsequent mappings of solutions across domains. Not only does this system require considerable computational power to solve, the time required to correctly implement this system is substantial. This is due to ensuring conservation of mass and consistent mappings of solutions across domains. However, the homogenisation procedure eliminates this problem by reducing the system to coupled system of PDEs with a series of cell problems. This removes the need for moving boundaries and domain mappings, which considerably reduces implementation time.

We made the assumption prior to the homogenisation procedure that the water content was primarily dominated by the water uptake from plant roots, and was negligibly affected by compaction effects. To justify this assumption, we validated

the homogenisation procedure by comparing the homogenised set of equations to the full set of governing equations, which showed solutions that differed by a maximum of $\lesssim 2\%$ between the actual and effective tuber radius, and $\lesssim 2\%$ between the actual and effective nutrient concentration. Furthermore, we showed that the computation time between the homogenised and full sets of equations differed by a factor of $\mathcal{O}(10^3)$ for a set of eight periodic cells. However, the time required to solve the full set of equations would increase substantially for a greater number of cells, for example, a large cluster of potatoes in soil, whilst the homogenised set of equations would require approximately the same amount of time. In addition, we found that the considerable reduction in computation time did not compromise the results, as we observed that a high level of accuracy is retained. This can aid in analysing large series of case studies for solute movement in poroelastic domains, such as modelling fertiliser applications for optimal crop growth in arable fields.

Chapter 6

Conclusions and Further Work

In this thesis we have developed mathematical models to describe multiple soil processes in different soil structures. The key processes we considered were water movement, solute transport, dynamic ponding and soil compaction. Particular attention was paid to the surface of the soil that resulted from different cultivation methods. Each of the four technical chapters of this thesis were concerned with modelling a particular aspect of the processes described above. In this chapter, we summarise the results and consider ways in which this work could be extended.

In Chapter 2 we developed a system of equations that described the movement of water in soil for a generalised ridge and furrow soil domain. Soil water movement was coupled to dynamic ponding on the ridged soil surface as a function of rainfall, surface runoff, infiltration and surface topology. We validated the model using data from a ridge and furrow study that measured the infiltration time of a pond into a loam soil, and found a difference of $\approx 4\%$ between the results of the study and the results found in the simulation using the model.

In Chapter 3, we extended the model from Chapter 2 to include solute transport to develop a coupled system of equations for water movement, solute transport and dynamic ponding in generalised ridge and furrow systems. Using the model we presented a comparison of water and solute movement between two key soil geometries: a ridge and furrow geometry, and a flat planting geometry. We simulated the movement of solutes with varying mobility and degradation in the two geometries to observe how the structure of the soil surface topology influences solute movement. The numeric modelling results showed that the ridge and furrow structure could either impede or increase the penetration of solutes in soil, depending on the immediate rainfall activity after a solute application and the quantity of roots in the soil. For scenarios in which rainfall generated substantial ponding immediately after a solute application, we found that water infiltration

from the surface acted as a dominant transport mechanism for solutes in the furrow of the soil. This caused solutes in the soil adjacent to the furrow to move to a significantly greater depth when compared to the flat soil domain, where the influence of ponding is not as substantial. However, we found that these trends are reversed for scenarios where there is not considerable ponding after a solute application. In these cases we observed that, with the presence of roots in the ridges, this caused a dominant pressure gradient to form between the soil water and root xylem. This in turn, caused the solute in the ridge and furrow domain to move toward the roots, where the solute accumulated into a concentrated spot adjacent to the root zone. This effect impedes the movement of the solute compared to the flat soil, as the majority was contained in the ridge and had reduced influence from furrow ponding. This mechanism can potentially reduce the quantity of solute that penetrates deep into the soil.

In Chapter 4, we focused on modelling water movement in the plough layer of soil in which crops were present. Using the model developed in Chapter 2, we constructed a domain that contained harvestable crop products, *i.e.*, potato tubers. We modelled water uptake by the roots and impedance by crops. We used multiple scale homogenisation to derive a set of approximate equations that described water movement in this area of soil, which accounted for the effect of harvestable crop products obstructing water movement. We validated the homogenisation procedure by comparing the approximate set of homogenised equations to the full set of equations for two different water regimes: partially saturated and variably saturated soil. We found there to be a difference of $\lesssim 2\%$ between the two sets of solutions for each of these cases. Furthermore, we identified that the time required to conduct the simulations was reduced by a factor of $\mathcal{O}(10^2)$ seconds when using the homogenised equations.

In Chapter 5 we focused on the area of soil contained in the plough layer. We derived a set of equations to describe the movement of nutrients in partially saturated soil that contains growing potato tubers. The soil was modelled as a three-phase poroelastic material, which was deformed by the growth of the tubers, where the growth of each tuber was dependent on the uptake of nutrients via a sink term representing root uptake. We used multiple scale homogenisation to develop an approximate set of equations that described the macoscopic transport of nutrients and the effective growth of potato tubers in the soil. We validated the homogenisation procedure by comparing the homogenised set of equations to the full set of governing equations, which showed the solutions differed by a maximum of $\lesssim 2\%$ between the actual and effective tuber radius, and $\lesssim 2\%$ between the actual and effective nutrient concentration. We showed that the computation time

between the homogenised and full sets of equations differed by a factor of $\mathcal{O}(10^3)$.

There are several natural ways to evolve the work conducted in this thesis. The mathematical model in Chapter 3 for water and solute movement in a generalised ridge and furrow soil domain can be extended in several directions. One of the key extensions is consistent experimental verification of the mathematical model in ridge and furrow fields. Although the numerical simulations replicate the results found qualitatively in experimental studies, there is a lack of specific water and solute data sets with which to compare and parameterise the model. Experimental measurements of water and solute movement in ridge and furrow structures would allow us to fully calibrate the model leading to more accurate results.

Along with experimental support, there are many ways to incorporate multiple new components into the models themselves. For example, it is well known that different cultivation methods alter the porosity, water retention permeability and structure within the plough layer of soil. Hence, understanding the spatial resolution of different soil parameters such as porosity and suction pressure would allow for a more representative system. Similarly, knowledge of aspects such as the root architecture would influence the movement of water and solutes in soil. These are simple additions given the implementation of the mathematical model. Hence, these types of extensions would require minimum work to implement successfully, however, acquisition of the data would require additional experiments. Adding new physics such as transpiration or other biological processes into the model may also be an additional path to explore, such as incorporating above-ground processes to generate a complete system of water and solute movement in crops.

In the original derivation of the ponding model, we considered the soil surface and below, *i.e.*, the soil system only. However, we are aware that the foliage from potato plants can influence the distribution of solutes that are applied to soil due to the leaves obstructing direct movement to the ground. Coupling the solute and water movement in the below ground system with a mathematical model for the above ground system including plant obstruction would encompass a more realistic approach.

In Chapter 5, we developed a mathematical model that described solute movement in a poroelastic soil domain in which there were growing crops. A clear progression to extend this mathematical model is to incorporate water movement such that within the poroelastic soil domain there is both water movement and solute transport. Creating a coupled system of solute and water movement in a poroelastic domain would encompass the key processes that are active in the plough layer of soil. This could then be incorporated into the model from Chapter 3 to have a

distinctive ‘sub-model’ in the plough layer of soil that accounted for the growth of tubers in soil. Additionally, this could be further extended by incorporating other factors, such as tuber densities varying with depth, since in the model derivation we assumed a uniform distribution of tubers. This would generate a more complete description of ridge and furrow systems, which could then be used to understand the optimum depth and growth conditions for crops such as potatoes.

In this thesis we have developed new models to describe ridge and furrow soil geometries that will form the backbone of future developments in this field. With the rapid improvements in computation power, a complete mathematical system describing the processes in and above soil may soon be a reality.

Bibliography

[1] Food Department for Environment and Rural Affairs, "The British survey of fertiliser practice fertiliser use on farm for the 2016 crop year," 2017.

[2] Food Department for Environment and Rural Affairs, "Agriculture in the united kingdom 2016," 2017.

[3] Food Department for Environment and Rural Affairs, "Pesticide usage survey report 263 - arable crops in the United Kingdom 2016," 2017.

[4] J. N. Pretty, C. Brett, D. Gee, R. Hine, C. Mason, J. Morison, H. Raven, M. Rayment, and G. Van der Bijl, "An assessment of the total external costs of UK agriculture," *Agricultural systems*, vol. 65, no. 2, pp. 113–136, 2000.

[5] R. Tirado and M. Allsopp, "Phosphorus in agriculture: problems and solutions," *Greenpeace Research Laboratories Technical Report (Review)*, vol. 2, 2012.

[6] R. Xu, R. Kuang, E. Pay, H. Dou, and G. R. de Snoo, "Factors contributing to overuse of pesticides in western china," *Environmental Sciences*, vol. 5, no. 4, pp. 235–249, 2008.

[7] A. N. Sharpley, S. Chapra, R. Wedepohl, J. Sims, T. C. Daniel, and K. Reddy, "Managing agricultural phosphorus for protection of surface waters: Issues and options," *Journal of environmental quality*, vol. 23, no. 3, pp. 437–451, 1994.

[8] R. Austin, "Yield of wheat in the United Kingdom: recent advances and prospects," *Crop Science*, vol. 39, no. 6, pp. 1604–1610, 1999.

[9] G. R. Conway and J. N. Pretty, *Unwelcome harvest: agriculture and pollution*. Routledge, 2013.

[10] P. J. Withers, A. Edwards, and R. Foy, "Phosphorus cycling in UK agriculture and implications for phosphorus loss from soil," *Soil use and Management*, vol. 17, no. 3, pp. 139–149, 2001.

[11] A. Johnston and P. Poulton, "role of phosphorus in crop production and soil fertility: 150 years of field experiments at rothamsted, United Kingdom," in *Phosphate fertilizers and the environment: proceedings of an international workshop/edited by JJ Schultz*, Tampa, Fla.: International Fertilizer Development Center, 1992.

[12] A. L. Heathwaite and P. O'Sullivan, "Sequential inorganic chemical analysis of a core from slapton ley, devon, UK," *Hydrobiologia*, vol. 214, no. 1, pp. 125–135, 1991.

[13] R. W. Scholz, A. E. Ulrich, M. Eilittä, and A. Roy, "Sustainable use of phosphorus: a finite resource," *Science of the Total Environment*, vol. 461, pp. 799–803, 2013.

[14] P. Déry and B. Anderson, "Peak phosphorus," *Energy Bulletin*, vol. 13, 2007.

[15] R. H. Phipps and J. Park, "Environmental benefits of genetically modified crops: global and european perspectives on their ability to reduce pesticide use," *Journal of Animal and Feed sciences*, vol. 11, no. 1, pp. 1–18, 2002.

[16] C. A. Damalas, "Understanding benefits and risks of pesticide use," *Scientific Research and Essays*, vol. 4, no. 10, pp. 945–949, 2009.

[17] D. B. Jaynes and J. Swan, "Solute movement in uncropped ridge-tilled soil under natural rainfall," *Soil Science Society of America Journal*, vol. 63, no. 2, pp. 264–269, 1999.

[18] L. Alletto, Y. Coquet, P. Benoit, D. Heddadj, and E. Barriuso, "Tillage management effects on pesticide fate in soils. a review," *Agronomy for sustainable development*, vol. 30, no. 2, pp. 367–400, 2010.

[19] H. Vereecken, A. Schnepf, J. W. Hopmans, M. Javaux, D. Or, T. Roose, J. Vanderborght, M. Young, W. Amelung, M. Aitkenhead, *et al.*, "Modeling soil processes: Review, key challenges, and new perspectives," *Vadose Zone Journal*, vol. 15, no. 5, 2016.

[20] T. Roose, S. Keyes, K. Daly, A. Carminati, W. Otten, D. Vetterlein, and S. Peth, "Challenges in imaging and predictive modeling of rhizosphere processes," *Plant and Soil*, vol. 407, no. 1-2, pp. 9–38, 2016.

[21] K. Daly, L. Cooper, N. Koebernick, J. Evaristo, S. Keyes, A. Van Veelen, and T. Roose, "Modelling water dynamics in the rhizosphere," *Rhizosphere*, 2017.

[22] D. D. Richter and D. Markewitz, "How deep is soil?," *BioScience*, vol. 45, no. 9, pp. 600–609, 1995.

[23] M. Baldwin, C. E. Kellogg, and J. Thorp, *Soil classification*. Bobbs-Merrill Indianapolis, 1938.

[24] D. Boorman, J. M. Hollis, and A. Lilly, *Hydrology of soil types: a hydrologically-based classification of the soils of United Kingdom*. Institute of Hydrology, 1995.

[25] F. P. Shepard, "Nomenclature based on sand-silt-clay ratios," *Journal of Sedimentary Research*, vol. 24, no. 3, 1954.

[26] C. K. Wentworth, "A scale of grade and class terms for clastic sediments," *The journal of geology*, vol. 30, no. 5, pp. 377–392, 1922.

[27] S. A. Barber, *Soil nutrient bioavailability: a mechanistic approach*. John Wiley & Sons, 1995.

[28] D. A. Angers and J. Caron, "Plant-induced changes in soil structure: processes and feedbacks," *Biogeochemistry*, vol. 42, no. 1-2, pp. 55–72, 1998.

[29] W. H. Wischmeier and J. Mannering, "Relation of soil properties to its erodibility 1," *Soil Science Society of America Journal*, vol. 33, no. 1, pp. 131–137, 1969.

[30] H. L. Bohn, R. A. Myer, and G. A. O'Connor, *Soil chemistry*. John Wiley & Sons, 2002.

[31] C. D. Shackelford and D. E. Daniel, "Diffusion in saturated soil. ii: Results for compacted clay," *Journal of Geotechnical Engineering*, vol. 117, no. 3, pp. 485–506, 1991.

[32] N. C. Brady and H. O. Buckman, "The nature and properties of soils.," 1974.

[33] J. M. Tisdall and J. Oades, "Organic matter and water-stable aggregates in soils," *European Journal of Soil Science*, vol. 33, no. 2, pp. 141–163, 1982.

[34] J. Six, R. Conant, E. A. Paul, and K. Paustian, "Stabilization mechanisms of soil organic matter: implications for c-saturation of soils," *Plant and soil*, vol. 241, no. 2, pp. 155–176, 2002.

[35] R. L. Daddow and G. Warrington, *Growth-limiting soil bulk densities as influenced by soil texture*. Watershed Systems Development Group, USDA Forest Service Fort Collins, CO, 1983.

[36] C. J. Rhodes, "Feeding and healing the world: through regenerative agriculture and permaculture," *Science progress*, vol. 95, no. 4, pp. 345–446, 2012.

[37] D. K. Todd, *Groundwater hydrology 2ed*. John Wiley, 1980.

[38] R. G. Shepherd, "Correlations of permeability and grain size," *Groundwater*, vol. 27, no. 5, pp. 633–638, 1989.

[39] D. Han, *Concise hydrology*. Bookboon, 2010.

[40] J. Bear and Y. Bachmat, *Introduction to modeling of transport phenomena in porous media*, vol. 4. Springer Science & Business Media, 2012.

[41] T. Roose and A. Fowler, "A mathematical model for water and nutrient uptake by plant root systems," *Journal of theoretical biology*, vol. 228, no. 2, pp. 173–184, 2004.

[42] M. Hattendorf, M. Redelfs, B. Amos, L. Stone, and R. Gwin, "Comparative water use characteristics of six row crops," *Agronomy Journal*, vol. 80, no. 1, pp. 80–85, 1988.

[43] W. Lewis and R. Rowberry, "Some effects of planting depth and time and height of hilling on kennebec and sebago potatoes," *American Potato Journal*, vol. 50, no. 9, pp. 301–310, 1973.

[44] D. Robinson, "A comparison of soil-water distribution under ridge and bed cultivated potatoes," *Agricultural Water Management*, vol. 42, no. 2, pp. 189–204, 1999.

[45] W. Fahong, W. Xuqing, and K. Sayre, "Comparison of conventional, flood irrigated, flat planting with furrow irrigated, raised bed planting for winter wheat in china," *Field Crops Research*, vol. 87, no. 1, pp. 35–42, 2004.

[46] C. Mundy, N. G. Creamer, C. R. Crozier, and L. G. Wilson, "Potato production on wide beds: Impact on yield and selected soil physical characteristics," *American journal of potato research*, vol. 76, no. 6, pp. 323–330, 1999.

[47] D. D. Steele, R. G. Greenland, and H. M. Hatterman-Valenti, "Furrow vs hill planting of sprinkler-irrigated russet burbank potatoes on coarse-textured soils," *American journal of potato research*, vol. 83, no. 3, pp. 249–257, 2006.

[48] X.-L. Wang, F.-M. Li, Y. Jia, and W.-Q. Shi, "Increasing potato yields with additional water and increased soil temperature," *Agricultural Water Management*, vol. 78, no. 3, pp. 181–194, 2005.

[49] M. O. Jordan, K. A. Kelling, B. Lowery, F. J. Arriaga, and P. E. Speth, "Hill shape influences on potato yield, quality, and nitrogen use efficiency," *American journal of potato research*, vol. 90, no. 3, pp. 217–228, 2013.

[50] M. Leistra and J. J. Boesten, "Pesticide leaching from agricultural fields with ridges and furrows," *Water, Air, & Soil Pollution*, vol. 213, no. 1-4, pp. 341–352, 2010.

[51] J. Benjamin, A. Blaylock, H. Brown, and R. Cruse, "Ridge tillage effects on simulated water and heat transport," *Soil and Tillage Research*, vol. 18, no. 2, pp. 167–180, 1990.

[52] R. A. Feddes, P. Kowalik, K. Kolinska-Malinka, and H. Zaradny, "Simulation of field water uptake by plants using a soil water dependent root extraction function," *Journal of Hydrology*, vol. 31, no. 1-2, pp. 13–26, 1976.

[53] J. Tisdall and A. Hodgson, "Ridge tillage in australia: a review," *Soil and tillage research*, vol. 18, no. 2-3, pp. 127–144, 1990.

[54] D. Fryrear, "Soil losses by wind erosion," *Soil Science Society of America Journal*, vol. 59, no. 3, pp. 668–672, 1995.

[55] D. Armbrust, W. Chepil, and F. Siddoway, "Effects of ridges on erosion of soil by wind 1," *Soil Science Society of America Journal*, vol. 28, no. 4, pp. 557–560, 1964.

[56] J. Kouwenhoven, "Yield, grading and distribution of potatoes in ridges in relation to planting depth and ridge size," *Potato Research*, vol. 13, no. 1, pp. 59–77, 1970.

[57] R. Li, X. Hou, Z. Jia, Q. Han, X. Ren, and B. Yang, "Effects on soil temperature, moisture, and maize yield of cultivation with ridge and furrow mulching in the rainfed area of the loess plateau, china," *Agricultural Water Management*, vol. 116, pp. 101–109, 2013.

[58] J. Kettering, M. Ruidisch, C. Gaviria, Y. S. Ok, and Y. Kuzyakov, "Fate of fertilizer 15n in intensive ridge cultivation with plastic mulching under a monsoon climate," *Nutrient cycling in agroecosystems*, vol. 95, no. 1, pp. 57–72, 2013.

[59] G. A. Lehrsch, R. Sojka, and D. Westermann, "Nitrogen placement, row spacing, and furrow irrigation water positioning effects on corn yield," *Agronomy Journal*, vol. 92, no. 6, pp. 1266–1275, 2000.

[60] C. D. Ockleford, "Scientific opinion on the report of the focus groundwater working group (focus, 2009): assessment of higher tiers," *EFSA Journal*, vol. 11, no. 6, 2013.

[61] C. Van Loon, "The effect of water stress on potato growth, development, and yield," *American Potato Journal*, vol. 58, no. 1, pp. 51–69, 1981.

[62] M. Pérombelon, "Potato blackleg: epidemiology, host-pathogen interaction and control," *Netherlands Journal of Plant Pathology*, vol. 98, no. 2, pp. 135–146, 1992.

[63] M. Perombelon and R. Lowe, "Studies on the initiation of bacterial soft rot in potato tubers," *Potato Research*, vol. 18, no. 1, pp. 64–82, 1975.

[64] R. Czajkowski, M. C. Perombelon, J. A. van Veen, and J. M. van der Wolf, "Control of blackleg and tuber soft rot of potato caused by pectobacterium and dickeya species: a review," *Plant pathology*, vol. 60, no. 6, pp. 999–1013, 2011.

[65] M. Pavek and R. Thornton, "Planting depth influences potato plant morphology and economic value," *American journal of potato research*, vol. 86, no. 1, p. 56, 2009.

[66] D. Firman, P. O'Brien, and E. Allen, "Predicting the emergence of potato sprouts," *The Journal of Agricultural Science*, vol. 118, no. 1, pp. 55–61, 1992.

[67] W. H. Bohl and S. L. Love, "Effect of planting depth and hilling practices on total, us no. 1, and field greening tuber yields," *American journal of potato research*, vol. 82, no. 6, pp. 441–450, 2005.

[68] J. Bear, *Hydraulics of groundwater*. Courier Corporation, 2012.

[69] D. D. Joseph and L. Tao, "Lubrication of a porous bearing stokes solution," *Journal of Applied Mechanics*, vol. 33, no. 4, pp. 753–760, 1966.

[70] L. Tao and D. Joseph, "Fluid flow between porous rollers," *Journal of Applied Mechanics*, vol. 29, no. 2, pp. 429–433, 1962.

[71] D. Nield, "The Beavers–Joseph boundary condition and related matters: a historical and critical note," *Transport in porous media*, vol. 78, no. 3, p. 537, 2009.

[72] G. S. Beavers and D. D. Joseph, "Boundary conditions at a naturally permeable wall," *Journal of fluid mechanics*, vol. 30, no. 1, pp. 197–207, 1967.

[73] A. Mikelic and W. Jäger, "On the interface boundary condition of beavers, joseph, and saffman," *SIAM Journal on Applied Mathematics*, vol. 60, no. 4, pp. 1111–1127, 2000.

[74] G. S. Beavers, E. M. Sparrow, and R. A. Magnuson, "Experiments on coupled parallel flows in a channel and a bounding porous medium," *Journal of Basic Engineering*, vol. 92, no. 4, pp. 843–848, 1970.

[75] G. t. Taylor, "A model for the boundary condition of a porous material. part 1," *Journal of Fluid Mechanics*, vol. 49, no. 2, pp. 319–326, 1971.

[76] G. Beavers, E. Sparrow, and B. Masha, "Boundary condition at a porous surface which bounds a fluid flow," *AIChE Journal*, vol. 20, no. 3, pp. 596–597, 1974.

[77] P. G. Saffman, "On the boundary condition at the surface of a porous medium," *Studies in applied mathematics*, vol. 50, no. 2, pp. 93–101, 1971.

[78] J.-L. Auriault, "About the beavers and joseph boundary condition," *Transport in porous media*, vol. 83, no. 2, pp. 257–266, 2010.

[79] N. Jarvis, P.-E. Jansson, P. Dik, and I. Messing, "Modelling water and solute transport in macroporous soil. i. model description and sensitivity analysis," *European Journal of Soil Science*, vol. 42, no. 1, pp. 59–70, 1991.

[80] J. Kool and J. Parker, "Analysis of the inverse problem for transient unsaturated flow," *Water Resources Research*, vol. 24, no. 6, pp. 817–830, 1988.

[81] A. Gardenas, J. Hopmans, B. Hanson, and J. Simunek, "Two-dimensional modeling of nitrate leaching for various fertigation scenarios under micro-irrigation," *Agricultural water management*, vol. 74, no. 3, pp. 219–242, 2005.

[82] T. Vogel, H. Gerke, R. Zhang, and M. T. Van Genuchten, "Modeling flow and transport in a two-dimensional dual-permeability system with spatially variable hydraulic properties," *Journal of hydrology*, vol. 238, no. 1-2, pp. 78–89, 2000.

[83] N. Patel and T. Rajput, "Dynamics and modeling of soil water under subsurface drip irrigated onion," *Agricultural water management*, vol. 95, no. 12, pp. 1335–1349, 2008.

[84] D. L. Ficklin, S. L. Letsinger, H. Gholizadeh, and J. T. Maxwell, "Incorporation of the penman–monteith potential evapotranspiration method into a palmer drought severity index tool," *Computers & Geosciences*, vol. 85, pp. 136–141, 2015.

[85] T. Ramos, J. Simunek, M. Goncalves, J. Martins, A. Prazeres, N. Castanheira, and L. Pereira, "Field evaluation of a multicomponent solute transport model in soils irrigated with saline waters," *Journal of Hydrology*, vol. 407, no. 1-4, pp. 129–144, 2011.

[86] D. Rocha, F. Abbasi, and J. Feyen, "Sensitivity analysis of soil hydraulic properties on subsurface water flow in furrows," *Journal of irrigation and drainage engineering*, vol. 132, no. 4, pp. 418–424, 2006.

[87] M. Camporese, C. Paniconi, M. Putti, and S. Orlandini, "Surface-subsurface flow modeling with path-based runoff routing, boundary condition-based coupling, and assimilation of multisource observation data," *Water Resources Research*, vol. 46, no. 2, 2010.

[88] S. J. Kollet and R. M. Maxwell, "Integrated surface–groundwater flow modeling: A free-surface overland flow boundary condition in a parallel groundwater flow model," *Advances in Water Resources*, vol. 29, no. 7, pp. 945–958, 2006.

[89] S. Weill, E. Mouche, and J. Patin, "A generalized richards equation for surface/subsurface flow modelling," *Journal of Hydrology*, vol. 366, no. 1-4, pp. 9–20, 2009.

[90] D. Tian and D. Liu, "A new integrated surface and subsurface flows model and its verification," *Applied mathematical modelling*, vol. 35, no. 7, pp. 3574–3586, 2011.

[91] S. Panday and P. S. Huyakorn, "A fully coupled physically-based spatially-distributed model for evaluating surface/subsurface flow," *Advances in Water Resources*, vol. 27, no. 4, pp. 361–382, 2004.

[92] X. Li, D. Su, and Q. Yuan, "Ridge-furrow planting of alfalfa (medicago sativa l.) for improved rainwater harvest in rainfed semiarid areas in northwest china," *Soil and Tillage Research*, vol. 93, no. 1, pp. 117–125, 2007.

[93] M. Banti, T. Zissis, and E. Anastasiadou-Partheniou, "Furrow irrigation advance simulation using a surface–subsurface interaction model," *Journal of Irrigation and Drainage Engineering*, vol. 137, no. 5, pp. 304–314, 2010.

[94] H. Ebrahimian, A. Liaghat, M. Parsinejad, E. Playán, F. Abbasi, and M. Navabian, "Simulation of 1d surface and 2d subsurface water flow and nitrate transport in alternate and conventional furrow fertigation," *Irrigation science*, vol. 31, no. 3, pp. 301–316, 2013.

[95] E. Bautista, A. Warrick, and T. Strelkoff, "New results for an approximate method for calculating two-dimensional furrow infiltration," *Journal of irrigation and drainage engineering*, vol. 140, no. 10, p. 04014032, 2014.

[96] D. Zerihun, C. Sanchez, N. Lazarovitch, A. Warrick, A. Clemmens, and E. Bautista, "Modeling flow and solute transport in irrigation furrows," *Irrigation Drainage System Engineering*, vol. 3, p. 124, 2014.

[97] E. Bautista, "Effect of infiltration modeling approach on operational solutions for furrow irrigation," *Journal of Irrigation and Drainage Engineering*, vol. 142, no. 12, p. 06016012, 2016.

[98] M. Tabuada, Z. Rego, G. Vachaud, and L. Pereira, "Two-dimensional infiltration under furrow irrigation: modelling, its validation and applications," *Agricultural water management*, vol. 27, no. 2, pp. 105–123, 1995.

[99] A. G. Segeren and T. J. Trout, "Hydraulic resistance of soil surface seals in irrigated furrows," *Soil Science Society of America Journal*, vol. 55, no. 3, pp. 640–646, 1991.

[100] L. A. Richards, "Capillary conduction of liquids through porous mediums," *Physics*, vol. 1, no. 5, pp. 318–333, 1931.

[101] M. T. Van Genuchten, "A closed-form equation for predicting the hydraulic conductivity of unsaturated soils 1," *Soil science society of America journal*, vol. 44, no. 5, pp. 892–898, 1980.

[102] H. Darcy, "Les fontaines publique de la ville de dijon," *Dalmont, Paris*, vol. 647, 1856.

[103] D. Lesczynski and C. Tanner, "Seasonal variation of root distribution of irrigated, field-grown russet burbank potato," *American Potato Journal*, vol. 53, no. 2, pp. 69–78, 1976.

[104] B. Yang, P. S. Blackwell, and D. F. Nicholson, "A numerical model of heat and water movement in furrow-sown water repellent sandy soils," *Water Resources Research*, vol. 32, no. 10, pp. 3051–3061, 1996.

[105] T. Wohling and G. Schmitz, "Physically based coupled model for simulating 1d surface-2d subsurface flow and plant water uptake in irrigation furrows. i. model development," *Journal of irrigation and drainage engineering*, 2007.

[106] C. Shock, E. Feibert, and L. Saunders, "Potato yield and quality response to deficit irrigation," *HortScience*, vol. 33, no. 4, pp. 655–659, 1998.

[107] S. Duncan, K. Daly, P. Sweeney, and T. Roose, "Mathematical modelling of water and solute movement in ridge plant systems with dynamic ponding," *European Journal of Soil Science*, 2017.

[108] M. Office, *National Meteoroloigcal Library and Archive Fact Sheet 3 - Water in the atmosphere*. 2012.

[109] J. Morin and Y. Benyamini, "Rainfall infiltration into bare soils," *Water Resources Research*, vol. 13, no. 5, pp. 813–817, 1977.

[110] F. Liu, A. Shahnazari, M. N. Andersen, S.-E. Jacobsen, and C. R. Jensen, "Physiological responses of potato (solanum tuberosum l.) to partial root-zone drying: Aba signalling, leaf gas exchange, and water use efficiency," *Journal of Experimental Botany*, vol. 57, no. 14, pp. 3727–3735, 2006.

[111] P. R. Amestoy, I. S. Duff, J.-Y. L'Excellent, and J. Koster, "Mumps: a general purpose distributed memory sparse solver," in *International Workshop on Applied Parallel Computing*, pp. 121–130, Springer, 2000.

[112] A. A. Siyal, K. L. Bristow, and J. Šimůnek, "Minimizing nitrogen leaching from furrow irrigation through novel fertilizer placement and soil surface management strategies," *Agricultural Water Management*, vol. 115, pp. 242–251, 2012.

[113] S. H. Ahmadi, F. Plauborg, M. N. Andersen, A. R. Sepaskhah, C. R. Jensen, and S. Hansen, "Effects of irrigation strategies and soils on field grown potatoes: root distribution," *Agricultural Water Management*, vol. 98, no. 8, pp. 1280–1290, 2011.

[114] M. Kirkham, D. Keeney, and W. Gardner, "Uptake of water and labelled nitrate at different depths in the root zone of potato plants grown on a sandy soil," *Agro-ecosystems*, vol. 1, pp. 31–44, 1974.

[115] E. Steudle, R. Oren, and E.-D. Schulze, "Water transport in maize roots: measurement of hydraulic conductivity, solute permeability, and of reflection

coefficients of excised roots using the root pressure probe," *Plant Physiology*, vol. 84, no. 4, pp. 1220–1232, 1987.

[116] D. Rawsthorne and B. Brodie, "Relationship between root growth of potato, root diffusate production, and hatching of globodera rostochiensis," *Journal of Nematology*, vol. 18, no. 3, p. 379, 1986.

[117] P. Gandar and C. Tanner, "Leaf growth, tuber growth, and water potential in potatoes 1," *Crop Science*, vol. 16, no. 4, pp. 534–538, 1976.

[118] R. Azooz and M. Arshad, "Soil infiltration and hydraulic conductivity under long-term no-tillage and conventional tillage systems," *Canadian Journal of Soil Science*, vol. 76, no. 2, pp. 143–152, 1996.

[119] J. Wayman, "Experiments to investigate some of the problems in mechanisation associated with the cultivation of potatoes in beds," *European Potato Journal*, vol. 12, no. 4, pp. 200–214, 1969.

[120] L. Huaccho and R. J. Hijmans, *A global geo-referenced database of potato distribution for 1995-1997 (GPOT97)*. International Potato Center (CIP), 1999.

[121] A. Alva, T. Hodges, R. Boydston, and H. Collins, "Effects of irrigation and tillage practices on yield of potato under high production conditions in the pacific northwest," *Communications in Soil Science and Plant Analysis*, vol. 33, no. 9-10, pp. 1451–1460, 2002.

[122] R. F. Spalding and M. E. Exner, "Occurrence of nitrate in groundwater-a review," *Journal of environmental quality*, vol. 22, no. 3, pp. 392–402, 1993.

[123] J. Smelt, C. Schut, A. Dekker, and M. Leistra, "Movement and conversion of aldicarb and its oxidation products in potato fields," *Netherlands Journal of Plant Pathology*, vol. 87, no. 5, pp. 177–191, 1981.

[124] K. Kung, "Ground truth about water flow pattern in a sandy soil and its influences on solute sampling and transport modeling," in *International conference and workshop on the validation of flow and transport models for the unsaturated zone*, pp. 224–230, 1988.

[125] S. Clay, O. Clay, W. Koskinen, and G. Malzer, "Agrichemical placement impacts on alachlor and nitrate movement through boil in a ridge tillage system," *Journal of Environmental Science & Health Part B*, vol. 27, no. 2, pp. 125–138, 1992.

[126] J. Hatfield, R. Allmaras, G. Rehm, and B. Lowery, "Ridge tillage for corn and soybean production: environmental quality impacts," *Soil and tillage research*, vol. 48, no. 3, pp. 145–154, 1998.

[127] D. Ressler, R. Horton, J. Baker, and T. Kaspar, "Testing a nitrogen fertilizer applicator designed to reduce leaching losses," *Applied Engineering in Agriculture*, vol. 13, no. 3, pp. 345–350, 1997.

[128] R. S. Kanwar, T. S. Colvin, and D. L. Karlen, "Ridge, moldboard, chisel, and no-till effects on tile water quality beneath two cropping systems," *Journal of Production Agriculture*, vol. 10, no. 2, pp. 227–234, 1997.

[129] J. Waddell and R. Weil, "Effects of fertilizer placement on solute leaching under ridge tillage and no tillage," *Soil and Tillage Research*, vol. 90, no. 1-2, pp. 194–204, 2006.

[130] M. Ruidisch, S. Bartsch, J. Kettering, B. Huwe, and S. Frei, "The effect of fertilizer best management practices on nitrate leaching in a plastic mulched ridge cultivation system," *Agriculture, ecosystems & environment*, vol. 169, pp. 21–32, 2013.

[131] J. Mailhol, P. Ruelle, and I. Nemeth, "Impact of fertilisation practices on nitrogen leaching under irrigation," *Irrigation science*, vol. 20, no. 3, pp. 139–147, 2001.

[132] J. Benjamin, L. Ahuja, and R. Allmaras, "Modelling corn rooting patterns and their effects on water uptake and nitrate leaching," *Plant and Soil*, vol. 179, no. 2, pp. 223–232, 1996.

[133] F. Abbasi, F. J. Adamsen, D. J. Hunsaker, J. Feyen, P. Shouse, and M. T. Van Genuchten, "Effects of flow depth on water flow and solute transport in furrow irrigation: Field data analysis," *Journal of irrigation and drainage engineering*, vol. 129, no. 4, pp. 237–246, 2003.

[134] M. Sardin, D. Schweich, F. Leij, and M. T. Genuchten, "Modeling the nonequilibrium transport of linearly interacting solutes in porous media: A review," *Water Resources Research*, vol. 27, no. 9, pp. 2287–2307, 1991.

[135] A. Ogata and R. Banks, *A solution of the differential equation of longitudinal dispersion in porous media: fluid movement in earth materials*, vol. 411. US Government Printing Office, 1961.

[136] M. T. Van Genuchten, W. Alves, *et al.*, "Analytical solutions of the one-dimensional convective-dispersive solute transport equation," tech. rep., United States Department of Agriculture, Economic Research Service, 1982.

[137] R. White, "The transport of chloride and non-diffusible solutes through soil," *Irrigation Science*, vol. 6, no. 1, pp. 3–10, 1985.

[138] S. Iqbal, A. K. Guber, and H. Z. Khan, "Estimating nitrogen leaching losses after compost application in furrow irrigated soils of pakistan using hydrus-2d software," *Agricultural Water Management*, vol. 168, pp. 85–95, 2016.

[139] H. Gerke and M. V. Genuchten, "A dual-porosity model for simulating the preferential movement of water and solutes in structured porous media," *Water resources research*, vol. 29, no. 2, pp. 305–319, 1993.

[140] V. D. Cvetkovic and A. M. Shapiro, "Mass arrival of sorptive solute in heterogeneous porous media," *Water resources research*, vol. 26, no. 9, pp. 2057–2067, 1990.

[141] J.-C. Mailhol, D. Crevoisier, and K. Triki, "Impact of water application conditions on nitrogen leaching under furrow irrigation: Experimental and modelling approaches," *Agricultural Water Management*, vol. 87, no. 3, pp. 275–284, 2007.

[142] D. Crevoisier, Z. Popova, J.-C. Mailhol, and P. Ruelle, "Assessment and simulation of water and nitrogen transfer under furrow irrigation," *Agricultural water management*, vol. 95, no. 4, pp. 354–366, 2008.

[143] A. Tafteh and A. R. Sepaskhah, "Application of hydrus-1d model for simulating water and nitrate leaching from continuous and alternate furrow irrigated rapeseed and maize fields," *Agricultural Water Management*, vol. 113, pp. 19–29, 2012.

[144] T. Roose, A. Fowler, and P. Darrah, "A mathematical model of plant nutrient uptake," *Journal of mathematical biology*, vol. 42, no. 4, pp. 347–360, 2001.

[145] P. H. Nye and P. B. Tinker, *Solute movement in the soil-root system*, vol. 4. Univ of California Press, 1977.

[146] J. B. Weber, G. G. Wilkerson, and C. F. Reinhardt, "Calculating pesticide sorption coefficients (kd) using selected soil properties," *Chemosphere*, vol. 55, no. 2, pp. 157–166, 2004.

[147] B. K. Singh, A. Walker, and D. Wright, "Persistence of chlorpyrifos, fenamiphos, chlorothalonil, and pendimethalin in soil and their effects on soil microbial characteristics," *Bulletin of Environmental Contamination and Toxicology*, vol. 69, no. 2, pp. 181–188, 2002.

[148] B. Sattelmacher, F. Klotz, and H. Marschner, "Influence of the nitrogen level on root growth and morphology of two potato varieties differing in nitrogen acquisition," *Plant and soil*, vol. 123, no. 2, pp. 131–137, 1990.

[149] A. Asfary, A. Wild, and P. Harris, "Growth, mineral nutrition and water use by potato crops," *The Journal of Agricultural Science*, vol. 100, no. 1, pp. 87–101, 1983.

[150] J. Lipiec, J. Kuś, A. Słowińska-Jurkiewicz, and A. Nosalewicz, "Soil porosity and water infiltration as influenced by tillage methods," *Soil and Tillage research*, vol. 89, no. 2, pp. 210–220, 2006.

[151] D. Rowell, M. Martin, and P. Nye, "The measurement and mechanism of ion diffusion in soils iii. the effect of moisture content and soil-solution concentration on the self-diffusion of ions in soils," *European Journal of Soil Science*, vol. 18, no. 2, pp. 204–221, 1967.

[152] T. Noda, Y. Takahata, T. Sato, H. Ikoma, and H. Mochida, "Combined effects of planting and harvesting dates on starch properties of sweet potato roots," *Carbohydrate Polymers*, vol. 33, no. 2-3, pp. 169–176, 1997.

[153] I. S. Fomsgaard, "Degradation of pesticides in subsurface soils, unsaturated zone-a review of methods and results," *International Journal of Environmental Analytical Chemistry*, vol. 58, no. 1-4, pp. 231–245, 1995.

[154] P. J. Rice, T. A. Anderson, and J. R. Coats, "Degradation and persistence of metolachlor in soil: Effects of concentration, soil moisture, soil depth, and sterilization," *Environmental toxicology and chemistry*, vol. 21, no. 12, pp. 2640–2648, 2002.

[155] G. D. Bending and M. S. Rodriguez-Cruz, "Microbial aspects of the interaction between soil depth and biodegradation of the herbicide isoproturon," *Chemosphere*, vol. 66, no. 4, pp. 664–671, 2007.

[156] N. A. Streck, F. L. M. de Paula, D. A. Bisognin, A. B. Heldwein, and J. Dellai, "Simulating the development of field grown potato (solanum tuberosum l.)," *Agricultural and Forest Meteorology*, vol. 142, no. 1, pp. 1–11, 2007.

[157] J. Smethurst, D. Clarke, and W. Powrie, "Seasonal changes in pore water pressure in a grass covered cut slope in london clay," *Géotechnique*, vol. 56, no. 8, pp. 523–537, 2006.

[158] J. Smethurst, D. Clarke, and W. Powrie, "Factors controlling the seasonal variation in soil water content and pore water pressures within a lightly vegetated clay slope," *Géotechnique*, vol. 62, no. 5, pp. 429–446, 2012.

[159] A. Fließbach and P. Mäder, "Short-and long-term effects on soil microorganisms of two potato pesticide spraying sequences with either glufosinate or dinoseb as defoliants," *Biology and fertility of soils*, vol. 40, no. 4, pp. 268–276, 2004.

[160] "Commission regulation (eu) 2018/78 of 16 january 2018 amending annexes ii and iii to regulation (ec) no 396/2005 of the european parliament and of the council as regards maximum residue levels for 2-phenylphenol, bensulfuron-methyl, dimethachlor and lufenuron in or on certain products," *Official Journal of the European Union*, pp. 6–30, 2018.

[161] X. Chen, X. Zhao, P. Wu, Z. Wang, F. Zhang, and Y. Zhang, "Water and nitrogen distribution in uncropped ridgetilled soil under different ridge width," *African Journal of Biotechnology*, vol. 10, no. 55, pp. 11527–11536, 2011.

[162] J. Hamlett, J. Baker, and R. Horton, "Water and anion movement under ridge tillage: a field study," *Transactions of the ASAE*, vol. 33, no. 6, pp. 1859–1866, 1990.

[163] B. Bargar, J. Swan, and D. Jaynes, "Soil water recharge under uncropped ridges and furrows," *Soil Science Society of America Journal*, vol. 63, no. 5, pp. 1290–1299, 1999.

[164] F. Abbasi, J. Feyen, and M. T. Van Genuchten, "Two-dimensional simulation of water flow and solute transport below furrows: model calibration and validation," *Journal of Hydrology*, vol. 290, no. 1-2, pp. 63–79, 2004.

[165] P. Darrah, D. Jones, G. Kirk, and T. Roose, "Modelling the rhizosphere: a review of methods for 'upscaling' to the whole-plant scale," *European Journal of Soil Science*, vol. 57, no. 1, pp. 13–25, 2006.

[166] S. D. Keyes, K. R. Daly, N. J. Gostling, D. L. Jones, P. Talboys, B. R. Pinzer, R. Boardman, I. Sinclair, A. Marchant, and T. Roose, "High resolution synchrotron imaging of wheat root hairs growing in soil and image based

modelling of phosphate uptake," *New Phytologist*, vol. 198, no. 4, pp. 1023–1029, 2013.

[167] P. R. Adler, M. A. Sanderson, A. A. Boateng, P. J. Weimer, and H.-J. G. Jung, "Biomass yield and biofuel quality of switchgrass harvested in fall or spring mention of trade names or commercial products in this publication is solely for the purpose of providing specific information and does not imply recommendation or endorsement by the usda.," *Agronomy Journal*, vol. 98, no. 6, pp. 1518–1525, 2006.

[168] L. Cueto-Felgueroso and R. Juanes, "A phase field model of unsaturated flow," *Water resources research*, vol. 45, no. 10, 2009.

[169] J. Bear, *Dynamics of fluids in porous media*. Courier Corporation, 2013.

[170] D. Łydżba, "Homogenisation theories applied to porous media mechanics," *Journal of theoretical and applied mechanics*, vol. 36, no. 3, pp. 657–679, 1998.

[171] G. Pavliotis and A. Stuart, *Multiscale methods: averaging and homogenization*. Springer Science & Business Media, 2008.

[172] U. Hornung, *Homogenization and porous media*, vol. 6. Springer Science & Business Media, 2012.

[173] J. B. Keller, "Darcy's law for flow in porous media and the two-space method," *Nonlinear partial differential equations in engineering and applied sciences*, vol. 31, pp. 429–443, 1980.

[174] K. R. Daly and T. Roose, "Homogenization of two fluid flow in porous media," *Proc. R. Soc. A*, vol. 471, no. 2176, p. 20140564, 2015.

[175] M. Sharma, "Wave propagation in a general anisotropic poroelastic medium: Biot's theories and homogenisation theory," *Journal of Earth System Science*, vol. 116, no. 4, p. 357, 2007.

[176] T. Arbogast, J. Douglas, Jr, and U. Hornung, "Derivation of the double porosity model of single phase flow via homogenization theory," *SIAM Journal on Mathematical Analysis*, vol. 21, no. 4, pp. 823–836, 1990.

[177] K. Daly and T. Roose, "Determination of macro-scale soil properties from pore-scale structures: model derivation," *Proc. R. Soc. A*, vol. 474, no. 2209, p. 20170141, 2018.

[178] M. Bruna and S. J. Chapman, "Diffusion in spatially varying porous media," *SIAM Journal on Applied Mathematics*, vol. 75, no. 4, pp. 1648–1674, 2015.

[179] K. Chamsri, "Derivation of darcy's law using homogenization method," *World Academy of Science, Engineering and Technology, International Journal of Mathematical, Computational, Physical, Electrical and Computer Engineering*, vol. 7, no. 9, pp. 1399–1403, 2013.

[180] T. Miyazaki, *Water flow in soils*. CRC Press, 2005.

[181] J. Kool, J. Parker, and M. T. Van Genuchten, "Determining soil hydraulic properties from one-step outflow experiments by parameter estimation: I. theory and numerical studies 1," *Soil Science Society of America Journal*, vol. 49, no. 6, pp. 1348–1354, 1985.

[182] M. Hamza and W. Anderson, "Soil compaction in cropping systems: A review of the nature, causes and possible solutions," *Soil and tillage research*, vol. 82, no. 2, pp. 121–145, 2005.

[183] E. Detournay and A. H.-D. Cheng, "Fundamentals of poroelasticity," in *Analysis and design methods*, pp. 113–171, Elsevier, 1995.

[184] H. Wang, *Theory of linear poroelasticity with applications to geomechanics and hydrogeology*. Princeton University Press, 2000.

[185] V. Papathanasopoulou, D. Fotiadis, G. Foutsitzi, and C. Massalas, "A poroelastic bone model for internal remodeling," *International Journal of Engineering Science*, vol. 40, no. 5, pp. 511–530, 2002.

[186] S. C. Cowin, "Bone poroelasticity," *Journal of biomechanics*, vol. 32, no. 3, pp. 217–238, 1999.

[187] J.-M. Kim, "Fully coupled poroelastic governing equations for groundwater flow and solid skeleton deformation in variably saturated true anisotropic porous geologic media," *Geosciences Journal*, vol. 8, no. 3, p. 291, 2004.

[188] H. F. Wang, "Quasi-static poroelastic parameters in rock and their geophysical applications," *pure and applied geophysics*, vol. 141, no. 2-4, pp. 269–286, 1993.

[189] E. Moeendarbary, L. Valon, M. Fritzsche, A. R. Harris, D. A. Moulding, A. J. Thrasher, E. Stride, L. Mahadevan, and G. T. Charras, "The cytoplasm of living cells behaves as a poroelastic material," *Nature materials*, vol. 12, no. 3, p. 253, 2013.

[190] T. Mitchison, G. Charras, and L. Mahadevan, "Implications of a poroelastic cytoplasm for the dynamics of animal cell shape," in *Seminars in cell & developmental biology*, vol. 19, pp. 215–223, Elsevier, 2008.

[191] M. A. Biot, "General theory of three-dimensional consolidation," *Journal of applied physics*, vol. 12, no. 2, pp. 155–164, 1941.

[192] P. A. Netti, L. T. Baxter, Y. Boucher, R. Skalak, and R. K. Jain, "Macro-and microscopic fluid transport in living tissues: Application to solid tumors," *AIChE journal*, vol. 43, no. 3, pp. 818–834, 1997.

[193] T. Roose, P. A. Netti, L. L. Munn, Y. Boucher, and R. K. Jain, "Solid stress generated by spheroid growth estimated using a linear poroelasticity model," *Microvascular research*, vol. 66, no. 3, pp. 204–212, 2003.

[194] P. Cardaliaguet, P.-L. Lions, and P. Souganidis, "A discussion about the homogenization of moving interfaces," *Journal de mathématiques pures et appliquées*, vol. 91, no. 4, pp. 339–363, 2009.

[195] P.-L. Lions and P. E. Souganidis, "Homogenization of degenerate second-order pde in periodic and almost periodic environments and applications," in *Annales de l'Institut Henri Poincare (C) Non Linear Analysis*, vol. 22, pp. 667–677, Elsevier, 2005.

[196] S. Lee and V. Sundararaghavan, "Multi-scale homogenization of moving interface problems with flux jumps: application to solidification," *Computational mechanics*, vol. 44, no. 3, pp. 297–307, 2009.

[197] S. Lee and V. Sundararaghavan, "Multi-scale modeling of moving interface problems with flux and field jumps: Application to oxidative degradation of ceramic matrix composites," *International journal for numerical methods in engineering*, vol. 85, no. 6, pp. 784–804, 2011.

[198] L. Rayleigh, "Lvi. on the influence of obstacles arranged in rectangular order upon the properties of a medium," *The London, Edinburgh, and Dublin Philosophical Magazine and Journal of Science*, vol. 34, no. 211, pp. 481–502, 1892.

[199] U. Essien, A. Akankpo, and M. Igboekwe, "Poisson's ratio of surface soils and shallow sediments determined from seismic compressional and shear wave velocities," *International Journal of Geosciences*, vol. 5, no. 12, p. 1540, 2014.

[200] P. Vardanega and M. Bolton, “Stiffness of clays and silts: Normalizing shear modulus and shear strain,” *Journal of Geotechnical and Geoenvironmental Engineering*, vol. 139, no. 9, pp. 1575–1589, 2013.

[201] X. Xu, D. Vreugdenhil, and A. A. v. Lammeren, “Cell division and cell enlargement during potato tuber formation,” *Journal of Experimental Botany*, vol. 49, no. 320, pp. 573–582, 1998.

[202] C. Parker, M. Carr, N. Jarvis, M. Evans, and V. Lee, “Effects of subsoil loosening and irrigation on soil physical properties, root distribution and water uptake of potatoes (solanum tuberosum),” *Soil and tillage research*, vol. 13, no. 3, pp. 267–285, 1989.

[203] B. M. Das, *Advanced soil mechanics*. Crc Press, 2013.

European Journal of Soil Science

European Journal of Soil Science, March 2018, **69**, 265–278 doi: 10.1111/ejss.12503

Mathematical modelling of water and solute movement in ridge plant systems with dynamic ponding

S. J. Duncan[a], K. R. Daly[a], P. Sweeney[b] & T. Roose[a]

[a]*Faculty of Engineering and the Environment, Bioengineering department, building 5, University of Southampton, Southampton, SO171BJ, UK, and* [b]*Syngenta, Jealott's Hill, Bracknell RG42 6EY, UK*

Summary

We present a mathematical model that describes the movement of water and solutes in a ridge and furrow geometry. We focus on the effects of two physical processes: root water uptake and pond formation in the furrows. Special attention is paid to the physical description of ponding as an effect of transient rain events. We focus on phenomena taking place in the furrow cross-section, not on the drainage along the furrow. The resulting model comprises a coupled system of partial and ordinary differential equations that describe the mathematical interplay between solute transport, water movement and furrow pond depth. The system of equations is solved numerically using finite element techniques. We conducted numerical simulations to determine how mobile solutes with low buffer powers penetrate into the soil. We considered two cases: low rainfall, in which pond formation does not occur, and high rainfall, in which significant ponding is observed in the furrows. We found, in the presence of roots, that mobile solutes collected into a concentrated spot adjacent to the root system independent of rainfall intensity. In the absence of roots, however, we observed that water infiltration from ponding acted as the dominant transport mechanism for mobile solutes. This resulted in deep solute penetration into the soil when compared with non-ponded furrows.

Highlights

- Effect of furrow ponding and plant water uptake on solute movement in ridged fields.
- We developed a mathematical model that describes ponding in furrows from rainfall events.
- Solute 'hot spots' formed in soil from surface ponding and root water uptake.
- We estimate reduced risk to solute leaching under the effects of ponding when roots are present in soil.

Introduction

In arable farming, a specific form of row production known as a ridge and furrow geometry is frequently used to cultivate crops such as potatoes (Steele *et al*., 2006). This geometry is formed when the soil surface is adapted to form a periodic series of peaks and troughs. This allows water to flow across the field, providing water to the plants whilst preventing waterlogging of the roots (Tisdall & Hodgson, 1990). However, under certain rainfall conditions, this can lead to pond formation in the furrows that can result in decreased yields for crops such as potatoes (van Loon, 1981). An understanding of water movement and ponding in ridge and furrow geometries will help in developing strategies for crop and soil management.

Correspondence: T. Roose. E-mail: t.roose@soton.ac.uk
Received 23 March 2017; revised version accepted 28 September 2017

There is growing uncertainty about whether ridge and furrow geometries present greater potential for the movement of mobile plant protection products to groundwater than flat fields, because none of the models currently used for regulatory purposes to estimate solute movement to groundwater after application can model this system explicitly (EFSA, 2013). Consequently, a universal multiplier has been proposed to extrapolate between estimates of residues calculated for flat fields and those in ridge and furrow geometries (EFSA, 2013). In the absence of extensive and expensive field data, mathematical models designed to model solute movement explicitly in ridges and furrow geometries can provide insight into understanding the effects of ponding in these systems.

Mathematical modelling of water movement in ridge and furrow systems has been studied increasingly in recent years (Ebrahimian *et al*., 2013; Bautista *et al*., 2014; Sanchez *et al*., 2014), often for semiarid soil where the ridge and furrow geometry is used to facilitate irrigation. Because of the lack of rain in these environments,

precipitation and surface runoff are often disregarded because furrow irrigation management is the main priority.

In this paper, we develop a general mathematical model for solute movement in ridge and furrow soil, taking account of surface ponding and water movement from transient rainfall events to understand how solutes move in United Kingdom environments. We consider the movement of water and solutes in temperate soils with no formal irrigation, but subjected to substantial rain that results in ponding on the soil surface. The model presented can then be customized for specific fertilizers or pesticide-like solutes by including other soil processes such as biodegradation, microbial mineralization and air volatilization to determine how a particular solute will behave under a specific rainfall regime.

Several models for pond infiltration have been presented in the literature (Ebrahimian *et al*., 2013; Bautista *et al*., 2016). However, these models describe irrigation and drainage longitudinally along a furrow (often using the zero-inertia model for a moving body of water). To describe dynamic ponding from transient rainfall events, we developed a model that captures the filling and draining of a pond on the soil surface. In addition, we consider root-water uptake in the ridges of the geometry. We assess soil ponding from a mechanical perspective and incorporate Dirichlet and flux boundary conditions to represent areas of ponding and water-free surfaces, respectively (Camporese *et al*., 2010). We shall disregard fluid drainage along the length of the furrow because our main concern is ponding from rainfall, rather than irrigation that transports water down the furrow.

To study the effects of solute movement under the influence of surface ponding, we coupled water movement with solute transport in soil. We incorporated the movement of solutes into the model to understand better how nutrients, fertilizers and pesticides move under the effect of surface ponding in the presence and absence of roots. The physical characteristics of solutes can lead to adverse effects on the local environment; however, mathematical modelling enables us to develop strategies to reduce these negative effects by either aiding or impeding solute penetration into the soil (i.e. to promote the movement of low-mobility fertilizers or to reduce the leaching of high-mobility solutes).

Previous modelling of ridge and furrow system behaviour typically used software packages such as HYDRUS-2D, WinSRFR and so on (Ebrahimian *et al*., 2013; Sanchez *et al*., 2014; Bautista *et al*., 2016). Although they enable easy implementation of fluid flow models, we chose to use general finite element software (COMSOL Multiphysics®, Stockholm, Sweden, www.comsol.com) because it allows us to generalize fluid flow and surface ponding. It provides greater flexibility and easier implementation of new physics without relying on the functionality of software.

Our model presented in this paper consists of a coupled system of two partial differential equations (PDEs): one for the movement of water in soil and one for the transport of solutes. We also introduce an additional ordinary differential equation (ODE) that is coupled to the system of PDEs to describe dynamic ponding. It should be noted that we disregard any effects of soil moisture from heat transfer in soil because our focus is surface ponding and soil waterlogging in a temperate UK environment.

Mathematical model

In this section, we derive a model for simultaneous water and solute movement in variably saturated soil that accounts for the ridge and furrow geometry and the effects of dynamic surface ponding. The movement of solutes in soil is known to depend considerably on the degree of water saturation (Nye & Tinker, 1977). Therefore, we constructed a coupled water and solute movement model to connect soil water pore pressure with solute concentration. We assume that solutes do not create osmotic pressure gradients that influence fluid flow (i.e. fluid flow influences solute movement, but not *vice versa*).

The symmetry and periodicity of the ridge and furrow structure enable us to describe the complete system with a single half-period of the ridge and furrow geometry. The geometry used in this study is shown in Figure 1 by the domain Λ, which was chosen to be consistent with the dimensions for typical ridge and furrow geometries (Steele *et al*., 2006; Li *et al*., 2007). We approximate the soil surface $\partial\Lambda_S$ (see Figure 1) by the periodic function:

$$\chi(x) = A\cos(Bx) + C, \tag{1}$$

where A is the variation in soil depth, B is the ridge wave number and C is the average soil depth.

Water movement in variably saturated soil

To describe water movement in ridged soil systems, we assume there may be regions of soil that are fully saturated (i.e. directly under the pond) and regions that are partially saturated. To account for this, we constructed a model that can switch between a partially and a fully saturated soil environment with a moving interface between the two regions.

For water movement in variably saturated soil, Richards' equation is used (Kollet & Maxwell, 2006; Weill *et al*., 2009). This equation is derived by combining the equation for mass balance of soil water flow (Richards, 1931):

$$\phi\frac{\partial S}{\partial t} + \nabla\cdot\mathbf{u} = -F_w, \quad \mathbf{x}\in\Lambda, \tag{2}$$

with Darcy's law,

$$\mathbf{u} = -\frac{\kappa(S)}{\mu}\left(\nabla p + \rho g\,\hat{\boldsymbol{k}}\right), \quad \mathbf{x}\in\Lambda. \tag{3}$$

The result is Richards' equation in mixed form:

$$\phi\frac{\partial S}{\partial t} + \nabla\cdot\left[-\frac{\kappa(S)}{\mu}\left(\nabla p + \rho g\,\hat{\boldsymbol{k}}\right)\right] = -F_w, \quad \mathbf{x}\in\Lambda, \tag{4}$$

where ϕ is the soil porosity, S is the relative saturation (i.e. $S=\phi_l/\phi$, where ϕ_l is the volumetric water content), $\mathbf{u}$ is the volume flux of water, $\kappa(S)$ is the relative hydraulic permeability, μ is the viscosity

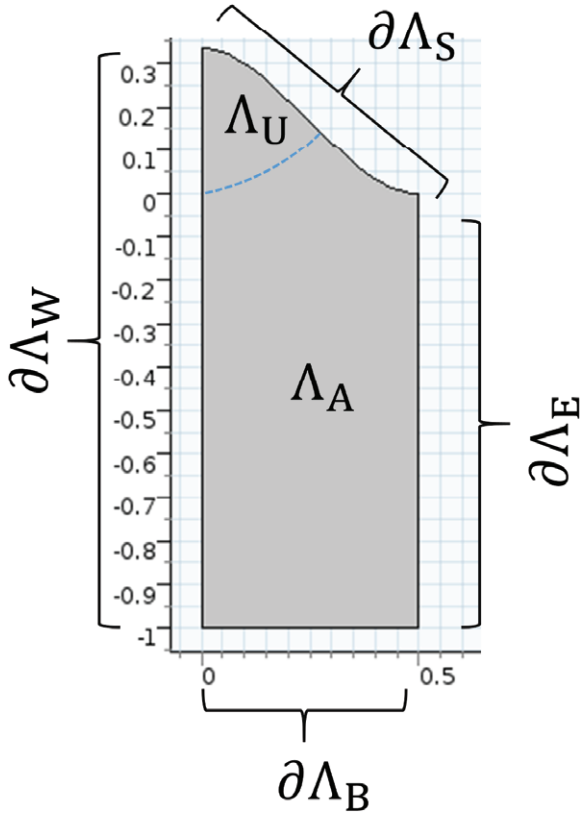

Figure 1 Half of a ridge and furrow period, where Λ is the total soil domain such that $\Lambda = \Lambda_A \cup \Lambda_U$, Λ_A is the region of soil with no roots, Λ_U is the region of soil with roots present, $\partial\Lambda_S$ is the soil surface boundary, $\partial\Lambda_B$ is the base of the domain, $\partial\Lambda_W$ is the left boundary adjacent to the ridge and $\partial\Lambda_E$ is the right boundary adjacent to the furrow. The curve $\partial\Lambda_S$ is generated from the values $A = C = 0.1\dot{6}$ and $B = 2\pi$ used in the periodic function $\chi(x)$ (Equation (1)).

of water, p is the soil water pore pressure, ρ is the density of water, g is the acceleration due to gravity, $\hat{\mathbf{k}}$ is a unit vector in the upwards direction and F_w is a sink term that describes water uptake via plant roots.

The root water uptake function, F_w, is given by the difference in soil water pore pressure and the pressure in plant roots (Roose & Fowler, 2004a) and is assumed to be active only where roots are present. We split Λ into two regions, Λ_U is the zone in which roots take up water and Λ_A is the region in which there are no roots. Hence, we write:

$$F_w = \begin{cases} \lambda_c \left(p - p_r\right), & \mathbf{x} \in \Lambda_U \\ 0, & \mathbf{x} \in \Lambda_A \end{cases}, \tag{5}$$

where λ_c is the product of the root surface area density and water conductivity of the plant root cortex and p_r is the pressure in the root xylem.

We express S as a function of p using the van Genuchten pressure-saturation relation (van Genuchten, 1980) (also called the suction characteristic):

$$S(p) = \left[\left(\frac{p_a - p}{p_c}\right)^{\frac{1}{1-m}} + 1\right]^{-m}, \tag{6}$$

where p_a is the atmospheric pressure, p_c is the characteristic suction pressure and m is a van Genuchten parameter. The parameters p_c and m are determined experimentally for each soil (van Genuchten, 1980). Note that we choose to set $p_a = 0$, such that p is defined as the gauge pressure relative to the atmospheric pressure (Roose & Fowler, 2004a).

To describe the relative permeability $\kappa(S)$, we used a second van Genuchten formula (van Genuchten, 1980):

$$\kappa(S) = \kappa_s S^{\frac{1}{2}} \left[1 - \left(1 - S^{\frac{1}{m}}\right)^m\right]^2, \tag{7}$$

where κ_s is the saturated hydraulic permeability.

Combining Richards' equation (4) with the van Genuchten equations (6)–(7) (van Genuchten, 1980), we can write the water movement model in terms of p only:

$$\phi \frac{\partial S(p)}{\partial p}\frac{\partial p}{\partial t} + \nabla \cdot \left\{ -\frac{\kappa\left[S(p)\right]}{\mu}\left(\nabla p + \rho g \hat{\mathbf{k}}\right)\right\} = -F_w, \quad \mathbf{x} \in \Lambda, \tag{8}$$

where,

$$\frac{\partial S(p)}{\partial p} = \frac{m\left[\left(\frac{-p}{p_c}\right)^{\frac{1}{1-m}} + 1\right]^{-m-1}\left(\frac{-p}{p_c}\right)^{\frac{m}{1-m}}}{p_c(1-m)} \tag{9}$$

and

$$\kappa\left[S(p)\right] = \kappa_s \left[\left(\frac{-p}{p_c}\right)^{\frac{1}{1-m}} + 1\right]^{\frac{-m}{2}} \times \left(1 - \left\{1 - \left[\left(\frac{-p}{p_c}\right)^{\frac{1}{1-m}} + 1\right]^{-1}\right\}^m\right)^2. \tag{10}$$

Richards' equation is frequently used to describe water movement in partially saturated soil. However, we can adapt Equations (8)–(10) such that they can represent both a saturated and partially saturated soil. To adapt Richards' equation for variably saturated soil, we use similar methods to those used previously by others (Kollet & Maxwell, 2006; Weill *et al.*, 2009; Bautista *et al.*, 2014) that reduce Richards' equation to saturated Darcy flow in the event of full saturation (for $p \geq 0$). We do this by modifying Equations (8)–(10) in two ways. First, for $p \geq 0$ we eliminate the term $\phi \frac{\partial S(p)}{\partial p}\frac{\partial p}{\partial t}$ from Equation (8) by setting $\frac{\partial S(p)}{\partial p} = 0$, which in turn reduces Richards' equation to Darcy flow. Thus, to describe the movement of water in variably saturated soil, we impose the condition:

$$\overline{\frac{\partial S(p)}{\partial p}} = \begin{cases} 0 & \text{for} \quad S = 1 \quad p \geq 0 \\ \frac{\partial S(p)}{\partial p} & \text{for} \quad 0 < S < 1 \quad p < 0 \end{cases}. \tag{11}$$

To implement Equation (11) as a closed-form expression, we use a smoothing approximation to the Heaviside function $H(x)$ to set $\frac{\partial S(p)}{\partial p} \to 0$ as $p \to 0$. This imitates the piecewise Equation (11) while retaining a level of smoothness over a narrow transition region about $p = 0$ to aid in numerical simulation. We add the smoothed Heaviside function $H_S(p)$, such that:

$$\left[1 - H_S(p)\right] \phi \frac{\partial S(p)}{\partial p} \frac{\partial p}{\partial t} + \nabla \cdot \left\{ -\frac{\kappa\left[S(p)\right]}{\mu} \left(\nabla p + \rho g \hat{\mathbf{k}}\right) \right\} = -F_w, \tag{12}$$

where

$$H_S(p) = \frac{1}{2}\left[1 + \tanh(\sigma p)\right], \tag{13}$$

and $\frac{1}{\sigma}$ defines the width of transition between $\frac{\partial S(p)}{\partial p}$ and 0 around $p = 0$.

Second, when Richards' equation is reduced to Darcy flow, the function $\kappa[S(p)]$ is required to be constant in the fully saturated soil regime. Thus, we introduce a second condition:

$$\overline{\kappa\left[S(p)\right]} = \begin{cases} \kappa_s & p \geq -\varepsilon \\ \kappa\left[S(p)\right] & p < -\varepsilon \end{cases}, \tag{14}$$

where ε is a small transition pressure that acts as the interface between the saturated and partially saturated soil regions. We introduced ε to avoid discontinuities in the numerical solution to Equation (12). These discontinuities come from the second term in Equation (12) because we need to evaluate $\frac{d\kappa[S(p)]}{dp}\Big|_{p=0}$. However, $\frac{d\kappa[S(p)]}{dp}$ is singular at the transition between fully and partially saturated soil, such that $\lim_{p\to 0^-}\left(\frac{d\kappa[S(p)]}{dp}\right) = \infty$. Hence, we introduce ε such that $\frac{d\kappa[S(0)]}{dp}$ is never evaluated. If we did not do this, the numerical procedure would fail to converge. The parameter ε differs from σ because ε is applied strictly to the negative side of p, whereas σ smooths either side of the pressure $p = 0$.

Soil surface boundary condition

To form a complete description of the ridge and furrow system, we derive boundary conditions that are imposed on the edges of Λ, and a novel and original ODE for a moving surface point interface for dynamic water ponding on the soil surface that is coupled to Richards' equation for water infiltration into soil.

To represent ponding, which is often present in ridge and furrow systems (Tabuada *et al.*, 1995; Vogel *et al.*, 2000), we split the boundary $\partial\Lambda_S$ (see Figure 1) into two distinct regions. This is shown in Figure 2, where $\partial\Lambda_R$ is the surface of soil that is not ponded (i.e. where rain penetrates the soil directly) and $\partial\Lambda_P$ is the region on which ponding occurs. Note that we allow the point x_0 connecting $\partial\Lambda_R$ and $\partial\Lambda_P$ to move in time (i.e. $x_0 = x_0(t)$), such that the pond height can change transiently.

We assume the pond boundary condition on $\partial\Lambda_P$ can be represented by a hydrostatic boundary condition (Tabuada *et al.*, 1995; Vogel *et al.*, 2000; Kollet & Maxwell, 2006). On the soil surface

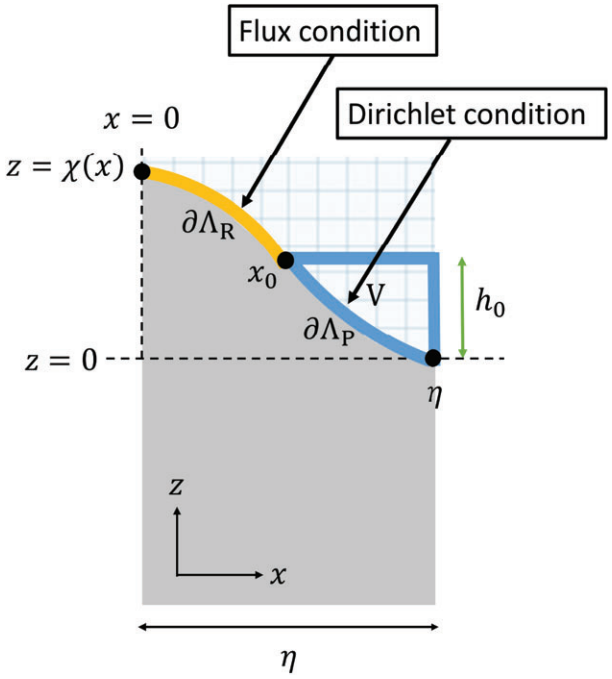

Figure 2 Half of a ridge and furrow period, where $\partial\Lambda_P$ is the soil surface boundary on which ponding occurs, $\partial\Lambda_R$ is the soil surface that is not ponded, x_0 is the point on the soil surface $\partial\Lambda_S$ where the pond begins, η is the width of the half period of ridged domain, h_0 is the maximum depth of the pond, $\chi(x)$ is the curve for the soil surface $\partial\Lambda_S$ and V is the volume of the pond.

directly under the pond, we apply the pressure that results from the height of the water column in the pond above it; that is:

$$p = \rho g h(x,t), \quad \mathbf{x} \in \partial\Lambda_P, \tag{15}$$

where $h(x,t)$ is the depth of the pond.

Precipitation landing on the bare soil $\partial\Lambda_R$ enters the soil domain by a combination of capillary forces and gravitational effects. Therefore, we implement a normal fluid flux condition on $\partial\Lambda_R$ (Yang *et al.*, 1996), such that:

$$\mathbf{n} \cdot \left\{ \frac{\overline{\kappa\left[S(p)\right]}}{\mu} \left(\nabla p + \rho g \hat{\boldsymbol{k}}\right) \right\} = \omega(t), \quad \mathbf{x} \in \partial\Lambda_R, \tag{16}$$

where $\omega(t) = \min\{\Gamma(t), I_c\}$, $\mathbf{n}$ is the unit normal vector pointing outwards from Λ, $\Gamma(t)$ is the volume flux of water per unit area of soil surface (i.e. rain), I_c is the infiltration capacity of the soil and $\omega(t)$ is the volume flux of water entering the soil per unit surface area. In the event of sufficiently heavy rain, the quantity of water that can enter the soil system is limited by the infiltration capacity of the soil I_c. Any excess rain that exceeds I_c (i.e. $\Gamma(t) > I_c$) is defined

as the surface runoff $R_o(t)$, and is quantified by:

$$R_o(t) = \begin{cases} \left\{ \left[\Gamma(t) - I_c\right] \cdot \int_0^{x_0(t)} \sqrt{1 + \left(\frac{d\chi(x)}{dx}\right)^2}\, dx \right\}, & \Gamma(t) > I_c \\ 0, & \Gamma(t) \le I_c \end{cases}, \tag{17}$$

where $\chi(x)$ is the generalized curve of $\partial\Lambda_S$, given by Equation (1).

To determine the change in pond depth for the boundary conditions imposed on $\partial\Lambda_R$ and $\partial\Lambda_P$, we implement an additional ODE that is coupled to the governing water movement model, Equations (12)–(14). This connects the volume of water in the pond $V(t)$, the rate of rainfall $\Gamma(t)$, the surface runoff $R_o(t)$ and the flux $\mathbf{u}$ entering the soil domain from the pond (i.e. the quantity of water leaving the pond and infiltrating into the soil).

We define the maximum depth of the pond $h_0(t)$ (see Figure 2) at a given time t to be:

$$h_0(t) = \chi\left[x_0(t)\right], \tag{18}$$

where $x_0(t)$ is the x co-ordinate at which the pond starts (i.e. the partition between $\partial\Lambda_R$ and $\partial\Lambda_P$). It should be noted that for $h_0(t)$ to have this definition, the vertical datum $z = 0$ is measured from the base of the soil curve $\chi(x)$ (see Figure 2). This allows the hydrostatic boundary condition Equation (15) to be re-written such that:

$$p = \rho g\left[h_0(t) - \chi(x)\right], \quad \mathbf{x} \in \partial\Lambda_P, \tag{19}$$

where $h_0(t) - \chi(x) = h(x,t)$.

In addition, a length η is chosen to represent half a ridge and furrow period (see Figure 2). It follows that for a given pond volume $V(t)$, the partition of the pond boundary $x_0(t)$ is calculated by:

$$V(t) = h_0(t) \cdot \left[\eta - x_0(t)\right] - \int_{x_0(t)}^{\eta} \chi(x)\, dx. \tag{20}$$

The change in pond volume $V(t)$ is defined to be

$$\frac{dV(t)}{dt} = \Gamma(t) \cdot \left[\eta - x_0(t)\right] + R_o(t) - \int_{x_0(t)}^{\eta} \mathbf{u} \cdot \mathbf{n}|_{\partial\Lambda_P}\, dx, \tag{21}$$

where $\Gamma(t) \cdot [\eta - x_0(t)]$ is the rainfall entering the pond, $R_o(t)$ is the surface runoff and $\int_{x_0(t)}^{\eta} \mathbf{u} \cdot \mathbf{n}|_{\partial\Lambda_P}\, dx$ is the quantity of water leaving the pond and infiltrating into the soil by the boundary condition on $\partial\Lambda_P$, Equation (19) (Wöhling & Schmitz, 2007). We substitute Equation (20) into Equation (21) such that:

$$\frac{\partial}{\partial t}\left\{ h_0(t) \cdot \left[\eta - x_0(t)\right] - \int_{x_0(t)}^{\eta} \chi(x)\, dx \right\} = \Gamma(t) \cdot \left[\eta - x_0(t)\right] + R_o(t) - \int_{x_0(t)}^{\eta} \mathbf{u} \cdot \mathbf{n}|_{\partial\Lambda_P}\, dx, \tag{22}$$

where $h_0(t)$ is defined by Equation (18). Equation (22) describes the change in the position of the pond boundary $x_0(t)$, given the rainfall entering the pond, surface runoff and water infiltration from the pond into the surrounding soil. To calculate $\mathbf{u}$, Equation (22) is coupled with Richards' equation by Equations (12)–(14) and the boundary condition Equation (19).

Through successive application of the Leibniz integral rule and the chain rule, for the generic function $z = \chi(x)$, Equation (22) can be expressed explicitly as a function of $\frac{dx_0(t)}{dt}$; that is:

$$\begin{aligned} &\frac{dx_0(t)}{dt}\left\{ \eta \frac{\partial\chi\left[x_0(t)\right]}{\partial x_0(t)} - \chi\left[x_0(t)\right] - x_0(t)\frac{\partial\chi\left[x_0(t)\right]}{\partial x_0(t)} \right\} \\ &- \left[\frac{\partial}{\partial t}\int_{x_0(t)}^{\eta} \chi(x)\, dx\right] = \Gamma(t) \cdot \left[\eta - x_o(t)\right] + R_o(t) \\ &+ \int_{x_0(t)}^{\eta} \left(\left\{ \frac{\partial\chi(x)}{\partial x} \frac{\overline{\kappa\left[S(p)\right]}}{\mu}\left(\partial_x p\right) - \frac{\overline{\kappa\left[S(p)\right]}}{\mu}\left(\partial_z p + \rho g\right) \right\}\Bigg|_{\partial\Lambda_P} \right. \\ &\left. \times \left[1 + \left(-\frac{\partial\chi(x)}{\partial x}\right)^2\right]^{-0.5} \right) dx. \end{aligned} \tag{23}$$

Note that for the boundary condition on $\partial\Lambda_P$, Equation (19), to be active, we impose the condition that a minimum pond depth threshold must be reached before water leaves the pond and infiltrates into the soil:

$$p = \rho g\left[h_0(t) - \chi(x)\right] \text{ for } \chi\left[x_0(t)\right] > x_{\min}, \tag{24}$$

where $x_{\min}$ is the minimum pond depth. We impose this condition to aid numerical computation because a pond that is much smaller than the mesh size can lead to convergence problems for the numerical solver. However, we chose the threshold to be sufficiently small that it has a negligible effect on the results.

Lateral boundary conditions

For the boundaries $\partial\Lambda_E$ and $\partial\Lambda_W$, we set a zero flux boundary condition:

$$\mathbf{n} \cdot \left\{ \frac{\overline{\kappa\left[S(p)\right]}}{\mu}\left(\nabla p + \rho g\hat{\boldsymbol{k}}\right) \right\} = 0, \quad \mathbf{x} \in \partial\Lambda_E \cup \partial\Lambda_W. \tag{25}$$

Therefore, there is no lateral water movement into or out of Λ.

Boundary condition at the base of the soil

For the boundary at the base of the domain $\partial\Lambda_B$, we set a Dirichlet boundary condition (Banti *et al.*, 2011). This describes a constant saturation level at a constant depth (i.e. 1 m below $z = 0$) (see Figure 2). Thus, we impose the condition:

$$p = p_0, \quad \mathbf{x} \in \partial\Lambda_B. \tag{26}$$

Initial conditions

For the initial pressure condition $p\big|_{t=0}$, we impose the steady state pressure profile that forms when roots are not present:

$$p\big|_{t=0} = p_\infty(\mathbf{x}), \quad \mathbf{x} \in \Lambda. \tag{27}$$

Furthermore, we assume there is no surface ponding present on $\partial\Lambda_S$ at $t = 0$:

$$x_0(t)\big|_{t=0} = \eta, \tag{28}$$

such that the pond depth is $\chi[x_0(t)|_{t=0}] = 0$.

The system of Equations (12), (14), (16), (19) and (23)–(28) completes the description of the coupled water balance in the presence of surface ponding.

Solute movement in variably saturated soil

In this section, we introduce a mathematical model for solute movement in soil. We couple it with the water movement model derived above, thereby constructing a model for simultaneous water and solute movement in soil. The model is coupled by a similar approach to that used by Roose & Fowler (2004b). It should be noted that we assume that there is no solute uptake by plant roots or degradation of the solute from other soil processes. Here we deal only with the solute transport problem of solutes that are not actively taken up by plant roots, although it is trivial to customize and extend the model to accommodate solute uptake by plant roots or other soil processes. Examples of passive solutes include non-ionic strongly lipophilic substances, which are taken up minimally by barley (*Hordeum vulgare* L.) plants because of their lipophilicity (Briggs *et al*., 1982, 1983).

To model the movement of solutes in soil, we use the advection–diffusion equation (Nye & Tinker, 1977; Barber, 1995):

$$\frac{\partial}{\partial t}\left[\left(\phi_l + b\right)c\right] + \nabla\cdot(c\mathbf{u}) = \nabla\cdot\left(\phi_l D\nabla c\right), \tag{29}$$

where D is the solute diffusion coefficient in the soil pore water, ϕ_l is the volumetric water content, c is the solute concentration in the pore water, $\mathbf{u}$ is the volume flux of water and b is the buffer power of the solute. We assume b to be constant in this model. However, it is trivial to extend b to more complex adsorption isotherms (i.e. Langmuir or Freundlich).

The volumetric water content ϕ_l is related to the soil water pore pressure p by the suction characteristic $\phi_l = \phi S(p)$. In addition, we state that $\mathbf{u}$ in Equation (29) is described by Darcy's law, as in the water movement model, Equation (3). Finally, we assume D can be expressed by the power law:

$$D = D_f \phi^d S(p)^d, \tag{30}$$

where D_f is the diffusion coefficient in free liquid and d is the impedance factor of the solute that accounts for the tortuosity of the solute moving through the soil pore space (Nye & Tinker, 1977).

Combining Equations (29) and (30) with Equations (12)–(14) that govern water movement, the model for solute movement is given by:

$$\begin{aligned}\frac{\partial c}{\partial t}\left[b + S(p)\phi\right] + \frac{\partial p}{\partial t}\left\{\left[1 - H_S(p)\right]\frac{\partial S(p)}{\partial p}\phi\, c\right\} \\ + \nabla\cdot\left[-D_f\phi^{d+1}S(p)^{d+1}\nabla c\right] \\ + \nabla\cdot\left\{-\frac{c\kappa\overline{\left[S(p)\right]}}{\mu}\left(\nabla p + \rho g\,\hat{\mathbf{k}}\right)\right\} = 0.\end{aligned} \tag{31}$$

Note that for the solute model to be valid for a variably saturated soil domain, a similar condition to Equation (14) has been imposed. This condition sets the 'time' coefficient $[b + S(p)\phi]$, the diffusion coefficient $[-D_f\phi^{d+1}S(p)^{d+1}]$ and the advection coefficient $\left\{\frac{c\kappa\overline{[S(p)]}}{\mu}\right\}$ to be constant at full saturation. Thus, these coefficients do not change under different magnitudes of pressure in a fully saturated environment.

The solute model Equation (31) is coupled to the water movement model Equations (12)–(14) to achieve a system of PDEs that describes simultaneous water and solute movement in soil.

Soil surface boundary condition

For the application of solutes to a soil surface, we assume that this would be during dry conditions or when rainfall is sufficiently low that it does not break the minimum pond depth $x_{\min}$. Therefore, on the boundary $\partial\Lambda_S$ we impose a flux condition similar to Equation (16), such that:

$$\begin{aligned}\mathbf{n}\cdot\left(\left[D_f\phi^{d+1}S(p)^{d+1}\nabla c\right] + \left\{\frac{c\kappa\overline{\left[S(p)\right]}}{\mu}\left(\nabla p + \rho g\hat{\mathbf{k}}\right)\right\}\right) \\ = c_m(t), \quad \mathbf{x} \in \partial\Lambda_S,\end{aligned} \tag{32}$$

where $c_m(t)$ is the volume flux of solute per unit soil surface area per unit time entering the soil domain.

Lateral boundary conditions

For the boundaries $\partial\Lambda_E$ and $\partial\Lambda_W$ on the lateral sides of the domain Λ (see Figure 1), we set a zero flux boundary condition:

$$\begin{aligned}\mathbf{n}\cdot\left(\left[D_f\phi^{d+1}S(p)^{d+1}\nabla c\right] + \left\{\frac{c\kappa\overline{\left[S(p)\right]}}{\mu}\left(\nabla p + \rho g\hat{\mathbf{k}}\right)\right\}\right) \\ = 0, \quad \mathbf{x} \in \partial\Lambda_E \cup \partial\Lambda_W.\end{aligned} \tag{33}$$

Therefore, there is no lateral solute movement into or out of Λ.

Boundary condition at the base of the soil

During our numerical simulations, we observed that the domain was sufficiently large to avoid any solute reaching the base. Therefore, we can implement either a zero flux boundary on $\partial\Lambda_B$ or a Dirichlet boundary corresponding to the initial condition. The choice is inconsequential given that any solute movement in numerical simulations is contained in the top of the geometry. Therefore, we impose a zero flux condition:

$$\mathbf{n}\cdot\left(\left[D_f\phi^{d+1}S(p)^{d+1}\nabla c\right]+\left\{\frac{c\kappa\overline{\left[S(p)\right]}}{\mu}\left(\nabla p+\rho g\hat{\mathbf{k}}\right)\right\}\right)=0,\quad \mathbf{x}\in\partial\Lambda_B. \tag{34}$$

To validate the zero flux condition, we checked that there was zero solute concentration on $\partial\Lambda_B$ throughout the numerical simulation (i.e. no solute reaches the base of Λ).

Initial conditions

We aimed to observe the effect of ponding on solute movement in previously solute-free soil. Therefore, we impose a uniform zero initial concentration across Λ with:

$$c|_{t=0}=0,\quad \mathbf{x}\in\Lambda. \tag{35}$$

Parameter values

There are 24 parameters in the model derived in the section above. These parameters are: ϕ, m, k_s, μ, g, ρ, p_c, D_f, d, b, ε, σ, x_{min}, $\omega(t)$, $c_m(t)$, p_0, $p_\infty(\boldsymbol{x})$, λ_c, p_r and I_c for the coupled model, and the four parameters A, B, C and η for the construction of Λ. These parameters are summarized in Tables 1 and 2.

Geometric, soil, environmental, plant and solute parameter values

To replicate the dimensions of ridge and furrow geometries, we used the values $\eta=0.5$ m, $A=C=\frac{1}{6}$ m and $B=2\pi$ m^{-1} (Steele *et al*., 2006; Li *et al*., 2007). Furthermore, potato (*Solanum tuberosum*, L) is shallow rooted with the majority of its roots in the plough layer (i.e. the top 0.3 m of soil) (Lesczynski & Tanner, 1976). Therefore, we chose the size of the soil root region Λ_U to be the top 0.3 m of soil extending radially from the top of the ridge (see Figure 1).

Several of the model parameters depend on the soil, for example ϕ, m, k_s and p_c; the values of these for several soil types are listed in Table 1 (van Genuchten, 1980). Potatoes are frequently grown in ridge and furrow geometries of silt loam soil (Ahmadi *et al*., 2011). Therefore, we used the parameter values for the 'Silt Loam G.E.3' soil from Table 1 (i.e. $\phi=0.396$, $m=0.51$, $k_s=5.2\times10^{-14}$ m^2 and $p_c=23\,200$ Pa) (van Genuchten, 1980).

We took values from the literature for the environmental and fluid parameters. For the viscosity of water we used $\mu=8.9\times10^{-4}$ kg m^{-1} s^{-1} (Watson *et al*., 1980), for acceleration due to gravity $g=9.81$ m s^{-2} and for the density of water $\rho=1000$ kg m^{-3}.

Table 1 Parameter values for various soil types (van Genuchten, 1980), where ϕ is the porosity of the soil, κ_s is the saturated hydraulic permeability, p_c is the characteristic suction pressure and m is the van Genuchten parameter

Soil type	ϕ	κ_s (m^2)	p_c (Pa)	m
Hygiene sandstone	0.250	1.14×10^{-12}	12 400	0.90
Silt loam G.E.3	0.396	5.2×10^{-14}	23 200	0.51
Guelph loam (drying)	0.520	3.26×10^{-13}	8500	0.51
Beit netofa clay	0.446	8.62×10^{-16}	64 500	0.15

The typical range of the impedance coefficient d is between 0.5 and 2 (Nye & Tinker, 1977); an increase in volumetric moisture content leads to an increase in impedance factor (Rowell *et al*., 1967). Given that we aimed to simulate surface ponding with fully saturated soil near the surface of the geometry, we used $d=2$.

Values of the diffusion coefficient of a solution in free liquid, D_f, for simple electrolytes tend to be within the range of $1\times10^{-9}-3\times10^{-9}$ m^2 s^{-1} (Shackelford & Daniel, 1991); we used a value in the middle of this range, $D_f=2\times10^{-9}$ m^2 s^{-1}.

For the parameters in the water–root uptake term, F_w, λ_c and p_r, we selected typical values for potato plants. The parameter λ_c is the product of the root surface area density and water conductivity of the root cortex, which can be expressed by:

$$\lambda_c=k_r l_d, \tag{36}$$

where l_d is the root length density and k_r is the radial conductivity of root cortex per unit root length. For the root length density, we assigned the value $l_d=4\times10^4$ m m^{-3} (Kirkham *et al*., 1974; Lesczynski & Tanner, 1976). In maize (*Zea mays* L.) roots, the parameter k_r is given the value 7.85×10^{-10} m^2 s^{-1}MPa^{-1} (Roose & Fowler, 2004a). Maize and potato roots have been found to have similar root radii (Rawsthorne & Brodie, 1986; Steudle *et al*., 1987); therefore, we assume that this value of k_r is also representative of potato roots in soil. This leads to the parameter value $\lambda_c=3.14\times10^{-5}$ s^{-1}MPa^{-1}.

To describe root pressure p_r, there are models for the root pressure distribution within a single root (Roose & Fowler, 2004a). To simulate large areas of soil consisting of many roots, therefore, we used an average root pressure to describe the plant root system. The root pressure p_r can vary considerably in potatoes depending on several factors, including soil saturation and atmospheric conditions (Gandar & Tanner, 1976). Liu *et al*. (2006) found that the root water potential changes substantially based on the method of irrigation applied to the crop. A value of $p_r\approx-0.01$ MPa was present in the roots for a fully irrigated system and of $\approx(-0.02,-0.2)$ MPa for areas of soil with partial root drying. Given that we aimed to model frequent heavy rain events that promote considerable ponding, we chose the values $p_r=-0.05$ MPa and $p_r=-0.1$ MPa depending

Table 2 Model parameter values used in numerical simulation

Parameter	Description	Value	Units	References
ρ	Density of water	1×10^{3}	kg m^{-3}	–
g	Acceleration due to gravity	9.81	m s^{-2}	–
b	Buffer power	2	–	Barber (1995)
D_f	Diffusion coefficient in free liquid	2×10^{-9}	m^2 s^{-1}	Shackelford & Daniel (1991)
m	van Genuchten parameter	0.5	–	van Genuchten (1980)
ϕ	Porosity	0.396	–	van Genuchten (1980)
κ_s	Saturated water permeability	5.2×10^{-14}	m^2	van Genuchten (1980)
p_c	Characteristic soil suction	23 200	Pa	van Genuchten (1980)
d	Impedance factor	2	–	Nye & Tinker (1977) and Roose & Fowler (2004b)
μ	Viscosity of water	8.9×10^{-4}	kg m^{-1} s^{-1}	Watson *et al*. (1980)
λ_c	Root surface area density water conductivity	3.14×10^{-5}	s^{-1}MPa^{-1}	Kirkham *et al*. (1974), Lesczynski & Tanner (1976), Rawsthorne & Brodie (1986), Steudle *et al*. (1987) and Roose & Fowler (2004a)
p_r	Root xylem pressure	-0.05, -0.1	MPa	Liu *et al*. (2006)
ε	Saturated – partially saturated interface	0.1	Pa	–
x_{min}	Minimum pond depth	3×10^{-4}	m	–
I_c	Infiltration capacity	1.6×10^{-6}	m s^{-1}	Morin & Benyamini (1977)
A	Variation in soil depth	$0.1\dot{6}$	m	Steele *et al*. (2006) and Li *et al*. (2007)
B	Ridge wave number	2π	m^{-1}	Steele *et al*. (2006); Li *et al*. (2007)
C	Average soil depth	$0.1\dot{6}$	m	Steele *et al*. (2006) and Li *et al*. (2007)
η	Geometry width	0.5	m	Steele *et al*. (2006) and Li *et al*. (2007)

on the simulated rainfall regime (see *Rainfall, infiltration capacity and solute application parameters* for the applied rainfall regimes).

For the parameters ε and $x_{\min}$, we selected small values that have a negligible effect on the numerical solution; for ε we chose 10^{-4} kPa. Given that pressure in soil is often measured in $\mathcal{O}(10)$ kPa, we assumed that ε was sufficiently small to avoid affecting the numerical results. Furthermore, for $x_{\min}$, which determines the minimum pond depth, we chose $x_{\min}=3\times10^{-4}$ m. Therefore, the hydrostatic boundary condition Equation (19) is activated once the pond depth surpasses 0.3 mm.

For the parameter σ in the smoothed Heaviside function $H_{\mathrm{S}}(p)$, we assigned $\sigma=1000$ Pa^{-1}; this limits the width of the transition between partially and fully saturated soil regions such that the transition is completed across 0.001 Pa. We conducted a series of simulations for decreasing values of σ to determine when differences between results became negligible. We tested and confirmed that this value had a negligible effect on numerical computation given that soil water pore pressure is typically several orders of magnitude higher than $\mathcal{O}\left(10^{-6}\right)$ kPa.

We ran several numerical simulations for a mobile solute to determine how ponding and root water uptake affect the transport of mobile solutes in soil. For this we selected a buffer power of $b=2$. Examples of solutes with a similar buffer power include the nutrient boron (Barber, 1995), and the pesticide Dimethylamonium chloride (Njoroge *et al*., 2016).

Boundary and initial condition parameters values

We assigned values to the remaining parameters in the boundary and initial conditions to complete the system of equations that makes up the solute ponding model.

For p_0, which describes a constant saturation at the base of the geometry, we assigned a value of $p_0=-10$ kPa. This equates to a saturation level of approximately $S\approx0.9$ for a silt loam soil, thereby replicating a shallow water table. For the initial condition of soil water pore pressure, $p_\infty(\mathbf{x})$, we chose the steady state profile that forms in the absence of plant roots. As a result of capillary forces and gravity, this leads to a constant pressure gradient from the base to the top of the geometry of:

$$p_\infty(\mathbf{x})=-p_\infty^{\mathrm{m}}z-p_\infty^{\mathrm{c}},\qquad \mathbf{x}\in\Lambda, \tag{37}$$

where $p_\infty^{\mathrm{m}}=9825$ Pa and $p_\infty^{\mathrm{c}}=19\,825$ Pa.

Rainfall, infiltration capacity and solute application parameter values

Here we describe the solute application and rainfall regime used in the numerical simulations. There are several case studies that could be examined with varying solute applications, rainfall events, infiltration capacities and so on; therefore, it is not possible to cover an exhaustive series of case studies. We chose a series of scenarios to observe the effects surface ponding and root water uptake from vegetation have on the transport of mobile solutes in soil.

We simulated solute and water movement over a 16-week period because this time-frame is typical of a single season potato crop (Noda *et al*., 1997). To observe the effect of water uptake from plant roots and ponding on the soil surface, we simulated heavy and light rain both with and without roots for a mobile solute; four simulations in total. The rainfall regimes are shown in Figure 3.

In the light rainfall regime (Figure 3), we simulated one rain event every week (midweek) throughout the 16-week period that lasted

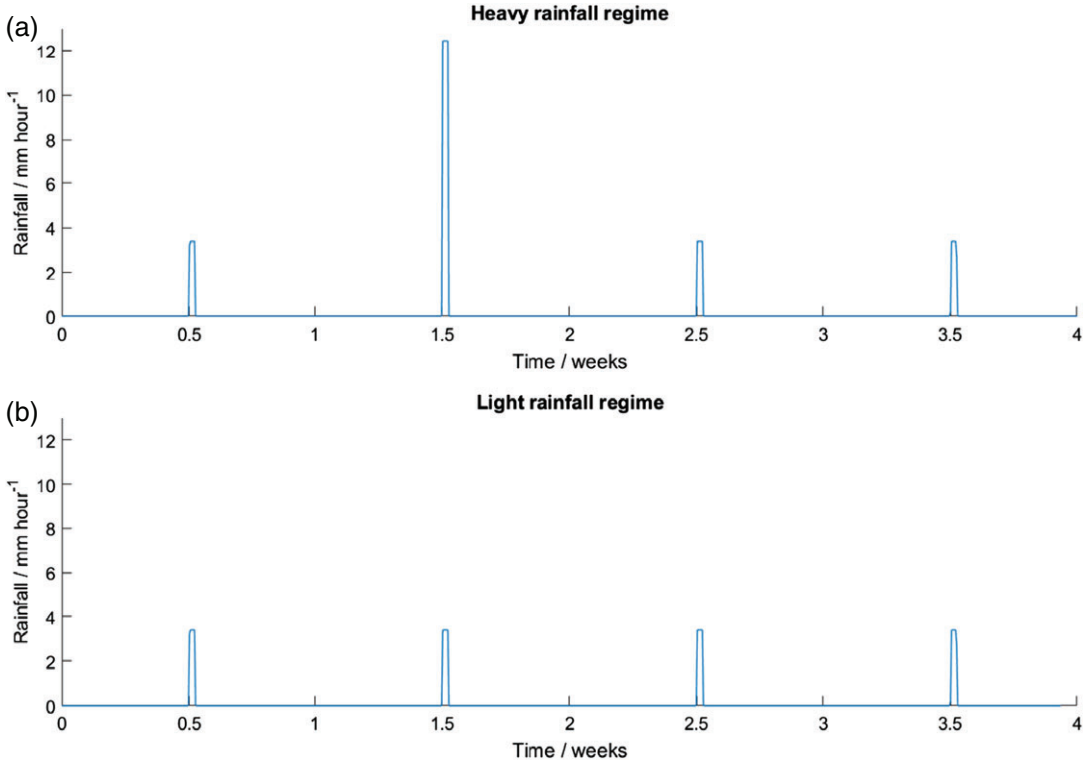

Figure 3 (a, b) The heavy and light rainfall regimes used in the numerical simulations, respectively.

4 hours and had an intensity of 4 mm hour^{-1}. This is not sufficient to generate soil surface ponding because all rainfall infiltrates into the soil. In this case we imposed a root pressure p_r of −0.1 MPa because this quantity of rainfall will result in a drier soil compared with the heavy rainfall regime.

For heavy rainfall (Figure 3), we simulated a rain event every week (midweek). In weeks 1, 3 and 4 we simulated a rain event that lasted 4 hours with an intensity of 4 mm hour^{-1}, and in week 2 we simulated an event that lasted 4 hours with an intensity of 12.5 mm hour^{-1}. This heavier rain caused ponding in the furrows of the geometry. This 4-week routine was repeated throughout the simulation. For heavy rain we imposed a root pressure p_r of −0.05 MPa because ponding saturated the soil.

The infiltration capacity I_c of soil is known to depend on several factors, including tillage methods (Azooz & Arshad, 1996), volumetric water content, soil type and recent rain events. Therefore, it is difficult to assign a single value to the infiltration capacity of a soil. Morin & Benyamini (1977) found that steady state infiltration of bare loam soil was reached after approximately 20 minutes into a rain event. Given that we simulated rain events an order of magnitude longer than this, we assigned a constant value for the infiltration capacity. Morin & Benyamini (1977) found that the steady state infiltration rate of bare loam soil is $1.3 - 2.2 \times 10^{-6}$ m s^{-1}. Given this, we assigned a value I_c of 1.75 × 10^{-6} m s^{-1}.

At the beginning of the simulation, a solute was applied to the soil surface over a period of 24 hours, with a total application of 1 kg ha^{-1}; an application rate of $c_m(t) = 1.157 \times 10^{-9}$ kg m^{-2} s^{-1}.

Numerical solutions

Before we consider the two rainfall scenarios described above we validated the model first with previous data from ponding in ridge and furrow geometries.

Model validation

We validated the model with data from the ponding study by Siyal *et al*. (2012). They created a trapezoidal ridge and furrow geometry with a loam soil in which a constant flow of water flowed longitudinally down the furrow until a pond height of 0.1 m was reached. Once the desired pond height was reached, the flow of water was stopped and the time required for the pond to infiltrate fully into the soil was measured.

The model derived in this paper uses a sinusoidal curve to model the periodic surface of ridge and furrow structures. It is impossible to resolve a piecewise trapezoidal surface with the sinusoidal surface Equation (1). Nevertheless, we constructed a geometry with Equation (1) that minimizes the differences between the trapezoidal structure in Siyal *et al*. (2012). This was achieved with the geometry parameters $A = C = 0.12$ m, $B = 2\pi$ m^{-1} and $\eta = 0.5$ m for the soil surface $\partial\Lambda_S$ in Equation (1).

In Siyal *et al*. (2012), the time taken to generate the 0.1-m-deep pond was 5.6 hours, and the time required for the water to infiltrate fully into the soil was 16 hours. To replicate these conditions, we simulated a rain event that lasted 5.6 hours with an intensity of 14.8 mm hour^{-1} to equate the total pond volume in the simulated

sinusoidal geometry with that of ponded water in Siyal *et al*. (2012).

We conducted a simulation to measure the time required for the pond to infiltrate the soil fully with the parameters estimated experimentally for the soil used in Siyal *et al*. (2012); that is, $\phi = 0.43$, $\kappa_s = 2.63 \times 10^{-13}$ m^2 (assuming the fresh water properties $\rho = 1000$ kg m^{-3}, $\mu = 8.9 \times 10^{-4}$ kg m^{-1} s^{-1} and $g = 9.81$ m s^{-2}), $m = 0.36$ and $P_c \approx 2500$ Pa. We used the COMSOL Multiphysics® finite element package to solve our model (implementation of the model is described in the Appendix).

In the numerical simulation, we found that the pond caused by the 5.6-hour rain event dissipated into the soil fully after approximately $15.\dot{3}$ hours. This led to a difference of ≈4% between these results with the model derived in this paper and those of Siyal *et al*. (2012).

These results give us confidence that the model derived in this paper can accurately describe time-variable ponding for loam soil.

Saturation results

Figure 4 shows the effect of ponding on the water profile of the ridged domain Λ by a series of $S(p)$ plots within the domain Λ, for the first ponding rain event from the simulation with the heavy rainfall regime and in the absence of plant roots. The times chosen were selected to emphasize the formation, growth and dissipation of a pond in the furrow. Note that each $S(p)$ plot in Figure 4 has a different colour scale bar. Because large soil pore water pressure differences form throughout the simulation, the saturation gradients that result from ponding would otherwise be reduced in appearance if the scale considered both low and high saturation when a ponding event was present.

Figure 4 (a–c) shows the water distribution before, during and at the end of the first rain event, respectively. Figure 4 (d–i) shows the water profile within the soil domain Λ after the rain has finished, showing the effect of surface ponding on the water movement in the soil.

At the start of the rain event, $t = 0$ (Figure 4a), we observe steady state conditions that are formed from the boundary conditions imposed on the domain. This causes a constant pressure gradient to form throughout the geometry in which the base of the soil is the most saturated. As the rain starts, we can see the effect of the rain in the top of the soil domain. At 2 hours after the rain starts (Figure 4b), a pond has formed in the furrow of the domain. This equates to a pond depth of approximately 4 cm. During the remaining rain the pond steadily increases to a maximum height of approximately 7 cm.

Once the rain has stopped, the effect from surface ponding becomes evident. Figure 4(d) shows that 6 hours after the rain, saturation in the ridge of the geometry has decreased as the non-ponded soil begins to drain. However, the furrow is still fully saturated as the pond on the soil surface gradually infiltrates into the soil. The pond on the surface continues to infiltrate for approximately 24 hours. The ponding effect on the water profile is shown in Figure 4(e,f) for 12 and 18 hours after the rain, respectively. These plots show the diminishing size of the pond and movement of water from the top of the geometry to the base. The soil in the ridges of the geometry has dried considerably faster than in the furrows; this is to be expected given the effect of surface ponding.

Thirty-six hours after the rain event (Figure 4g), the pond has fully infiltrated the soil and the water profile is returning to equilibrium. Two weeks after the rain event (Figure 4i), a steady state equilibrium is achieved in the system. This water movement cycle is then repeated for the second, third and fourth ponding rain events for the remaining simulation.

Solute transport results

Figure 5 shows the solute concentration profiles within Λ for the mobile solute (with buffer power $b = 2$) at the end of the 16-week simulations for different rainfall regimes and root water uptake. There were four combinations of rainfall intensity (ponded and non-ponded) and root presence in the ridges of the domain. The solute profiles at the end of the 16-week period are markedly different in each of the four cases.

Figure 5(a) shows the combination of ponded rain without root presence. The effect of ponding in the furrow is clear, and the solute adjacent to the furrow has penetrated much deeper into the soil than that in the ridge. The shape of the solute profile in the furrow corresponds to the fully saturated region of soil that was displayed in Figure 4 because infiltration of water from the pond acts as a carrier mechanism for the solute. Because the soil has a given infiltration capacity, the ridge of the domain can absorb a finite amount of water only, and excess water enters the pond. This causes the solute near the ridge to move fairly uniformly into the soil.

The results in Figure 5(a) are quite different from those in Figure 5(b) for the non-ponded rain without roots. Because all of the rain infiltrated the soil, the solute penetrates almost uniformly. However, there is a larger concentration of solute in the ridge of the domain. After a rain event, the first region of soil to dry out is the ridge of the geometry (Figure 4). Because solute movement depends on the saturation conditions, this reduction in relative saturation causes a decrease in movement of the solute in the ridge of the geometry. Therefore, any solute contained in the ridge after drying has occurred, remains there until the succeeding rain event.

Figure 5(c,d) shows the solute profiles for the heavy and light rain events with roots present in the ridge of the geometry. For both regimes, we imposed root pressures p_r of −0.05 and −0.1 MPa, respectively, to account for the difference in water available to the plant roots. In both cases, the solute collects into a concentrated spot at the edge of the root domain. This is caused by the difference in soil pore water pressure and the pressure in the root xylem because any water that infiltrates the soil surface is drawn towards the plant roots, which acts as a carrier mechanism for the solute movement. Therefore, solute in the furrow of the domain is transported to the root system, resulting in the formation of a concentrated solute spot.

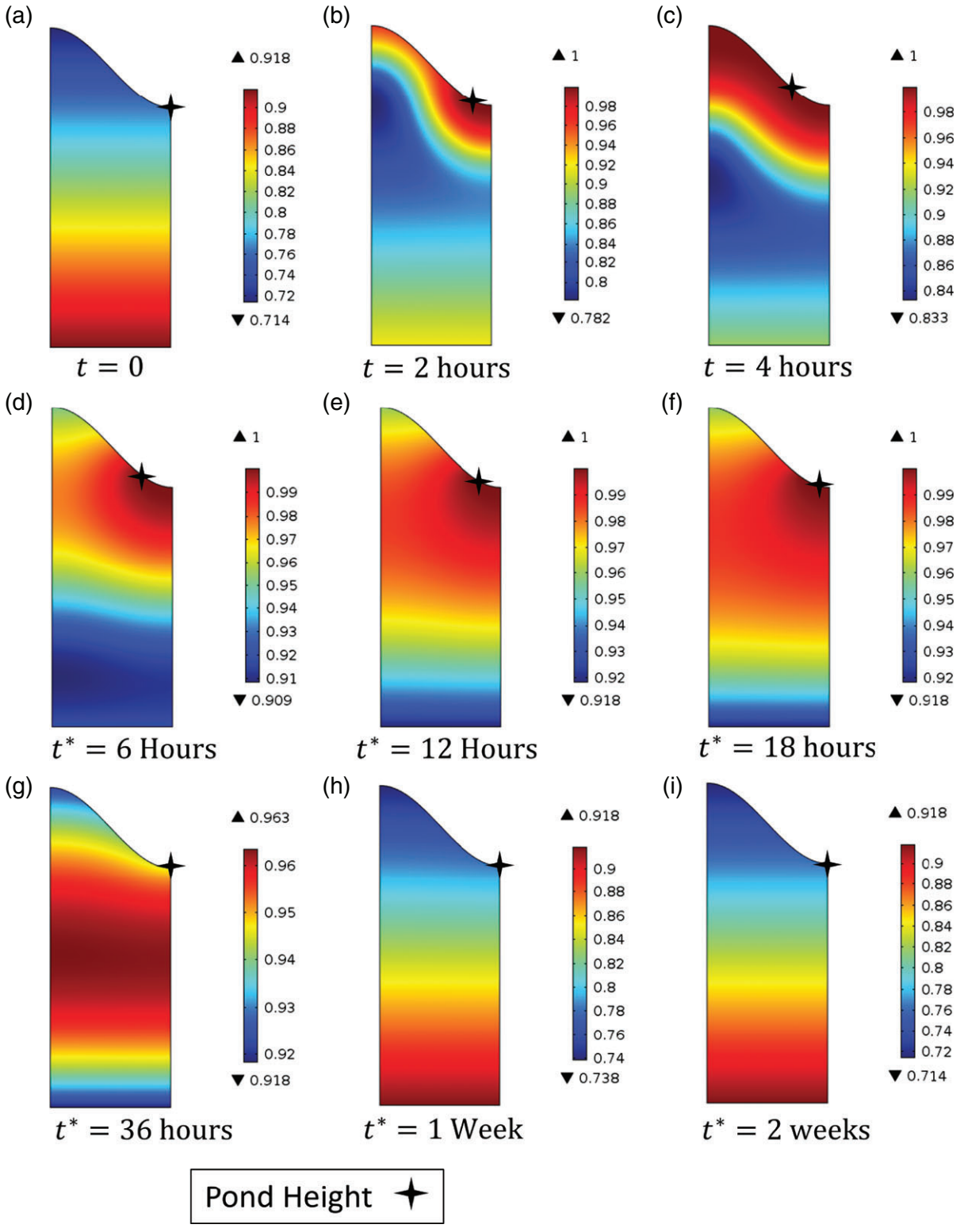

Figure 4 Time series of saturation $S(p)$ plots across the domain Λ at various times before, during and after the first rain event described by the heavy rainfall regime and no plants. The first three plots (a–c) show the water profile before, during and at the end of the rainfall event, respectively, where $t = 0$ represents the start of the 4-hour rain event. The last six plots (d–i) show the water profile after the rain event, where $t^* = 0$ denotes the end of the rain event. The pond location $x_0(t)$ is indicated by a black star along the surface curve of the geometry.

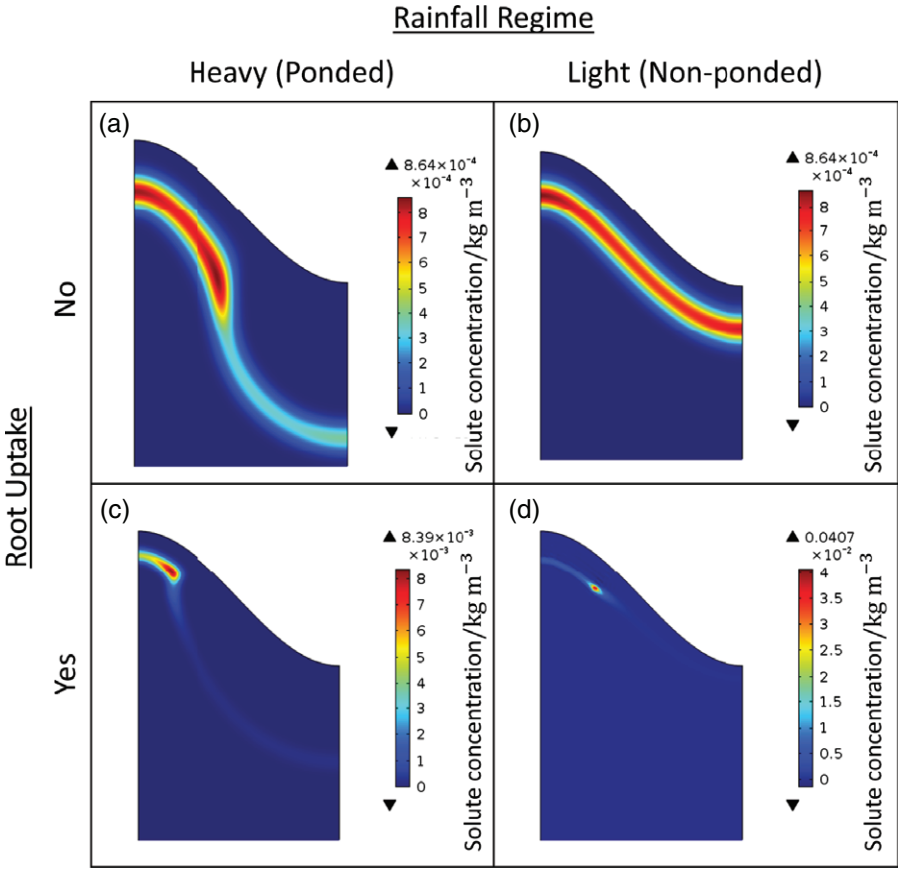

Figure 5 Solute concentration profiles for a mobile solute (buffer power $b = 2$) 16 weeks after solute application under the two rainfall regimes: (a) shows the results from the heavy rainfall regime (which causes ponding) without water uptake in the ridges of the geometry, (b) is the light rainfall regime without root uptake, (c) is the heavy rainfall regime with root uptake and (d) is the light rainfall regime with root uptake.

Figure 5(d) shows a more concentrated and condensed spot formation in the light rainfall regime. This is because of the greater pressure difference between the soil pore water pressure and the pressure in the root xylem, and the reduction in available water. This reduces the diffusion of the solute and forms a more concentrated spot. In the heavy rainfall regime a spot with greater saturation has formed. This enables a larger rate of diffusion, resulting in increased dispersion of the solute.

Figure 5(c) still shows the effects of ponding on the soil surface. As the quantity of water overcomes the pressure gradient between the soil and plant roots, this causes a fraction of the solute to penetrate deep into the soil. However, the quantity of solute that penetrates deep into the soil is greatly reduced compared with the simulation without plant roots (Figure 5a).

Conclusions

We developed a coupled system of PDEs that describe the movement of water and solutes in soil. Furthermore, we incorporated an ODE to represent dynamic ponding as a function of rainfall, surface runoff and infiltration of water from a pond into the soil. We validated the pond model using data from a ridge and furrow study that measures the infiltration time of a pond into a loam soil, and found a ≈4% difference only between the results of the study and model simulations.

We found that when roots are absent in ridge and furrow soils, ponding can have a considerable effect on the penetration of solutes that are applied in the furrow of the geometry. This is directly affected by the size of the pond that forms in the furrows, which results from the quantity of rainfall and infiltration capacity of the soil. As the infiltration capacity of the soil decreases, the total volume of water immediately infiltrating the soil decreases and generates a larger pond in the furrow. This leads to a greater quantity of water infiltrating into the furrow, and transporting the solute deep into the soil. This can lead to deep solute penetration, which can cause substantial solute leaching.

The effects of solute penetration can be reduced by the presence of plant roots in the ridges of the domain. With the addition of vegetation to the ridges of the soil, the movement of water was dominated by the pressure gradient between the soil pore pressure and the pressure in the root xylem. Hence, the majority of infiltrated water from rainfall or ponding is moved towards the plant roots in the ridges of the system, which leads to solutes collecting adjacent to the root system. This could substantially reduce the quantity of solutes that move deep into the soil with heavy rain and surface ponding. Knowledge of this solute movement mechanism can aid targeted solute application on ridged surfaces to avoid leaching and contamination, and also promote crop yields in which solute application can be directed to provide greater efficiency for crops and plants.

Acknowledgements

Simon J Duncan acknowledges receipt of a BBSRC Syngenta Case PhD studentship BB/L5502625/1. Tiina Roose and Keith R Daly are funded by ERC Consolidation grant 646809 DIMR.

Image data for the figures in this paper are available at the University of Southampton ePrints depository http://dx.doi.org/10.5258/SOTON/400479

Conflict of interest statement

Paul Sweeney is an employee of Syngenta Ltd and Simon Duncan is funded by BBSRC Syngenta Case PhD studentship.

Appendix

Numerical solution of the model with COMSOL Multiphysics

Here we describe how we used the COMSOL Multiphysics (Version 5.1) finite element package to solve the model derived in this paper. We implemented the coupled system of PDEs for simultaneous water and solute movement, with the addition of an ODE for dynamic ponding on the soil surface.

Coupled water and solute model

We used COMSOL's inbuilt 'General Form PDE' to set up the coupled system of PDEs, Equations (12) and (31). This takes the form:

$$e_a \frac{\partial^2 \mathbf{r}}{\partial t^2} + d_a \frac{\partial \mathbf{r}}{\partial t} + \nabla \cdot \mathbf{\Theta} = f, \tag{A1}$$

where $\mathbf{r} = [S\ c]^T$ and e_a, d_a, $\mathbf{\Theta}$ and f are parameters to be defined by the user. To write the model in this form, the parameters were set up to replicate Equations (12) and (31) such that;

$$e_a = \begin{bmatrix} 0 & 0 \\ 0 & 0 \end{bmatrix}, d_a = \begin{bmatrix} \left[1 - H_S(p)\right] \phi \frac{\partial S}{\partial p} & 0 \\ c\left[1 - H_S(p)\right] \phi \frac{\partial S}{\partial p} & b + \phi S(p) \end{bmatrix},$$

$$\mathbf{\Theta} = \begin{bmatrix} -\frac{\kappa[S(p)]}{\mu}\left(\nabla p + \rho g \hat{\mathbf{k}}\right) \\ -D_f \phi^{d+1} S(p)^{d+1} \nabla c - \frac{c\kappa[S(p)]}{\mu}\left(\nabla p + \rho g \hat{\mathbf{k}}\right) \end{bmatrix},$$

$$f = \begin{bmatrix} -\lambda_c (p - p_r) \\ 0 \end{bmatrix}. \tag{A2}$$

For the ODE to describe a moving pond, Equation (23), we used the inbuilt ODE equation 'Global ODE' to calculate $x_0(t)$. The 'Global ODE' takes the form:

$$f\left(q, q_t, q_{tt}, t\right) = 0. \tag{A3}$$

To write Equation (23) in this form, the 'Global ODE' is set up such that:

$$\left\{AB\left[x_0(t) - \eta\right] \sin\left(Bx_0(t)\right)\right\} \frac{dx_0(t)}{dt} - \left[\Upsilon_r(t) + \Upsilon_p(x,t)\right] = 0, \tag{A4}$$

where:

$$\Upsilon_r(t) = \omega(t)\left(\eta - x_0(t)\right) + R_o(t), \tag{A5}$$

and

$$\Upsilon_p(x,t) = \int_{x_0(t)}^{\eta} \frac{\left(\frac{\kappa(p)}{\mu}\left(\partial_z p + \rho g\right)\right) + \left(AB \sin(Bx) \frac{\kappa(p)}{\mu} \partial_x p\right)}{\sqrt{\left(1 + (AB \sin(Bx))^2\right)}}. \tag{A6}$$

The integral in Equation (A6) was calculated with the inbuilt 'Boundary Integration Component Coupling' by a summation over the nodes along the top domain boundary.

Boundary conditions

For the flux boundaries used, Equations (16), (25), (32), (33) and (34), we used the inbuilt flux boundary condition that takes the form:

$$\mathbf{n} \cdot \mathbf{\Theta} = g_1 - g_2 \mathbf{r}, \tag{A7}$$

where g_1 and g_2 depend on the specific flux boundary. Similarly, for the constant boundary condition, Equation (26), we used the inbuilt Dirichlet boundary condition. This takes the form:

$$\mathbf{r} = r_0, \tag{A8}$$

where the parameter value used is described in the parameters section.

For the constant hydrostatic boundary, Equation (19), we could not impose the generic inbuilt Dirichlet boundary condition because it treats the constant boundary as a step function such that:

$$p = \begin{cases} \rho g\left[h_0(t) - \chi(x)\right], & \mathbf{x} \in \partial\Lambda_P \\ 0, & \mathbf{x} \in \partial\Lambda_R \end{cases}. \tag{A9}$$

This in turn leads to a permanent fully saturated boundary along the bare soil surface $\partial\Lambda_R$. To avoid this problem, we re-write Equation (19) as a flux condition along $\partial\Lambda_P$ such that:

$$\boldsymbol{n} \cdot \mathbf{\Theta} = k_\infty \left\{\rho g\left[h_0(t) - \chi(x)\right] - p\right\}, \tag{A10}$$

where $k_\infty \gg 1$. As k_∞ increases, Equation ((A10)) reduces to $p = \rho g[h_0(t) - \chi(x)]$. Therefore, Equation (19) can be approximated and imposed as a flux condition along the partition $\partial\Lambda_P$ only, providing k_∞ is significantly large. We chose $k_\infty = 1 \times 10^6$ because this is sufficiently large to cause $\mathbf{n} \cdot \mathbf{\Theta} \approx 0$.

References

Ahmadi, S.H., Plauborg, F., Andersen, M.N., Sepaskhah, A.R., Jensen, C.R. & Hansen, S. 2011. Effects of irrigation strategies and soils on field grown potatoes: root distribution. *Agricultural Water Management*, **98**, 1280–1290.

Azooz, R.H. & Arshad, M.A. 1996. Soil infiltration and hydraulic conductivity under long-term no-tillage and conventional tillage systems. *Canadian Journal of Soil Science*, **76**, 143–152.

Banti, M., Zissis, T. & Anastasiadou-Partheniou, E. 2011. Furrow irrigation advance simulation using a surface–subsurface interaction model. *Journal of Irrigation and Drainage Engineering*, **137**, 304–314.

Barber, S.A. 1995. *Soil Nutrient Bioavailability: A Mechanistic Approach*. John Wiley & Sons, Toronto.

Bautista, E., Warrick, A.W. & Strelkoff, T.S. 2014. New results for an approximate method for calculating two-dimensional furrow infiltration. *Journal of Irrigation and Drainage Engineering*, **140**, 04014032.

Bautista, E., Warrick, A., Schlegel, J., Thorp, K. & Hunsaker, D. 2016. Approximate furrow infiltration model for time-variable ponding depth. *Journal of Irrigation and Drainage Engineering*, **142**, 04016045.

Briggs, G.G., Bromilow, R.H. & Evans, A.A. 1982. Relationships between lipophilicity and root uptake and translocation of non-ionised chemicals by barley. *Pest Management Science*, **13**, 495–504.

Briggs, G.G., Bromilow, R.H., Evans, A.A. & Williams, M. 1983. Relationships between lipophilicity and the distribution of nonionised chemicals in barley shoots following uptake by the roots. *Pest Management Science*, **14**, 492–500.

Camporese, M., Paniconi, C., Putti, M. & Orlandini, S. 2010. Surface-subsurface flow modeling with path-based runoff routing, boundary condition-based coupling, and assimilation of multisource observation data. *Water Resources Research*, **46**, W02512.

Ebrahimian, H., Liaghat, A., Parsinejad, M., Playán, E., Abbasi, F. & Navabian, M. 2013. Simulation of 1D surface and 2D subsurface water flow and nitrate transport in alternate and conventional furrow fertigation. *Irrigation Science*, **31**, 301–316.

EFSA 2013. Scientific opinion on the report of the FOCUS groundwater working group (FOCUS, 2009): assessment of lower tiers. *EFSA Journal*, **11**, 3114.

Gandar, P. & Tanner, C. 1976. Potato leaf and tuber water potential measurements with a pressure chamber. *American Potato Journal*, **53**, 1–14.

van Genuchten, M.T. 1980. A closed-form equation for predicting the hydraulic conductivity of unsaturated soils. *Soil Science Society of America Journal*, **44**, 892–898.

Kirkham, M.B., Keeney, D.R. & Gardner, W.R. 1974. Uptake of water and labelled nitrate at different depths in the root zone of potato plants grown on a sandy soil. *Agro-Ecosystems*, **1**, 31–44.

Kollet, S.J. & Maxwell, R.M. 2006. Integrated surface–groundwater flow modeling: a free-surface overland flow boundary condition in a parallel groundwater flow model. *Advances in Water Resources*, **29**, 945–958.

Lesczynski, D.B. & Tanner, C.B. 1976. Seasonal variation of root distribution of irrigated, field-grown russet Burbank potato. *American Potato Journal*, **53**, 69–78.

Li, X., Su, D. & Yuan, Q. 2007. Ridge-furrow planting of alfalfa (Medicago sativa L.) for improved rainwater harvest in rainfed semiarid areas in Northwest China. *Soil and Tillage Research*, **93**, 117–125. Check original to see whether Roman or italic.

Liu, F., Shahnazari, A., Andersen, M.N., Jacobsen, S.-E. & Jensen, C.R. 2006. Physiological responses of potato (*Solanum tuberosum* L.) to partial root-zone drying: ABA signalling, leaf gas exchange, and water use efficiency. *Journal of Experimental Botany*, **57**, 3727–3735.

van Loon, C.D. 1981. The effect of water stress on potato growth, development, and yield. *American Potato Journal*, **58**, 51–69.

Morin, J. & Benyamini, Y. 1977. Rainfall infiltration into bare soils. *Water Resources Research*, **13**, 813–817.

Njoroge, S.M., Munyao, T.M. & Osano, O. 2016. Modeling relationship between organic carbon partition coefficient and pesticides solubility of pesticides used along the shore of Lake Naivasha, Kenya. *American Journal of Environmental Engineering*, **6**, 33–37.

Noda, T., Takahata, Y., Sato, T., Ikoma, H. & Mochida, H. 1997. Combined effects of planting and harvesting dates on starch properties of sweet potato roots. *Carbohydrate Polymers*, **33**, 169–176.

Nye, P.H. & Tinker, P.B. 1977. *Solute Movement in the Soil-Root System*. University of California Press, Berkeley and Los Angeles, CA.

Rawsthorne, D. & Brodie, B. 1986. Relationship between root growth of potato, root diffusate production, and hatching of *Globodera rostochiensis*. *Journal of Nematology*, **18**, 379–384.

Richards, L.A. 1931. Capillary conduction of liquids through porous mediums. *Journal of Applied Physics*, **1**, 318–333.

Roose, T. & Fowler, A.C. 2004a. A model for water uptake by plant roots. *Journal of Theoretical Biology*, **228**, 155–171.

Roose, T. & Fowler, A.C. 2004b. A mathematical model for water and nutrient uptake by plant root systems. *Journal of Theoretical Biology*, **228**, 173–184.

Rowell, D.L., Martin, M.W. & Nye, P.H. 1967. The measurement and mechanism of ion diffusion in soils III. The effect of moisture content and soil-solution concentration on the self-diffusion of ions in soils. *Journal of Soil Science*, **18**, 204–221.

Sanchez, C.A., Zerihun, D., Lazarovitch, N., Warrick, A., Clemmens, A. & Bautista, E. 2014. Modeling flow and solute transport in irrigation furrows. *Irrigation & Drainage Systems Engineering*, **3**, 124.

Shackelford, C.D. & Daniel, D.E. 1991. Diffusion in saturated soil. I: background. *Journal of Geotechnical Engineering*, **117**, 467–484.

Siyal, A.A., Bristow, K.L. & Šimůnek, J. 2012. Minimizing nitrogen leaching from furrow irrigation through novel fertilizer placement and soil surface management strategies. *Agricultural Water Management*, **115**, 242–251.

Steele, D., Greenland, R. & Hatterman-Valenti, H. 2006. Furrow vs hill planting of sprinkler-irrigated russet burbank potatoes on coarse-textured soils. *American Journal of Potato Research*, **83**, 249–257.

Steudle, E., Oren, R. & Schulze, E.-D. 1987. Water transport in maize roots measurement of hydraulic conductivity, solute permeability, and of reflection coefficients of excised roots using the root pressure probe. *Plant Physiology*, **84**, 1220–1232.

Tabuada, M., Rego, Z., Vachaud, G. & Pereira, L. 1995. Two-dimensional infiltration under furrow irrigation: modelling, its validation and applications. *Agricultural Water Management*, **27**, 105–123.

Tisdall, J.M. & Hodgson, A.S. 1990. Ridge tillage in Australia: a review. *Soil & Tillage Research*, **18**, 127–144.

Vogel, T., Gerke, H., Zhang, R. & van Genuchten, M.T. 2000. Modeling flow and transport in a two-dimensional dual-permeability system with spatially variable hydraulic properties. *Journal of Hydrology*, **238**, 78–89.

Watson, J.T.R., Basu, R. & Sengers, J.V. 1980. An improved representative equation for the dynamic viscosity of water substance. *Journal of Physical and Chemical Reference Data*, **9**, 1255–1290.

Weill, S., Mouche, E. & Patin, J. 2009. A generalized Richards equation for surface/subsurface flow modelling. *Journal of Hydrology*, **366**, 9–20.

Wöhling, T. & Schmitz, G.H. 2007. Physically based coupled model for simulating 1D surface–2D subsurface flow and plant water uptake in irrigation furrows. I: model development. *Journal of Irrigation and Drainage Engineering*, **133**, 538–547.

Yang, B., Blackwell, P.S. & Nicholson, D.F. 1996. A numerical model of heat and water movement in furrow-sown water repellent sandy soils. *Water Resources Research*, **32**, 3051–3061.

European Journal of Soil Science

European Journal of Soil Science, 2018 doi: 10.1111/ejss.12711

Mathematical modelling of water and solute movement in ridged versus flat planting systems

S. J. Duncan[a], K. R. Daly[a], P. Sweeney[b] & T. Roose[a]

[a]*Bioengineering Department, Faculty of Engineering and the Environment, University of Southampton, Southampton, SO17 1BJ, UK, and* [b]*Department of Product Safety, Syngenta, Jealott's Hill, Bracknell, RG42 6EY, UK*

Summary

We compared water and solute movement between a ridge and furrow geometry and that of flat soil with a mathematical model. We focused on the effects of two physical processes: root water uptake and pond formation on the soil surface. The mathematical model describes the interaction between solute transport, water movement and surface pond depth. Numerical simulations were used to determine how solutes of varying mobility and rates of degradation penetrated into the two soil geometries over a growing season. Both the ridge and furrow or flat soil geometries could reduce solute leaching, but this depended on several factors. Rain immediately after a solute application was a key factor in determining solute penetration into soil. In cases with delayed rain after a solute application, solutes in ridge and furrow geometries collected adjacent to the root system, resulting in reduced solute penetration compared to the flat soil geometry. In contrast, substantial rain immediately after a solute application resulted in ponding where water infiltration acted as the dominant transport mechanism. This resulted in increased solute penetration in the ridge and furrow geometry compared to the flat soil geometry.

Highlights

- We studied solute movement controlled by ponding in ridge and furrow and flat fields.
- We found the ridged soil could impede or increase leaching compared to the flat soil.
- Solute hot-spots formed in ridge and furrow soil because of root water uptake.
- Time between solute application and rainfall is a key factor for solute penetration.

Introduction

In arable farming several methods of planting are used to cultivate crops (Fahong *et al.*, 2004). Two planting methods are addressed in this paper: ridge and furrow planting (Robinson, 1999) and flat planting (Lewis & Rowberry, 1973). A ridge and furrow geometry is formed when the soil surface is modified to form a periodic series of peaks (ridges) and troughs (furrows). This allows water to flow across the field, providing water to the plants whilst preventing waterlogging of the roots (Tisdall & Hodgson, 1990). One crop that is traditionally grown in ridge and furrow geometries is the potato (*Solanum tuberosum,* L.) (Wayman, 1969), which is an essential crop in temperate European environments (Huaccho & Hijmans, 1999).

Correspondence: T. Roose. E-mail: t.roose@soton.ac.uk

Declaration of conflict of interest: Paul Sweeney is an employee of Syngenta Ltd and Simon Duncan is funded by BBSRC Syngenta Case PhD studentship.

Received 14 September 2017; revised version accepted 4 June 2018

There have been several experimental efforts to determine the difference in potato growth and production between ridge and furrow planting and other tillage methods. Such methods include wide beds (Mundy *et al.*, 1999), flat planting (Lewis & Rowberry, 1973) and furrow-only planting (Steele *et al.*, 2006). Both ridge and furrow and flat planting result in similar yields and tuber size (Lewis & Rowberry, 1973; Alva *et al.*, 2002), but ridge and furrow planting has been found to be the preferred method of tillage (Jordan *et al.*, 2013) because of ease of harvesting (Leistra & Boesten, 2010b), slow seed germination (Benjamin *et al.*, 1990) and nutrient replenishment in the soil (Feddes *et al.*, 1976).

Growing evidence suggests that ridge and furrow systems might be vulnerable to solute leaching (Lehrsch *et al.*, 2000; Alletto *et al.*, 2010; Kettering *et al.*, 2013). Experimentally, solutes have been applied to ridges and furrows of potato fields to determine the depth of solute penetration in different areas of the soil (Smelt *et al.*, 1981; Kung, 1988; Leistra & Boesten, 2010a). In these cases, the solute in the furrows moved to a greater absolute depth in soil, supporting the suggested vulnerability of the ridge and

furrow geometry to solute leaching. Furthermore, a recent European Food Safety Authority report indicated that ridge and furrow soil surfaces can increase leaching six-fold compared with flat surfaces (EFSA, 2013). However, there is also evidence that ridge and furrow planting can reduce leaching if solute management techniques are used (Jaynes & Swan, 1999). These techniques can reduce the negative environmental effect (Hatfield *et al.*, 1998), even compared with flat planting (Ressler *et al.*, 1997).

In this study, we determined the water and solute movement mechanisms and key environmental factors that affect leaching in ridge and furrow and flat planting systems. This will enable us to understand how the soil geometry affects transport within the soil. Understanding the key factors that affect solute leaching will allow us to determine qualitatively the increased risk to solute leaching between the two planting methods. This knowledge will assist us in developing solute application protocols unique to each planting method to reduce solute leaching and maintain greater nutrient availability to the crops.

Specifically, we modelled the transport of solutes with varying mobility and degradation in both soil geometries over 24-week periods. During this time, vegetation was present in soil for the first 16 weeks (i.e. a full growing season). Special attention was paid to ponding on the soil surface because we considered a temperate environment in the UK where there are often large amounts of rain. It should be noted that we assumed that there was no solute uptake by plant roots. In this paper we are only concerned with the solute transport problem (i.e. modelling the 'worst case scenario'), which applies directly to passive solutes.

Mathematical model

We used the water–solute–pond model developed in Duncan *et al.* (2018) to study water and solute movement in a cross-section of a ridge and furrow (or flat) geometry. Here we state the equations and parameters used in the model; for a full derivation see Duncan *et al.* (2018). The governing equations are:

$$\phi\frac{\partial S(p)}{\partial t}+\nabla\cdot\left\{-\frac{\kappa_s}{\mu}S(p)^{\frac{1}{2}}\left[1-\left(1-S(p)^{\frac{1}{m}}\right)^m\right]^2\left(\nabla p+\rho g\hat{\mathbf{k}}\right)\right\}=\begin{cases}-\lambda_c\left(p-p_r\right), & \mathbf{x}\in\Lambda_U\\ 0, & \mathbf{x}\in\Lambda_A\end{cases}, \tag{1}$$

$$\frac{\partial c}{\partial t}\left[b+S(p)\phi\right]+\frac{\partial p}{\partial t}\left\{\frac{\partial S(p)}{\partial p}\phi c\right\}+\nabla\cdot\left[-D_f\phi^{d+1}S(p)^{d+1}\nabla c\right]+\nabla\cdot\left\{-\frac{c\kappa_s}{\mu}S(p)^{\frac{1}{2}}\left[1-\left(1-S(p)^{\frac{1}{m}}\right)^m\right]^2\left(\nabla p+\rho g\hat{\mathbf{k}}\right)\right\}=-\xi c,\quad \mathbf{x}\in\Lambda, \tag{2}$$

where ϕ is the soil porosity, $S(p)$ is the relative saturation, μ is the viscosity of water, p is the soil water pore pressure, ρ is the density of water, g is the acceleration due to gravity, $\hat{\mathbf{k}}$ is a unit vector in the upwards direction, κ_s is the saturated hydraulic permeability, m is a van Genuchten parameter, λ_c is the product of the root surface area density and water conductivity of the plant root cortex, p_r is the pressure in the root xylem, D_f is the diffusion coefficient in free liquid, d is the impedance factor of the solute that accounts for the tortuosity of the solute moving through the pore space, c is the solute concentration in the pore water, ξ is the solute decay rate constant related to bacterial and other degradation processes, b is the buffer power, and Λ is a generalized ridge and furrow geometry (see Figure 1 in Duncan *et al.* (2018)) with subdomains Λ_U and Λ_A for regions where roots are present and absent respectively.

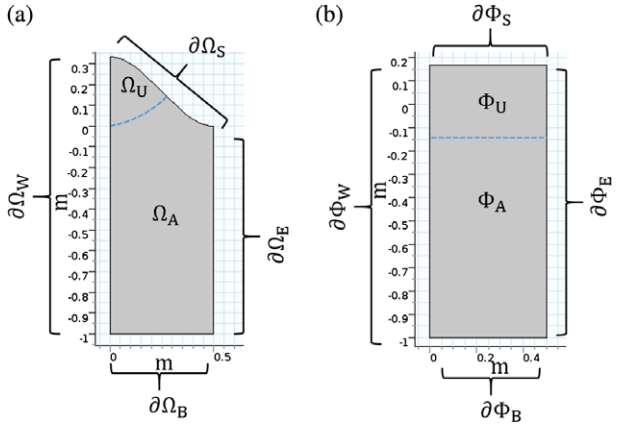

Figure 1 Simulated soil domains for a (a) ridge and furrow and (b) flat soil geometry, where Ω and Φ are the total cross-sectional areas of the two domains, $\partial\Omega_S$ and $\partial\Phi_S$ are the soil surface boundaries, $\partial\Omega_B$ and $\partial\Phi_B$ are the base boundaries, $\partial\Omega_W$, $\partial\Phi_W$, $\partial\Omega_E$ and $\partial\Phi_E$ are the lateral boundaries, Ω_A and Φ_A are the areas without root activity and Ω_U and Φ_U are the areas of soil containing root activity.

The boundary and initial conditions imposed on Λ are:

$$p=\rho g h(x,t),\quad \mathbf{x}\in\partial\Lambda_P, \tag{3}$$

$$\mathbf{n}\cdot\left\{\frac{\kappa_s}{\mu}S(p)^{\frac{1}{2}}\left[1-\left(1-S(p)^{\frac{1}{m}}\right)^m\right]^2\left(\nabla p+\rho g\hat{\mathbf{k}}\right)\right\}=\min\left\{\Gamma(t),I_c\right\},\quad \mathbf{x}\in\partial\Lambda_R, \tag{4}$$

$$\frac{dx_0(t)}{dt}=f\left(R_F(t),I_f(t),R_o(t)\right), \tag{5}$$

$$\mathbf{n}\cdot\left(\left[D_f\phi^{d+1}S(p)^{d+1}\nabla c\right]+\left\{\frac{c\kappa_s}{\mu}S(p)^{\frac{1}{2}}\left[1-\left(1-S(p)^{\frac{1}{m}}\right)^m\right]^2\left(\nabla p+\rho g\hat{\mathbf{k}}\right)\right\}\right)=c_m(t),\quad \mathbf{x}\in\partial\Lambda_S, \tag{6}$$

$$\mathbf{n}\cdot\left\{\frac{\kappa_s}{\mu}S(p)^{\frac{1}{2}}\left[1-\left(1-S(p)^{\frac{1}{m}}\right)^m\right]^2\left(\nabla p+\rho g\hat{\mathbf{k}}\right)\right\}=0,\quad \mathbf{x}\in\partial\Lambda_E\cup\partial\Lambda_W, \tag{7}$$

$$\mathbf{n}\cdot\Bigg(\left[D_{\mathrm{f}}\phi^{d+1}S(p)^{d+1}\,\boldsymbol{\nabla}c\right] + \left\{\frac{c\kappa_{\mathrm{s}}}{\mu}S(p)^{\frac{1}{2}}\left[1-\left(1-S(p)^{\frac{1}{m}}\right)^{m}\right]^{2}\left(\boldsymbol{\nabla}p+\rho g\hat{\mathbf{k}}\right)\right\}\Bigg)=0,$$

$$\mathbf{x}\in\partial\Lambda_{\mathrm{E}}\cup\partial\Lambda_{\mathrm{W}} \tag{8}$$

$$p=p_0,\qquad \mathbf{x}\in\partial\Lambda_{\mathrm{B}}, \tag{9}$$

$$c=c|_{t=0},\qquad \mathbf{x}\in\partial\Lambda_{\mathrm{B}}, \tag{10}$$

$$p|_{t=0}=p_{\infty}(\mathbf{x}),\qquad \mathbf{x}\in\Lambda, \tag{11}$$

$$x_0(t)\big|_{t=0}=\eta, \tag{12}$$

$$c|_{t=0}=0,\qquad \boldsymbol{x}\in\Lambda, \tag{13}$$

where $\partial\Lambda_{\mathrm{S}}$ is the soil surface boundary defined by the curve,

$$\chi(x)=A\cos(Bx)+C, \tag{14}$$

where A is the variation in soil depth, B is the ridge wave number and C is the average soil depth, $\partial\Lambda_{\mathrm{P}}$ is the region of $\partial\Lambda_{\mathrm{S}}$ where ponding occurs (see Figure 2 in Duncan *et al.* (2018)), $\partial\Lambda_{\mathrm{R}}$ is the region of $\partial\Lambda_{\mathrm{S}}$ that is not ponded (i.e. where rainfall penetrates the soil directly), and the interface between the two regions ($\partial\Lambda_{\mathrm{R}}$ and $\partial\Lambda_{\mathrm{P}}$) is defined by the moving boundary point $x_0(t)$ (see Figure 2 in Duncan *et al.* (2018)), $\partial\Lambda_{\mathrm{E}}$ and $\partial\Lambda_{\mathrm{W}}$ are the lateral boundaries of Λ, $\partial\Lambda_{\mathrm{B}}$ is the boundary at the base of Λ, $h(x,t)$ is the depth of the pond, $c_{\mathrm{m}}(t)$ is the volume flux of solute per unit soil surface area per unit time entering the soil domain, $\mathbf{n}$ is the unit normal vector pointing outwards of Λ, $\Gamma(t)$ is the volume flux of water per unit soil surface area (i.e. rainfall), I_{c} is the infiltration capacity of the soil, p_0 is the prescribed pressure at the base of the domain, η is the width of Λ, $R_{\mathrm{F}}(t)$ is rainfall landing directly into the pond, $I_{\mathrm{f}}(t)$ is the infiltration of water from the pond into the soil, $R_{\mathrm{o}}(t)$ is surface runoff, $c|_{t=0}$ is the initial solute concentration and $p_{\infty}(\mathbf{x})$ is the initial pressure profile.

Parameter values

There are 22 parameters in the model used in this study. These parameters are: ϕ, m, k_{s}, μ, g, ρ, p_{c}, D_{f}, d, b, $\Gamma(t)$, $c_{\mathrm{m}}(t)$, p_0, $p_{\infty}(\mathbf{x})$, λ_{c}, ξ, p_{r} and I_{c} for the coupled model, and the four parameters A, B, C and η for the construction of Λ. These parameters are summarized in Tables 1 and 2.

Geometric, soil, environmental, plant and solute parameter values

To model the differences in solute and water movement between ridge and furrow and flat geometries, we construct two domains. These domains are shown in Figure 1, where Ω is the ridge and furrow geometry and Φ is the flat geometry. The flat geometry Φ can be reduced to a one-dimensional problem; however, for ease of comparison we present it as a two-dimensional (2-D) geometry.

To replicate the dimensions of ridge and furrow geometries, we use the values $\eta=0.5$ m, $A=C=\frac{1}{6}$ m and $B=2\pi$ m^{-1} for the geometry Ω (Steele *et al.*, 2006; Li *et al.*, 2007). Furthermore, for the flat geometry we set $A=B=0, C=\frac{1}{6}$ m and $\eta=0.5$ m. To compare 'like for like' scenarios, we ensure that the ridge and furrow and flat geometries have the same total volume of soil.

Potatoes are a shallow-rooted crop in which the majority of roots are within the plough layer (i.e. the top 30 cm of soil) (Lesczynski & Tanner, 1976). Therefore, in the ridge and furrow geometry we chose the size of the soil root region Ω_{U} to be the top 30 cm of soil extending radially from the top of the ridge. Similarly, for the flat soil geometry we chose the soil root region Φ_{U} to be the top

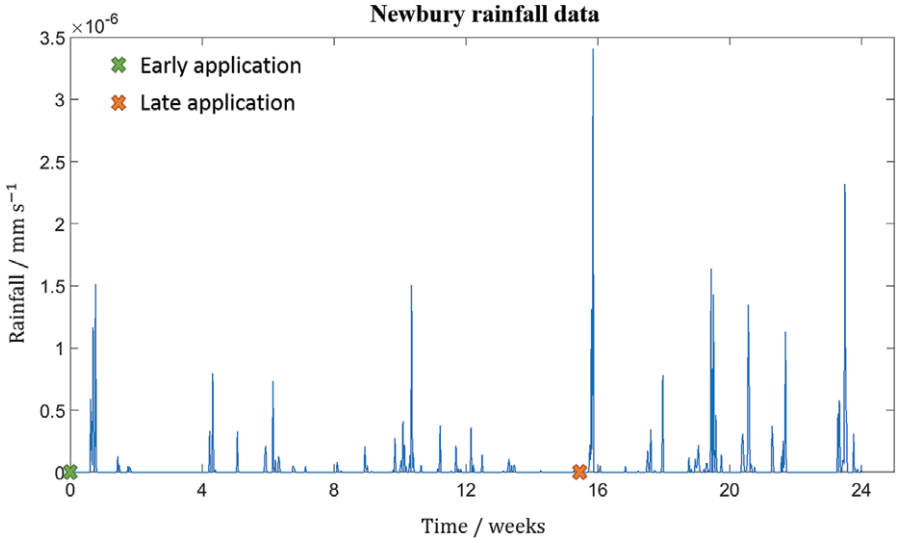

Figure 2 Newbury site experimental rainfall data over a 6-month period between 1 June 2006 and 31 December 2006. The green and orange crosses indicate the time of early and late solute applications, respectively.

Table 1 Model parameter values used in numerical simulation

Parameter	Description	Value	Units	Reference
ρ	Density of water	1×10^{3}	kg m^{-3}	–
g	Acceleration due to gravity	9.81	m s^{-2}	–
b	Buffer power	0.1/1/10	–	–
D_{f}	Diffusion coefficient in free liquid	2×10^{-9}	m^2 s^{-1}	(Shackelford & Daniel, 1991)
m	Van Genuchten parameter	0.5	–	(van Genuchten, 1980)
ϕ	Porosity	0.396	–	(van Genuchten, 1980)
κ_{s}	Saturated water permeability	5.2×10^{-14}	m^2	(van Genuchten, 1980)
p_{c}	Characteristic soil suction	23 200	Pa	(van Genuchten, 1980)
d	Impedance factor	2	–	(Nye & Tinker, 1977; Roose & Fowler, 2004b)
μ	Viscosity of water	1×10^{-3}	kg m^{-1} s^{-1}	–
λ_{c}	Product of root surface area density and water conductivity	$0-2.355\times10^{-5}$	s^{-1}MPa^{-1}	(Lesczynski & Tanner, 1976; Rawsthorne & Brodie, 1986; Steudle *et al.*, 1987; Roose & Fowler, 2004a)
p_{r}	Root xylem pressure	-0.05	MPa	(Liu *et al.*, 2006)
t^*_λ	Solute half-life	10/50/500	Days	–
I_{c}	Infiltration capacity	1.6×10^{-6}	m s^{-1}	(Morin & Benyamini, 1977)
A	Variation in soil depth	$0.1\dot{6}/0$	m	(Steele *et al.*, 2006; Li *et al.*, 2007)
B	Ridge wave number	$2\pi/0$	m^{-1}	(Steele *et al.*, 2006; Li *et al.*, 2007)
C	Average soil depth	$0.1\dot{6}/0$	m	(Steele *et al.*, 2006; Li *et al.*, 2007)
η	Geometry width	0.5	m	(Steele *et al.*, 2006; Li *et al.*, 2007)

Table 2 Matrix of simulated solutes used in numerical simulation

	Extremely mobile $b=0.1$	Highly mobile $b=1$	Moderately mobile $b=10$
High degradation, $t^*_\lambda = 10$days	Solute α_1	Solute β_1	Solute γ_1
Medium degradation, $t^*_\lambda = 50$ days	Solute α_2	Solute β_2	Solute γ_2
Low degradation, $t^*_\lambda = 500$ days	Solute α_3	Solute β_3	Solute γ_3

30 cm of soil (see Figure 1). There is a difference in the total root active soil between Ω_{U} and Φ_{U}, but this is taken into account when establishing the parameter for root length density (see below).

Several of the parameters in the model depend on the soil, including $\phi, m, \kappa_{\mathrm{s}}$ and p_{c}. Potatoes are frequently grown in silt loam soil (Shock *et al.*, 1998). Therefore, we chose to use the parameter values for the 'Silt Loam G.E.3' soil from van Genuchten (1980) (i.e. $\phi=0.396$, $m=0.51$, $\kappa_{\mathrm{s}}=5.2\times10^{-14}$ m^2 and $p_{\mathrm{c}}=23\,200$ Pa). Note that in some cases different tillage methods applied to soil can alter the porosity of the system. However, to ensure a 'like for like' comparison, we kept the porosity the same in both soil domains to ensure that any differences we observed were an effect of the soil geometry and not dependent on small variations in local porosity within the soil.

We took values from the literature for the environmental and fluid parameters. For the viscosity of water we used $\mu=1\times10^{-3}$ kg m^{-1} s^{-1}, for acceleration due to gravity $g=9.81$ m s^{-2} and for the density of water $\rho=1000$ kg m^{-3}.

The typical range of the impedance coefficient d is between 0.5 and 2 (Nye & Tinker, 1977). Furthermore, increased volumetric moisture content leads to an increase in the impedance factor for a solute (Rowell *et al.*, 1967). Given that we are modelling a temperate UK climate with frequent heavy rain events, we took d to be at the upper bound of this range (i.e. $d=2$).

Values of the diffusion coefficient D_{f} in a solution of free liquid for simple electrolytes range from $1\times10^{-9}$to 3×10^{-9} m^2 s^{-1} (Shackelford & Daniel, 1991). Therefore, we chose the value to be in the middle of this range (i.e. $D_{\mathrm{f}}=2\times10^{-9}$ m^2 s^{-1}).

The parameter λ_{c} is the product of the root surface area density and the water conductivity of the root cortex; this can be expressed as:

$$\lambda_{\mathrm{c}} = k_{\mathrm{r}} l_{\mathrm{d}}(t)\,, \tag{15}$$

where $l_{\mathrm{d}}(t)$ is the root length density and k_{r} is the radial conductivity of the root cortex per unit root length.

We simulated 24 weeks of solute and water movement in soil, in which vegetation was present for the first 16 weeks, which is typical for a potato crop (Noda *et al.*, 1997). For potato plants the root length density changes significantly over a 16-week growing period (Lesczynski & Tanner, 1976). Lesczynski & Tanner (1976) found that over the first 30 days the root length density develops to approximately $l_{\mathrm{d}}=3\times10^{4}$ m m^{-3} in the plough layer of soil. This then remains fairly constant until approximately 90 days, at which the root length density declines. To represent this growth and development, we assigned $l_{\mathrm{d}}(t)$ the piecewise function (in m m^{-3}) as follows:

$$l_{\mathrm{d}}(t) = \begin{cases} 1\times10^{3}\,t & 0 \le t < 30 \text{ days} \\ 3\times10^{4} & 30 \le t < 90 \text{ days} \\ 3\times10^{4} - \left(1\times10^{3}\right)\times(t-90) & 90 \le t < 120 \text{ days} \\ 0 & 120 < t \text{ days} \end{cases}. \tag{16}$$

These results were obtained with ridge and furrow planting; therefore, we must account for this when determining a root length density function for the flat soil geometry. To have the same total root length in Ω and Φ, we scale $l_d(t)$ in the flat geometry by the ratio of the two root active areas Ω_U and Φ_U. This ensures a 'like for like' comparison between the two geometries.

For maize (*Zea mays,* L.) roots, the parameter k_r is given the value 7.85×10^{-10} m^{2}s^{-1}MPa^{-1} (Roose & Fowler, 2004a). Maize and potato roots have similar root radii and structure (Rawsthorne & Brodie, 1986; Steudle *et al.*, 1987); therefore, we assumed that this value of k_r is also representative of potato roots in soil.

To describe root pressure p_r, there are models for root pressure distribution within a single root (Roose & Fowler, 2004a). However, to simulate large areas of soil consisting of many roots, we used an average root pressure to describe the plant root system. The root pressure p_r can vary considerably in potatoes depending on several factors, including soil saturation and atmospheric conditions (Gandar & Tanner, 1976). Liu *et al.* (2006) found that the root water potential changed considerably based on the method of irrigation applied to the crop. They found that p_r was ≈ -0.01 MPa in the roots of a fully irrigated system and $\approx(-0.02, -0.2)$ MPa for areas of soil with partial root drying. Given that we model frequent rain events that promote ponding, we chose the value $p_r = -0.05$ MPa.

The infiltration capacity I_c of soil depends on several factors, including volumetric water content, soil type and tillage methods (Azooz & Arshad, 1996). Therefore, it is difficult to assign a single value to the infiltration capacity of a soil. Morin & Benyamini (1977) found that steady state infiltration of bare loam soil was reached after approximately 20 minutes into a rain event. However, the rain data we used (see 'Rainfall and solute application parameter values') has a time resolution of 1 hour, which is considerably larger than the time required to reach steady state infiltration. Therefore, we averaged the infiltration capacity over each rain event. Morin & Benyamini (1977) found that the steady state rate of infiltration of bare loam soil is between 1.3 and 2.2×10^{-6} m s^{-1}. Given this, we chose to assign the value $I_c = 1.3 \times 10^{-6}$ m s^{-1}.

We show results of numerical simulations for multiple hypothetical solutes with varying rates of degradation and buffering capacity to determine the differences in solute movement between the ridge and furrow and flat soil geometries. In Table 2 we give a matrix of the solute parameters that were used in the simulations.

We chose to model extremely mobile solutes $(\alpha_1, \alpha_2, \alpha_3)$ with a buffer power of $b = 0.1$, highly mobile solutes $(\beta_1, \beta_2, \beta_3)$ with a buffer power of $b = 1$ and moderately mobile solutes $(\gamma_1, \gamma_2, \gamma_3)$ with a buffer power of $b = 10$.

It is generally accepted that rates of degradation of pesticide-like solutes in soil decrease with depth (Fomsgaard, 1995). Therefore, one value for the decay constant is not valid for the entirety of the soil domains in Figure 1. For the pesticides isoproturon and metolachlor, the half-life is approximately doubled between the initial 0–30 cm of soil and 1 m below the soil surface (Rice *et al.*, 2002; Bending & Rodriguez-Cruz, 2007). Hence, for spatially varying degradation, we impose the function:

$$t_\lambda(\mathbf{x}) = t^*_\lambda + |z_A| t^*_\lambda, \tag{17}$$

where t^*_λ is the half-life of the solute in the plough layer and $|z_A|$ is the absolute depth below the soil surface.

For the rapidly degrading solutes $(\alpha_1, \beta_1, \gamma_1)$ we chose the value for the half life $t^*_\lambda = 10$ days, for a moderately fast degrading solute $(\alpha_2, \beta_2, \gamma_2)$ we selected the value $t^*_\lambda = 50$ days and for slowly degrading solutes $(\alpha_3, \beta_3, \gamma_3)$ we selected the value $t^*_\lambda = 500$ days. It follows that the half-life t^*_λ relates to the solute decay constant ξ by:

$$\xi = \frac{\ln(2)}{t_\lambda(\mathbf{x})}. \tag{18}$$

Boundary and initial condition parameter values

For the parameter p_0 that describes a constant saturation at the base of the geometry, we assigned the pressure value $p_0 = -10$ kPa. This equates to a saturation level of approximately $S \approx 0.9$ for a silt loam soil, thereby replicating a shallow water table. For the soil water pore pressure initial condition $p_\infty(\mathbf{x})$, we chose to impose the steady state profile that forms when the domain has no plant roots. As a result of capillary forces and gravity, this leads to a constant pressure gradient from the base to the top of the geometry, such that:

$$p_\infty(\mathbf{x}) = -p^m_\infty z - p^c_\infty, \quad \mathbf{x} \in \Omega \cup \Phi, \tag{19}$$

where $p^m_\infty = 9825$ Pa and $p^c_\infty = 19\,825$ Pa.

Rainfall and solute application parameter values

We simulated solute and water movement over a 24-week period in which vegetation was present for the first 16 weeks. Potatoes are typically planted from April to June and are harvested in September to November (Noda *et al.*, 1997). Therefore, we simulated this 'growth and harvesting' time frame with an additional 8 weeks to determine how solutes move once the crops are harvested.

For the volume flux of water per unit soil surface area $\Gamma(t)$ (i.e. rainfall), we used 6 months of rain field data from a site in Newbury, UK, between 1 June 2006 and 31 December 2006. These data are shown in Figure 2. The data were recorded from instruments that were installed on a slope next to the A34 Newbury bypass (United Kingdom Ordnance Survey grid reference SU455652). Acquisition of the data is described in Smethurst *et al.* (2006).

We applied the solutes at one of two times during the numerical simulations; these are denoted as the early and late applications. For the early application, solute was applied to the soil surface at the start of the simulation over the initial 24 hours, with a total application of 1 kg ha^{-1} (i.e. an application rate of $c_m(t) = 1.157 \times 10^{-9}$ kg m^{-2} s^{-1}). Similarly, for the late application a solute was applied for 24 hours with the same rate of application at the beginning of the 15th week. These can be seen in Figure 2. The early and late application times were chosen to

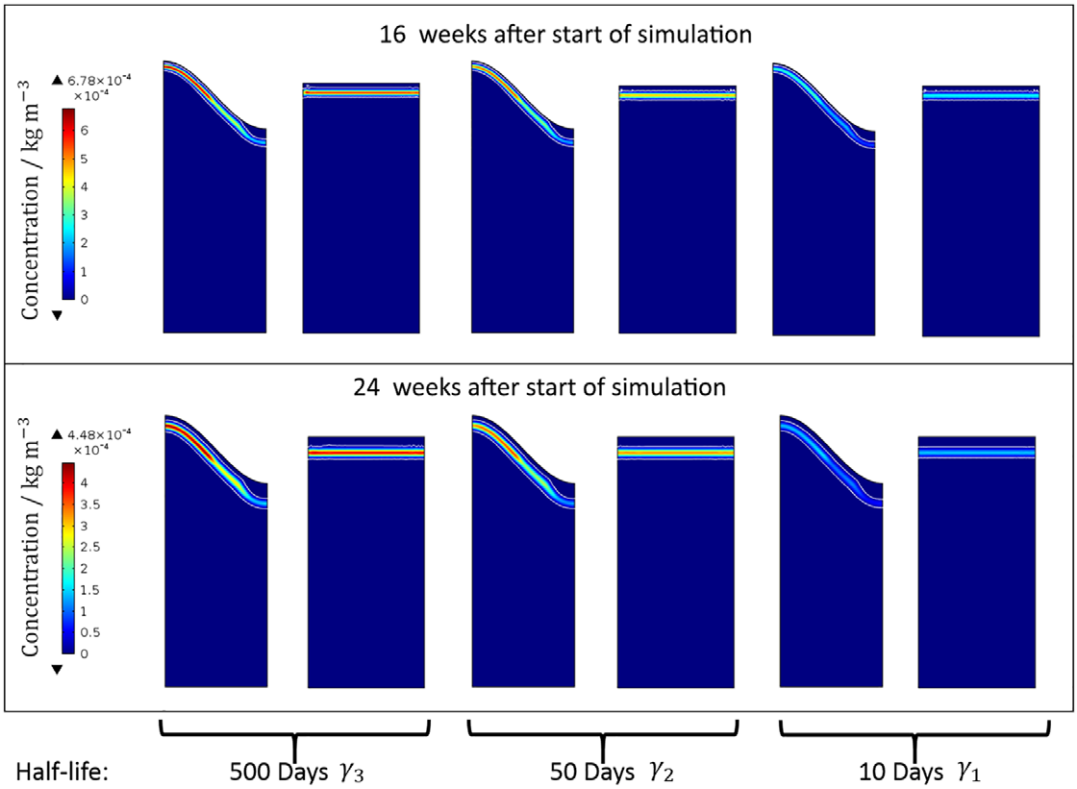

Figure 3 Early-application solute profiles in the ridged and flat domains for the moderately mobile solutes ($\gamma_1, \gamma_2, \gamma_3$) 16 and 24 weeks after solute application. A white contour line for the safety threshold of 10 µg l^{-1}is also plotted. The ridge and furrow and flat geometries are the same as those shown in Figure 1.

determine how solute movement is affected during a growing and degrading root system, respectively. For the early application, the solute was applied as soon as the root system began to grow and the late application was applied shortly after the root length density began to decrease.

Results

We performed a total of 36 simulations; nine simulations for the ridged geometry with an early application (for all nine hypothetical solutes in Table 2), nine for the ridged geometry with a late application, nine for the flat geometry with an early application and nine simulations for the flat geometry with a late application.

Early application results

Figure 3 shows the results for the early application of solutes for both the ridged and flat planting systems for the moderately mobile solutes (i.e. solutes γ_1, γ_2 and γ_3) (see Table 2). The results in Figure 3 show the solute profiles in the two soil geometries at 16 and 24 weeks after the solute application. At 16 weeks after the solute application, water uptake from vegetation stops because this simulates harvesting and the removal of crops, and 24 weeks after solute application is the end of the simulation time frame. Furthermore, an additional contour plot of concentration 10 µg l^{-1} (shown in white) was added to each profile, because this concentration is frequently used as a pesticide safety threshold for root and tuber vegetables (EU, 2018). In Figures 4 and 5 we show the results for the highly mobile (β_1, β_2, β_3) and extremely mobile (α_1, α_2, α_3) solutes, respectively.

For the moderately mobile solutes ($\gamma_1, \gamma_2, \gamma_3$), there was no significant penetration of the solutes into either of the soil geometries because of the buffer power of the solutes (see Figure 3). However, several features of the solute movement can be identified. First, the solute adjacent to the furrow has penetrated deeper into the soil than that contained in the ridge. Experimentally, deep furrow penetration has been attributed to the effects of ponding in the furrow of the geometry from soil surface runoff (Leistra & Boesten, 2010a), which is evident in the simulation results.

Furthermore, we note that because roots take up water, solute is drawn up towards the ridges through the difference between the soil water pore pressure and pressure in the root system. Chen *et al.* (2011) found that in ridge and furrow structures, water that infiltrated into the furrows of the system was transported to the ridges, which in turn reduced water movement directly below the ridge. In the simulations, this resulted in greater concentrations of solute in the ridges of the system from water transporting the solute. This coincides with the results of Smelt *et al.* (1981), who found that most solute residues were in the ridges of the ridge and furrow structures at the end of the growing season. Similarly,

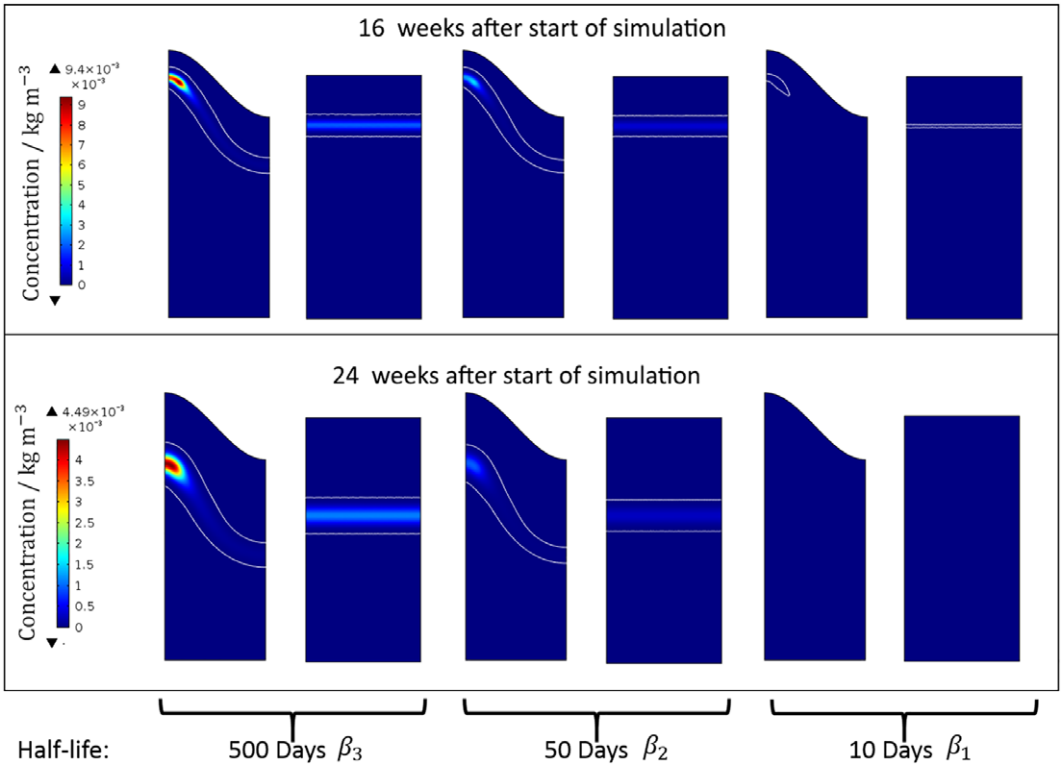

Figure 4 Early-application solute profiles in the ridged and flat domains for the highly mobile solutes ($\beta_1, \beta_2, \beta_3$) 16 and 24 weeks after solute application. A white contour line for the safety threshold of 10 μg l^{-1}is also plotted. The ridge and furrow and flat geometries are the same as those shown in Figure 1.

Jaynes & Swan (1999) found substantially larger concentrations in the ridges of the structure than the furrows.

In the flat soil geometry, the solute moved down uniformly and was temporarily impeded by the roots in the plough layer. When we compared the solute penetration between the flat and ridged soils, we found that the solute in the flat geometry moved to a greater absolute depth below the soil surface than that in the ridges. This result concurs with that of Hamlett *et al.* (1990), who identified that placing solutes on the ridges of the structure substantially reduced the amount leached compared with the flat field application. Jaynes & Swan (1999) supported this hypothesis, and in addition found that applications to the ridges could provide increased quantities of solute to the plant (i.e. nutrients and fertilizers).

We observed, however, that the solute in the flat soil penetrated less than that in the furrows of the ridged soil. This can be explained by the distribution of ponding on the two soil geometries. When ponding occurred on the flat soil, the ponding depth was considerably shallower than on the ridged soil because the pond was spread uniformly over the entire soil surface, whereas for the ridged soil the pond was only in the furrow. This in turn, causes a greater body of water to infiltrate into the furrow, causing deep solute penetration in this region of the geometry, but reducing the penetration of solutes in the ridges of the geometry.

Similar properties are evident in Figure 4 (for the solutes β_1, β_2, β_3) and Figure 5 (for the solutes α_1, α_2, α_3) for the simulations containing highly and extremely mobile solutes, respectively. For the highly mobile solutes β_1, β_2 and β_3 in the ridged system (Figure 4), the effect of solute accumulation in the ridges is more pronounced. In the ridge simulation containing solute β_3 at 16 weeks after solute application, there is a large quantity of solute in the region of soil adjacent to the plant roots because of water transport to the ridges created by the ridge and furrow geometry (Bargar *et al.*, 1999; Chen *et al.*, 2011).

At 24 weeks (the end of the simulation), the solute has penetrated into the soil as a concentrated spot that diffuses out slowly. We know that solute movement was reduced there when there was root uptake in soil (Benjamin *et al.*, 1996). Roots are only present for the first 16 weeks; therefore, for the remaining 8 weeks the solute is affected more by rain moving into the ridges. Hence, we observed deeper solute penetration in the later portion of the simulation. Furthermore, we note that for the highly degrading solute β_1, the concentration decreased below the 10 μg l^{-1} threshold for both soil geometries. This was due to the combination of fast dispersion and short half-life. In either geometry, it is the slowly degrading solutes (α_3, β_3, γ_3) that are of critical importance.

Figure 5 shows the results for the extremely mobile solutes α_1, α_2 and α_3. For the solute α_3, we found that a quantity of solute left the base of both soil geometries. In the ridge simulation, as an effect of the solute accumulating in the ridges, the solute moved down the soil profile as a highly concentrated spot. Given that the solute was drawn up into the ridges early in the simulation, the majority of the solute was not affected by later ponding in the furrows.

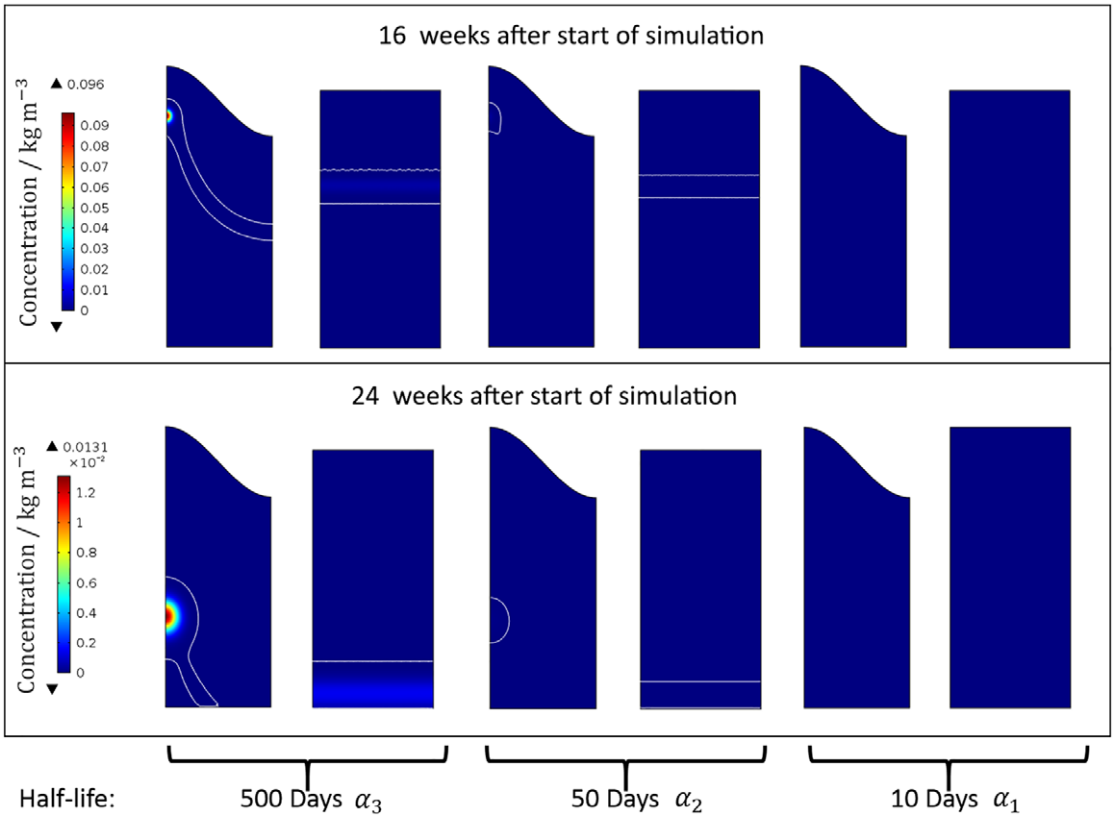

Figure 5 Early-application solute profiles in the ridged and flat domains for the extremely mobile solutes ($\alpha_1, \alpha_2, \alpha_3$) 16 and 24 weeks after solute application. A white contour line for the safety threshold of 10 μg l^{-1}is also plotted. The ridge and furrow and flat geometries are the same as those shown in Figure 1.

Therefore, the solute moves down solely under the influence of the rain that entered the ridge of the soil, and takes longer to reach the base of the geometry. In the flat geometry, however, all of the solute was affected by ponding (albeit considerably less than in the furrow of the ridged soil). This led to large quantities of the solute reaching the base of the geometry. The total amount of solute that crossed the base of the geometry was 0.26 mg in the ridged system and 3.5 mg in the flat system. These findings support the results observed by Hamlett *et al.* (1990) and Jaynes & Swan (1999), who found that placing solutes on the ridges of the structure substantially reduced leaching compared with the flat field application. Applying solute solely to the ridges negated the effects of ponding, which reduced the penetration depth in the soil. Furthermore, root uptake reduced solute movement in the ridges (Benjamin *et al.*, 1996). This caused the solute to remain near the surface, allowing for easy solute extraction from the soil after harvesting.

In the ridge and furrow simulations, we observed that, as an effect of water uptake from plant roots, movement of the solute from the furrow to the ridges protected the solute from deep penetration, which would otherwise result from furrow ponding. Flat ground has a uniform surface that offered no protection; therefore, all the solute was affected by ponding and rainfall. Therefore, the average depth of the solute was reduced in the ridged soil compared with the flat soil when this solute movement mechanism was present.

Late application results

Figure 6 shows the solute profiles for the early and late applications of the solutes α_3, β_3 and γ_3 (i.e. those with slow degradation) in the two soil geometries at the end of the simulations. For simulations with the early application the solutes were in the soil for a full 24 weeks, and for the late application the solutes were in the soil for 9 weeks. We chose to show the results of the slowly degrading solutes only because they showed the most extreme behaviour and highlight the effects of surface ponding best. Nevertheless, the other solutes showed a similar qualitative behaviour.

From the results in Figure 6 we can highlight several key features. In the simulations with the late application of solutes α_3, β_3 and γ_3 in the ridge and furrow geometry, a substantial quantity of solute penetrates into the furrow. This is considerably different from the simulations of solute profile in the early application to the ridge and furrow, in which the solutes move towards the ridge and form a concentrated spot.

There appear to be three reasons for differences in the solute profiles between the early and late applications to the ridge and furrow soil. First, for the late application simulation, the time that the solute was in the soil was less than for the early application. Therefore, in simulations of the late application there was not as much time for the solute to be transported towards the ridge of the structure by water that infiltrated into the furrows and moved

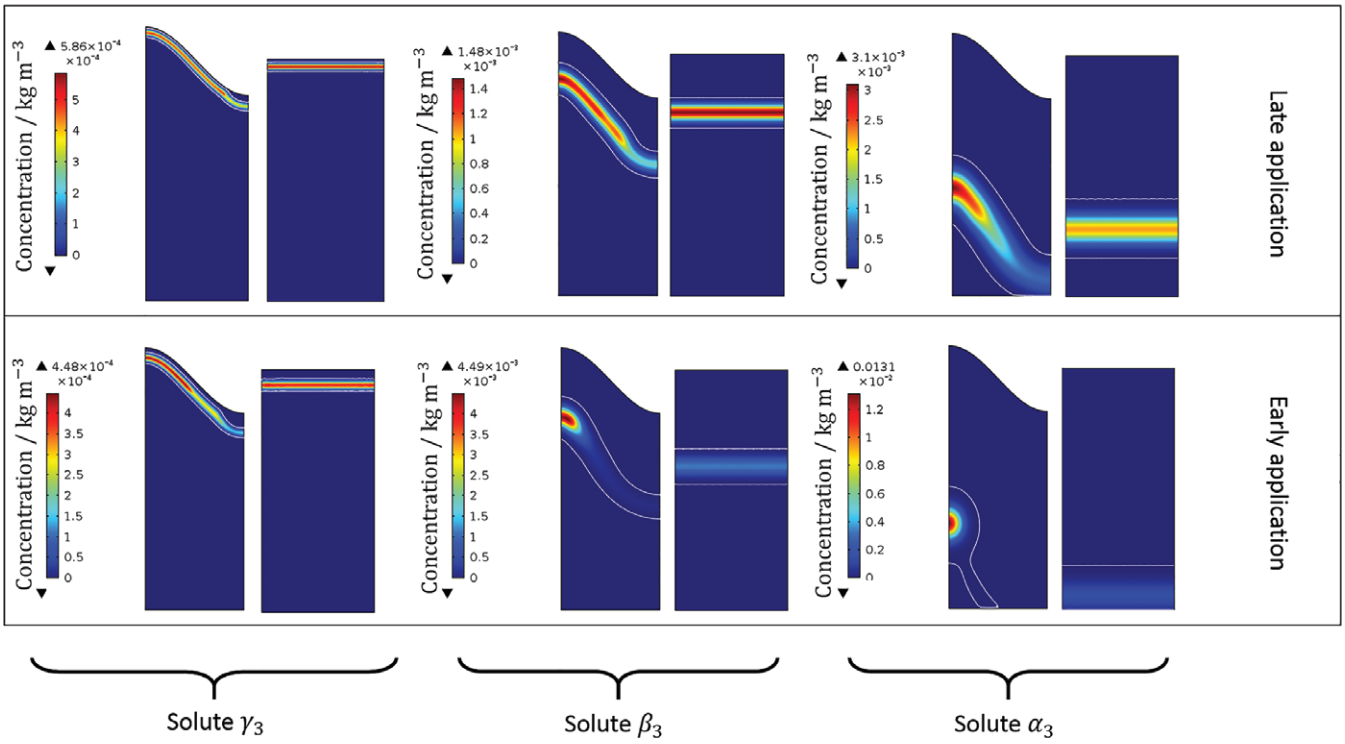

Figure 6 Early- and late-application solute profiles in the ridged and flat domains for the slow degrading solutes (α_3, β_3, γ_3) at the end of the 24-week simulations. A white contour line for the safety threshold of 10 μg l^{-1}is also plotted. The ridge and furrow and flat geometries are the same as those shown in Figure 1.

to the ridges (Bargar *et al.*, 1999; Chen *et al.*, 2011). Second, for the late application the root length density was beginning to decline such that the root uptake was not as strong as earlier in the simulated growing season (refer to Equation (16)). Consequently, the difference in the soil water pore pressure between the ridge and the furrow decreased, which resulted in less movement of water and solute towards the ridge and greater solute penetration (Benjamin *et al.*, 1996). The third reason for the reduction in spot formation was rain that occurred immediately after the late application. Figure 2 shows that there was an intense rain event shortly after the late application, which caused considerable ponding in the furrow of the soil. Given that the solute had been applied recently to the soil, there had not been sufficient time for it to collect in the ridges. Therefore, the solute contained in the region of soil adjacent to the furrow moved deep into the soil by water infiltration from the pond because surface runoff leading to pond infiltration acts as a key transport mechanism for the solute (Leistra & Boesten, 2010a).

From the rainfall data shown in Figure 2, we can see that during the second 3-month period (representing the winter months) there are more frequent 'high-intensity' rain events than during the first 3 months. In simulations of the late application, this caused solute in the furrow of the ridged geometry to move deep into the soil and did not allow formation of a spot in the ridges. This made the solute in the furrow vulnerable to leaching because large amounts of water infiltration can generate substantial dispersion of solutes in ridged soil (Abbasi *et al.*, 2004). The effect of the 'time of ponding' is evident in the difference between the simulation results for early and late applications of the solute α_3 in the ridged soil. In the early application, the solute collected in the ridges of the system because of little ponding and a growing root system, and then proceeded to move down as a concentrated spot as the root length density decreased. For the late application with immediate surface ponding and a lack of roots, the solute moved down the profile with a wider distribution under the influence of infiltration of water from the pond.

For the simulations of the extremely mobile solute α_3, in several cases some solute left the system from the base of the geometry. Furthermore, the total quantity that crossed the base of the domain depended on the soil geometry and time of application. In simulations of the early application, 0.26 mg of solute leached in the ridge geometry, whereas it was 3.5 mg for the flat system. For the late application, however, the amount leached was 0.15 mg in ridge geometry and it was zero in the flat system.

The model results suggest that the optimal geometry to reduce solute leaching depends on two key aspects: the immediate rainfall regime after solute application, and the quantity of roots in the soil. In simulations of the early solute application, the amount of rain was not sufficient to generate substantial furrow ponding. This allowed the solute to move towards the ridges of the system under the influence of water movement, which is often observed in ridge and furrow soils (Bargar *et al.*, 1999; Chen *et al.*, 2011). This protects the solute from future furrow ponding because root uptake

can reduce solute movement in the ridges (Benjamin *et al.*, 1996). In contrast, for simulations of the late application there was an immediate heavy rain event after solute application that caused substantial ponding. This generated more ponding in the ridged than the flat soil, which resulted in the solute in the furrow being transported deeper into the soil. This made the ridge and furrow system substantially more vulnerable to solute leaching than the flat soil. Therefore, substantial rain that causes ponding after a solute application may make the ridged system more susceptible to solute leaching.

Time of rain versus solute leaching

From the results above, we ran a series of simulations to test the hypothesis that the time between solute application and a heavy rain event influences the quantity of leaching in ridged soil. We set up five ridged and five flat soil simulations in which a solute (with the same properties as the solute α_3) was applied uniformly to each soil. One heavy rain event that would generate substantial ponding was then simulated at different times after the solute application in each simulation. The rain event was chosen to last for 4 hours and have a rainfall intensity of 12 mm hour^{-1}, and the times between solute application and the rain event were chosen to be 1, 2 and 4 days, 1 and 2 weeks. One day after the rain event, the total amount of solute that crossed the plough layer was then calculated. The plough layer was chosen to be the soil above the horizontal line of −0.15 m in both soil geometries shown in Figure 1.

Figure 7 shows the total amount of solute (as a percentage of solute applied) that crossed the horizontal line of −0.15 m in the soil geometries. For the simulations where the heavy rain event was 1 day after solute application, there were trace amounts of leaching in the flat geometry. However, in the ridged geometry 11% of solute applied leached past the plough layer.

In the simulations for longer periods of time between the solute application and the rain event, the relation between the amounts of solute that were leached in the two geometries changed. In the ridge and furrow simulations, as the time between solute application and rain event increased more of the solute moved towards the ridges of the soil by water transport from the furrows (Chen *et al.*, 2011). This caused less solute to be affected by the ponding and water infiltration from the heavy rain event, and less solute moved below the plough layer. For example, when the time period between solute application and rain was 14 days, approximately 1.5% of the solute applied was leached below the plough layer.

The flat geometry, however, showed the opposite behaviour. As the time between solute application and the rain event increased, more solute was leached past the plough layer. This resulted from solute diffusion in the system before the rain event. We simulated an extremely mobile solute; therefore, the longer it was in the system the more it diffused. This meant that the rain and pond infiltration had a greater effect on transport of the solute. In the simulation with a 14-day period between solute application and the rain event, the total amount of solute leached was approximately 11%.

Figure 7 illustrates a crossover between the total quantities of solute leached in the plough layer for the two geometries after approximately 8 days. In the case study of an extremely mobile solute and a single heavy rain event in a silt loam soil, there was less than 8 days between solute application and the rain event and the flat geometry reduced leaching more. However, with more than 8 days between solute application and rain, the ridge and furrow geometry reduced leaching more than for the flat geometry because the solute moved towards the ridges and created a 'zone of protection' from ponding. This crossover period, however, can change considerably depending on the mobility of solute, rainfall regime and type of plant roots. For example, in scenarios where the applied solute is less mobile and root densities in the soil are less, the time for ridge accumulation will be longer, thereby delaying the crossover period. Nevertheless, these results suggested that specific situations determine whether the ridge and furrow or the flat soil are better at reducing leaching.

Discussion

In previous research, ridge and furrow planting has often been shown to lead to greater leaching of solutes than the flat system

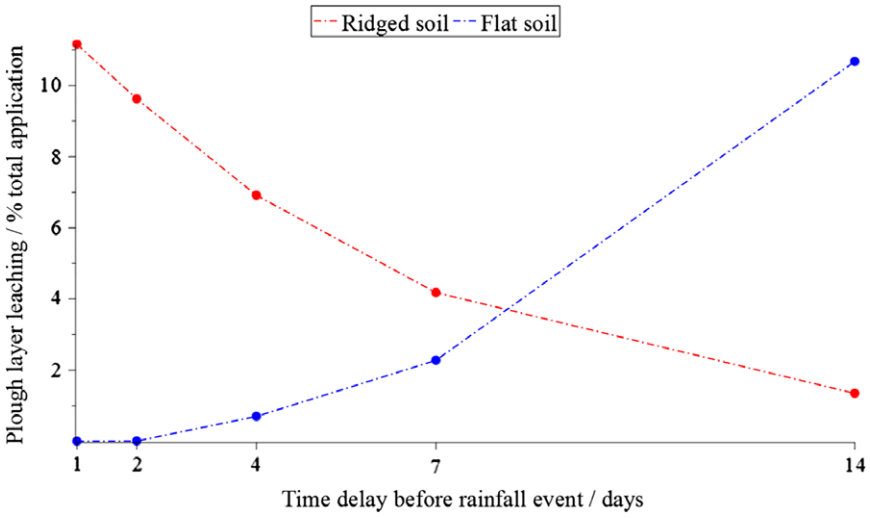

Figure 7 Total amount of solute leached beyond the plough layer in the ridge and furrow soil, Ω, and flat soil, Φ, for simulations that delayed the period of time between a solute application and a heavy rain event.

(Lehrsch *et al.*, 2000; Alletto *et al.*, 2010; Kettering *et al.*, 2013). However, certain application procedures might reduce leaching in ridged fields more than in flat fields (Ressler *et al.*, 1997; Hatfield *et al.*, 1998; Jaynes & Swan, 1999). This latter supports our findings; we observed that water movement from the furrows to the ridges (Bargar *et al.*, 1999) can transport solutes into the adjacent root zones of the structure and while held there by plant roots (Benjamin *et al.*, 1996) they reduced the effect from dominant surface runoff and subsequent infiltration (Leistra & Boesten, 2010a). Therefore, ridge and furrow systems can reduce solute leaching.

We made several key assumptions, however, to ensure that any differences observed depended on the geometry (i.e. by comparing the ridge and furrow and flat geometries directly). Therefore, it might be of interest to incorporate specific factors of ridge and furrow geometry to determine the magnitude and severity of the mechanisms that were observed.

One of the key factors to consider is the soil water content in each of the ridge and furrow and flat geometries. Water movement is the key transport mechanism for solutes in soil (Nye & Tinker, 1977); therefore, it is vital to characterize the soil water profile accurately in both the ridge and furrow and flat soil geometries. In the mathematical model, we imposed a boundary condition at the base of the domains to replicate a shallow water table approximately 1 m below the soil surface. This allowed us to model solute movement within an idealized soil domain. However, with high spatial resolution field data to determine the soil water profile in the ridge and furrow and flat geometries we could indicate how different water profiles might affect the solute dynamics and mechanisms that we observed (i.e. solute penetration from furrow ponding and transport to the ridges from the furrow).

Understanding the water profile in soil would aid accurate determination of the mechanics of infiltration of rain into the soil. We used rainfall data with a resolution of 1 hour for a 6-month period, which limits the accuracy of identifying any change in infiltration capacity. This could play a key role in determining the severity of ponding and therefore the movement of solutes from the furrow to the ridges. Thus, understanding the infiltration capacity and soil water content with higher temporal and spatial resolution might aid our understanding of the magnitude of the effects observed.

Coupling knowledge of the water profile with the antecedent moisture conditions of the soil domains would enable us to model the movement of solutes applied to the soil more accurately. We modelled the initial water profile to be that formed under steady state conditions in the absence of roots, which is unlikely to resolve true field conditions accurately. Knowledge of past conditions would enable us to determine accurate initial conditions for the soil at the beginning of the simulations. This information could have a marked effect on several factors, such as the infiltration capacity, water table height and initial solute movement.

To understand further the observed solute accumulation and hot spot formation mechanisms, knowledge of the root architecture would play a key role. This would enable us to understand the distribution of root pressures in the root zones (i.e. the ridges of the system) and to predict the spatial distribution of solutes that collect in the ridges of the soil geometry. This would provide a more quantitative analysis of specific case studies relating to different solutes and root systems.

Earlier, we stated that to obtain a 'like for like' comparison, we kept the porosity between the ridge and furrow and flat systems the same. However, we know that some tillage methods can affect the porosity of the soil. Therefore, it would be useful to determine how any effect from tillage would affect solute movement from the furrows to the ridges and also spot formation in the ridges. This could have a substantial effect on the time required for the solute in the furrows to move to the ridges of the system.

Conclusions

Our modelling results bridged the gap between two contrasting findings for ridge and furrow systems because previous literature suggested that these soil systems might be vulnerable to solute leaching or can reduce solute leaching. We found the ridge and furrow structure could either impede or increase the penetration of solutes in soil depending on the rainfall activity immediately after solute application and the quantity of roots in the soil. In scenarios where there was considerable rain that generated substantial ponding immediately after solute application, we found that water infiltration from the surface acted as a strong transport mechanism for solutes in the furrow. This caused solutes in the furrow to move to a greater depth compared with the flat ground profile, where the effect of ponding was less substantial.

We found, however, that these trends were reversed when there was no ponding after solute application. Instead, roots in the ridges caused a dominant pressure gradient to form between the soil water pore pressure and pressure in the root xylem. This caused the solute in the ridged system to move towards the soil with abundant roots, where the solute accumulated adjacent to the root zone in the ridges. This effect impeded the movement of the solute compared with the flat field because solute was in the ridge and therefore not influenced by future ponding events in the furrow.

We determined that the vulnerability of the ridged system stemmed from immediate ponding on the soil surface after the application of a solute, and was not a function of the surface topology itself. Our results suggested that one of the important factors that should be considered when applying solutes to the soil surface is the immediate water treatment (i.e. rainfall or irrigation after the solute application) as this can have a substantial influence on solute penetration and leaching in ridged fields.

Acknowledgements

SJD acknowledges receipt of a BBSRC Syngenta Case PhD studentship BB/L5502625/1. TR and KRD are funded by ERC Consolidation grant 646809 DIMR.

All data supporting this study are openly available from the University of Southampton repository at https://doi.org/10.5258/SOTON/D0611.

References

Abbasi, F., Feyen, J. & van Genuchten, M.T. 2004. Two-dimensional simulation of water flow and solute transport below furrows: model calibration and validation. *Journal of Hydrology*, **290**, 63–79.

Alletto, L., Coquet, Y., Benoit, P., Heddadj, D. & Barriuso, E. 2010. Tillage management effects on pesticide fate in soils. A review. *Agronomy for Sustainable Development*, **30**, 367–400.

Alva, A.K., Hodges, T., Boydston, R.A. & Collins, H.P. 2002. Effects of irrigation and tillage practices on yield of potato under high production conditions in the Pacific Northwest. *Communications in Soil Science and Plant Analysis*, **33**, 1451–1460.

Azooz, R.H. & Arshad, M.A. 1996. Soil infiltration and hydraulic conductivity under long-term no-tillage and conventional tillage systems. *Canadian Journal of Soil Science*, **76**, 143–152.

Bargar, B., Swan, J. & Jaynes, D. 1999. Soil water recharge under uncropped ridges and furrows. *Soil Science Society of America Journal*, **63**, 1290–1299.

Bending, G.D. & Rodriguez-Cruz, M.S. 2007. Microbial aspects of the interaction between soil depth and biodegradation of the herbicide isoproturon. *Chemosphere*, **66**, 664–671.

Benjamin, J., Blaylock, A., Brown, H. & Cruse, R. 1990. Ridge tillage effects on simulated water and heat transport. *Soil &Tillage Research*, **18**, 167–180.

Benjamin, J., Ahuja, L. & Allmaras, R. 1996. Modelling corn rooting patterns and their effects on water uptake and nitrate leaching. *Plant and Soil*, **179**, 223–232.

Chen, X., Zhao, X., Wu, P., Wang, Z., Zhang, F. & Zhang, Y. 2011. Water and nitrogen distribution in uncropped ridgetilled soil under different ridge width. *African Journal of Biotechnology*, **10**, 11527–11536.

Commision Regulation 2018. Commision Regulation (EU) 2018/78 of 16 January 2018 amending Annexes II and III to Regulation (EC) No 396/2005 of the European Parliament and of the Council as regards maximum residue levels for 2-phenylphenol, bensulfuron-methyl, dimethachlor and lufenuron in or on certain products. *Official Journal of the European Union*, **61**, 6–30.

Duncan, S., Daly, K., Sweeney, P. & Roose, T. 2018. Mathematical modelling of water and solute movement in ridge plant systems with dynamic ponding. *European Journal of Soil Science*, **69**, 265–278.

European Food Safety Authority 2013. Scientific opinion on the report of the FOCUS groundwater working group (FOCUS, 2009): assessment of lower tiers. *EFSA Journal*, **11**, 3114.

Fahong, W., Xuqing, W. & Sayre, K. 2004. Comparison of conventional, flood irrigated, flat planting with furrow irrigated, raised bed planting for winter wheat in China. *Field Crops Research*, **87**, 35–42.

Feddes, R.A., Kowalik, P., Kolinska-Malinka, K. & Zaradny, H. 1976. Simulation of field water uptake by plants using a soil water dependent root extraction function. *Journal of Hydrology*, **31**, 13–26.

Fomsgaard, I.S. 1995. Degradation of pesticides in subsurface soils, unsaturated zone – a review of methods and results. *International Journal of Environmental Analytical Chemistry*, **58**, 231–245.

Gandar, P. & Tanner, C. 1976. Potato leaf and tuber water potential measurements with a pressure chamber. *American Potato Journal*, **53**, 1–14.

van Genuchten, M.T. 1980. AcClosed-form equation for predicting the hydraulic conductivity of unsaturated soils. *Soil Science Society of America Journal*, **44**, 892–898.

Hamlett, J., Baker, J. & Horton, R. 1990. Water and anion movement under ridge tillage: a field study. *Transactions of the ASAE*, **33**, 1859–1866.

Hatfield, J.L., Allmaras, R.R., Rehm, G.W. & Lowery, B. 1998. Ridge tillage for corn and soybean production: environmental quality impacts. *Soil & Tillage Research*, **48**, 145–154.

Huaccho, L. & Hijmans, R.J. 1999. *A global geo-referenced database of potato distribution for 1995–1997 (GPOT97)*. International Potato Center (CIP), Lima, Peru.

Jaynes, D.B. & Swan, J. 1999. Solute movement in uncropped ridge-tilled soil under natural rainfall. *Soil Science Society of America Journal*, **63**, 264–269.

Jordan, M.O., Kelling, K.A., Lowery, B., Arriaga, F.J. & Speth, P.E. 2013. Hill shape influences on potato yield, quality, and nitrogen use efficiency. *American Journal of Potato Research*, **90**, 217–228.

Kettering, J., Ruidisch, M., Gaviria, C., Ok, Y.S. & Kuzyakov, Y. 2013. Fate of fertilizer 15N in intensive ridge cultivation with plastic mulching under a monsoon climate. *Nutrient Cycling in Agroecosystems*, **95**, 57–72.

Kung, K. 1988. Ground truth about water flow pattern in a sandy soil and its influences on solute sampling and transport modeling. In: *International Conference and Workshop on the Validation of Flow and Transport Models for the Unsaturated Zone* (eds P. Wierenga & D. Bachelet), pp. 224–230. New Mexico State University, Las Cruces, NM.

Lehrsch, G.A., Sojka, R. & Westermann, D. 2000. Nitrogen placement, row spacing, and furrow irrigation water positioning effects on corn yield. *Agronomy Journal*, **92**, 1266–1275.

Leistra, M. & Boesten, J.J. 2010a. Measurement and computation of movement of bromide ions and carbofuran in ridged humic-sandy soil. *Archives of Environmental Contamination and Toxicology*, **59**, 39–48.

Leistra, M. & Boesten, J.J. 2010b. Pesticide leaching from agricultural fields with ridges and furrows. *Water, Air, & Soil Pollution*, **213**, 341–352.

Lesczynski, D.B. & Tanner, C.B. 1976. Seasonal variation of root distribution of irrigated, field-grown Russet Burbank potato. *American Potato Journal*, **53**, 69–78.

Lewis, W.C. & Rowberry, R.G. 1973. Some effects of planting depth and time and height of hilling on Kennebec and Sebago potatoes. *American Potato Journal*, **50**, 301–310.

Li, X., Su, D. & Yuan, Q. 2007. Ridge-furrow planting of alfalfa (Medicago sativa L.) for improved rainwater harvest in rainfed semiarid areas in Northwest China. *Soil & Tillage Research*, **93**, 117–125.

Liu, F., Shahnazari, A., Andersen, M.N., Jacobsen, S.-E. & Jensen, C.R. 2006. Physiological responses of potato (Solanum tuberosum L.) to partial root-zone drying: ABA signalling, leaf gas exchange, and water use efficiency. *Journal of Experimental Botany*, **57**, 3727–3735.

Morin, J. & Benyamini, Y. 1977. Rainfall infiltration into bare soils. *Water Resources Research*, **13**, 813–817.

Mundy, C., Creamer, N., Crozier, C. & Wilson, L.G. 1999. Potato production on wide beds: impact on yield and selected soil physical characteristics. *American Journal of Potato Research*, **76**, 323–330.

Noda, T., Takahata, Y., Sato, T., Ikoma, H. & Mochida, H. 1997. Combined effects of planting and harvesting dates on starch properties of sweet potato roots. *Carbohydrate Polymers*, **33**, 169–176.

Nye, P.H. & Tinker, P.B. 1977. *Solute Movement in the Soil-Root System*. University of California Press, Berkeley and Los Angeles, CA.

Rawsthorne, D. & Brodie, B. 1986. Relationship between root growth of potato, root diffusate production, and hatching of Globodera rostochiensis. *Journal of Nematology*, **18**, 379.

Ressler, D., Horton, R., Baker, J. & Kaspar, T. 1997. Testing a nitrogen fertilizer applicator designed to reduce leaching losses. *Applied Engineering in Agriculture*, **13**, 345–350.

Rice, P.J., Anderson, T.A. & Coats, J.R. 2002. Degradation and persistence of metolachlor in soil: effects of concentration, soil moisture, soil

depth, and sterilization. *Environmental Toxicology and Chemistry*, **21**, 2640–2648.

Robinson, D. 1999. A comparison of soil-water distribution under ridge and bed cultivated potatoes. *Agricultural Water Management*, **42**, 189–204.

Roose, T. & Fowler, A.C. 2004a. A model for water uptake by plant roots. *Journal of Theoretical Biology*, **228**, 155–171.

Roose, T. & Fowler, A.C. 2004b. A mathematical model for water and nutrient uptake by plant root systems. *Journal of Theoretical Biology*, **228**, 173–184.

Rowell, D.L., Martin, M.W. & Nye, P.H. 1967. The measurement and mechanism of ion diffusion in soils III. The effect of moisture content and soil-solution concentration on the self-diffusion of ions in soils. *Journal of Soil Science*, **18**, 204–221.

Shackelford, C.D. & Daniel, D.E. 1991. Diffusion in saturated soil. I: background. *Journal of Geotechnical Engineering*, **117**, 467–484.

Shock, C., Feibert, E. & Saunders, L. 1998. Potato yield and quality response to deficit irrigation. *Hortscience*, **33**, 655–659.

Smelt, J., Schut, C., Dekker, A. & Leistra, M. 1981. Movement and conversion of aldicarb and its oxidation products in potato fields. *Netherlands Journal of Plant Pathology*, **87**, 177–191.

Smethurst, J., Clarke, D. & Powrie, W. 2006. Seasonal changes in pore water pressure in a grass covered cut slope in London Clay. *Geotechnique*, **56**, 523–537.

Steele, D., Greenland, R. & Hatterman-Valenti, H. 2006. Furrow vs hill planting of sprinkler-irrigated russet Burbank potatoes on coarse-textured soils. *American Journal of Potato Research*, **83**, 249–257.

Steudle, E., Oren, R. & Schulze, E.-D. 1987. Water transport in maize roots measurement of hydraulic conductivity, solute permeability, and of reflection coefficients of excised roots using the root pressure probe. *Plant Physiology*, **84**, 1220–1232.

Tisdall, J.M. & Hodgson, A.S. 1990. Ridge tillage in Australia: a review. *Soil & Tillage Research*, **18**, 127–144.

Wayman, J. 1969. Experiments to investigate some of the problems in mechanisation associated with the cultivation of potatoes in beds. *European Potato Journal*, **12**, 200–214.